Contributions to the Mathematical and Numerical Analysis of Multiscale Kinetic Equations

Thomas Rey

▶ **To cite this version:**

Thomas Rey. Contributions to the Mathematical and Numerical Analysis of Multiscale Kinetic Equations. Numerical Analysis [math.NA]. Université de Lille, 2023. tel-04032898

HAL Id: tel-04032898
https://theses.hal.science/tel-04032898

Submitted on 16 Mar 2023

HAL is a multi-disciplinary open access archive for the deposit and dissemination of scientific research documents, whether they are published or not. The documents may come from teaching and research institutions in France or abroad, or from public or private research centers.

L'archive ouverte pluridisciplinaire **HAL**, est destinée au dépôt et à la diffusion de documents scientifiques de niveau recherche, publiés ou non, émanant des établissements d'enseignement et de recherche français ou étrangers, des laboratoires publics ou privés.

HABILITATION À DIRIGER LES RECHERCHES

Discipline : Mathématiques

Université de Lille, CNRS, Inria, UMR 8524

École Doctorale MADIS-631

présentée et soutenue publiquement le 17 Février 2023 par

Thomas Rey

Contributions à l'analyse mathématique et numérique d'équations cinétiques multi-échelles

---

Contributions to the Mathematical and Numerical Analysis of Multiscale Kinetic Equations

---

Après avis de :

Vincent Calvez	*Directeur de Recherche CNRS à l'Université Claude Bernard Lyon 1*
Axel Klar	*Professor à la Technische Universität Kaiserslautern*
Gabriella Puppo	*Professor à La Sapienza Università di Roma*

Devant la commission formée de :

Vincent Calvez	*Directeur de Recherche CNRS à l'Université Claude Bernard Lyon 1*, rapporteur
Claire Chainais-Hillairet	*Professeure des Universités à l'Université de Lille*, garante
Francis Filbet	*Professeur des Universités à l'Université Toulouse 3 Paul Sabatier*, examinateur
François Golse	*Professeur des Universités à l'École Polytechnique*, président
Axel Klar	*Professor à la Technische Universität Kaiserslautern*, rapporteur
Clément Mouhot	*Professor à l'Université de Cambridge*, examinateur
Gabriella Puppo	*Professor à La Sapienza Università di Roma*, rapporteuse

à Camille, Raphaël et Fred <3

Remerciements

I would first like to express my deepest gratitude to Gabriella Puppo, Vincent Calvez and Axel Klar for their time spent to read and evaluate thoroughly this manuscript. I would also like to extend this gratitude first to Claire Chainais-Hillairet for accepting to be my mentor for this Habilitation, and helping me so much in all the process. I also like to deeply thanks François Golse for accepting being part of the committee. And finally, last but not least, I couldn't thank enough Francis Filbet and Clément Mouhot, for being constantly helpful and caring since the beginning of my research, almost 14 years ago.

I am also extremely indebted to all the colleagues at Université de Lille, without whom nothing would have been possible. First, I have to thank the ANEDP team which welcomed me in Lille. Next in this list comes the Centre Inria de l'Université de Lille, where part of this work was carried out, specially the Rapsodi research team (and of course the sister team Paradyse) and all the local support team. The Laboratoire Paul Painlevé in a whole is an extremely nice place to do research, and I am deeply grateful to all the researchers and administrative staff which were always present for help and advice. The same goes of course to the Département de Mathématiques, whose staff is fundamental for the smooth run of... basically everything.

Nothing in this thesis could have been done without all my wonderful collaborators, whether they are senior established people or bright younglings, soon to be researchers.

Such a list wouldn't be complete without mentioning my family and my friends. They have provided love, guidance, encouragement and support in all these years, and this manuscript could not exist without them.

Contents

1 Introduction **1**

List of publications . . . 3

1.1 On kinetic equations and related models . . . 5

1.1.1 Microscopic scale . . . 5

1.1.2 Macroscopic scale . . . 5

1.1.3 Mesoscopic scale and kinetic formalism . . . 6

1.2 The Boltzmann equation . . . 8

1.3 Some kinetic models of interest in this thesis . . . 11

1.3.1 The BGK Operator . . . 11

1.3.2 The granular gases equation . . . 12

1.3.3 Multiple species Boltzmann equation . . . 12

1.3.4 Quantum Boltzmann equation . . . 13

1.3.5 Run-and-tumble chemotactic motion. . . . 14

1.4 Other topics . . . 15

1.5 Notations and functional setting . . . 16

2 Spectral Methods **19**

2.1 From kinetic equations to Discrete Velocity Models . . . 20

2.2 Fourier-Galerkin spectral methods for the Boltzmann equation . . . 21

2.2.1 The classical spectral method . . . 21

2.2.2 A good domain truncation is tricky . . . 22

2.2.3 The fast spectral method . . . 24

2.2.4 Stability and consistency . . . 25

2.3 Structure preserving spectral methods . . . 27

2.3.1 Equilibrium preserving Fourier spectral methods . . . 27

2.3.2 Numerical simulations of the equilibrium preserving method . . . 29

2.3.3 Moment preserving Fourier spectral methods . . . 31

2.4 Towards high performance computing applications . . . 36

2.5 Perspectives . . . 41

3 On the Granular Gases Equation **43**

3.1 The granular gases equation . . . 44

3.1.1 Cauchy theory of the granular gases equation . . . 49

3.1.2 Large time behavior . . . 50

3.1.3 Compressible hydrodynamic limits . . . 52

3.2 Spectral methods for the granular gases operator . . . 56

3.2.1 The direct Fourier spectral method . . . 57
3.2.2 The fast Fourier spectral method . . . 57
3.3 Numerical experiments and results . . . 59
3.4 Perspectives . . . 65

4 Asymptotic Behaviors of Numerical Kinetic Equations 67
4.1 Hydrodynamic limits of kinetic equations . . . 68
4.1.1 Chapman-Enskog expansion . . . 68
4.1.2 On the linearized Boltzmann operator . . . 70
4.1.3 Hierarchy of fluid descriptions . . . 73
4.2 Asymptotic Preserving numerical methods . . . 75
4.2.1 Projective integration . . . 77
4.2.2 Telescopic projective integration . . . 79
4.2.3 Parameters for projective and telescopic projective integration . . . 81
4.2.4 Applications to single species gases . . . 83
4.2.5 Applications to gas mixtures . . . 90
4.3 Discrete Hypocoercivity . . . 96
4.3.1 L^2—Hypocoercivity . . . 97
4.3.2 The full implicit scheme . . . 97
4.3.3 The discrete AP and hypocoercivity properties . . . 99
4.4 Hybridization through domain indicators . . . 101
4.4.1 Domain indicators . . . 101
4.4.2 Numerical simulations . . . 103
4.5 Perspectives . . . 107

Bibliography 109

CHAPTER 1 | Introduction

The Boltzmann is magnificent. I have almost finished it. He is a masterly expounder. I am firmly convinced that the principles of the theory are right, which means that I am convinced that in the case of gases we are really dealing with discrete mass points of definite finite size, which are moving according to certain conditions

Albert Einstein
Private letter [163]

Contents

List of publications 3
1.1 On kinetic equations and related models 5
1.2 The Boltzmann equation 8
1.3 Some kinetic models of interest in this thesis 11
1.4 Other topics 15
1.5 Notations and functional setting 16

Modern societies face major challenges in science, technology and industry, induced by the complexity of our dynamically evolving world. Examples are pollution, traffic and mobility, financial systems, climate and disease spreading, to name but a few. In all these domains, mathematical models and computer simulations are indispensable tools, because they allow designing and optimizing systems using virtual (simulated) prototypes, in situations where physical prototypes can be impossible, unethical or impractical. Many of the systems above consist of large numbers of particles that interact in a highly non-intuitive way. In pollution, these particles can be fine dust or aerosol particles, in mobility they are individual vehicles, in financial systems, they are individual banks or even consumers, etc. Current challenges force scientists to take into account with more detail the precise interactions between individual particles, as these directly influence the behavior that emerges at the macroscopic scale of interest. However, to date, computer simulation of such interacting particle systems is usually done with highly approximate (macroscopic) models to reduce the computational complexity. An intermediate approach to address the coarseness of these macroscopic models consists of using a so-called kinetic description of the system.

Kinetic theory is a cornerstone of modern physics. It can be traced back to the works in thermodynamics of Daniel Bernoulli, Amedeo Avogadro and Sadi Carnot in the late eighteenth and early nineteenth centuries [17, 12, 53]. One of the earliest mathematical contributions to what would be later called the kinetic theory of rarefied gases is not due to Ludwig Boltzmann, but to James Clerk Maxwell in one of his first essays [165]. In that work, Maxwell studied the stability of Saturn's rings, and concluded that for such large structures to be stable, they must be composed of "independent satellites", interacting by collisions. Note that this essay was published more than 15 years before the seminal works by the same Maxwell and of course Boltzmann [166, 30], that would properly introduce what we now know as the Boltzmann equation for rarefied gases. It is historically the first mathematical occurrence of a kinetic equation.

Kinetic equations were hence first used to represent a gas as a set of particles undergoing instantaneous collisions interspersed with ballistic motion. Nowadays, these models appear in a variety of sciences and applications, such as astrophysics, aerospace and nuclear engineering, semiconductors, fusion processes in plasmas, as well as biology, finance and social sciences. The common mathematical structure of such models consists in a combination of a linear transport term with one or more stiff, nonlinear interaction terms, which together dictate the time evolution of the distribution of particles in a six-dimensional position-velocity phase space.

This dissertation is devoted to the study of multi-scale kinetic equations, both theoretically and numerically. These equations usually take the form of Boltzmann-like systems. More precisely, for a given nonnegative initial condition f_0, they describe the evolution of a particle distribution function $f^\varepsilon = f^\varepsilon(t,x,v)$, for $t \geq 0$, $x \in \Omega \subset \mathbb{R}^d$ for $d \leq 3$ and $v \in \mathbb{R}^d$, solution to the scaled, initial-boundary value problem

$$\begin{cases} \varepsilon^\alpha \dfrac{\partial f^\varepsilon}{\partial t} + v \cdot \nabla_x f^\varepsilon = \dfrac{1}{\varepsilon^\beta} \mathcal{Q}(f^\varepsilon), \\ \\ f^\varepsilon(0,x,v) = f_0(x,v), \end{cases} \tag{1.1}$$

where the collision operator $\mathcal{Q}$ will be described in the next sections and ε is a small parameter describing the *rarefaction* of the gas. The open set Ω is a bounded Lipschitz-continuous domain of $\mathbb{R}^d$, which means that the model (1.1) will also have to be supplemented with boundary conditions. The nonnegative parameters α and β will allow to study different types of asymptotic behaviors.

This problematic has inspired the research I have carried out so far. The following sections will describe these problems with more details, providing an overview of the state of the art in kinetic theory. The next chapters will then focus on some of the works I authored after my PhD thesis (*i.e.* since October 2012). More precisely,

- Chapter 2 presents the works [FPR15, PR17, DLNR18, PR21, PR22] which concern spectral methods for various kinetic models;
- Chapter 3 reviews the works [GdSMM+15, JR17, CHMR21] I carried out on the topic of granular gases;
- Chapter 4 reviews the works [FR15, MRS17, MRS19, BHR20, BR22] I co-authored on Asymptotic-Preserving and related numerical methods.

Each of these three main chapters, albeit related, are mostly independent. They are concluded with some open perspectives. Some works which couldn't fit in these three large categories will be briefly presented at the end of this current introductory Chapter.

List of publications

[BDMR20] S. Billiard, M. Derex, L. Maisonneuve, and T. Rey. Convergence of knowledge in a cultural evolution model with population structure, random social learning and credibility biases. *Math. Models Methods Appl. Sci.*, 30(14):2691–2723, 2020.

[BHR20] M. Bessemoulin-Chatard, M. Herda, and T. Rey. Hypocoercivity and Diffusion Limit of a Finite Volume Scheme for Linear Kinetic Equations. *Math. Comput.*, 89(323):1093–1133, November 2020.

[BLRT22] S. Billiard, H. Leman, T. Rey, and V. C. Tran. Continuous limits of large plant-pollinator random networks and some applications. *To appear in Maths in A.*, 2022.

[BR22] R. Bailo and T. Rey. Projective and Telescopic Projective Integration for Non-Linear Kinetic Mixtures. *J. Comput. Phys.*, 458:111082111082, 1 June 2022 2022.

[CHMR21] J. A. Carrillo, J. Hu, Z. Ma, and T. Rey. Recent development in kinetic theory of granular materials: analysis and numerical methods. In G. Albi, S. Merino-Aceituno, A. Nota, and M. Zanella, editors, *Trails in Kinetic Theory*. Springer, 2021.

[DLNR18] G. Dimarco, R. Loubère, J. Narski, and T. Rey. An efficient numerical method for solving the Boltzmann equation in multidimensions. *J. Comput. Phys.*, 353:46–81, 2018.

[EKR20] A. El Keurti and T. Rey. Finite Volume Method for a System of Continuity Equations Driven by Nonlocal Interactions. In *Finite Volumes for Complex Applications IX - Methods, Theoretical Aspects, Examples: FVCA 9, Bergen*, volume 323, pages 233–241. Springer, Springer Nature, 2020.

[FPR15] F. Filbet, L. Pareschi, and T. Rey. On steady-state preserving spectral methods for homogeneous Boltzmann equations. *C. R. Acad. Sci. Paris, Ser. I*, 353(4):309–314, 2015.

[FR13] * F. Filbet and T. Rey. A Rescaling Velocity Method for Dissipative Kinetic Equations - Applications to Granular Media. *J. Comput. Phys.*, 248:177–199, 2013.

[FR15] F. Filbet and T. Rey. A Hierarchy of Hybrid Numerical Method for Multi-Scale Kinetic Equations. *SIAM J. Sci. Comput.*, 37(3):A1218–A1247, 2015.

[GdSMM+15] M. I. García de Soria, P. Maynar, S. Mischler, C. Mouhot, T. Rey, and E. Trizac. Towards an H-theorem for granular gases. *J. Stat. Mech. Theory Exp.*, 2015(11):P11009, 2015.

[JR17] P.-E. Jabin and T. Rey. Hydrodynamic Limit of Granular Gases to Pressureless Euler in Dimension 1. *Q. Appl. Math.*, 75:155–179, 2017.

[MPR13] * C. Mouhot, L. Pareschi, and T. Rey. Convolutive Decomposition and Fast Summation Methods for Discrete-Velocity Approximations of the Boltzmann Equation. *ESAIM Math. Model. Numer. Anal.*, 47(5):1515–1531, 2013.

[MR21] A. Mouton and T. Rey. On Deterministic Numerical Methods for the Quantum Boltzmann-Nordheim Equation. I. Spectrally Accurate Approximations, Bose-Einstein Condensation, Fermi-Dirac Saturation. arXiv preprint 2110.13735, 2021.

[MRS17] W. Melis, T. Rey, and G. Samaey. Projective Integration for Nonlinear BGK Kinetic Equations. In C. Cancès and P. Omnes, editors, *Finite Volumes for Complex Applications VIII - Hyperbolic, Elliptic and Parabolic Problems*, volume 200, pages 145–153, Cham, 2017. Springer International Publishing.

[MRS19] W. Melis, T. Rey, and G. Samaey. Projective and telescopic projective integration for the nonlinear BGK and Boltzmann equations. *SMAI J. Comput. Math.*, 5:53–88, 2019.

[PR17] L. Pareschi and T. Rey. Residual equilibrium schemes for time dependent partial differential equations. *Comput. Fluids*, 156:329–342, 2017.

[PR21] L. Pareschi and T. Rey. On the stability of equilibrium preserving spectral methods for the homogeneous Boltzmann equation. *App. Math. Letters*, 120:107187, October 2021.

[PR22] L. Pareschi and T. Rey. Moment preserving Fourier-Galerkin spectral methods and application to the Boltzmann equation. *SIAM J. Numer. Anal.*, 2022.

[Rey12] * T. Rey. Blow Up Analysis for Anomalous Granular Gases. *SIAM J. Math. Anal.*, 44(3):1544–1561, 2012.

[Rey13] * T. Rey. A Spectral Study of the Linearized Boltzmann Equation for Diffusively Excited Granular Media. Preprint arXiv 1310.7234, 2013.

[RT13] * T. Rey and G. Toscani. Large-time Behavior of the Solutions to Rosenau Type Approximations to the Heat Equation. *SIAM J. App. Math.*, 73(4):1416–1438, 2013.

[RT16] T. Rey and C. Tan. A Rescaling Velocity Method for Collisional Kinetic Equations – Application to Flocking. *SIAM J. Numer. Anal.*, 54(2):641–664, 2016.

Note. The starred publications were written during my PhD. As such, they are not presented in this thesis. They can be cited in the text when relevant.

1.1 On kinetic equations and related models

Kinetic equations now cover a very wide array of physically and biologically relevant systems. We shall present in this Section some of the models I worked on since defending my PhD.

Consider a system of indistinguishable particles contained in a domain Ω observed on a time interval $[0, T)$ with $T \in [0, \infty]$. There are three levels of description of this type of many-particle system.

1.1.1 Microscopic scale

In classical mechanics, a system of N particles of mass 1 can be completely described by their positions $(X_i(t))_{i\in\{1,\dots,N\}}$ and velocities $(V_i(t))_{i\in\{1,\dots,N\}}$ at time $t \in [0, T]$. The dynamics of i-th particle, governed by its interaction with the environment and the other particles is given by Newton's equations of motion [156]

$$\forall i = 1, \dots, N, \quad \begin{cases} \dfrac{dX_i}{dt}(t) &= V_i(t), \\ \dfrac{dV_i}{dt}(t) &= F_i(t, X_i(t), V_i(t)). \end{cases} \tag{1.2}$$

In the second equation $F_i(t, X_i(t), V_i(t))$ denotes the force field at time t on particle i which is located at $X_i(t)$ and has velocity $V_i(t)$. If particles are interacting with one another, then the force field F_i depends on the positions and velocities of the other particles. Typically, if the particles interact through an interaction potential ϕ (for instance through gravitational or electrostatic interactions), then

$$F_i(t, X_i, V_i) = -\sum_{j\neq i} \nabla\phi(X_i(t) - X_j(t)).$$

This makes (1.2) a system of 2N coupled ordinary differential equations. In a gas or a plasma the number N of particles is typically of the size of the Avogadro number, that is $N \approx 6.10^{23}$ per mole. The size of this system of equations makes it almost impossible to extract any relevant qualitative information of the dynamics or perform numerical simulations of the system. Therefore, while it allows for an exhaustive description of the physical system, the microscopic scale is intractable in practice.

1.1.2 Macroscopic scale

Macroscopic models result in the continuous descriptions of matter. Instead of considering each discrete particle, one applies Newton's laws to infinitesimal volumes in the space domain Ω [157]. This leads to partial differential equations on macroscopic observable quantities such as the

- Macroscopic density $\rho : (t, x) \mapsto \rho(t, x) \in [0, \infty)$;
- Mean velocity $\boldsymbol{u} : (t, x) \mapsto \boldsymbol{u}(t, x) \in \mathbb{R}^d$;
- Temperature $T : (t, x) \mapsto T(t, x) \in [0, \infty)$.

In the context of gas dynamics the equations linking these quantities are for instance the Euler or Navier-Stokes equations. An example of such macroscopic model is Euler's equations of compressible

gas dynamics, in the case of a perfect monoatomic gas in dimension $d = 3$, which are given by

$$\begin{cases} \partial_t \rho + \nabla_x \cdot (\rho\, \boldsymbol{u}) = 0\,, \\ \partial_t (\rho \boldsymbol{u}) + \nabla_x \cdot (\rho\, \boldsymbol{u} \otimes \boldsymbol{u}) + \nabla_x (\rho \mathrm{T}) = 0\,, \\ \partial_t (\rho (\frac{1}{2}|\boldsymbol{u}|^2 + \frac{3}{2}\mathrm{T})) + \nabla_x \cdot (\rho\, \boldsymbol{u} (\frac{1}{2}|\boldsymbol{u}|^2 + \frac{5}{2}\mathrm{T})) = 0\,, \end{cases} \tag{1.3}$$

While the complexity of the microscopic scale stems from the huge number of equations, it comes in the macroscopic viewpoint from the infinite dimensional dynamics. Such models are well-suited for practical use since qualitative analysis as well as numerical simulations are (difficult but) tractable. Nevertheless in some applications, such as the description of the reentry of a shuttle in the high atmosphere or of a plasma in a tokamak, too much of the information of the microscopic scale has been lost and a more precise mathematical description is needed.

1.1.3 Mesoscopic scale and kinetic formalism

The mesoscopic scale is an intermediate viewpoint between the microscopic and the macroscopic scale. In this scale, the system at time t can be described statistically in the single particle phase space, by considering the distribution function $f \equiv f(t, x, v)$ that is the number density of particles which are located at the position $x \in \Omega$ and have velocity $v \in \mathbb{R}^d$ at time t. More precisely, if $\omega \subset \Omega$ and $\mathcal{V} \subset \mathbb{R}^d$ are (measurable) subsets of the space and velocity domains, then the total number of particles to be found in ω with velocities in $\mathcal{V}$ at time t is

$$\iint_{\omega \times \mathcal{V}} f(t, x, v)\, \mathrm{d}x\, \mathrm{d}v\,.$$

Velocity moments and global quantities. The kinetic distribution function is related to macroscopic quantities through velocity moments. The latter thus plays a very important role in kinetic theory. More precisely, from a given distribution function f, one can define the related *macroscopic density*

$$\rho(t, x) \;=\; \int_{\mathbb{R}^d} f(t, x, v)\, \mathrm{d}v\,, \tag{1.4}$$

current density

$$j(t, x) \;=\; \int_{\mathbb{R}^d} v\, f(t, x, v)\, \mathrm{d}v \in \mathbb{R}^d\,, \tag{1.5}$$

mean velocity

$$\boldsymbol{u}(t, x) \;=\; \frac{1}{\rho(t, x)} \int_{\mathbb{R}^d} v\, f(t, x, v)\, \mathrm{d}v \;=\; \frac{j(t, x)}{\rho(t, x)} \in \mathbb{R}^d\,, \tag{1.6}$$

temperature

$$\mathrm{T}(t, x) \;=\; \frac{1}{d\, \rho(t, x)} \int_{\mathbb{R}^d} |v - \boldsymbol{u}(t, x)|^2 f(t, x, v)\, \mathrm{d}v\,, \tag{1.7}$$

and *local kinetic energy*

$$\mathrm{E}(t, x) \;=\; \frac{1}{2} \int_{\mathbb{R}^d} |v|^2 f(t, x, v)\, \mathrm{d}v \;=\; \left(\frac{1}{2} |\boldsymbol{u}(t, x)|^2 + \frac{d}{2} \mathrm{T}(t, x) \right) \rho(t, x)\,. \tag{1.8}$$

By integrating some velocity moments in the space variable, one obtains global quantities (which depend only on time) of the given physical system such as *the total mass / total number of particles*[1]

$$\mathrm{M}(t) \;=\; \iint_{\Omega\times\mathbb{R}^d} f(t,x,v)\,\mathrm{d}v\,\mathrm{d}x \;=\; \int_{\Omega} \rho(t,x)\,\mathrm{d}x\,, \tag{1.9}$$

and the *global entropy* of the system

$$\mathrm{H}(t) = \int_{\Omega\times\mathbb{R}^d} f(t,x,v)\log(f(t,x,v))\,\mathrm{d}x\;\mathrm{d}v\,. \tag{1.10}$$

Free transport and linear Vlasov equation. The simplest kinetic equation, describing a population of particles travelling on straight lines at constant speed without any interaction is given by the so-called *free transport equation*

$$\partial_t f(t,x,v) + v\cdot\nabla_x f(t,x,v) \;=\; 0\,. \tag{1.11}$$

If the particles are all subject to a given external force $\mathrm{F}\equiv\mathrm{F}(t,x,v)$ and are not interacting with one another, then the kinetic equation driving the system is the linear Vlasov equation

$$\partial_t f(t,x,v) + v\cdot\nabla_x f(t,x,v) + \nabla_v\cdot(\mathrm{F}(t,x,v)f(t,x,v)) \;=\; 0\,. \tag{1.12}$$

The microscopic counterpart of this equation is Newton's system (1.2) with $\mathrm{F}_i = \mathrm{F}$ for all $i\in\{1,\dots,\mathrm{N}\}$. Actually in this simple setting the link between the microscopic and mesoscopic scale can be made rigorous easily. Indeed from (1.2) we can define the empirical distribution

$$\mu_{\mathrm{N}}(t) = \sum_{i=1}^{\mathrm{N}} \lambda_i \delta_{(\mathrm{X}_i(t),\mathrm{V}_i(t))}\,,$$

where for $(x,v)\in\Omega\times\mathbb{R}^d$, $\delta_{(x,v)}$ is the Dirac distribution at (x,v) in the phase space and $\lambda_i\in\mathbb{R}$. In particular, if the trajectories $(\mathrm{X}_i(t),\mathrm{V}_i(t))\in\Omega\times\mathbb{R}^d$, $i=1,\dots\mathrm{N}$ solve Newton's equations (1.2) with an external force $\mathrm{F}_i=\mathrm{F}$, the empirical distribution μ_{N} solves the linear Vlasov equation (1.12) in $\mathcal{D}'((0,\mathrm{T})\times\Omega\times\mathbb{R}^d)$.

Maxwellian distribution. One very important object in kinetic theory is the so-called *Maxwellian distribution* function. It is given by the following Gaussian with mass $\rho\in\mathbb{R}$, average $\boldsymbol{u}\in\mathbb{R}^d$ and covariance matrix $\mathrm{T}\mathrm{I}_d$

$$\mathcal{M}_{(\rho,\boldsymbol{u},\mathrm{T})}(v) \;=\; \frac{\rho}{(2\pi\mathrm{T})^{d/2}}\exp\left(-\frac{|v-\boldsymbol{u}|^2}{2\mathrm{T}}\right). \tag{1.13}$$

Physically, if the particle velocity density is given by (1.13), then the gas is said to be at *local thermodynamical equilibrium* or just *local equilibrium*.

The Maxwellian links the mesoscopic scale to the macroscopic scale. More precisely, if ρ, $\boldsymbol{u}$ and T are given smooth functions and the function

$$(t,x,v) \;\mapsto\; \mathcal{M}_{(\rho(t,x),\boldsymbol{u}(t,x),\mathrm{T}(t,x))}(v)\,.$$

solves the free transport equation (1.11) then $(\rho,\boldsymbol{u},\mathrm{T})$ solves the compressible Euler system (1.3).

[1] We recall that the mass of one particle has been taken equal to one.

1.2 The Boltzmann equation

When we start from a system of particles without interactions between particles, the linear Vlasov equation naturally arises. In the case of interacting particles, one can derive (at least formally, sometimes rigorously [106, 135, 192]) nonlinear kinetic models in the limit $N \to \infty$. The problem of the rigorous mathematical derivation of nonlinear kinetic models from microscopic dynamics is still a largely open and an important research problem, that can be traced back to Hilbert[2].

Briefly, from the position and velocities of the N particles, one introduces the joint distribution function for all of the particles $F_N(t, x_1, \dots, x_N, v_1, \dots, v_N)$ which will solve a Liouville equation. Then, by integration, one writes an equation on the single particle distribution, defined by the marginal

$$f_N^{(1)}(t, x, v) = \int_{(\mathbb{R}^d \times \mathbb{R}^d)^{N-1}} F_N(t, x, x_2, \dots, x_N, v, v_2, \dots, v_N)\, dx_2 \dots dx_N\, dv_2 \dots dv_N\,,$$

and tries to take limits as $N \to \infty$ to obtain an equation on $f = \lim f_N^{(1)}$. The single particle distribution will actually be linked to other marginals, $f_N^{(2)} \equiv f_N^{(2)}(t, x, v, y, w), \dots, f_N^{(N)} = F_N$ of F_N through the so-called BBGKY hierarchy of equations. Several assumptions are necessary to achieve this limiting process, one being the molecular chaos assumption, stating that at the limit particles are uncorrelated $f_N^{(2)} \sim f \otimes f \equiv f(t,x,v)f(t,y,w)$ as $N \to \infty$. Depending on scaling assumptions made in the limiting process and on the initial microscopic system under consideration, two types of models may arise at the limit.

- The first class of model that can be obtained is called *mean-field kinetic equations*, or mean-field *Vlasov* equations [136]. This type of kinetic equation describes the collective effect on one particle of every other particles. Often this assumption is called *long range interactions*. Since it is not the main topic of this dissertation, the interested reader can consult [200, 178, 184, 177, 136].
- The second type of model is called *collisional kinetic equations*, or *Boltzmann* type equations [106]. In contrast to mean field models, collisional kinetic equations arise from microscopic dynamics with *short range interactions*. Instead of collective effects, the important part here is binary interactions between pairs of particles.

Hybrid models which combine the features of Vlasov and Boltzmann equations are also frequently used in applications and studied mathematically as well.

The Boltzmann equation is a well-known and important collisional kinetic model for a dilute gas of particles interacting at short distance. For instance it can be used to describe the air in the high atmosphere where molecules only interact when they collide. It is one of the main model studied in this dissertation.

Underlying assumptions. In order to derive the equation in its seminal 1872 paper [30], Boltzmann made several assumptions, which we are going to briefly recall here:

[2] "As to the axioms of the theory of probabilities, it seems to me desirable that their logical investigation should be accompanied by a rigorous and satisfactory development of the method of mean values in mathematical physics, and in particular in the kinetic theory of gases. ... Boltzmann's work on the principles of mechanics suggests the problem of developing mathematically the limiting processes, there merely indicated, which lead from the atomistic view to the laws of motion of continua." D. Hilbert [126]

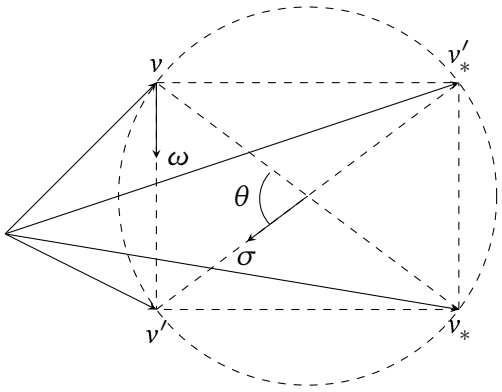

Figure 1.1: Geometry of elastic collisions.

The first assumption is that particles interact via *binary collisions*. This has to be understood in the sense that two particles trajectories are strongly deviated in a short time if they become close to one another. Implicitly, we assume that the gas is *dilute enough* that the effect of interactions involving more than two particles can be neglected.

Moreover, collisions are *localized in space and time*, namely they are happening at given point (t,x).

The collisions are elastic, namely *momentum and kinetic energy are conserved*. Let v' and $v'_* \in \mathbb{R}^d$ be the pre-collisional (before collisions) and $v, v_* \in \mathbb{R}^d$ post-collisional velocities (after collisions). Then we assume that

$$\left\{ \begin{array}{rcl} v+v_* & = & v'+v'_*\,, \\ |v|^2+|v_*|^2 & = & |v'|^2+|v'_*|^2\,. \end{array} \right. \tag{1.14}$$

Observe that this is a system of $d+1$ scalar equations with $2d$ scalar unknowns so we expect to describe all solutions thanks to $d-1$ scalar parameters. There are several ways to define solutions. A first way is the so called *ω-representation*

$$\left\{ \begin{array}{rcl} v' & = & v-(\omega\cdot(v-v_*))\omega\,, \\ v'_* & = & v_*+(\omega\cdot(v-v_*))\omega\,, \end{array} \right. \tag{1.15}$$

for a given $\omega \in \mathbb{S}^{d-1}$. A second way is the so-called *σ-representation*

$$\left\{ \begin{array}{l} v' = \dfrac{v+v_*}{2}+\sigma\dfrac{|v-v_*|}{2}\,, \\ v'_* = \dfrac{v+v_*}{2}-\sigma\dfrac{|v-v_*|}{2}\,, \end{array} \right. \tag{1.16}$$

where $\sigma \in \mathbb{S}^{d-1}$. On Fig. 1.1, the geometry relating these quantities is illustrated in the phase space.

Besides, collisions are assumed to be *microreversible*. It means that the microscopic dynamics is reversible, namely unchanged by changing the sign of time and velocity.

Finally, Boltzmann made the *molecular chaos assumption*: the velocities of two particles which are about to collide are uncorrelated. Mathematically it means that the joint probability distribution of two particles velocities is given by the tensor product of the probability distribution of the velocity of a single particle. See the book [106] for an extensive discussion on this topic.

The equation and its basic properties. From there the Boltzmann equation can be (at least formally) derived. It describes the evolution of f and reads with nonscaled variables as

$$\partial_t f + v \cdot \nabla_x f = \mathcal{Q}_{\mathcal{B}}(f,f)\,, \tag{1.17}$$

where $\mathcal{Q}_{\mathcal{B}}$ denotes the *collision operator*. It is a *non-local bilinear* integral operator acting on functions in the velocity variable only. It reads for any ϕ and $\psi \in \mathcal{C}_c^0(\mathbb{R}^d)$,

$$\mathcal{Q}_{\mathcal{B}}(\phi,\psi) = \iint_{\mathbb{R}^d\times\mathbb{S}^{d-1}} \big[\phi(v')\psi(v'_*) - \phi(v)\psi(v_*)\big]\mathrm{B}(v-v_*,\sigma)\,\mathrm{d}v_*\,\mathrm{d}\sigma\,, \tag{1.18}$$

where $v', v'_*, v, v_* \in \mathbb{R}^d$ and $\sigma \in \mathbb{R}^{d-1}$ are related by (1.16).

In addition, the *collision kernel* B has the general form

$$\mathrm{B}(v-v_*,\sigma) \;=\; |v-v_*|\,\Sigma(|v-v_*|,\cos\theta)\,, \qquad \text{with } \Sigma > 0 \tag{1.19}$$

where Σ is the *cross-section* corresponding to interparticle force and θ is the *deviation angle* satisfying $\cos(\theta) = \left\langle \frac{v-v_*}{|v-v_*|}, \sigma \right\rangle$. This term conserves a trace of the type of interaction between particles at the microscopic level.

Let us observe that provided that the angular cross-section is integrable on the unit sphere (the so-called *Grad's cut-off* assumption [121]), the collision operator is formally the difference between two terms

$$\mathcal{Q}_{\mathcal{B}}(\phi,\psi) = \mathcal{Q}^+_{\mathcal{B}}(\phi,\psi) - \mathcal{Q}^-_{\mathcal{B}}(\phi,\psi),$$

where

$$\mathcal{Q}^+_{\mathcal{B}}(\phi,\psi) = \iint_{\mathbb{R}^d\times\mathbb{S}^{d-1}} \mathrm{B}\,\phi'\psi'_*\,\mathrm{d}v_*\,\mathrm{d}\sigma\,, \quad \mathcal{Q}^-_{\mathcal{B}}(\phi,\psi) = \phi\int_{\mathbb{R}^d}\psi_*\left(\int_{\mathbb{S}^{d-1}}\mathrm{B}\,\mathrm{d}\sigma\right)\mathrm{d}v_*\,,$$

where we used the shorthand notation f_*, f' and f'_* to designate $f(v_*)$, $f(v')$ and $f(v'_*)$ respectively.

From this decomposition the time derivative of the distribution is the sum of three contributions in the Boltzmann equation (1.17). As in the Vlasov equation the term $v\cdot\nabla_x f(t,x,v)$ accounts for the transport of particles in the physical space at their velocity v. The *gain term* $\mathcal{Q}^+_{\mathcal{B}}(f,f)(t,x,v)$ accounts for the increase of particles with velocity v from all the collisions between pairs of particles with velocities v' and v'_*. The *loss term* $-\mathcal{Q}^+_{\mathcal{B}}(f,f)(t,x,v)$ stands for the decrease of particles with velocity v due to collisions with particles with velocity v_*, thus changing the velocities of the pair by v' and v'_*.

The Boltzmann equation conserves mass, momentum and kinetic energy thanks to the following property of the collision kernel: for all ϕ, ψ and $\varphi \in \mathcal{C}_c^0(\mathbb{R}^d)$,

$$\int_{\mathbb{R}^d}\mathcal{Q}_{\mathcal{B}}(\phi,\psi)(v)\,\varphi(v)\,\mathrm{d}v = \frac{1}{2}\iiint_{\mathbb{R}^d\times\mathbb{R}^d\times\mathbb{S}^{d-1}}\phi\psi_*\big[\varphi'+\varphi'_*-\varphi-\varphi_*\big]\mathrm{B}(u,\sigma)\,\mathrm{d}v\,\mathrm{d}v_*\,\mathrm{d}\sigma\,. \tag{1.20}$$

As a consequence, for all $f \in \mathrm{L}^\infty(\mathbb{R}^3)$ and $i = 1,\dots,d$,

$$\int_{\mathbb{R}^d}\mathcal{Q}_{\mathcal{B}}(f,f)\,\mathrm{d}v = \int_{\mathbb{R}^d}\mathcal{Q}_{\mathcal{B}}(f,f)\,v_i\,\mathrm{d}v = \int_{\mathbb{R}^d}\mathcal{Q}_{\mathcal{B}}(f,f)\,|v|^2\,\mathrm{d}v = 0\,. \tag{1.21}$$

These are the only functions of v with such properties. We call them *collisional invariants*. They allow us to show Boltzmann's celebrated *H-Theorem* [211]:

Theorem 1.2.1 (H-Theorem). *Let $f = f(t,x,v)$ be a smooth solution to Boltzmann equation (1.17). Let us define the* kinetic entropy *as*

$$\mathcal{H}[f](t,x) := \int_{\mathbb{R}^d} f(t,x,v)(\log(f(t,x,v))-1)\,\mathrm{d}v\,, \tag{1.22}$$

and the entropy dissipation *as*

$$\mathcal{I}[f](t,x) := \int_{\mathbb{R}^d} v\, f(t,x,v)(\log(f(t,x,v))-1)\,\mathrm{d}v\,. \tag{1.23}$$

One has the following entropy dissipation inequality*:*

$$\frac{\partial}{\partial t}\mathcal{H}[f](t,x) + \nabla_x \cdot \mathcal{I}[f](t,x) \leq 0. \tag{1.24}$$

Moreover, $\mathcal{H}[f] = 0$ if and only if f is a Maxwellian *distribution $\mathcal{M}$.*

Most of the results presented in this manuscript will deal with the properties of the solutions to the Boltzman equation, in both the theoretical and numerical points of view, and in many regimes of interests. Before entering into these details, let us present some less classical kinetic models, that will also be studied in these chapters.

1.3 Some kinetic models of interest in this thesis

1.3.1 The BGK Operator

A collision operator which has the same properties of conservation of moments and dissipation of entropy of the Boltzmann operator is the BGK operator [20], and its Ellipsoidal Statistical (ES-BGK) extension [8]. It consists in replacing the *bilinear* collision operator $\mathcal{Q}_{\mathcal{B}}$ by a *nonlinear* relaxation operator, which matches the same hydrodynamic limit than the Boltzmann operator. The advantage is essentially computational, since it is very easy to compute this operator numerically, compared to the full Boltzmann operator.

Let us define the so-called *stress tensor* as

$$\rho_f\, \Theta_f(t,x) = \int_{\mathbb{R}^3} (v-\boldsymbol{u})\otimes(v-\boldsymbol{u}) f(t,x,v)\,\mathrm{d}v.$$

Therefore the temperature is related to the stress tensor as $\mathrm{T} = \mathrm{Trace}(\Theta_f)/3$. We finally introduce the corrected tensor

$$\mathcal{T}_f(t,x) \;=\; \big[(1-\beta)\,\mathrm{T}\,\mathbf{I} \;+\; \beta\,\Theta_f\big](t,x),$$

which can be viewed as a linear combination of the initial stress tensor Θ_f and of the isotropic stress tensor $\mathrm{T}\,\mathbf{I}$ developed by a Maxwellian distribution. The parameter $-\infty < \beta < 1$ is used to modify the value of the *Prandtl number* through the formula

$$0 \leq \;\mathrm{Pr} = \frac{1}{1-\beta} \leq +\infty \quad \text{for} \quad \beta \in (-\infty\,,\,1).$$

The correct Prandtl number for a monoatomic gas of hard spheres is equal to $2/3$, namely obtained here for $\beta = -1/2$ whereas the classical BGK operator, obtained for $\beta = 0$, has a Prandtl number equal to 1.

To define the ESBGK operator, we introduce a *corrected Gaussian* $\mathcal{G}[f]$ defined by

$$\mathcal{G}[f] = \frac{\rho}{\sqrt{\det(2\pi\mathcal{T}_f)}} \exp\left(-\frac{(v-\boldsymbol{u})\mathcal{T}_f^{-1}(v-\boldsymbol{u})}{2}\right)$$

and the corresponding collision operator is now

$$\mathcal{Q}_{\mathcal{BGK}}(f) = \nu(\mathcal{G}[f] - f), \tag{1.25}$$

where ν is the collision frequency from the Boltzmann operator, namely $\nu = \mathcal{Q}_{\mathcal{B}}^{-}(f, \mathcal{M})$.

1.3.2 The granular gases equation

A granular gas is a set of particles which interacts by energy dissipating collisions also known as inelastic collisions. This inelasticity is characterized using a collision mechanics where mass and momentum are conserved and kinetic energy is dissipated. Thus, the collision phenomenon is a non-microreversible process. The velocities of the colliding pairs (v, v_*) and (v', v'_*) are related by

$$v' = v - \frac{1+e}{2}((v-v_*)\cdot\sigma)\sigma, \qquad v'_* = v_* + \frac{1+e}{2}((v-v_*)\cdot\sigma)\sigma,$$

where $\sigma \in \mathbb{S}^{d-1}$ and the constant $e \in [0,1]$ is the dissipation parameter, known as *restitution coefficient*. One has

$$\begin{cases} v' + v'_* = v + v_*, \\ |v'|^2 + |v'_*|^2 - |v|^2 - |v_*|^2 = -\dfrac{1-e^2}{2}|(v-v_*)\cdot\sigma|^2 \le 0. \end{cases} \tag{1.26}$$

This microscopic mechanism allows us to describe the granular collision operator $\mathcal{Q}_{\mathcal{I}}$: for all ϕ, ψ and $\varphi \in \mathcal{C}_c^0(\mathbb{R}^d)$,

$$\int_{\mathbb{R}^d} \mathrm{Q}_{\mathcal{I}}(\phi,\psi)\,\varphi\,\mathrm{d}v := \frac{1}{2}\int_{\mathbb{R}^d\times\mathbb{R}^d\times\mathbb{S}^{d-1}} |v-v_*|\,\phi_*\psi\left(\varphi' + \varphi'_* - \varphi - \varphi_*\right)d\sigma\,\mathrm{d}v\,\mathrm{d}v_*. \tag{1.27}$$

Taking $\varphi(v) = 1$, v and $|v|^2$ in (1.27), the relations (1.26) yield conservation of mass and momentum at the kinetic level and dissipation of kinetic energy. The decrease of the energy, together with conservation of positivity, mass and momentum, imply that the equilibria of the collision operator are Dirac distributions $\rho\,\delta_u(v)$ where the density ρ and momentum ρu are prescribed by the initial condition. A major difficulty with this equation is the lack of decaying entropy functional: a discussion on this question can be found in my work [GdSMM+15], described in Chapter 3.

1.3.3 Multiple species Boltzmann equation

A multiple species gas mixture (such as the rarefied upper atmosphere) can be described by a system of N Boltzmann equations (1.1), coupled through the collision operators describing inter- and intra-species collisions:

$$\frac{\partial f_i}{\partial t} + v\cdot\nabla_x f_i = \mathcal{Q}_i(\mathrm{F}), \quad \forall 1 \le i \le \mathrm{N}. \tag{1.28}$$

The density of each specie is given by f_i, and $\mathrm{F} = (f_1, \ldots, f_{\mathrm{N}})$. The multiple-species collision operator is given by a sum of Boltzmann operators (1.18)

$$\mathcal{Q}_i(\mathrm{F}) := \sum_{j=1}^{\mathrm{N}} \mathcal{Q}_{\mathcal{B}}(f_i, f_j), \tag{1.29}$$

where inter-species collisions are given by

$$\begin{cases} v' = \dfrac{1}{m_i + m_j}\left(m_i v + m_j v_* + m_j |v - v_*|\sigma\right), \\ v'_* = \dfrac{1}{m_i + m_j}\left(m_i v + m_j v_* - m_i |v - v_*|\sigma\right). \end{cases}$$

The nonnegative quantity m_i denotes the molecular mass of the specie i. A whole hierarchy of reduced ES-BGK-type equations for this model also exists, we refer the interested reader to the recent review paper [123].

Whereas the mathematical properties of the classical Boltzmann equation for a single specie gas and its derivation from Newtonian dynamics are now quite well known, such questions on the multiple species case are still open. The most recent theoretical results on this topic come from the series of papers [44, 43], that prove existence, uniqueness, positivity and exponential trend to equilibrium for the full nonlinear multi-species Boltzmann equation (1.28) in a perturbative, polynomially-weighted and isotropic $L^1_v L^\infty_x$ setting.

On the numerical level, the most advanced numerical methods use a Fourier approach: a fast spectral algorithm recently introduced in [217] to numerically compute the collision operator (1.29). Nevertheless, the numerical method introduced by these authors is not capable of dealing with the stiff regimes of small ε or large mass ratios m_i/m_j. The paper [BR22] presented in Chapter 4 solves this problem, by using a novel strategy of time integration, the so-called Projective Integration framework.

1.3.4 Quantum Boltzmann equation

The *Nordheim equation* (or quantum Boltzmann equation) models the time evolution of a phase-space density $f = f(t, x, k)$, describing the probability to find at time $t \geq 0$ a quantum particle localized at the infinitesimal position $\mathrm{d}x\,\mathrm{d}k$, where $x \in \Omega \subset \mathbb{R}^3$ and $k \in \mathbb{R}^3$. The quantity k designates the energy level of the particle and corresponds to the "velocity" variable v in (1.1). Its total momentum is then given by $p = \hbar k$, where $\hbar$ is the reduced Planck constant.

This equation was first formulated by Uehling and Uhlenbeck in the seminal paper [210], starting from a classical Boltzmann equation with heuristic arguments. It can be used to model both bosons and fermions gases, possibly trapped by the confining potential V. The quantum collision operator can be expressed as:

$$\begin{aligned} \mathcal{Q}(f)(k) = \int_{\mathbb{R}^9} & \delta_0\left(k + k_* - k' - k'_*\right)\delta_0\left(\mathrm{E} + \mathrm{E}_* - \mathrm{E}' - \mathrm{E}'_*\right) \\ & \left[f'_* f'(1 \pm \hbar f)(1 \pm \hbar f_*) - f_* f\left(1 \pm \hbar f'\right)\left(1 \pm \hbar f'_*\right)\right] \mathrm{d}k_*\,\mathrm{d}k'\,\mathrm{d}k'_*, \end{aligned} \tag{1.30}$$

where $\mathrm{E}(x, k) := \mathrm{V}(x) + |k|^2/2$ is the total energy of the boson/fermion. Taking pluses in (1.30) corresponds to the boson case (namely integer spin particles such as photons), whereas minuses corresponds to the fermion case (half-integer spin particles such as electrons or protons). This collision operator preserves mass, momentum and kinetic energy by construction.

Due to its high dimensionality, the study of the full quantum Boltzmann equation is still widely open. The equation is indeed posed in the usual six-dimensional kinetic phase space. Moreover, the

collision operator is defined by a seven-fold integral (thanks to the Dirac deltas) itself. This causes a lot of difficulty, both theoretically and numerically. For example, in the space homogeneous (namely $f = f(t,k)$) bosonic case, it is well known that the particle distribution function f can develop finite time blow-up (weak convergence towards Dirac deltas even if the kinetic energy is conserved), the so-called *Bose-Einstein condensation*.

The study of the main mathematical properties of the collision operator (1.30) has been done in [90, 164, 45], allowing to understand almost completely the Cauchy problem (existence, stability, creation and propagation of moments, convergence towards the equilibrium) in the space homogeneous setting, without confining potential. The recent breakthrough [91] proved rigorously the Bose-Einstein condensation in the bosonic case, under very mild hypotheses on the moments of the initial condition. Nevertheless, the precise blowup behavior (localization of the explosion, rates, etc.) is still open. Finally, the theoretical study of the full space dependent problem is also mostly open, apart from some recent results concerning the anisotropic setting and Bose-Einstein condensates that can be found in [162].

The numerical study of this equation is also difficult for all these reasons. The first attempt to compute numerically the collision operator, in a simplified setting (taking advantage of some very specific symmetry properties) was done in the work [185]. Extensions of this idea were introduced in [131] by exploiting the convolution-like structure of the collision operator. This approach is similar to [MPR13] for the classical Boltzmann equation. The full extent of this convolution idea was used in [98], allowing to write a fast (spectral) method able to compute the full collision operator with the "reasonably low" numerical cost of $\mathcal{O}(\mathrm{N}^5 \log(\mathrm{N}))$ operations, where N is the number of unknowns in each velocity dimension, and with spectral accuracy. Extension of this method to the space inhomogeneous case was then done in the series of works [132, 130] for the fermionic (electrons) case only. Nevertheless, these works only deal with the simplified 1-dimensional (1d) in x, 2-dimensional in k setting and use an approximation of the collision operator (1.30). Even the slightly more realistic 1d in x, 3d in k case was never tackled up to our knowledge, not to mention the full 3d in x, 3d in k case. One should also note the earlier attempts from [140, 148], where a diffusive relaxation system was used, as an approximation of the full equation (1.1).

1.3.5 Run-and-tumble chemotactic motion.

The *Othmer, Dumbar and Alt kinetic equation* [183] describes biological phenomena of bacterial chemotactic motion such as *Escherichia Coli* or *Bacillus Subtilis* using a collisional kinetic equation of the form (1.1), with a relaxation-like collision operator. It describes the population of bacteria with a probability distribution function $f(t,x,v)$, where the kinetic variable v is usually bounded, because it models the bacterial velocity. It can be written as the following, nonlinear kinetic equation:

$$\begin{aligned} \frac{\partial f}{\partial t} + v \cdot \nabla_x f &= \int_{\mathrm{V}} \mathrm{T}[\mathrm{S}](x,v,v') f' \,\mathrm{d}v' - \int_{\mathrm{V}} \mathrm{T}[\mathrm{S}](x,v',v) f \,\mathrm{d}v', \\ -\Delta \mathrm{S} + \mathrm{S} &= \int_{\mathrm{V}} f(t,x,v)\,\mathrm{d}v. \end{aligned} \tag{1.31}$$

It also fits in the collisional framework (1.1), even though the collision operator, of linear Boltzmann type, is supplemented with a Poisson equation. The nonlinearity is due to the coupling of the nutrient quantity S with this Poisson equation, describing the nutrient consumption by the bacteria. The

kernel T describes the rate of jump and reorientation of the bacteria, giving its name to the "run-and-tumble" model. The core of the modeling for this class of equations then relies on this tumbling kernel. This topic has been for example summarized in the review paper [202].

This model has been investigated mathematically in the landmark paper [194], and has since generated a huge interest from the mathematical biology community. Some of its mathematical properties are now well known, and have been summarized in the paper [50]. In particular, after diffusive scaling, its fluid dynamic limit is given by the Patlak-Keller-Segel equation, which is known to exhibits complex blow-up behaviors.

Nevertheless, its numerical approximations are still not completely understood. Let us mention the AP, but first order in time numerical method introduced in [58] for dealing with some very simplified tumbling kernels only, in first dimension of space and velocity. Another first order scheme was then introduced in [104] and has the advantage of being able to deal with the two dimensional case (in space and velocity) with a rigorous treatment of the boundary conditions. This scheme is however not AP. Finally, the recent work [49] introduced a new numerical method using Case's orthogonal polynomial, which is high order in the velocity space.

1.4 Other topics

The works [RT16, EKR20, BDMR20, MR21, BLRT22] will not be exposed in this *Habilitation*. Let me give here a few words about their content.

The work [RT16] deals with an extension of the so-called Rescaling Velocity Method that I introduced during my PhD Thesis in [FR13]. In this paper, we discuss kinetic descriptions of flocking models, of the so-called Cucker-Smale [68] and Motsch-Tadmor [176] types. These models are given by Vlasov-type equations where the interactions taken into account are only given long-range bi-particles interaction potential. We introduce a new exact rescaling velocity method, which extend the one introduced in [FR13] to mean field models. It allows in particular to observe numerically the flocking behavior of the solutions to these equations, without a need of remeshing or taking a very fine grid in the velocity space. To stabilize the exact method, we also introduce a modification of the classical upwind finite volume scheme which preserves the physical properties of the solution, such as momentum conservation. We present an analysis of the new finite volume fluxes, as well as numerical simulations of this new method on both toy and full models.

In [EKR20], in collaboration with A. El Keurti, we propose a a new finite volume method for computing numerical approximations of a system of nonlocal transport equation modeling interacting species. This system can be seen as a nonlocal extension of the classical Lotka-Volterra equations. This method is based on the work [73], where the nonlocal continuity equations are treated as conservative transport equations with a nonlocal, nonlinear, rough velocity field. We analyze some properties of the method, and illustrate the results with numerical simulations.

In [BDMR20], in collaboration with S. Billiard, M. Derex and L. Maisonneuve, we develop a new mathematical model that aims to describe the dynamics of knowledge creation and propagation among interacting individuals. Understanding how knowledge is created and propagates within groups is crucial to explain how human populations have evolved through time. Computers, spaceships and scientific theories have not been invented by single, isolated individuals. Instead, they

result from a collective process by which innovations are gradually added to an existing pool of knowledge, most often over multiple generations [41, 190]. The ability to learn from others (*social learning*) is pivotal to this process because it allows innovations to be passed from individual to individual and from generation to generation. Anthropologists have relied on different theoretical models to address this question. In this work, we introduce a mathematically oriented model that shares properties with individual based approaches, inhomogeneous Markov chains and learning algorithms, such as those introduced in [67, 68]. After deriving the model, we study some of its mathematical properties, and establish theoretical and quantitative results in a simplified case. Finally, we run numerical simulations to illustrate some properties of the model.

In [MR21], we consider with A. Mouton a Fourier spectral method for the Boltzmann-Nordheim equation (1.30). This equation, modeled on the seminal Boltzmann equation, describes using a statistical physics formalism the time evolution of a gas composed of bosons or fermions. Using the spectral-Galerkin algorithm introduced in [98], together with some novel parallelization techniques and rescaling in velocity, we investigate some of the conjectured properties of the large time behavior of the solutions to this equation. In particular, we show that this numerical method is able to reproduce very accurately some of the main mathematical features of this equation, including the convergence towards singular steady states. These phenomena are known in the literature as *Fermi-Dirac saturation* and *Bose-Einstein condensation*).

In [BLRT22], in collaboration with S. Billiard, H. Leman and V.-C. Tran, we study a stochastic individual-based model of interacting plant and pollinator species through a bipartite graph: each species is a node of the graph, an edge representing interactions between a pair of species. The dynamics of the system depends on the between- and within-species interactions: pollination by insects increases plant reproduction rate but has a cost which can increase plant death rate, depending on pollinators density. Pollinators reproduction is increased by the resources harvested on plants. Each species is characterized by a trait corresponding to its degree of generalism. This trait determines the structure of the interactions graph and the quantity of resources exchanged between species. Our model includes in particular nested or modular networks. Deterministic approximations of the stochastic measure-valued process by systems of ordinary differential equations or integro-differential equations are established and studied as in [105], when the population is large or when the graph is dense and can be replaced with a graphon. The long-time behaviors of these limits are studied and central limit theorems are established to quantify the difference between the discrete stochastic individual-based model and the deterministic approximations. Finally, studying the continuous limits of the interaction network and the resulting PDEs, we show that nested plant-pollinator communities are expected to collapse towards a coexistence between a single pair of species of plants and pollinators.

1.5 Notations and functional setting

Here follows a list of useful concepts and notations which will be used throughout the manuscript.

Partial derivatives.

- Given a smooth scalar function $\psi : \mathrm{I} \times \Omega \to \mathbb{R}$ for some open sets $\mathrm{I} \subset \mathbb{R}$ and $\Omega \subset \mathbb{R}^d$ for $d \in \mathbb{N}^*$,

we define the *partial derivative* of ψ with respect to y by

$$\frac{\partial \psi}{\partial y} \text{ ou } \partial_y \psi.$$

- The *gradient* of ψ with respect to the vector $X \in \Omega$ will be denoted by

$$\nabla_X \psi = \left(\partial_{x_i} \psi\right)_{i \in \{1,\dots,d\}}.$$

- The *laplacian* of ψ with respect to $X \in \Omega$ will be denoted by

$$\Delta_X \psi = \nabla_X \cdot \nabla_x \psi = \sum_{i=1}^{d} \partial_{x_i}^2 \psi.$$

- In the case where the smooth function $\psi : I \times \mathbb{R}^d \to \mathbb{R}^d$ is vector valued, its *divergence* with respect to $X \in \Omega$ is denoted by

$$\mathrm{div}_X \psi = \nabla_X \cdot \psi = \sum_{i=1}^{d} \partial_{x_i} \psi_i.$$

Some functional spaces.

- Let $d \in \mathbb{N}^*$, $p \in [1, +\infty]$, $q \in \mathbb{R}_+$, $m : \mathbb{R}^d \to \mathbb{R}_+$ integrable and $f : \mathbb{R}^d \to \mathbb{R}$ measurable. The *weighted Lebesgue space* $L^p(m)$ is defined using the weighted norm

$$\|f\|_{L^p(m)}^p := \int_{\mathbb{R}^d} |f(x)|^p \, m(x) \, \mathrm{d}x.$$

  It will be denoted by L^p, $L^p(\mathrm{d}x)$ or $L^p(\mathbb{R}^d)$ when $m = 1$.
- In the case where $m(x) = \langle x \rangle := \sqrt{1 + |x|^2}$, we shall use the shorthand notation L^p_q, defined by the norm

$$\|f\|_{L^p_q}^p := \int_{\mathbb{R}^d} |f(x)|^p \, \langle x \rangle^{p\,q} \, \mathrm{d}x,$$

- For $s \in \mathbb{N}$, the *polynomially weighted Sobolev space* $W^{s,p}_q$ is defined through the norm

$$\|f\|_{W^{s,p}_q}^p := \sum_{|k| \le s} \int_{\mathbb{R}^d} \left|\partial^k f(x)\right|^p \langle x \rangle^{p\,q} \, \mathrm{d}x.$$

- The case $p = 2$ is denoted as the Sobolev space $H^s_q := W^{s,2}_q$. It can be equivalently defined using Fourier transform with the norm

$$\|f\|_{H^s_q}^2 := \left\|\mathcal{F}\left(f \, \langle \cdot \rangle^s\right)\right\|_{L^2_q}.$$

- The space $\mathcal{M}^q$ is the space of the measures on $\mathbb{R}^d$ with finite moments up to order q.

Fourier transforms.

- The space of orthogonal polynomials of degree at most $N \ge 0$ over $\mathbb{R}^d$ is defined as

$$\mathbb{P}^N = \mathrm{Span}\left\{e^{ik\cdot v} \mid -N \le k_j \le N,\ j = 1, \dots, d.\right\}.$$

  The orthogonal projector onto this space is denoted by $\mathcal{P}_N$. In particular, one has for any $f \in L^2$

$$\langle f - \mathcal{P}_N f, \phi \rangle = 0, \qquad \forall\ \phi \in \mathbb{P}^N,$$

  where $\langle \cdot, \cdot \rangle$ is the canonical inner product of L^2.

- The *Fourier transform* of a function $f : \mathbb{R}^d \to \mathbb{R}$ is defined by

$$\mathcal{F}(f)(\xi) := \int_{\mathbb{R}^d} f(\mathrm{X})\, e^{i\mathrm{X}\cdot\xi}\, d\mathrm{X}, \quad \forall\, \xi \in \mathbb{R}^d.$$

  One can also use the shorthand notation $\widehat{f}(\xi) := \mathcal{F}(f)(\xi)$.
- For any *multi-index* $k = \{k_1, \ldots, k_d\} \in \mathbb{Z}^d$, the k^{th} Fourier coefficient of an L–periodic function $f : [-\mathrm{L}, \mathrm{L}]^d \to \mathbb{R}$ is given by

$$\hat{f}_k = \frac{1}{2\mathrm{L}} \int_{[-\mathrm{L},\mathrm{L}]^d} f(x)\, e^{-i\frac{\pi}{\mathrm{L}}x\cdot k}\, \mathrm{d}x.$$

  For a given $\mathrm{N} \in \mathbb{N}^*$, the *truncated Fourier series* of f is given by

$$f_{\mathrm{N}}(x) = \sum_{-\mathrm{N}\le k\le \mathrm{N}} \hat{f}_k\, e^{i\frac{\pi}{\mathrm{L}}x\cdot k}, \quad \forall x \in [-\mathrm{L}, \mathrm{L}]^d.$$

Convolutions.

- Given two integrable functions $\psi_1, \psi_2 : \mathbb{R}^d \to \mathbb{R}$, their *convolution* $*_{\mathrm{X}}$ with respect to the variable $\mathrm{X} \in \mathbb{R}^d$ is given by

$$\psi_1 *_{\mathrm{X}} \psi_2(\mathrm{X}) := \int_{\mathbb{R}^d} \psi_1(\mathrm{X}-\mathrm{Y})\, \psi_2(\mathrm{Y})\, d\mathrm{Y}, \quad \forall \mathrm{X} \in \mathbb{R}^d.$$

- Given $\mathrm{N} \in \mathbb{N}^*$ and two N–periodic sequences u, v, their *discrete periodic convolution* $*_{\mathrm{N}}$ is given by

$$(u_1 *_{\mathrm{N}} u_2)_k = \sum_{j=1}^{\mathrm{N}} u_j\, v_{k-j}, \quad \forall k \in \{1, \ldots, \mathrm{N}\}.$$

Miscellaneous concepts.

- The *tensor product* of two vectors $a, b \in \mathbb{R}^d$ is the square matrix $a \otimes b$ defined by $(a \otimes b)_{i,j} = a_i\, b_j$
- An operator $\mathrm{T} : \mathrm{X} \to \mathrm{Y}$ bounded between two Banach spaces is said to be a *Fredholm* operator if $\dim \ker \mathrm{T} < \infty$ and $\operatorname{codim} \ker \mathrm{T} < \infty$.

CHAPTER

2 Spectral Methods

"When I finally got home and told my wife, she said: 'Are you crazy? There were bombs in the computer, and you rushed in?' " Dr. Lax recalled. "I said: 'I was so angry. I wanted to save the computer.' "

Peter Lax
The Mathematicians Who Ended the Kidnapping of an N.Y.U. Computer[14]

Contents

2.1 From kinetic equations to Discrete Velocity Models 20
2.2 Fourier-Galerkin spectral methods for the Boltzmann equation 21
2.3 Structure preserving spectral methods 27
2.4 Towards high performance computing applications 36
2.5 Perspectives 41

This chapter is based on the works [FPR15, PR17, DLNR18, PR21, PR22], *written in collaboration with Giacomo Dimarco, Francis Filbet, Raphaël Loubère, Jacek Narski, and Lorenzo Pareschi. Some parts are largely borrowed from these papers.*

Any *deterministic numerical method* for the computation of Boltzmann-like collision operators requires to work on a *bounded* velocity space. The approach considered for the majority of the collision operators we presented in Chapter 1 consists in adding some non physical binary collisions by periodizing the particle distribution function and the collision operator, and then using Fourier series to compute the truncated operator. This implies the loss of some local invariants, but a careful periodization allows at least the preservation of mass. This periodization is the basis of spectral methods, which are a large part of my work since my PhD.

Fourier techniques (also known as *Fourier spectral methods*) for the resolution of the Boltzmann equation have been first introduced independently in [186] and in [24], but were already evoked in the seminal paper [25]. They have since been investigated by a lot of authors, mathematicians, physicists and engineers, slowly percolating into the different communities as one of the methods of interest along Molecular Dynamics (MD) and Direct Simulation Monte Carlo (DSMC) [187, 188, 101, 108, 98, 216, 218, 217, 107, 128]. We will review in this Chapter some of the more striking

results on the approximation of collisional, Boltzmann-like collision operator that were obtained recently, as well as some of my contribution on this topic. Unless stated otherwise, the problems studied won't be scaled, and the Knudsen number $\varepsilon = 1$ through all this Chapter.

2.1 From kinetic equations to Discrete Velocity Models

In order to introduce a numerical method for the full kinetic equation (1.1), let us truncate the velocity space by fixing some given bounds and set a cubic grid in velocity space of N points with Δv the grid step which is taken equal in each direction. The continuous distribution function f is then replaced by a vector whose components are assumed to be approximations of the distribution function f at locations v_k:

$$\widetilde{f}_k(t,x) \approx f(t,x,v_k).$$

The *discrete velocity kinetic model* consists then in a set of N evolution equations in the velocity space for $\widetilde{f}_k$, $1 \le k \le \mathrm{N}$, of the form

$$\partial_t \widetilde{f}_k + v_k \cdot \nabla_x \widetilde{f}_k = \mathrm{Q}(\widetilde{f}_k), \tag{2.1}$$

where $\mathrm{Q}(\widetilde{f}_k)$ is a suitable approximation of the collision operator $\mathcal{Q}(f)$ at location k. Observe that, due to the truncation of the velocity space and to the finite number of points with which f is discretized, the moments of the discrete distribution function $\widetilde{f}_k$ are such that

$$\widetilde{\mathrm{U}}(t,x) = \sum_k \phi_k \widetilde{f}_k(t,x)\,\Delta v \neq \mathrm{U}(t,x), \tag{2.2}$$

with $\phi_k = (1, v_k, |v_k|^2)$ the discrete collision invariants, i.e. they are no longer those given by the continuous distribution f.

Since it is not the purpose of this Chapter, we are now free to introduce a discretization of the physical space into M control volumes. Further we define a time discretization $t^{n+1} = t^n + \Delta t$ starting at t^0, where Δt is the time step defined by an opportune CFL condition. The time index n varies between 0 and N_t so that the final time is $t_{\text{final}} = t^{n_t} = t^0 + \mathrm{N}_t \Delta t$.

Each equation of system (2.1) is solved by a time splitting procedure. We recall here a first order splitting approach: first a transport step solves the left-hand side, whereas a collision stage solves the right-hand side using the solution from the transport step as initial data:

$$\begin{aligned}
&\textit{Transport stage} \quad &&\longrightarrow \quad \begin{cases} \partial_t f_k + v_k \cdot \nabla_x f_k = 0, \\ f_k(0) = f_k^n; \end{cases} \\
&\textit{Collision stage} \quad &&\longrightarrow \quad \begin{cases} \partial_t f_k^{n+1} = \mathrm{Q}(f_k^{n+1}), \\ f_k^{n+1}(0) = f_k(\Delta t). \end{cases}
\end{aligned}$$

In this Chapter we shall mainly focus on the discretization of the so-called *space homogeneous* collision stage

$$\frac{\partial f}{\partial t} = \mathcal{Q}(f,f). \tag{2.3}$$

2.2 Fourier-Galerkin spectral methods for the Boltzmann equation

In this Section, we will consider the full Boltzmann collision operator (1.20), and present a general method to build Fourier spectral approximation of this object. This method is prototypical of other types of collision operators, that will be described later with less details.

2.2.1 The classical spectral method

The first step to construct our spectral discretization is to truncate the integration domain of the Boltzmann integral (1.18) as done for the distribution f. As a consequence, we suppose the distribution function f to have compact support on the ball $\mathcal{B}_0(\mathrm{R})$ of radius R centered in the origin.

Proposition 2.2.1. *Let the distribution function f be compactly supported on the ball $\mathcal{B}_0(\mathrm{R})$ of radius* R *centered in the origin, then*

$$\mathrm{Supp}\,(\mathcal{Q}_{\mathcal{B}}(f,f)(v)) \subset \mathcal{B}_0(\sqrt{2}\mathrm{R}).$$

In particular, one can introduce a collision operator with cutoff by setting

$$\mathcal{Q}^{\mathrm{R}}(f,g)(v) = \iint_{\mathcal{B}_0(\mathrm{R})\times\mathbb{S}^{d-1}} \left[f(v')g(v'_*) - f(v)g(v_*)\right] \mathrm{B}(v-v_*,\sigma)\,\mathrm{d}v_*\,\mathrm{d}\sigma\,, \quad \forall v \in \mathbb{R}^d.$$

In order to write a spectral approximation which avoids superposition of periods, it is then sufficient that the distribution function $f(v)$ is restricted on the cube $[-\mathrm{T},\mathrm{T}]^d$ with $\mathrm{T} \geq (2+\sqrt{2})\mathrm{R}$. Successively, one should assume $f(v) = 0$ on $[-\mathrm{T},\mathrm{T}]^d \setminus \mathcal{B}_0(\mathrm{R})$ and extend $f(v)$ to a periodic function on the set $[-\mathrm{T},\mathrm{T}]^d$. Let observe that the lower bound for T can be improved. For instance, the choice $\mathrm{T} = (3+\sqrt{2})\mathrm{R}/2$ guarantees the absence of intersection between periods where f is different from zero [187]. However, since in practice the support of f increases with time, we can just minimize the errors due to aliasing.

To further simplify the notation, let us take $\mathrm{T} = \pi$ and hence $\mathrm{R} = \lambda\pi$ with $\lambda = 2/(3+\sqrt{2})$ in the following. We then obtain a spectral quadrature of our collision operator by projecting it onto the space of trigonometric polynomials of degree less or equal to N, i.e.

$$\hat{\mathrm{Q}}_k = \int_{[-\pi,\pi]^d} \mathcal{Q}^{\mathrm{R}}(f_{\mathrm{N}}, f_{\mathrm{N}}) e^{-ik\cdot v}\,\mathrm{d}v, \quad k = -\mathrm{N},\dots,\mathrm{N}. \tag{2.4}$$

By substituting the expression of the truncated Fourier series f_{N} in (2.4) one gets after some computations

$$\hat{\mathrm{Q}}_k = \sum_{\substack{l,m=-\mathrm{N}\\ l+m=k}}^{\mathrm{N}} \hat{f}_l \hat{f}_m \beta(l,m), \quad k = -\mathrm{N},\dots,\mathrm{N}, \tag{2.5}$$

where $\beta(l,m) = \hat{\mathrm{B}}(l,m) - \hat{\mathrm{B}}(m,m)$ are given by

$$\hat{\mathrm{B}}(l,m) = \int_{\mathcal{B}_0(2\lambda\pi)} \int_{\mathbb{S}^{d-1}} |q|\sigma(|q|,\cos\theta) e^{-i(l\cdot q^+ + m\cdot q^-)}\,\mathrm{d}\omega\,\mathrm{d}q. \tag{2.6}$$

with

$$q^+ = \frac{1}{2}(q+|q|\omega), \quad q^- = \frac{1}{2}(q-|q|\omega). \tag{2.7}$$

Let us notice that the naive evaluation of (2.5) requires $\mathcal{O}(n^2)$ operations, where $n = \mathrm{N}^d$. This causes the spectral method to be computationally very expensive, especially in dimension three. In order to reduce the number of operations needed to evaluate the collision integral, we shall introduce an FFT-based, convolution approach to our spectral method.

2.2.2 A good domain truncation is tricky

We shall now approximate the collision operator on a bounded domain starting from a representation which somehow conserves more symmetries of the collision operator when one truncates it in a bounded domain. We have the following *Carleman-like representation*

Lemma 2.2.2. *Introducing the change of variables $x = r\sigma/2$, $y = v_* - v - x$ the collision operator (1.18) can be rewritten in the form*

$$\mathcal{Q}(f,f)(v) = \int_{x\in\mathbb{R}^d}\int_{y\in\mathbb{R}^d} \widetilde{\mathrm{B}}(x,y)\,\delta(x\cdot y)\,[f(v+y)f(v+x) - f(v+x+y)f(v)]\,\mathrm{d}x\,\mathrm{d}y,$$

where

$$\widetilde{\mathrm{B}}(x,y) = \widetilde{\mathrm{B}}(|x|,|y|) = 2^{d-1}\,\mathrm{B}\left(\frac{|x|}{\sqrt{|x|^2+|y|^2}}, \sqrt{|x|^2+|y|^2}\right)(|x|^2+|y|^2)^{-\frac{d-2}{2}}. \tag{2.8}$$

We shall show that such representation yields better properties of the Fourier spectral method after truncation.

Let us consider the bounded domain $\mathcal{D}_\mathrm{T} = [-\mathrm{T},\mathrm{T}]^d$ $(0 < \mathrm{T} < +\infty)$. There are two possibilities of truncation to reduce the collision process in a box. First one can remove the collisions connecting with some points out of the box. This is the natural preliminary stage for deriving conservative schemes based on the discretization of the velocity. In this case there is no need for a truncation on the modulus of x and y since we impose them to stay in the box. (even if for some computational reason it could be useful to impose this truncation even in this case). It yields

$$\mathcal{Q}^{\mathrm{tr}}(f,f)(v) = \int\int_{\left\{x,y\in\mathbb{R}^d \;|\; v+x,\,v+y,\,v+x+y\in\mathcal{D}_\mathrm{T}\right\}} \widetilde{\mathrm{B}}(x,y)\,\delta(x\cdot y)\,[f(v+y)f(v+x) - f(v+x+y)f(v)]\,\mathrm{d}x\,\mathrm{d}y$$

defined for $v\in\mathcal{D}_\mathrm{T}$. One can easily check that the following weak form is satisfied by this operator

$$\int \mathcal{Q}^{\mathrm{tr}}(f,f)\,\varphi(v)\,\mathrm{d}v = \frac{1}{4}\int\int\int_{\left\{v,x,y\in\mathbb{R}^d \;|\; v,\,v+x,\,v+y,\,v+x+y\in\mathcal{D}_\mathrm{T}\right\}} \widetilde{\mathrm{B}}(x,y)\,\delta(x\cdot y)\,f(v+x+y)f(v)[\varphi(v+y)+\varphi(v+x)-\varphi(v+x+y)-\varphi(v)]\,\mathrm{d}v\,\mathrm{d}x\,\mathrm{d}y \tag{2.9}$$

and this implies conservation of mass, momentum and energy as well as the H-theorem on the entropy. The problem of this truncation on a bounded domain is the fact that we have changed the collision kernel itself by adding some artificial dependence on v, v_*, v', v'_*. In this way convolution-like properties are broken.

A different approach consists in truncating the integration in x and y by setting them to vary in $\mathcal{B}_0(\mathrm{R})$. For a compactly supported function f with support $\mathcal{B}_0(\mathrm{S})$, we take $\mathrm{R} = \mathrm{S}$ in order to

obtain all possible collisions. Since we aim at using the FFT algorithm to evaluate the resulting quadrature approximation, and hence make use of periodic distribution functions, we must take into account the aliasing effect due to periods superposition in the Fourier space. As for the spectral method a geometrical argument shows that using the periodicity of the function it is enough to take $\mathrm{T} \geq (3+\sqrt{2})\mathrm{S}/2$ to prevent intersections of the regions where f is different from zero.

The operator now reads

$$\mathcal{Q}^{\mathrm{R}}(f,f)(v) = \int_{x\in\mathcal{B}_0(\mathrm{R})} \int_{y\in\mathcal{B}_0(\mathrm{R})} \widetilde{\mathrm{B}}(x,y)\,\delta(x\cdot y)\,[f(v+y)f(v+x) - f(v+x+y)f(v)]\,\mathrm{d}x\,\mathrm{d}y$$

for $v \in \mathcal{D}_{\mathrm{T}}$. The interest of this representation is to preserve the real collision kernel and its properties.

In order to understand the possible effect of periods' superposition we can rely on the following weak form valid for any function φ *periodic* on $\mathcal{D}_{\mathrm{T}}$

$$\int_{\mathcal{D}_{\mathrm{T}}} \mathcal{Q}^{\mathrm{R}}(f,f)\,\varphi(v)\,\mathrm{d}v = \frac{1}{4}\int_{v\in\mathcal{D}_{\mathrm{T}}}\int_{x\in\mathcal{B}_0(\mathrm{R})}\int_{y\in\mathcal{B}_0(\mathrm{R})} \widetilde{\mathrm{B}}(x,y)\,\delta(x\cdot y)$$
$$f(v+x+y)f(v)\,[\varphi(v+y)+\varphi(v+x)-\varphi(v+x+y)-\varphi(v)]\,\mathrm{d}v\,\mathrm{d}x\,\mathrm{d}y. \quad (2.10)$$

About the conservation properties one can show that

1. The only invariant φ is 1: it is the only periodic function on $\mathcal{D}_{\mathrm{T}}$ such that

$$\varphi(v+y)+\varphi(v+x)-\varphi(v+x+y)-\varphi(v) = 0$$

   for any $v \in \mathcal{D}_{\mathrm{T}}$ and $x \perp y \in \mathcal{B}_{\mathrm{R}}$. It means that the mass is locally conserved but not necessarily the momentum and energy.
2. When f is even there is *global* conservation of momentum, which is 0 in this case. Indeed $\mathcal{Q}^{\mathrm{R}}$ preserves the parity property of the solution, which can be checked using the change of variable $x \to -x$, $y \to -y$.
3. The collision operator satisfies formally the H-theorem

$$\int_{v\in\mathbb{R}^d} \mathcal{Q}^{\mathrm{R}}(f,f)\log(f)\,\mathrm{d}v \leq 0.$$

4. If f has compact support included in $\mathcal{B}_{\mathrm{S}}$ with $\mathrm{T} \geq (3+\sqrt{2})\mathrm{S}/2$ and $\mathrm{R} = \mathrm{S}$, then no unphysical collisions occur and thus mass, momentum and energy are preserved. Obviously this compactness is not preserved with time since the collision operator spreads the support of f by a factor $\sqrt{2}$.

To sum up one could say that the lack of conservation originates from the fact that the geometry of the collision does not respect the periodization.

We quantified the lack of conservation recently:

Proposition 2.2.3 (Prop. 2.2 from [PR22]). *Assume that the solution to problem (2.3) satisfies for $\delta \ll 1$*

$$f(v,t) \leq \delta, \quad v \in [-\pi,\pi]^d \setminus \mathcal{B}_0(\mathrm{R})$$

with $\mathrm{R} = \lambda\pi$. *Then, one has the bound for* $\Phi(v) = (1, v_1, \dots, v_d, |v|^2)^{\mathrm{T}}$

$$\left\| \int_{[-\pi,\pi]^d} \mathrm{Q}^{\mathrm{R}}(f,f)\,\Phi(v)\,\mathrm{d}v \right\|_2 \leq \mathrm{C}\delta, \tag{2.11}$$

where $\mathrm{C} = \mathrm{C}(f,\mathrm{R})$ *and* $\|\cdot\|_2$ *denotes the euclidean norm of the vector.*

2.2.3 The fast spectral method

The main idea to develop a more efficient algorithm is to use the representation (2.10). Taking $\varphi(v) = e^{ik\cdot v}$ yields the following new spectral quadrature formula

$$\hat{\mathrm{Q}}_k = \sum_{\substack{l,m=-\mathrm{N} \\ l+m=k}}^{\mathrm{N}} \hat{\beta}_{\mathrm{F}}(l,m)\,\hat{f}_l\,\hat{f}_m, \quad k = -\mathrm{N}, \dots, \mathrm{N} \tag{2.12}$$

where $\hat{\beta}_{\mathrm{F}}(l,m) = \hat{\mathrm{B}}_{\mathrm{F}}(l,m) - \hat{\mathrm{B}}_{\mathrm{F}}(m,m)$ are now given by

$$\hat{\mathrm{B}}_{\mathrm{F}}(l,m) = \int_{\mathcal{B}_0(\mathrm{R})} \int_{\mathcal{B}_0(\mathrm{R})} \widetilde{\mathrm{B}}(x,y)\,\delta(x\cdot y)\,e^{i(l\cdot x + m\cdot y)}\,\mathrm{d}x\,\mathrm{d}y. \tag{2.13}$$

Now, in order to reduce the number of operation needed to evaluate (2.12), we look for a convolution structure. The aim is to approximate each $\hat{\beta}_{\mathrm{F}}(l,m)$ by a sum

$$\hat{\beta}_{\mathrm{F}}(l,m) \simeq \sum_{p=1}^{\mathrm{A}} \alpha_p(l)\alpha'_p(m),$$

where A represents the number of finite possible directions of collisions. This finally gives a sum of A discrete convolutions and, consequently, the algorithm can be computed in $\mathcal{O}(\mathrm{A}\,\mathrm{N}\log_2\mathrm{N})$ operations by means of standard FFT technique [198].

In order to get this convolution form, we make the decoupling assumption

$$\widetilde{\mathrm{B}}(x,y) = a(|x|)\,b(|y|). \tag{2.14}$$

This assumption is satisfied if $\widetilde{\mathrm{B}}$ is constant. This is the case of Maxwellian molecules in dimension two, and hard spheres in dimension three, the two most used cases. Indeed, using the variable hard sphere kernel in (2.8), one has

$$\widetilde{\mathrm{B}}(x,y) = 2^{d-1}\mathrm{C}_\alpha(|x|^2+|y|^2)^{-\frac{d-\alpha-2}{2}},$$

so that $\widetilde{\mathrm{B}}$ is constant if $d=2$, $\alpha=0$ and $d=3$, $\alpha=1$.

We start by dealing with dimension 2 and $\widetilde{\mathrm{B}}=1$, i.e. Maxwellian molecules. Here we write x and y in spherical coordinates $x=\rho e$ and $y=\rho' e'$ to get using (2.13)

$$\hat{\mathrm{B}}_{\mathrm{F}}(l,m) = \frac{1}{4}\int_{\mathbb{S}^1}\int_{\mathbb{S}^1} \delta(e\cdot e')\left[\int_{-\mathrm{R}}^{\mathrm{R}} e^{i\rho(l\cdot e)}\,d\rho\right]\left[\int_{-\mathrm{R}}^{\mathrm{R}} e^{i\rho'(m\cdot e')}\,d\rho'\right] de\,de'.$$

Then, denoting $\phi^2_{\mathrm{R}}(s) = \int_{-\mathrm{R}}^{\mathrm{R}} e^{i\rho s}\,d\rho$, for $s\in\mathbb{R}$, we have the explicit formula

$$\phi^2_{\mathrm{R}}(s) = 2\,\mathrm{R}\,\mathrm{Sinc}(\mathrm{R}s).$$

Plugging it in the expression of $\hat{\mathrm{B}}_{\mathrm{F}}(l,m)$ and using its parity properties yields

$$\hat{\mathrm{B}}_{\mathrm{F}}(l,m) = \int_0^{\pi} \phi_{\mathrm{R}}^2(l\cdot e_\theta)\,\phi_{\mathrm{R}}^2(m\cdot e_{\theta+\pi/2})\,d\theta.$$

Finally, a regular discretization of A equally spaced points $\theta_p = \pi p/\mathrm{A}$ of the unit sphere, which is spectrally accurate because of the periodicity of the function [151], gives

$$\hat{\mathrm{B}}_{\mathrm{F}}(l,m) = \frac{\pi}{\mathrm{M}} \sum_{p=1}^{\mathrm{A}} \alpha_p(l)\alpha'_p(m), \tag{2.15}$$

with

$$\alpha_p(l) = \phi_{\mathrm{R}}^2(l\cdot e_{\theta_p}), \qquad \alpha'_p(m) = \phi_{\mathrm{R}}^2(m\cdot e_{\theta_p+\pi/2}).$$

Concerning the 3D case with a hard-sphere collision kernels, taking a spherical parametrization (θ,φ) of $e\in\mathbb{S}^2_+$ and uniform grids of respective size A_1 and A_2 for θ and φ (again spectrally accurate because of the periodicity of the function) leads to the following quadrature formula for $\hat{\mathrm{B}}_{\mathrm{F}}(l,m)$

$$\hat{\mathrm{B}}_{\mathrm{F}}(l,m) = \frac{\pi^2}{\mathrm{A}_1\mathrm{A}_2} \sum_{p,q=0}^{\mathrm{A}_1,\mathrm{A}_2} \alpha_{p,q}(l)\alpha'_{p,q}(m)$$

where

$$\alpha_{p,q}(l) = \phi^3_{\mathrm{R},a}\left(l\cdot e_{(\theta_p,\varphi_q)}\right), \qquad \alpha'_{p,q}(m) = \psi^3_{\mathrm{R},b}\left(\Pi_{e^{\perp}_{(\theta_p,\varphi_q)}}(m)\right),$$

$$\phi^3_{\mathrm{R},a}(s) = \int_{-\mathrm{R}}^{\mathrm{R}} \rho\, a(\rho)\, e^{i\rho s}\,d\rho, \qquad \psi^3_{\mathrm{R},b}(s) = \int_0^{\pi} \sin\theta\,\phi^3_{\mathrm{R},b}(s\cos\theta)\,d\theta,$$

and for all p and q

$$(\theta_p,\varphi_q) = \left(\frac{p\,\pi}{\mathrm{A}_1}, \frac{q\,\pi}{\mathrm{A}_2}\right).$$

2.2.4 Stability and consistency

First, let us recall some classical results for Fourier approximations [198]. When no ambiguity with other spaces are possible, the space H^r_p will denote the subspace of H^r containing only periodic functions.

- Since the projection operator $\mathcal{P}_{\mathrm{N}}$ is self-adjoint on L^2, the following property holds

$$\langle \mathcal{P}_{\mathrm{N}} f,\varphi\rangle = \langle f,\mathcal{P}_{\mathrm{N}}\varphi\rangle = \langle \mathcal{P}_{\mathrm{N}} f,\mathcal{P}_{\mathrm{N}}\varphi\rangle \quad \forall\, f,\,\varphi\in \mathrm{L}^2_p([-\pi,\pi]^d).$$

- By Parseval's identity, one has for any $f\in\mathrm{L}^2_p([-\pi,\pi]^d)$

$$\|f\|^2_{\mathrm{L}^2_p} = (2\pi)^d \sum_{k=-\infty}^{\infty} |\hat{f}_k|^2, \qquad \|f_{\mathrm{N}}\|^2_{\mathrm{L}^2_p} = (2\pi)^d \sum_{k=-\mathrm{N}}^{\mathrm{N}} |\hat{f}_k|^2.$$

- If $f\in\mathrm{H}^r_p([-\pi,\pi]^d)$, one has the following *spectral accuracy* property: There is $\mathrm{C}>0$ such that

$$\|f-f_{\mathrm{N}}\|_{\mathrm{H}^r_p} \le \frac{\mathrm{C}}{\mathrm{N}^r}\|f\|_{\mathrm{H}^r_p}.$$

  In particular, the moments of f_{N} are also spectrally accurate: for $\phi\in\mathrm{L}^2_p([-\pi,\pi]^d)$, one has

$$|\langle f,\phi\rangle - \langle f_{\mathrm{N}},\phi\rangle| \le \|\phi\|_{\mathrm{L}^2_p}\|f-f_{\mathrm{N}}\|_{\mathrm{H}^r_p} \le \frac{\mathrm{C}}{\mathrm{N}^r}\|\phi\|_{\mathrm{L}^2_p}\|f\|_{\mathrm{H}^r_p}.$$

Using these classical results and some regularity properties of the truncated Boltzmann operator, one can prove the spectral consistency of the Fourier spectral methods:

Theorem 2.2.4 ([187]). *Let $f \in \mathrm{H}^r_p([-\pi,\pi]^d)$, $r \geq 0$ then there is $\mathrm{C} > 0$ such that*

$$\left\| \mathcal{Q}^{\mathrm{R}}(f,f) - \mathcal{Q}^{\mathrm{R}}_{\mathrm{N}}(f_{\mathrm{N}},f_{\mathrm{N}}) \right\|_2 \leq \frac{\mathrm{C}}{\mathrm{N}^r} \left(||f||_{\mathrm{H}^r_p} + \left\| \mathcal{Q}^{\mathrm{R}}(f_{\mathrm{N}},f_{\mathrm{N}}) \right\|_{\mathrm{H}^r_p} \right). \tag{2.16}$$

This theorem can be immediately extended to the fast spectral method thanks to the spectral accuracy of the numerical quadrature rules for periodic functions from [151]. Moreover, the seminal stability result [100] can be used to prove the stability and large time behavior of spectral methods for the Boltzmann equation. For that, let us first introduce a perturbed, truncated Boltzmann equation

$$\begin{cases} \dfrac{\partial f}{\partial t} = \mathcal{Q}^{\mathrm{R}}(f,f) + \mathrm{P}_\varepsilon(f), \\ f(v,0) = f_{0,\varepsilon}(v), \quad v \in [-\pi,\pi]^d, \end{cases} \tag{2.17}$$

where the perturbation $\mathrm{P}_\varepsilon(f)$ is smooth and "balanced", in the following sense :

Definition 2.2.1. *A family of operators P_ε is said to be a* stable *perturbation of the Boltzmann equation if it verifies the following properties:*

1. $\int \mathrm{P}_\varepsilon(f)\,\mathrm{d}v = 0$;
2. *there exists $r \geq 1$, C_1, $\mathrm{C}_r \geq 0$ such that*

$$\begin{cases} \|\mathrm{P}_\varepsilon(f)\|_{\mathrm{L}^1} \leq \mathrm{C}_1 \|f\|_{\mathrm{L}^1} \|f\|_{\mathrm{L}^1}, \\ \|\mathrm{P}_\varepsilon(f)\|_{\mathrm{H}^r_p} \leq \mathrm{C}_r \|f\|_{\mathrm{L}^1} \|f\|_{\mathrm{H}^r_p}. \end{cases} \tag{2.18}$$

3. *there exists a function $\varphi(\varepsilon)$ which goes to 0 when ε goes to 0 and such that*

$$\|\mathrm{P}_\varepsilon(f)\|_{\mathrm{H}^r_p} \leq \varphi(\varepsilon), \quad \forall r \geq 1.$$

Note that both classical and spectral Fourier method can be written in this framework, with

$$\mathrm{P}_\varepsilon(f_{\mathrm{N}},f_{\mathrm{N}}) = \mathcal{P}_{\mathrm{N}} \mathcal{Q}^{\mathrm{R}}(f_{\mathrm{N}},f_{\mathrm{N}}) - \mathcal{Q}^{\mathrm{R}}(f_{\mathrm{N}},f_{\mathrm{N}}).$$

One then has the stability and trends to equilibrium result for (2.17):

Theorem 2.2.5 (Thm 3.1 of [100]). *Let us consider the perturbed truncated Boltzmann equation (2.17), with a stable family of perturbations (P_ε) satisfying the hypotheses of Definition 2.2.1. Let $f_0 \in \mathrm{H}^r_p$ for $r > d/2$ be a nonzero, nonnegative function and $(f_{0,\varepsilon}) \in \mathrm{L}^1 \cap \mathrm{L}^2_p$ be a family of smooth perturbations of f_0:*

$$\int_{[-\pi,\pi]^d} f_{0,\varepsilon}\,\mathrm{d}v = \int_{[-\pi,\pi]^d} f_0\,\mathrm{d}v, \qquad \|f_0 - f_{0,\varepsilon}\|_{\mathrm{L}^1} \leq \psi(\varepsilon), \tag{2.19}$$

where $\psi(\varepsilon)$ goes to 0 when ε goes to 0.

Then there exists ε_0 depending only on the truncation parameter R, the collision kernel B, the constant in Definition 2.2.1 and $\|f_0\|_{\mathrm{H}^r_p}$ such that, for any $\varepsilon \in (0,\varepsilon_0)$,

1. *there exists a unique global smooth solution* f_ε *to* (2.17)*;*
2. *for any* $k < r$, $f_\varepsilon(t,\cdot) \in \mathrm{H}^k_p$*, uniformly in time;*
3. *the quantity of negative values of* f_ε *vanishes when* ε *goes to* 0*;*
4. *for any* $\mathrm{T} > 0$*, the solution* f_ε *of* (2.17) *converges in* $\mathrm{L}^\infty([0,\mathrm{T};\mathrm{H}^r_p)$ *towards a solution* f *to the unperturbed equation* (2.3) *when* ε *goes to* 0*;*
5. *as time goes to infinity, the solution* f_ε *converges in* H^r_p *towards a piecewise constant equilibrium* m_∞ *defined by the initial mass.*

Note that there are other more recent stability results, see [6, 129], but they do not cover the very critical point of the large-time behavior of the methods.

2.3 Structure preserving spectral methods

Although spectrally accurate, we have seen that Fourier spectral approaches does not preserve some of the conservations embedded in the collision operator (such as kinetic energy), and more importantly the Maxwellian equilibria. Indeed, such smooth distributions are not contained in the space of orthogonal polynomials. We shall present in this Section some strategies developed to deal with these problems.

2.3.1 Equilibrium preserving Fourier spectral methods

In order to improve the representation of the equilibria, an easy way is to rewrite the equation considered in such a way that the equilibria of the new models are zeros, quantities that we always figure in the approximation spaces. This strategy was introduced in the works [FPR15, PR17, PR21]. Although the method applies in principle to any evolution equation which possesses a global Maxwellian-type equilibrium and a polynomial nonlinearity, here we describe the method in the case of the homogeneous Boltzmann equation.

Let us start with the decomposition

$$f = \mathcal{M} + g, \tag{2.20}$$

with $\mathcal{M}$ the local Maxwellian equilibrium and g such that $\int_{\mathbb{R}^d} g\,\varphi\,\mathrm{d}v = 0$, $\varphi = 1, v, |v|^2$. When inserted into a Boltzmann-type collision operator, the decomposition (2.20) gives

$$\mathcal{Q}(f,f) = \mathcal{L}_{\mathcal{M}}(g) + \mathcal{Q}_{\mathcal{B}}(g,g). \tag{2.21}$$

where $\mathcal{L}(\mathcal{M},g) = \mathcal{Q}_{\mathcal{B}}(g,\mathcal{M}) + \mathcal{Q}_{\mathcal{B}}(\mathcal{M},g)$ is a linear operator. There are two major features in the decomposition (2.21):

1. it embeds the identity $\mathcal{Q}_{\mathcal{B}}(\mathcal{M},\mathcal{M}) = 0$;
2. the steady state of (2.21) is given by $g = 0$.

This type of *micro-macro* decomposition has been used *e.g.* in [159] to develop numerical methods which preserve asymptotic behaviors of some kinetic models.

To illustrate our method, let us consider now the space homogenous equation (2.3) that we rewrite using the micro-macro decomposition as

$$\frac{\partial g}{\partial t} = \mathcal{L}_{\mathcal{M}}(g) + \mathcal{Q}_{\mathcal{B}}(g,g), \quad f = \mathcal{M} + g. \tag{2.22}$$

We then write after truncation the Fourier spectral approximation of this micro-macro equation as

$$\frac{\partial g_N}{\partial t} = \mathcal{L}_N^R(M_N, g_N) + Q\_N^R(g_N, g_N), \quad f_N = M_N + g_N, \tag{2.23}$$

where $M_N = \mathcal{P}_N \mathcal{M}$, $g_N = \mathcal{P}_N g$, $\mathcal{L}_N^R(M_N, g_N) = \mathcal{P}_N \mathcal{L}_{\mathcal{M}_N}^R(g_N)$ and $\mathcal{Q}_N^R(g_N, g_N) = \mathcal{P}_N \mathcal{Q}^R(g_N, g_N)$ is either the classical of fast Fourier spectral approximation given by (2.12).

It is immediate to show that

Proposition 2.3.1. *The function $g_N \equiv 0$ is an admissible local equilibrium of the scheme (2.23) and therefore $f_N = M_N$ is a local equilibrium state.*

Spectral accuracy. Let us show that (2.23) is a spectrally accurate approximation to (2.22) provided that M_N is a spectrally accurate approximation of $\mathcal{M}$. This is clearly guaranteed if initially the support is large enough. Note that due to space homogeneity, $\mathcal{M}$ does not change in time and so does M_N. It is interesting to observe that the only difference between scheme (2.23) and the usual spectral method developed on the original formulation

$$\begin{aligned} \frac{\partial f_N}{\partial t} &= \frac{\partial g_N}{\partial t} \\ &= \mathcal{Q}_N^R(f_N, f_N), \\ &= \mathcal{L}_N^R(M_N, g_N) + \mathcal{Q}_N^R(g_N, g_N) + \mathcal{Q}_N^R(M_N, M_N) \end{aligned} \tag{2.24}$$

is due to the constant (in time) term $\mathcal{Q}_N^R(M_N, M_N) \neq 0$, which, as we will prove, is spectrally small and is not present in (2.23).

Since the Maxwellian $\mathcal{M}$ is smooth, its spectral projection M_N is spectrally small. One then has using Theorem 2.2.4 the spectral accuracy of the steady state preserving formulation

Theorem 2.3.2 (Theorem 2 from [FPR15]). *Let $f \in H_p^r([-\pi,\pi]^3)$, $r \geq 0$ then*

$$\begin{aligned} \left\| \mathcal{Q}^R(f,f) - \mathcal{L}_N^R(M_N, g_N) - \mathcal{Q}_N^R(g_N, g_N) \right\|_2 \leq \frac{C}{N^r} \Big(&\|f\|_{H_p^r} + \|\mathcal{M}\|_{H_p^r} \\ &+ \left\| \mathcal{Q}^R(f_N, f_N) \right\|_{H_p^r} + \left\| \mathcal{Q}^R(M_N, M_N) \right\|_{H_p^r} \Big). \end{aligned}$$

Stability. The equilibrium preserving method (2.22) can be written in the perturbed framework (2.17) as

$$\begin{cases} \dfrac{\partial f_N}{\partial t} = \mathcal{P}_N Q(f_N, f_N) - \mathcal{P}_N Q(M_N, M_N) = \mathcal{P}_N Q(f_N + M_N, f_N - M_N), \\ f_N(v,0) = \mathcal{P}_N f_0(v). \end{cases} \tag{2.25}$$

Assuming that the solution f to the homogeneous Boltzmann equation (2.3) remains bounded in L^1 at all times[1], we proved the stability of the equilibrium preserving method in [PR21].

Theorem 2.3.3 (Theorem 3.1 from [PR21]). *Consider a nonnegative initial data $f_0 \in H_p^k([\pi,\pi]^d)$ for $k > d/2$ and assume that there exists a nonnegative constant K with*

$$\|f(t) + M\|_{L^1} \leq K, \qquad \forall t \geq 0 \tag{2.26}$$

where f is the associated solution to (2.25). There exists $N_0 \in \mathbb{N}$ such that for all $N \geq N_0$:

[1] This result is yet to be proved, and is also an assumption in the paper [100].

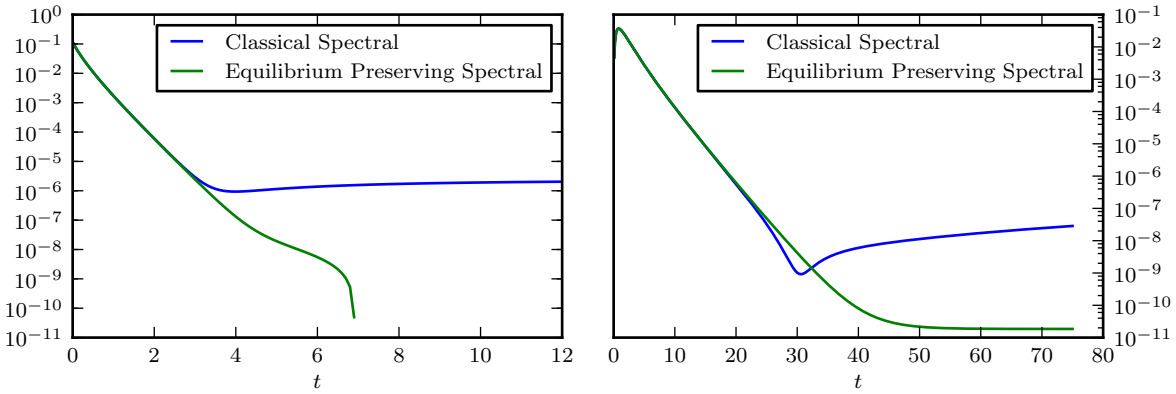

Figure 2.1: **Comparison of the classical and equilibrium preserving spectral methods.** Relative entropy $\mathcal{H}(f|\mathrm{M})(t)$ (left) and L^2 error $\|f(t)-f_{\mathrm{BKW}}(t)\|_2$ (right).

1. *There is a unique global smooth solution* f_{N} *to the problem* (2.25)*;*
2. *for any* $r<k$*, there exists* $\mathrm{C}_r>0$ *such that*

$$\|f_{\mathrm{N}}(t,\cdot)\|_{\mathrm{H}^r}\leq \mathrm{C}_r;$$

3. f_{N} *converges to a solution* f *of equation* (2.3) *with spectral accuracy, uniformly in time.*

2.3.2 Numerical simulations of the equilibrium preserving method

We present in this Section some numerical examples of the equilibrium preserving method, first for the Boltzmann equation, and then for some other models as in [PR17].

The Boltzmann equation Let us consider the space homogeneous Boltzmann equation in dimension 2, with Maxwell molecules:

$$\mathrm{B}(\cos\theta,|v-v_*|)=\frac{1}{2\pi}. \tag{2.27}$$

We compare the classical spectral method to the equilibrium preserving one. For this, we use an exact solution to the homogeneous Boltzmann equation, the so-called Bobylev-Krook-Wu (BKW) solution [25]. It is given by

$$f_{\mathrm{BKW}}(t,v)=\frac{\exp(-v^2/2\mathrm{S})}{2\pi\mathrm{S}^2}\left[2\,\mathrm{S}-1+\frac{1-\mathrm{S}}{2\,\mathrm{S}}\,v^2\right]$$

with $\mathrm{S}=\mathrm{S}(t)=1-\exp(-t/8)/2$.

For the resolution of the Boltzmann equation (2.3), we use the fast spectral method with $\mathrm{N}=32$ half-modes in each direction of the box $[-8,8]^2$. We take $\mathrm{M}=8$ angular discretizations[2]. Here, we insists that both the classical and steady-states preserving methods rely on the same numerical algorithm. The only difference between the two is the presence of some constant in time terms. In particular, both methods have the same computational cost, namely $\mathcal{O}\left(\mathrm{MN}\log_2\mathrm{N}\right)$.

[2]This is enough because of the spectral accuracy of quadrature methods for periodic functions.

Fig. 2.1 presents a comparison between both methods for the relative entropy of the solution f with respect to the global Maxwellian $\mathcal{M}$

$$\mathcal{H}(f|\mathcal{M})(t) := \int_{\mathbb{R}^d} f(t,v)\log\left(\frac{f(t,v)}{\mathcal{M}(v)}\right)\mathrm{d}v, \tag{2.28}$$

and the absolute L^2 error between the numerical solution $f(t,v)$ and the exact one $f_{\mathrm{BKW}}(t,v)$. We observe that for both quantities, the behavior of the equilibrium preserving method is better than the classical one. In particular, the former method achieves a nice monotonous decay of the relative entropy, without the large time increase of the classical spectral method. This is due to the fact that the equilibrium of this latter methods are constants. The behavior of the L^2 error is also monotonous for the steady-state preserving method, which is not the case for the classical one.

Note that the temperature of the solution given by Fourier spectral methods is not preserved, but grows almost linearly. At $t = 50$, the conservation error is of the order 10^{-4}. In contrast, the equilibrium preserving spectral methods improve greatly this behavior: although not perfectly conserved, the temperature of the solution has only deviated from a factor 10^{-7} from the exact quantity.

The porous medium equation We applied in [PR17] the micro-macro strategy to obtain an equilibrium preserving numerical method for the nonlinear porous medium equation (in self-similar form)

$$\partial_t u = \nabla_x \cdot (x\,u) + \Delta_x\,(u^m). \tag{2.29}$$

It is well known (see [57] for a comprehensive review) that the equilibria to this equation are given by the so-called Barrenblatt-Pattle distribution

$$u^{eq}(x) = \left(\mathrm{C} - \frac{m-1}{2m}|x|^2\right)_+^{1/(m-1)}, \quad \forall x \in \Omega,$$

where the constant C depends on the initial condition, and insures mass preservation. The solution to (2.29) converges exponentially fast toward this equilibrium profile.

In all our simulations, we will take $m = 5$ in the equation, and consider $d = 2$, $\Omega = [-10,10]\times[-10,10]$ as the computational domain, with an explicit solver needing a parabolic time step. The initial datum is chosen as:

$$u^{in}(x) = |x|^2 e^{-|x|^2/2}.$$

We take $\mathrm{N}_x = \mathrm{N}_y = 64$ points in each of the space dimensions. We compare the numerical results obtained with a first order non equilibrium-preserving upwind scheme **SU** (see [61]), its equilibrium preserving counterpart **REU**, and some second order, equilibrium preserving methods: the fully upwind **FU** (see [19]) and the Scharfetter-Gummel **SG** schemes (see [195]).

In Fig. 2.2, we compute the relative entropy

$$\mathcal{H}(u|u^{eq}) := -\int_\Omega \left((u-u^{eq}) + \frac{2}{m-1}(u^m - (u^{eq})^m)\right)\mathrm{d}x,$$

and the L^1 error for these four schemes. The quantities are expected to converge exponentially fast toward 0, and we can moreover compute the decay rate for the L^1 error, namely according to [57]

$$\|u(t) - u^{eq}\|_{\mathrm{L}^1} \le \mathrm{C}\exp\left(-\frac{d(m-1)+2}{(d+2)m-d}t\right).$$

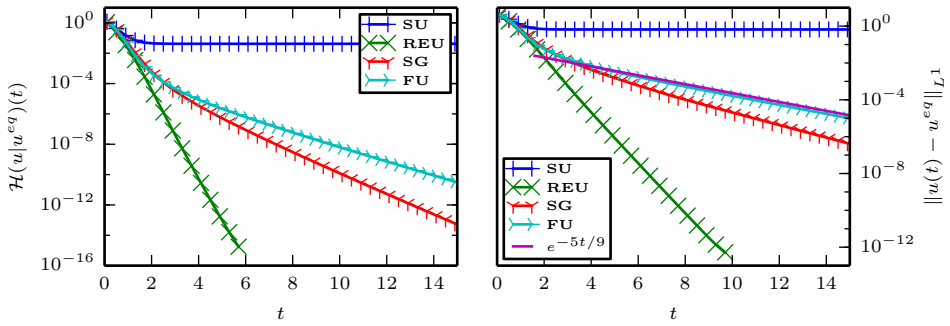

Figure 2.2: **Porous medium.** Time evolution of the relative entropy (left) and L^1 error (right), for the classical upwind (blue pluses), residual equilibrium upwind (green crosses), fully upwind (cyan arrows) and Scharfetter-Gummel (red y's) schemes.

As is expected again, the classical upwind (blue crosses) saturates, not being able to reach the machine 0, because of a wrong numerical equilibrium. On the contrary, the other three schemes behave properly regarding to their equilibrium preserving properties: they all succeed to capture the Barrenblatt-Pattle distribution. Nevertheless, we notice that only the fully upwind scheme (cyan arrows) from [19] is able to capture the correct decay rate. Our equilibrium preserving scheme converges too fast toward the equilibrium. According to other simulations in [PR17], we believe that this could be improved by switching to another numerical scheme, such as basic central discretization.

These observations are confirmed by Fig. 2.3, which presents in log scale the time evolution of the solution $u(t,x,0)$ for $x \in [-10,10]$ to (2.29) given by the standard upwind (a), residual equilibrium upwind (b) and fully upwind (c, for a reference solution) schemes. We observe that even if the rate of convergence is not correct, the use of a micro-macro equilibrium preserving approach allows the upwind scheme to compute very nicely the Barenblatt-Pattle distribution, the L^∞ error being of the same order of magnitude than the one obtained with the fully upwind scheme.

In [PR17], the same equilibrium preserving approach was used also with systems of hyperbolic conservation laws such as the shallow water equation, allowing to build well-balanced schemes, provided that one has an analytical expression of the equilibrium state of the system.

2.3.3 Moment preserving Fourier spectral methods

Although the micro-macro-based, equilibrium preserving approach allows for a correct reconstruction of the equilibrium with the Fourier spectral methods, such approach requires the knowledge of said equilibrium. Moreover, it does not solve the problem of the loss of collisional invariants such as the kinetic energy. To solve this problem we introduced a new approach in [PR22] which consists in changing the spectral projection $\mathcal{P}_N$ to constrain the conserved quantities. It is reminiscent of the works [29] and [108] for finite difference discretizations of the Fourier transformed Boltzmann equation.

Moment constrained Fourier approximation. We want to define a different projection operator on the space of trigonometric polynomials, $\mathcal{P}_N^c : L^2_p([-\pi,\pi]^d) \to \mathbb{P}^N$ such that it satisfies the moment

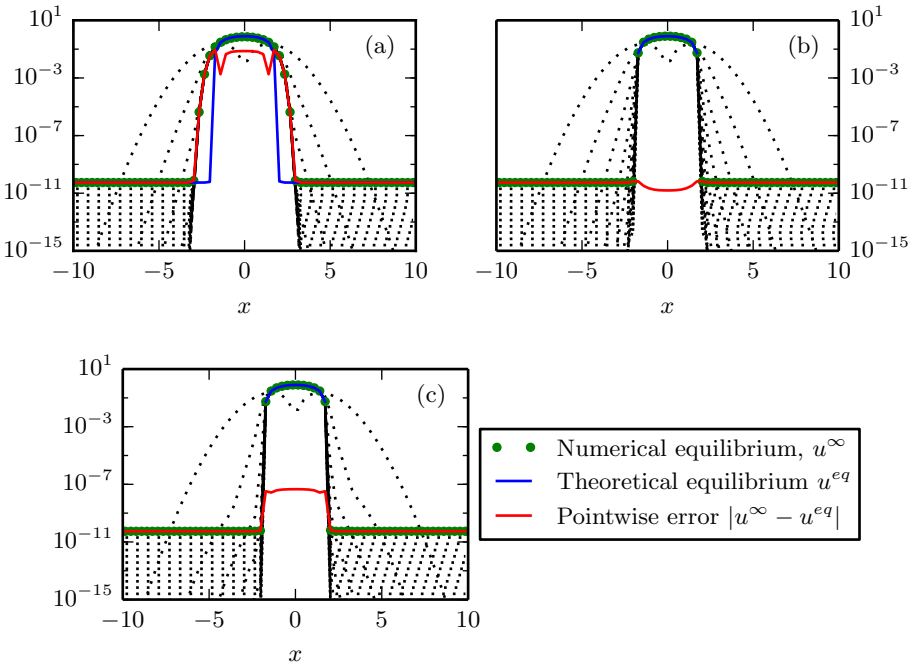

Figure 2.3: **Porous medium.** Trend to equilibrium (log scale) of the solutions obtained with the standard upwind (a), residual equilibrium upwind (b), and fully upwind (c) schemes, at $y = 0$.

constraints

$$\langle \mathcal{P}_{\mathrm{N}}^{c} f, \Phi \rangle = \langle f, \Phi \rangle, \quad \Phi = (1, v_1, \dots, v_d, |v|^2)^{\intercal} \in \mathbb{R}^{d+2},$$

while preserving the convergence properties of the finite Fourier series.

By analogies with Fourier series, it is natural to consider the following *constrained best approximation problem* in the space of trigonometric polynomials

$$f_{\mathrm{N}}^{c} = \operatorname{argmin} \left\{ \| g_{\mathrm{N}} - f \|_{\mathrm{L}^2_p}^2 \ : \ g_{\mathrm{N}} \in \mathbb{P}^{\mathrm{N}}, \ \langle g_{\mathrm{N}}, \Phi \rangle = \langle f, \Phi \rangle \right\}. \tag{2.30}$$

Since such a g_{N} is a trigonometric polynomial, we can represent it in the form $g_{\mathrm{N}} = \sum_{k=-\mathrm{N}}^{\mathrm{N}} \hat{g}_k e^{ik\cdot v}$, and then by Parseval's identity

$$\| g_{\mathrm{N}} - f \|_{\mathrm{L}^2_p}^2 = (2\pi)^d \sum_{k=-\infty}^{\infty} |\hat{g}_k - \hat{f}_k|^2,$$

where we assumed $\hat{g}_k = 0$, $|k_j| > \mathrm{N}$, $j = 1, \dots, d$.

Note that, since conservation of moments is built in g_{N}, one necessarily needs that

$$\langle g_{\mathrm{N}}, \Phi \rangle = (2\pi)^d \sum_{k=-\mathrm{N}}^{\mathrm{N}} \hat{g}_k \hat{\Phi}_k = \langle f, \Phi \rangle. \tag{2.31}$$

The minimization problem (2.30) can be solved using the Lagrange multiplier method. One can prove the following property [PR22]:

Definition 2.3.1. *For $f \in \mathrm{L}^2_p$, let us set $\mathrm{U} = (\rho, \rho u, \mathrm{E})^\intercal = \langle f, \Phi\rangle$ and $\mathrm{U}_\mathrm{N} = (\rho_\mathrm{N}, \rho u_\mathrm{N}, \rho e_\mathrm{N})^\top = \langle f_\mathrm{N}, \Phi\rangle$, where $\Phi(v) = (1, v_1, \dots, v_d, |v|^2)^\intercal$. One can define a* conservative projection $\mathcal{P}^c_\mathrm{N} f = f^c_\mathrm{N}$ *in* $\mathbb{P}^\mathrm{N}$*, where f^c_N is given by*

$$f^c_\mathrm{N} = \sum_{k=-\mathrm{N}}^{\mathrm{N}} \hat{f}^c_k \, e^{ik\cdot v}, \tag{2.32}$$

where the moment constrained Fourier coefficient *are defined as*

$$\hat{f}^c_k = \hat{f}_k + \hat{\mathrm{C}}^\intercal_k(\mathrm{U} - \mathrm{U}_\mathrm{N}), \qquad \hat{\mathrm{C}}^\intercal_k = \frac{1}{(2\pi)^d}\hat{\Phi}^\intercal_k \left(\sum_{h=-\mathrm{N}}^{\mathrm{N}} \hat{\Phi}_h \hat{\Phi}^\intercal_h \right)^{-1}. \tag{2.33}$$

Using this moment constrained projection, we were able to generalize the spectral accuracy of the usual Fourier projection:

Theorem 2.3.4 (Theorem 3.4 of [PR22]). *If $f \in \mathrm{H}^r_p([-\pi,\pi]^d)$, where $r \geq 0$ is an integer, we have*

$$\|f - f^c_\mathrm{N}\|_{\mathrm{H}^r_p} \leq \frac{\mathrm{C}_\Phi}{\mathrm{N}^r} \|f\|_{\mathrm{H}^r_p} \tag{2.34}$$

where the constant $\mathrm{C}_\Phi \geq 0$ depends on the spectral radius of the matrix $\langle \Phi, \Phi^\intercal \rangle$, and on $\|\Phi\|^2_{2,\mathrm{L}^2_p} = \sum_{j=1}^{d+2} \|\Phi_j\|^2_{\mathrm{L}^2_p}$ where Φ_j, $j = 1, \dots, d+2$ are the components of the vector Φ.

The conservative best approximation in least square (2.33) can be represented in terms of the standard projection $\mathcal{P}_\mathrm{N}$ as

$$\mathcal{P}^c_\mathrm{N} f = \mathcal{P}_\mathrm{N} f + \sum_{k=-\mathrm{N}}^{\mathrm{N}} \hat{\mathrm{C}}^\intercal_k \langle f - \mathcal{P}_\mathrm{N} f, \Phi\rangle.$$

The above representation emphasizes the analogies with the L^2 minimization problem solved in [108]. The main difference is represented by the continuous representation of the solution in the space of trigonometric polynomials which permits to demonstrate spectral accuracy of the resulting approximation. Note also that the same conservative projection remains valid even when performing mesh changes, for example by reducing or increasing the number of modes by keeping moment conservation and spectral accuracy.

Application to the Boltzmann equation. We define the moment constrained Fourier approximation of the truncated Boltzmann operator as the solution to the following problem

$$\mathcal{Q}^{\mathrm{R},c}_\mathrm{N}(f,f) = \operatorname{argmin}\left\{ \|g_\mathrm{N} - \mathcal{Q}^\mathrm{R}(f,f)\|^2_{\mathrm{L}^2_p} \ : \ g_\mathrm{N} \in \mathbb{P}^\mathrm{N}, \ \langle g_\mathrm{N}, \Phi\rangle = 0 \right\}, \tag{2.35}$$

or equivalently

$$\mathcal{Q}^{\mathrm{R},c}_\mathrm{N}(f,f) = \mathcal{P}_\mathrm{N}\mathrm{Q}^\mathrm{R}(f,f) - \sum_{k=-\mathrm{N}}^{\mathrm{N}} \hat{\mathrm{C}}^\intercal_k \langle \mathcal{P}_\mathrm{N}\mathcal{Q}^\mathrm{R}(f,f), \Phi\rangle. \tag{2.36}$$

The constrained, Fourier projected, homogeneous Boltzmann equation then reads

$$\begin{cases} \dfrac{\partial f^c_\mathrm{N}}{\partial t} = \mathcal{Q}^{\mathrm{R},c}_\mathrm{N}(f^c_\mathrm{N}, f^c_\mathrm{N}), \\ f^c_\mathrm{N}(v,0) = \mathcal{P}^c_\mathrm{N} f_0(v), \quad v \in [-\pi,\pi]^d. \end{cases} \tag{2.37}$$

Let us underline that (2.36) differs from the conservative projection in Definition 2.3.1 in the sense that the constrained minimization problem (2.35) is solved with respect to the physical conservation laws of the collision term in the whole space and not in the periodic box. A direct application of Definition 2.3.1, for which we have proved the spectral accuracy property in Theorem 2.3.4, will lead to the projected operator

$$\widetilde{\mathcal{Q}}_{\mathrm{N}}^{\mathrm{R},c}(f,f) = \mathcal{P}_{\mathrm{N}}\mathcal{Q}^{\mathrm{R}}(f,f) + \sum_{k=-\mathrm{N}}^{\mathrm{N}} \hat{\mathrm{C}}_k^{\mathsf{T}} \langle \mathcal{Q}^{\mathrm{R}}(f,f) - \mathcal{P}_{\mathrm{N}}\mathcal{Q}^{\mathrm{R}}(f,f), \Phi \rangle. \tag{2.38}$$

It is therefore clear that some smallness on $\langle \mathcal{Q}^{\mathrm{R}}(f,f), \Phi \rangle$ is necessary in order to prove spectral consistency of (2.37). According to Prop. 2.2.3, this is guaranteed if the solution satisfy a smallness assumption outside the ball $\mathcal{B}_0(\mathrm{R})$.

Theorem 2.3.5 (Theorem 4.2 of [PR22]). *Let $f \in \mathrm{L}^2_p([-\pi,\pi]^d)$ be such that for $\delta > 0$ there exists $\mathrm{R} = \mathrm{R}(\delta)$ providing the following smallness estimate on the moments of the truncated collision term*

$$\left\| \langle \mathrm{Q}^{\mathrm{R}}(f,f), \Phi \rangle \right\|_2 \leq \widetilde{\mathrm{C}}\delta. \tag{2.39}$$

Then for any $r \geq 1$, there exists a constant $\mathrm{C} = \mathrm{C}(\|f\|_{\mathrm{L}^2}, \mathrm{R}, r)$ such that

$$\left\| \mathcal{Q}^{\mathrm{R}}(f,f) - \mathcal{Q}_{\mathrm{N}}^{\mathrm{R},c}(f_{\mathrm{N}}^c, f_{\mathrm{N}}^c) \right\|_{\mathrm{L}^2_p} \leq \mathrm{C}\left(\|f - f_{\mathrm{N}}^c\|_{\mathrm{L}^2_p} + \frac{\|\mathrm{Q}^{\mathrm{R}}(f_{\mathrm{N}}^c, f_{\mathrm{N}}^c)\|_{\mathrm{H}^r_p}}{\mathrm{N}^r} + \delta \right).$$

Theorem 2.3.5 states that the rate of convergence of the moment constrained spectral approximation of the truncated Boltzmann collision operator depends on the regularity of the distribution f (which is usual, see [100]), and on the smallness of the moments of the truncated collision term evaluated at f (which is new). From a practical viewpoint, this is equivalent to assume a suitable decay of the tails of the initial data and a computational domain large enough to guarantee minimal loss of the collision invariants.

Corollary 2.3.6. *Let $f \in \mathrm{H}^r_p([-\pi,\pi]^d)$ for a given $r \geq 1$ be such that there exist $\mathrm{R} = \mathrm{R}(r,\mathrm{N})$ providing estimate (2.39) with $\delta = \delta' \mathrm{N}^{-r}$. There exists a constant $\mathrm{C} = \mathrm{C}\left(\|f\|_{\mathrm{H}^r_p}, \mathrm{R}\right)$ such that*

$$\left\| \mathcal{Q}^{\mathrm{R}}(f,f) - \mathcal{Q}_{\mathrm{N}}^{\mathrm{R},c}(f_{\mathrm{N}}^c, f_{\mathrm{N}}^c) \right\|_{\mathrm{L}^2} \leq \frac{\mathrm{C}}{\mathrm{N}^r} \left(\|f\|_{\mathrm{H}^p_r} + \|\mathcal{Q}^{\mathrm{R}}(f_{\mathrm{N}}^c, f_{\mathrm{N}}^c)\|_{\mathrm{H}^r_p} + \delta' \right).$$

Note that, achieving consistency and spectral accuracy for increasing values of N requires a vanishing error in terms of moments of the collision operator and, as a consequence, a truncation domain which depends on the number of modes N. This agrees well with the intuition that a larger computational support has to be used when the number of modes is increased as already observed in practice in [187].

After investigating the consistency of the moment preserving spectral methods, it is natural to wonder whether the constrained projection impacts the stability and long time behavior properties of the new spectral approach. We have the following Theorem.

Theorem 2.3.7 (Theorem 4.5 of [PR22]). *Let us consider an initial condition $f_0 \in \mathrm{H}^k_p([-\pi,\pi]^d) \geq 0$ for a given $k \geq d/2$ such that there exist $\mathrm{R} = \mathrm{R}(k,\mathrm{N})$ providing an uniform in time estimate (2.39) for the solution $f(t,v)$ to problem (2.3) with $\delta = \delta' \mathrm{N}^{-k+r}$ for any $r < k$. Assume that this $f(t,\cdot) \in \mathrm{L}^1$ for all t. There exists $\mathrm{N}_0 \in \mathbb{N}$ depending on the H^k_p norm of f_0 and on the spectral radius of the matrix $\langle \Phi, \Phi^{\mathrm{T}} \rangle$ such that for all $\mathrm{N} \geq \mathrm{N}_0$:*

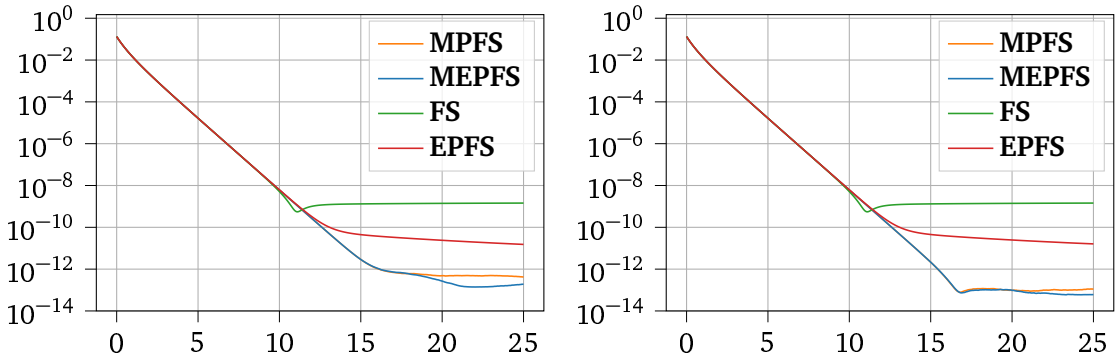

Figure 2.4: **Moment preserving spectral method.** Time evolution of $\|f_N - \mathcal{M}\|_{L^2}$ for the BKW solution, using $N = 32^2$ (left) and $N = 64^2$ (right).

1. *There is a unique global smooth solution* f_N^c *to the problem* (2.37)*;*
2. *For any* $r < k$*, there exists* $C_r > 0$ *such that*

$$\|f_N^c(t,\cdot)\|_{H_p^r} \leq C_r;$$

3. *this solution in everywhere positive for time large enough;*
4. *this solution* $f_N^c(t,\cdot)$ *converges to a solution* $f(t)$ *of the truncated Boltzmann equation* (2.3) *with spectral accuracy, uniformly in time;*

As in Section 2.3.1, the proof follows the perturbative framework developed in [100]. The main difference is that the constrained method preserves not only mass, but also momentum and kinetic energy, on the finite hypercube $[-\pi,\pi]^d$, without an H-theorem-like decay of the Boltzmann entropy a priori. As such, the equilibria of this new operator are not necessarily Gaussian (not even explicit), and one will not be able to perform the same spectral analysis of the linearized collision operator as was done in [100] to study its long time behavior. In addition, to recover spectral accuracy we need a smallness assumption on the error in the moments approximation of the collision term.

Numerical simulations. Let us now apply the conservative approximation to the fast spectral method for the Boltzmann equation by reproducing the test case of the Equilibrium Preserving method from Section 2.3.1, with the BKW initial data. For the velocity discretization, we choose $\Omega = [-12, 12]^2$, $N = 64^2$ then 128^2 points and $M = 8$ angular discretizations. Because the problem is not stiff, we use an explicit Runge-Kutta method of order 4 in time, with $\Delta t = 0.01$. We compare the fast spectral (**FS**) method with the moment preserving fast spectral (**MPFS**) method. We shall also compare our numerical experiments with the equilibrium preserving fast spectral (**EPFS**) method, and by taking a combination of the two approaches where we apply the equilibrium preserving method together with the moment preserving technique. Note that, this latter approach (referred to as **MEPFS**) preserves not only the moments but also the local Maxwellian equilibrium state.

Fig. 2.4 presents the time evolution of the L^2 error of the solution f_N with respect to the equilibrium distribution M, where we observe an exponential convergence towards $\mathcal{M}$. The behavior of the **EPFS** method is better than the classical **FS** which saturates around 10^{-9}, but both are outperformed by almost two order of magnitude by the new moment constrained **MPFS** method. Adding the

equilibrium preserving feature to this latter method slightly improve its accuracy, and the **MEPFS** scheme outperforms all the others in very large time. Moreover, and as expected, we also noticed in [PR22] that the new **MPFS** method preserves the moments up to machine precision.

2.4 Towards high performance computing applications

Boltzmann equation, as well as some related collisional kinetic models, have as we seen a lot of practical application in physics, biology and engineering. As such, having robust and efficient numerical methods is not enough: one also needs these methods to be implemented efficiently, in order to obtain relevant numerical results.

The Fast Kinetic Solver (FKS) has been developed in the series of works [74, 75, 76, 77], culminating in our work [DLNR18] to provide a large platform able to perform deterministic numerical simulations of many kinetic models in the full 3D/3D setting. This latter paper present the implementation of the fast spectral method in this platform. The FKS is based on the classical discrete velocity models (DVM) approach. As an alternative to finite volume strategies, the FKS platform focuses on semi-Lagrangian approaches [102] for the transport part. The main goal is to tackle the challenges related to the high dimensionality of the equations and with the difficulties related to the approximation of the collision integral.

In order to overcome the problem of this excessive computational cost, the Lagrangian technique exactly solves the transport step on the entire domain, without reprojecting the solution on the grid at each time step. The FKS approach was shown to be an efficient way to solve linear transport equations, and it has permitted the simulation of full six dimensions problems on a single processor machine [75]. Unfortunately the solutions computed with this method are limited to a first order in space and time precision.

Combining opportunely this semi-Lagrangian method with the fast spectral approach we have developed a method for solving the Boltzmann equation up to the six dimensional case for unsteady flows. In order to obtain such result we have constructed a parallel version of our algorithm taking advantages of Graphical-Processor-Unit (GPU) under CUDA language. The results from [DLNR18] presented in this Section show that we are nowadays ready and able to use kinetic equations to simulate realistic multidimensional flows. Up to our knowledge this is one of the first examples in literature of solution of the full multidimensional Boltzmann equation by means of deterministic schemes. Our main limitation to run extensive simulations remains at the present moment the lack of memory capacity due to the use of shared memory machines.

The semi-Lagrangian solver. The FKS belongs to the family of so-called semi-Lagrangian schemes which are typically applied to a Discrete Velocity Model (DVM) approximation of the original kinetic equation (1.1). Here, we shall present it to solve the Free Transport stage

$$\partial_t f_k + v_k \cdot \nabla_x f_k = 0.$$

We introduce a Cartesian uniform grid in the three dimensional physical space made of M points with Δx a scalar which represents the grid step (the same in each direction) in the physical space. Let $f^0_{j,k}$ be the point-wise values at time t^0 of the distribution f, $f^0_{j,k} = f(x_j, v_k, t^0)$. The idea is to

solve the transport stage continuously in space. To this aim we define at the initial time the function $\overline{f}_k^0(x)$ as a piecewise continuous function for all $x \in \Omega_j$, where $\Omega_j = [x_{j-1/2}; x_{j+1/2}]$ and $\Omega = \bigcup_j \Omega_j$. Hence starting from data $\overline{f}_{k,j}^0$ at time index 0, the exact solution of (1.1) is simply

$$\overline{f}_k^{*,1} = \overline{f}_k^0(x - v_k \Delta t), \qquad \forall x \in \Omega.$$

In other words, the entire function $\overline{f}_k^0$ is advected with velocity v_k during Δt unit of time and the $*$ superscript indicates that only the transport step has been solved so far. The extension of this procedure to the generic time step n gives

$$\overline{f}_k^{*,n+1} = \overline{f}_k^n(x - v_k \Delta t), \qquad \forall x \in \Omega, \tag{2.40}$$

where now, the key observation is that the discontinuities of the piecewise function $\overline{f}_k^n(x)$ do not lie on the interfaces of two different cells. Instead, the positions of the discontinuities depend entirely on the previous advection step and thus they may be located anywhere in the physical space. This means that if only the linear transport equation has to be solved, this approach gives the exact solution to the equation if the initial data is truly a piecewise constant function initially centered on the spatial mesh. As a direct consequence this part of the scheme is unconditionally stable, positive and conservative.

The collision steps. The effect of the collisional step is to change the amplitude of $\overline{f}_k(x)$. The idea is to solve the collision operator locally on the grid points, and, successively, extend these computed values to the full domain Ω. Thus we need to solve the following ordinary differential equation

$$\partial_t f_{j,k} = \mathcal{Q}(f_{j,k}), \tag{2.41}$$

where $f_{j,k} = f(x_j, v_k, t)$, for all velocities of the lattice $k = 1, \dots, \mathrm{N}$ and grid points $j = 1, \dots, \mathrm{M}$. The initial data for solving this equation is furnished by the result of the transport step obtained by (2.40) at points x_j of the mesh at time $t^{n+1} = t^n + \Delta t$, i.e. $\overline{f}_k^{*,n+1}(x_j)$, for all $k = 1, \dots, \mathrm{N}$, and $j = 1, \dots, \mathrm{M}$. Then, the solution of (2.41), locally on the grid points, reads if, for simplicity, a forward Euler scheme is used as

$$f_{j,k}^{n+1} = f_{j,k}^{*,n+1} + \Delta t\, \mathcal{Q}(f_{j,k}^{*,n+1}), \tag{2.42}$$

where $f_{j,k}^{*,n+1} = \overline{f}_k^{*,n+1}(x_j)$. To compute $\mathcal{Q}$, we use the fast spectral method presented in Section 2.2.3.

Numerical simulations. The work [DLNR18] consists in many numerical simulations to assess the validity and the quality of the FKS platform. We chose here to present some of the most advanced and computationally advanced ones.

Re-entry test in two dimensions with changing angle of attack in time. This test is inspired from re-entry test cases described in [77]. The computational domain is set to $\Omega = [0; 4] \times [0; 4]$. Within this domain we initiate three static objects, two small rectangles upfront ($[x_0; x_1] \times [y_0; y_1]$ and $[x_0; x_1] \times [y_0'; y_1']$) and one larger one behind ($[x_0'; x_1'] \times [(y_0 + y_0')/2; (y_1 + y_1')/2]$) where $x_0 = 1.5$, $x_1 = 1.7$, $x_0' = 1.8$, $x_1' = 2$, $y_0 = 1.7$, $y_1 = 1.95$, $y_0' = 2.05$, $y_1' = 2.3$. The computational mesh in physical space is made of 800×800 square cells. The velocity space is $[-10, 10]$ and is discretized

with 32^2 points. The initial density is set to $\rho(t=0)=1$, the velocity $(u_x,u_y)(t=0)=(3,0)$ and the temperature to $\mathrm{T}(t=0)=1$ everywhere. The final time is set to $t_{\text{final}}=10$. On the boundaries with the objects reflective boundary conditions are employed. Inflow boundary conditions are imposed to the west boundary whereas outflow boundary conditions are set elsewhere. The inflow boundary conditions are evolving in time and equal to

$$(u_x,u_y)_{\mathrm{BC}}(t)=\begin{cases}(3,0) & \text{if} \quad 0\le t\le t_1\\ (\sqrt{9-g^2(t)},g(t)) & \text{if} \quad t_1\le t\le t_2\\ (\frac{3\sqrt{2}}{2},\frac{3\sqrt{2}}{2}) & \text{if} \quad t_2\le t\le t_{\text{final}}\end{cases} \tag{2.43}$$

where $t_1=3/2$, $g(t)=t-t_1$ and $t_2=3\sqrt{2}/2+t_1$. Given these initial data, we expect a detached shock wave to occur upfront the objects and some complex wave pattern behind them. Moreover, setting the inflow boundary conditions to (2.43) splits the simulation into three stages. The first stage consists in the inflow boundary conditions facing the objects up to t_1. For this stage the upfront detached shock and the complex flow structure behind the objects are formed but they are not yet steady. Next, for the second stage, the inflow boundary condition is changing its direction by smoothly increasing the y component of $(u_x,u_y)_{\mathrm{BC}}(t)$ up to $t=t_2$. Note that this mimics a modification of the angle of attack of the objects with time. This change modifies the entire flow structure. Last, for the third stage the inflow boundary condition is fixed to $(u_x,u_y)_{\mathrm{BC}}=(u_0,v_0)$ up to the final time. As such the flow reaches an almost steady state.

In Fig. 2.5, we compare the BGK results (top row) with the Boltzmann ones (middle row) for intermediate iterations 4500, 12000 and 20000 for $\varepsilon=10^{-2}$ for the temperature. The bottom row presents the differences between the two models' temperature. The color legend is the same for the first two rows for both Figures, while for the bottom rows they are shown in the pictures.

The total amount of CPU time needed to compute the $\mathrm{N}_{\text{cycle}}=26000$ cycles for the BGK solution is 14.5h, while for Boltzmann model is 304h= 12.67d. The ratio is of the order 21 in favor of BGK. However, even if Boltzmann results demand a large amount of CPU time, we have seen that discrepancies do exist with respect to BGK model and in some cases, especially far from equilibrium, they cannot be ignored.

Three dimensional re-entry test case. The computational domain is set to $\Omega=[0,2]^3$ with a static cuboid placed in the center (see Fig. 2.6). The velocity space is $[-10,10]^3$ and discretized with 32^3 points. The relaxation parameter is set to $\varepsilon=0.3$. The initial density ρ is set to 1, the temperature $\mathrm{T}=1$ while the initial velocity is given by $(u_x,u_y,u_z)=(2,0,0)$. The final time is set to $t_{\text{final}}=0.6$ leading to 379 time steps. The inflow boundary conditions are imposed on the left boundary ($x=0$) while outflow boundary conditions on the remaining part of the boundary are imposed. Hard sphere molecules are considered for Boltzmann while for the BGK model the frequency ν is taken equal to $\mu=\mathrm{C}_\alpha 4\pi(2\lambda\pi)^\alpha$. The results are shown for the temperature and the density in Fig. 2.6.

From the analysis of such results it clearly emerges a difference in the profiles of the macroscopic quantities between the two models. We now analyze the performances. This test case was run on the EOS supercomputer at CALMIP, Toulouse France. The supercomputer is equipped with 612 computational nodes, each of them containing two Intel® Ivybridge 2.8GHz 10 core CPUs and 64 GB of RAM. Each CPU is equipped with 25MB of cache memory. The code was compiled with gcc-5.3.0 and executed on 90 computational nodes. That is to say, on 1800 computational cores in parallel. In the case of the Boltzmann collision operator the Fast Fourier Transforms were computed by means

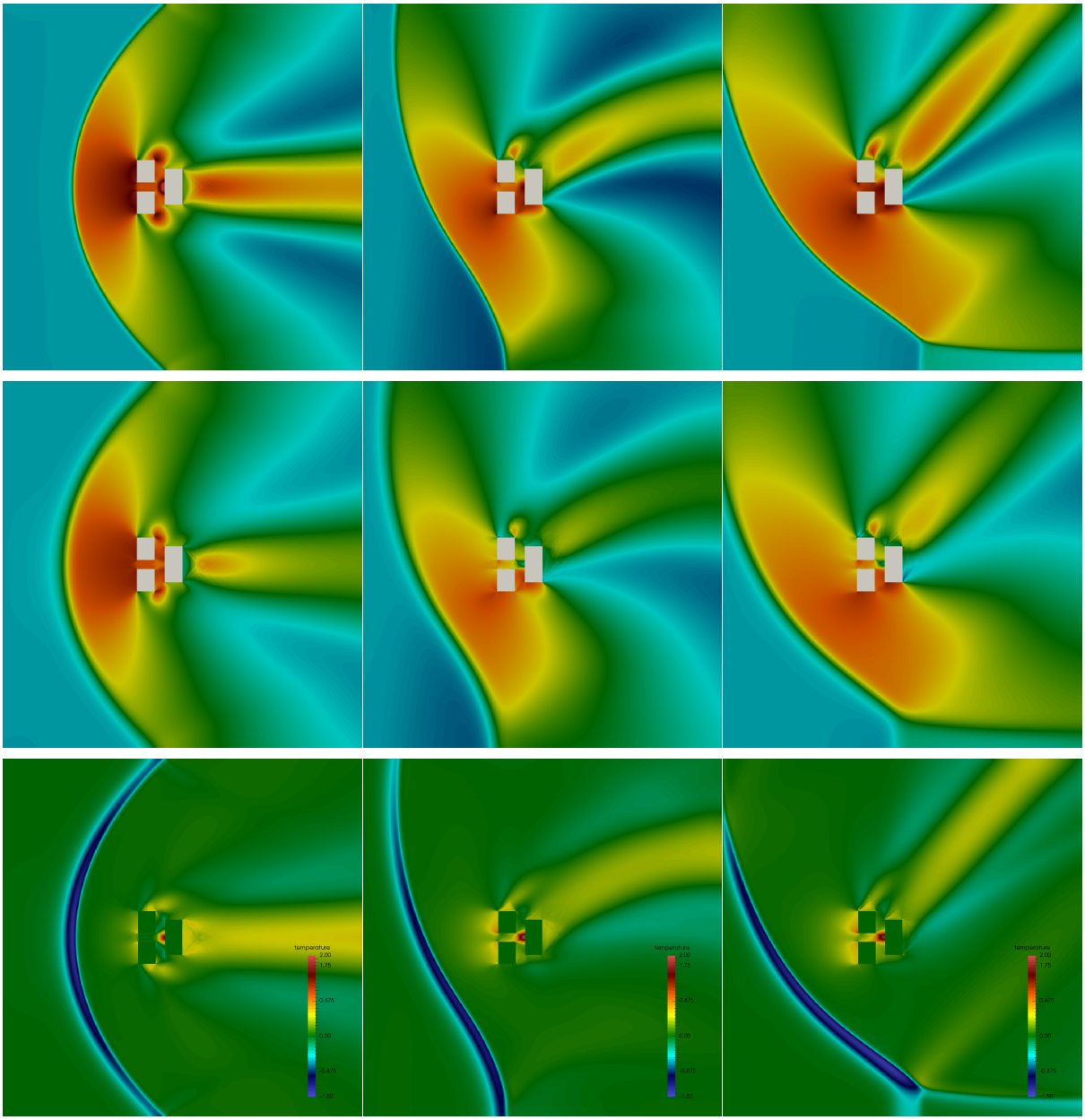

Figure 2.5: **Two dimensional re-entry test case for $\varepsilon = 10^{-2}$.** $M = 800 \times 800$ spatial cells and $N = 32^2$ velocity cells. BGK model (top row) Boltzmann model (middle row), difference between the two models (bottom row) at iterations 4500, 12000 and 20000. Temperature profile.

of the fftw library, version 3.3.4. The total runtime was equal to $t = 93713s$ $(26h)$ for the Boltzmann model. This is equivalent to 46000 computational hours (3.25 years) on a sequential machine. On the other hand, the runtime for the BGK model was only $t = 2174s$ $(0.6h)$ with a ratio 43 in favor of the simpler relaxation model.

The communications and MPI synchronization take 38% of the computational time for BGK equation. On the other hand, for the Boltzmann model the time spent on communications and synchronization amounts merely to 3.4% of the total runtime. This is due to extreme computational

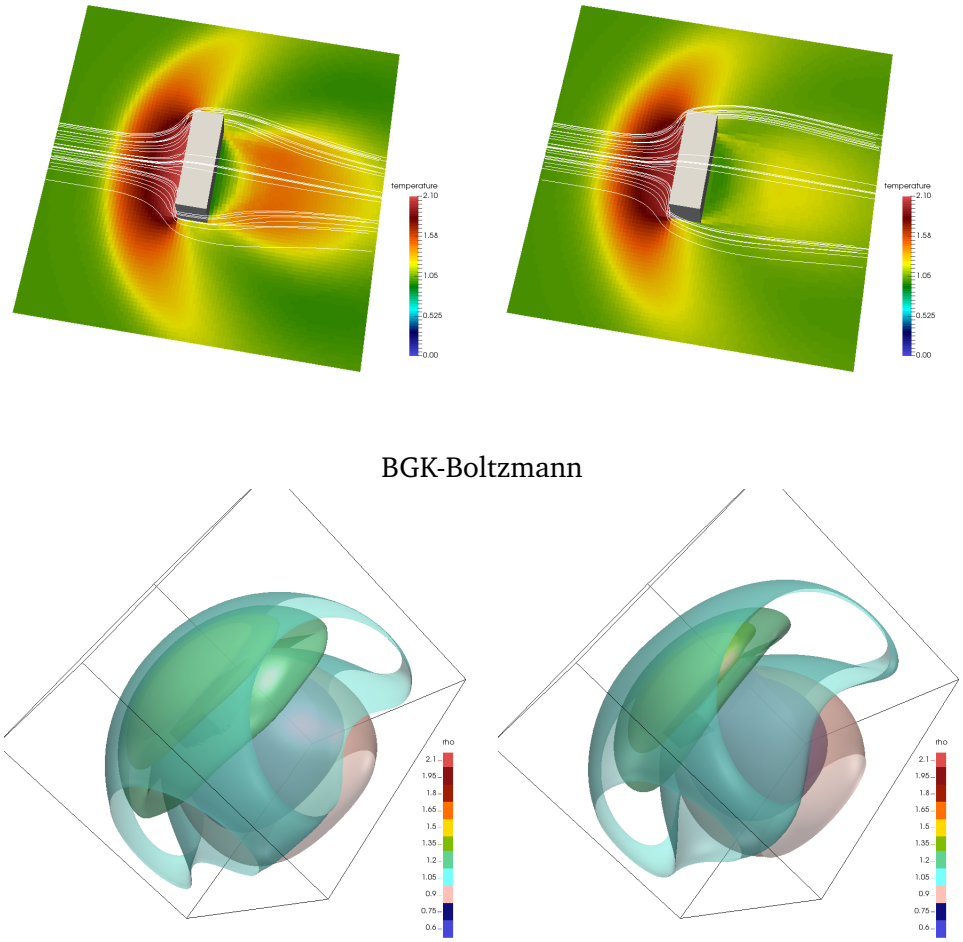

Figure 2.6: **Three dimensional re-entry test case for** $\varepsilon = 0.3$**.** $M = 90\times90\times90$ spatial cells and $N = 32^3$ velocity cells. BGK model (left column), Boltzmann model (right column) at time $t_{\text{final}} = 0.6$. Top row: temperature field with velocity streamlines, bottom row: isosurfaces of the density.

complexity of the three dimensional Boltzmann collision kernel.

2.5 Perspectives

Moment preserving spectral method for the Landau equation. The Landau equation is obtained by taking the grazing collision limit of the Boltzmann equation. This equation is used in plasma physics to model for example collisional plasmas in tokamacs. As such, it is extremely important to be able to simulate accurately and efficiently the solutions to this equation. Fourier spectral methods for this model have been designed, see e.g. [97]. They suffer the same lack of conservation than for the Boltzmann equation. Using our moment constraining approach could be a way to fix this problem.

Moment preserving spectral methods for arbitrary polynomial expansion. Any family of orthogonal polynomials over a weighted L^2 space can generate a spectral methods. Such families includes Hermite polynomials, Laguerre Polynomials, Sonine polynomials and so on [198]. The spectral methods obtained for each family have their own pros and cons, but never preserve the moments. An extension of our constraining approach to any family of orthogonal polynomials could solve this problem. This seems doable, with the use of general Hilbertian strategies.

Fast Kinetic Solver with geometry. A natural followup of the FKS work is now to improve the order in space of the semi-Lagrangian solver, and to be able to consider more complex geometries. This would require a very large computer engineering overhaul of the full FKS code. Extension to gas mixtures should also be desirable, but even more computationally costly.

CHAPTER

3 On the Granular Gases Equation

There are some questions in Astronomy, to which we are attracted rather on account of their peculiarity, as the possible illustration of some unknown principle, than from any direct advantage which their solution would afford to mankind.

James Clerk Maxwell
On the stability of the motion of Saturn's rings[165]

Contents

3.1 The granular gases equation 44
3.2 Spectral methods for the granular gases operator 56
3.3 Numerical experiments and results 59
3.4 Perspectives 65

This chapter is based on the works [GdSMM+15, JR17, CHMR21], *written in collaboration with Jose Antonio Carrillo, Maria Isabel Garcia de Soria, Jingwei Hu, Pierre-Emmanuel Jabin, Zheng Ma, Stéphane Mischler, Clement Mouhot and Emmanuel Trizac. Some parts are largely borrowed from these papers.*

Granular gases have been initially introduced to describe the nonequilibrium behavior of materials composed of a large number of unnecessarily microscopic particles, such as grains or sand. These particles form a gas, interacting *via* energy dissipating inelastic collisions. Statistical mechanics description of particle systems through inelastic collisions faces basic derivation problems such as the inelastic collapse [168], i.e. infinite many collisions in finite time. Nevertheless, the kinetic description of rapid granular flows [137, 115] has been able to compute transport coefficients for hydrodynamic descriptions successfully used in situations that are a long way from their supposed limits of validity, to describe, for instance, shock waves in granular gases [38], clustering [56], and the Faraday instability for vibrating thin granular layers [95, 38, 37, 55]. A large amount of practical systems can be described as a granular gas, such as for example spaceship reentry in a dusty atmosphere (Mars for instance), planetary rings [145, 9] and sorting behavior in vibrating layers of mixtures. A lot of other examples can be found in [69, 46].

Usually, a granular gas is composed of 10^6 to 10^{16} particles. The study of such a system will then be impossible with a direct approach, and we shall adopt a kinetic point of view, studying the behavior of a one-particle distribution function f, depending on time $t \geq 0$, space $x \in \Omega \subset \mathbb{R}^{d_x}$ and velocity $v \in \mathbb{R}^d$, for $d_x \leq d \in \{1, 2, 3\}$. The statistical mechanics description of the system has been then admitted in the physical community as the tool to connect the microscopic description to macroscopic system of balance laws in rapid granular flows [137, 115, 117] as in the classical rarefied gases [60]. In this first section, we shall review some basics on the inelastic Boltzmann equation, and present the mathematical state of the art since the previous review paper on the subject [212].

3.1 The granular gases equation

Microscopic dynamics. The microscopic dynamics can be summarized with the following hypotheses:

1. The particles interact via *binary* collisions. More precisely, the gas is rarefied enough so that collisions between 3 or more particles can be neglected.
2. These binary collisions are localized in space and time. In particular, all the particles are considered as point particles, even if they describe macroscopic objects.
3. Collisions preserve mass and momentum, but dissipate a fraction $1-e$ of the kinetic energy in the impact direction, where the inelasticity parameter $e \in [0, 1]$ is called *restitution coefficient*:

$$\begin{cases} v' + v'_* = v + v_*, \\ |v'|^2 + |v'_*|^2 - |v|^2 - |v_*|^2 = -\dfrac{1-e^2}{2} |(v - v_*) \cdot \omega|^2 \leq 0, \end{cases} \tag{3.1}$$

with $\omega \in \mathbb{S}^{d-1}$ being the impact direction. Using these conservations, one has the following two possible parametrizations (see also Fig. 3.2) of the post-collisional velocities, as a function of the pre-collisional ones:

- The ω-representation or reflection map, given for $\omega \in \mathbb{S}^{d-1}$ by

$$\begin{aligned} v' &= v - \frac{1+e}{2} ((v - v_*) \cdot \omega)\, \omega, \\ v'_* &= v_* + \frac{1+e}{2} ((v - v_*) \cdot \omega)\, \omega. \end{aligned} \tag{3.2}$$

- The σ-representation or swapping map, given for $\sigma \in \mathbb{S}^{d-1}$ by

$$\begin{aligned} v' &= \frac{v + v_*}{2} + \frac{1-e}{4}(v - v_*) + \frac{1+e}{4}|v - v_*|\sigma, \\ v'_* &= \frac{v + v_*}{2} - \frac{1-e}{4}(v - v_*) - \frac{1+e}{4}|v - v_*|\sigma. \end{aligned} \tag{3.3}$$

Remark 3.1.1. Taking $e = 1$ in both (3.2) and (3.3) yields the classical energy-conservative elastic collision dynamics, as illustrated in Fig. 3.1.

The geometry of collisions is more complex than the classical elastic one. Indeed, fixing $v, v_* \in \mathbb{R}^d$, denote by

$$\Omega_\pm := \frac{v + v_*}{2} \pm \frac{1-e}{2}(v_* - v), \qquad \mathrm{O} := \frac{v + v_*}{2} = \frac{v' + v'_*}{2}.$$

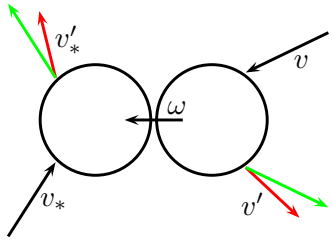

Figure 3.1: Geometry of the inelastic collision in the physical space (green is elastic, red is inelastic).

Then if $u := v - v_*$ is the *relative velocity*, one has

$$|\Omega_- - v'| = |\Omega_+ - v'_*| = \frac{1+e}{2}|u|,$$

namely $v' \in \mathcal{S}(\Omega_-, |u|(1+e)/2)$ and $v'_* \in \mathcal{S}(\Omega_+, |u|(1+e)/2)$, where $\mathcal{S}(x,r)$ is the sphere centered in x and of radius r (see also Fig. 3.2, to be compared with Fig. 1.1).

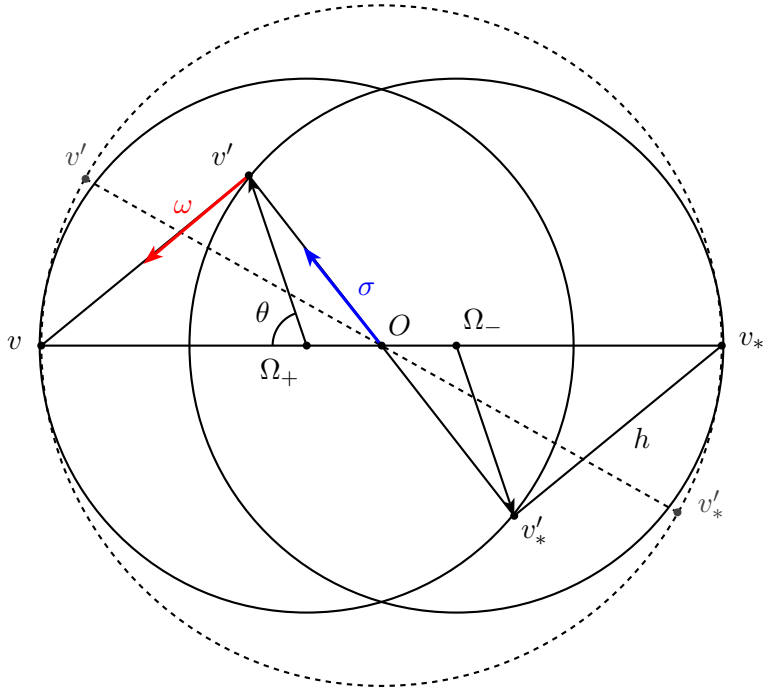

Figure 3.2: Geometry of the inelastic collision in the phase space (dashed lines represent the elastic case).

Restitution coefficient. The physics literature is quite divided on the question of whether the restitution coefficient e should be a constant or not [46]. Although most of the early mathematical results on the topic consider a constant e [212], it seems that this case is only realistic in dimension 1 of velocity (the so-called "collisional cannon" described in [46, Chapter 4] is a famous counter-example). The true realistic case considers that e depends on the relative velocity $|v - v_*|$ of the

colliding particles. Even more precisely, it must be close to the elastic case 1 for small relative velocities (namely no dissipation, elastic case), and decay towards 0 when this relative velocity is large. The first mathematical result on this direction can be found in [207], where

$$e(|v-v_*|) = \frac{1}{1+c\,|v-v_*|^\gamma}, \tag{3.4}$$

for a nonnegative constant c characterizing the inelasticity strength ($c=0$ being elastic), and $\gamma \in \mathbb{R}$.

Another important case is the so-called *viscoelastic* hard spheres one, thoroughly studied mathematically in a series of papers [4, 23, 5], where e is given by the implicit relation

$$e(|v-v_*|) + a|v-v_*|^{1/5} e(|v-v_*|)^{3/5} = 1, \tag{3.5}$$

for $a>0$. More details on the derivation of this expression can be found in [46, Chapter 3].

Finally, the case $e=0$ describes *sticky collisions*: the normal component of the kinetic energy being completely dissipated during impact, the particles stick and travel together in the tangent direction after impact. A derivation of the model from the microscopic dynamics on the line can be found in [42, 87].

Remark 3.1.2. This model is meaningful even in dimension 1, which is not the case for elastic collisions. Indeed, such monodimensional collisions are only

$$\{v', v'_*\} = \{v, v_*\},$$

meaning that the particle velocities are either swapped or preserved. The particles being indistinguishable, nothing happens[1]. In the 1d inelastic case, the collisions are given using (3.3) by

$$\{v', v'_*\} = \{v, v_*\} \quad \text{or} \quad \left\{\frac{v+v_*}{2} \pm \frac{e}{2}(v-v_*)\right\}$$

depending on the value of $\sigma \in \{\pm 1\}$.

The granular gases operator: Weak form. Using the microscopic hypotheses (1–2–3), one can derive the granular gases collision operator $\mathcal{Q}_\mathcal{I}$, by following the usual elastic procedure [212]. Its *weak form* in the σ-representation is given by

$$\begin{aligned}\int_{\mathbb{R}^d} \mathcal{Q}_\mathcal{I}(f,f)(v)\,\psi(v)\,\mathrm{d}v = \frac{1}{2}\int_{\mathbb{R}^d\times\mathbb{R}^d\times\mathbb{S}^{d-1}} f_* f\,\left(\psi' + \psi'_* - \psi - \psi_*\right) \\ \mathrm{B}(|v-v_*|, \cos\theta, \mathrm{E}(f))\,d\sigma\,\mathrm{d}v\,\mathrm{d}v_*,\end{aligned} \tag{3.6}$$

where the collision kernel is typically of the form $\mathrm{B}(|u|,\cos\theta,\mathrm{E}(f)) = \Phi(|u|)b(\cos\theta,\mathrm{E}(f))$, and $\mathrm{E}(f)$ is the kinetic energy of f, namely its second moment in velocity, the postcollisional velocities are computed by (3.3), and θ is the angle between σ and u. We shall assume in all the following of this section that the collision kernel is of *generalized hard sphere* type, namely

$$\mathrm{B}(|u|,\cos\theta,\mathrm{E})) = \Phi(|u|)\widehat{b}(\cos\theta,\mathrm{E}) = |u|^\lambda\, b(\cos\theta)\,\mathrm{E}^\gamma, \tag{3.7}$$

where $\lambda \in [0,1]$ ($\lambda=0$ being the simplified *Maxwellian pseudo-molecules case* and $\lambda=1$ the more relevant *hard sphere* case), $\gamma\in\mathbb{R}$ and the angular cross section b verifies

$$0 < \beta_1 \le b(x) \le \beta_2 < \infty, \quad \forall x \in [-1,1]. \tag{3.8}$$

[1] Because of that, the elastic collision operator is simply equal to 0 for a one-dimensional velocity space, the Boltzmann equation reducing only to the free transport equation.

Remark 3.1.3. Note that we assumed that the collision kernel B in (3.6) depends on the relative velocity, the angle of collision, and on $\mathrm{E}(f)$. These former dependencies are quite classical, but the latter is not. Nevertheless, it makes a lot of sense physically speaking, as one can see in [Rey12].

The weak form in the ω-representation can be written analogously as

$$\int_{\mathbb{R}^d} \mathcal{Q}_{\mathcal{I}}(f,f)(v)\,\psi(v)\,\mathrm{d}v = \frac{1}{2}\int_{\mathbb{R}^d\times\mathbb{R}^d\times\mathbb{S}^{d-1}} f_* f\,\left(\psi' + \psi'_* - \psi - \psi_*\right) \widetilde{\mathrm{B}}(|u|,\cos\theta,\mathrm{E}(f))\,d\omega\,\mathrm{d}v\,\mathrm{d}v_*, \tag{3.9}$$

where the postcollisional velocities are computed by (3.2), θ is the angle between ω and u, and

$$\widetilde{\mathrm{B}}(|u|,\cos\theta,\mathrm{E}) = |u|^{\lambda}\widetilde{b}(\cos\theta)\mathrm{E}^{\gamma}$$

with $\widetilde{b}(t) = 3|t|b(1-2t^2)$ for $-1 \le t \le 1$ by the change of variables between the σ- and the ω-representation, see [52] for details.

The granular gases operator: Strong form. Deriving a strong form of $\mathcal{Q}_{\mathcal{I}}$ with the reflection map in the ω-representation is a matter of a change of variables. However, deriving a strong form of $\mathcal{Q}_{\mathcal{I}}$ is not as easy as in the elastic case in the σ-representation since the collisional transform $(v, v_*, \sigma) \to (v', v'_*, \sigma)$ is not an involution and we have to go through the ω-representation, see [52] for details.

More precisely, given the restitution coefficient $e = e(|u|)$ depending on the relative velocity of the particles $u = v - v_*$, we assume the collisional transform's Jacobian for (3.2) is $\mathrm{J}(|u|,\cos\theta) \neq 0$ for all z. Notice $\mathrm{J} = e$ in the constant restitution case. It is in general a complicated expression of the relative speed $r = |u|$ and $s = \cos\theta$ involving e and its derivative. Then, the precollisional velocities read as

$$\begin{aligned} {}'v &= v - \frac{1+e}{2e}\left((v-v_*)\cdot\omega\right)\omega, \\ {}'v_* &= v_* + \frac{1+e}{2e}\left((v-v_*)\cdot\omega\right)\omega. \end{aligned} \tag{3.10}$$

The final strong from of the operator is $\mathcal{Q}_{\mathcal{I}}(f,f)(v) = \mathcal{Q}^+_{\mathcal{I}}(f,f)(v) - f(v)\mathrm{L}(f)(v)$ with the loss part of the operator given by

$$\mathrm{L}(f)(v) = \int_{\mathbb{R}^d\times\mathbb{S}^{d-1}} \widetilde{\mathrm{B}}(|v-v_*|,\cos\theta,\mathrm{E}(f)) f_*\,d\omega\,\mathrm{d}v_*$$

and the gain part of the operator in strong form written as

$$\mathcal{Q}^+_{\mathcal{I}}(f,f)(v) = \int_{\mathbb{R}^d\times\mathbb{S}^{d-1}} \widetilde{\Phi}^+_e(|u|,\cos\theta)\widetilde{b}^+_e(\cos\theta)\frac{\mathrm{E}^{\gamma}}{\mathrm{J}(|u|,\cos\theta)}\,{}'f\,{}'f_*\,d\omega\,\mathrm{d}v_*, \tag{3.11}$$

with $\widetilde{\Phi}^+_e(r,s)$ and $\widetilde{b}^+_e(s)$ given by

$$\widetilde{b}^+_e(s) = \widetilde{b}\left(\frac{s}{\sqrt{e^2+(1-e^2)s^2}}\right), \tag{3.12}$$

and

$$\widetilde{\Phi}_e^+(r,s) = \Phi\left(\frac{r}{e}\sqrt{e^2+(1-e^2)s^2}\right) = \left(\frac{r}{e}\sqrt{e^2+(1-e^2)s^2}\right)^\lambda. \tag{3.13}$$

Similarly, one can derive the following σ-representation:

$$\mathrm{L}(f)(v) = \int_{\mathbb{R}^d\times\mathbb{S}^{d-1}} \mathrm{B}(|v-v_*|,\cos\theta,\mathrm{E}(f))f_*\,d\sigma\,\mathrm{d}v_*$$

and

$$\mathcal{Q}_{\mathcal{I}}^+(f,f)(v) = \int_{\mathbb{R}^d\times\mathbb{S}^{d-1}} \Phi_e^+(|u|,\cos\theta)b_e^+(\cos\theta)\frac{\mathrm{E}^\gamma}{\mathrm{J}(|u|,\cos\theta)}\,{}'f\,{}'f_*\,d\sigma\,\mathrm{d}v_*, \tag{3.14}$$

with $\Phi_e^+(r,s)$ and $b_e^+(s)$ given by

$$b_e^+(s) = b\left(\frac{(1+e^2)s-(1-e^2)}{(1+e^2)-(1-e^2)s}\right)\frac{\sqrt{2}}{\sqrt{(1+e^2)-(1-e^2)s}}\,, \tag{3.15}$$

and

$$\Phi_e^+(r,s) = \Phi\left(\frac{r}{\sqrt{2}e}\sqrt{(1+e^2)-(1-e^2)s}\right) = \left(\frac{r}{\sqrt{2}e}\sqrt{(1+e^2)-(1-e^2)s}\right)^\lambda. \tag{3.16}$$

In these expressions, the precollisional velocities are given in the σ-representation by

$$\begin{aligned} {}'v &= \frac{v+v_*}{2} + \frac{1-e}{4e}(v-v_*) + \frac{1+e}{4e}|v-v_*|\sigma,\\ {}'v_* &= \frac{v+v_*}{2} - \frac{1-e}{4e}(v-v_*) - \frac{1+e}{4e}|v-v_*|\sigma. \end{aligned} \tag{3.17}$$

The granular gases collision operator has then the same structure of the elastic Boltzmann operator under Grad's cutoff assumption, namely it can be seen as the difference between the *inelastic* gain term $\mathcal{Q}_{\mathcal{I}}^+(f,f)$ and the loss term $f\,\mathrm{L}(f)$, which depends only on the chosen collision kernel, but not on the inelasticity.

We shall call *granular gases equation*, or inelastic Boltzmann equation, the collisional equation (1.1) with the collision operator $\mathcal{Q}_{\mathcal{I}}$:

$$\varepsilon^\alpha\frac{\partial f^\varepsilon}{\partial t} + v\cdot\nabla_x f^\varepsilon = \frac{\mathcal{Q}_{\mathcal{I}}(f^\varepsilon,f^\varepsilon)}{\varepsilon^\beta}. \tag{3.18}$$

Remark 3.1.4. Another popular approach to describe granular gases uses an *Enskog*-type collision operator. It is more relevant physically because it allows to keep the particles' radii δ positive, hence delocalizing the collision[2]. The strong form of the collision operator in the constant restitution coefficient case is given by

$$\begin{aligned} \mathcal{Q}_{\mathcal{E}}(f,f)(x,v) = \delta^{d-1}\int_{\mathbb{R}^d\times\mathbb{S}^{d-1}} &(\widetilde{\Phi}_e^+(|u|,\cos\theta)\widetilde{b}_e^+(\cos\theta)\frac{\mathrm{G}(\rho_+)}{e}\,{}'f_+\,{}'f_*\\ &-\mathrm{G}(\rho_-)f_-f_*)\,d\omega\,\mathrm{d}v_*, \end{aligned} \tag{3.19}$$

where we used the shorthand notation

$$g_\pm(x) := g(x\pm\delta\,\omega),$$

[2]Note that using a BBGKY approach [106] to derive (3.11) is not expected to succeed, because among other problems the macroscopic size of the particles composing a granular gas is incompatible with the Boltzmann-Grad scaling assumption.

and G is the *local* collision rate (also known as the *correlation* rate, see [212]). The global existence of renormalized solutions for the full granular gases equation (3.18) with the collision operator (3.19) has been established for both elastic and inelastic collisions in [92]. Existence and $L^1(dx\,dv)$ stability of such solutions has been proved in [220], for close to vacuum initial datum.

3.1.1 Cauchy theory of the granular gases equation

The space homogeneous setting. Most of the rigorous mathematical results concerning the granular gases equation are obtained in the space homogeneous setting, where $f = f(t,v)$ is the solution to

$$\begin{cases} \partial_t f = \dfrac{\mathcal{Q}_{\mathcal{I}}(f,f)}{\varepsilon}, \\ f(0,v) = f_{in}(v), \end{cases} \tag{3.20}$$

for a given scaling parameter $\varepsilon > 0$.

The first existence results for solution to (3.20) can be found in [26, 27]. These works deal with the generalized Maxwellian pseudo-molecule kernel (3.7) $\lambda = 0$, $b \equiv 1$ and $\gamma = 1/2$, with a velocity dependent restitution coefficient $e = e(|v - v_*|)$. Such a model allows to use some Fourier techniques to deal with the collision operator, altogether with the correct large time behavior for the kinetic energy, the so-called Haff's cooling Law (3.26), and the correct hydrodynamic limit (3.31). The main result of these works is the global well-posedness of the solutions to (3.20) in $L^1_2(\mathbb{R}^3)$, the convergence towards equilibrium, and the contraction in different metrics for the equation.

The physically relevant case of the hard sphere kernel $\lambda = 1$, $\gamma = 0$ was first considered in [207, 161] in the unidimensional case. This work establishes the global existence of measure solutions with finite kinetic energy for this problem. It also investigates the quasi-elastic $1 - e^2 \sim \varepsilon \to 0$ limit of the model, a nonlinear McNamara-Young-like friction equation.

The tail behavior of the equilibrium solution to the granular gases equation with a thermal bath $\Delta_v f$ was investigated in many papers, the main ones being [89, 28]:

Theorem 3.1.1 (From [28] and [89]). *Let $F(v) \geq 0$ for $v \in \mathbb{R}^d$ be a solution to the stationary equation*

$$\mathcal{Q}_{\mathcal{I}}(F,F) + \Delta_v F = 0$$

with all polynomial moments in velocity. Then,

$$F(v) \sim_{|v|\to\infty} \exp(-|v|^\alpha),$$

with $\alpha = 1$ in the Maxwellian molecules case and $\alpha = 3/2$ in the hard spheres case.

Indeed, the thermal bath gives an input of kinetic energy, preventing the appearance of trivial Dirac delta equilibria. It uses a careful estimate of the inelastic entropy production (3.23), and a fixed point argument for the existence and uniqueness of solutions.

The work [174] establishes the global well posedness of the granular gases equation without a thermal bath, for a general case of collision kernel (including (3.7)) and velocity dependent restitution coefficients:

Theorem 3.1.2 (Theorem 1.4 of [174]). *Let $0 \leq f_{in} \in L^1_3 \cap \in BV_4$. Then for any $T \in (0, T_c)$, where $T_c := \sup\{T > 0 : \mathcal{E}(f)(t) > 0, \forall\, t < T\}$ is the so-called* blowup time*, there exists an unique nonnegative solution $f \in \mathcal{C}(0,T;L^1_2) \cap L^\infty(0,T;L^1_3)$ of (3.20). It preserves mass and momentum, and converges in the weak-* topology of measures towards a Dirac delta.*

Their proof relies on careful estimates of the collision operator $\mathcal{Q}_\mathcal{I}$ in Orlicz space (specially the $L \log L$ space of finite entropy measures).

Remark 3.1.5. The related (but still mostly open) problem of the propagation of chaos was considered in [175] for a very simplified inelastic collision operator with a thermal bath.

Cauchy problem in the space dependent setting. The case of the space inhomogeneous setting[3] has been much less investigated.

The first result can be found in [15] in one dimension of space and velocity. This work establishes the existence and uniqueness of mild (perturbative) solutions, first for small $L^1(\mathrm{d}x\,\mathrm{d}v)$ initial data, and then for compactly supported initial data. The main argument is reminiscent from a work due to Bony in [32] concerning discrete velocity approximation of the Boltzmann equation in dimension 1.

The global existence of mild solutions in the general $\mathbb{R}^3_x \times \mathbb{R}^3_v$ setting, for a large class of velocity-dependent restitution coefficient, but for initial data close to vacuum, was obtained in [7]. The proof is based on a Kaniel-Shinbrot iteration on a very small functional space. The stability in $L^1(\mathbb{R}^3_x \times \mathbb{R}^3_v)$ under the same assumptions was established in [219]. Finally the existence and convergence to equilibrium in $\mathbb{T}^3_x \times \mathbb{R}^3_v$ for a weakly inhomogeneous granular gas[4] with a thermal bath was proved in [209], using a perturbative approach.

3.1.2 Large time behavior

Macroscopic properties of the granular gases operator. Modeling-wise, the main microscopic difference between a granular gas and a perfect molecular gas is the dissipation of the kinetic energy. Using the weak form (3.6) among with the microscopic relations (3.1) of the inelastic collision operator yields

$$\int_{\mathbb{R}^d} \mathcal{Q}_\mathcal{I}(f,f)(v) \begin{pmatrix} 1 \\ v \\ |v|^2 \end{pmatrix} \mathrm{d}v = \begin{pmatrix} 0 \\ 0 \\ -D(f) \end{pmatrix},$$

where $D(f) \geq 0$ is the *energy dissipation* functional, which depends only on the collision kernel:

$$D(f) := \int_{\mathbb{R}^d \times \mathbb{R}^d} f\, f_*\, \Delta(|v - v_*|, E(f))\, \mathrm{d}v\, \mathrm{d}v_*. \tag{3.21}$$

The quantity $\Delta(|u|, E)$ is the so-called *energy dissipation* rate, given using (3.1) by

$$\Delta(|u|, E) := \frac{1-e^2}{4} \int_{\mathbb{S}^{d-1}} |u \cdot \omega|^2\, B(|u|, \cos\theta, E)\, d\omega \geq 0, \quad \forall e \in [0,1]. \tag{3.22}$$

[3] Physically more realistic, in part because of the spontaneous loss of space homogeneity that has been observed in [116].

[4] Namely, the initial condition is chosen with a lot of exponential moments in velocity, and close to a space homogeneous profile.

This dissipation of kinetic energy has a major consequence on the behavior of the solutions to the granular gases equation. Combined with the conservation of mass and momentum, it implies (at least formally) an *explosive* behavior, namely convergence in the weak-* topology of solutions to (3.18) towards Dirac deltas, centered in the mean momentum $\boldsymbol{u}$:

$$f(t,\cdot) \rightharpoonup \delta_{v=\boldsymbol{u}}, \quad t \to \infty.$$

As for the entropy, it is not possible to obtain any entropy dissipation for this equation, in order to precise this large time behavior. Indeed taking $\psi(v) = \log f(v)$ in (3.6) yields

$$\begin{aligned}\int_{\mathbb{R}^d} \mathcal{Q}_{\mathcal{I}}(f,f)(v)\log f(v)\,\mathrm{d}v = \frac{1}{2}\int_{\mathbb{R}^d\times\mathbb{R}^d\times\mathbb{S}^{d-1}} f_* f\left[\log\left(\frac{f'f'_*}{f f_*}\right) - \frac{f'f'_*}{f f_*} + 1\right]\mathrm{B}\,d\sigma\,\mathrm{d}v\,\mathrm{d}v_* \\ + \frac{1}{2}\int_{\mathbb{R}^d\times\mathbb{R}^d\times\mathbb{S}^{d-1}} \left(f'_* f' - f_* f\right)\mathrm{B}\,d\sigma\,\mathrm{d}v\,\mathrm{d}v_*. \end{aligned} \tag{3.23}$$

The first term in (3.23), the elastic contribution, is nonpositive: this is Boltzmann's H-Theorem 1.2.1. Nevertheless, the second term has no sign: it is 0 only in the elastic case (because of the involutive *elastic* collisional transformation $(v, v_*, \sigma) \to (v', v'_*, \sigma)$). Boltzmann's entropy

$$\mathcal{H}(f) = \int_{\mathbb{R}^d} f(v)\log f(v)\,\mathrm{d}v$$

is then not dissipated by the solution of the granular gases equation if $e < 1$.

Kinetic energy dissipation and the Haff's cooling Law. In the space homogeneous setting with no thermostat, no entropy has been found, even numerically. One has then to use other macroscopic quantities to study the large time behavior of solutions to (3.18). Because of its explicit dissipation functional, kinetic energy is a good candidate for this. Moreover, being related to the variance, it allows to measure the concentration in velocity of the solution.

In order to have an explicit bound for the energy dissipation, let us assume that the collision kernel is of the general type (3.7). Using polar coordinates, it is straightforward to compute the dissipation rate (3.22):

$$\Delta(|u|,\mathrm{E}) = b_1\,\frac{1-e^2}{4}\,|u|^{\lambda+2}\mathrm{E}^{\gamma}, \quad b_1 = \left|\mathbb{S}^{d-2}\right|\int_0^{\pi}\cos^2(\theta)\sin^{d-3}(\theta)\,b(\cos(\theta))\,d\theta < \infty \tag{3.24}$$

Using the conservation of mass and momentum, one can always assume that the initial condition is of unit mass and zero momentum. Plugging (3.24) into (3.21) then yields using Hölder and Jensen inequalities

$$\frac{d}{dt}\mathrm{E}(f)(t) \le -b_1\,\frac{1-e^2}{4}\,\mathrm{E}(f)^{1+\gamma+\lambda/2}(t). \tag{3.25}$$

In particular, one will have the following large time behaviors: Setting $\mathrm{C}_e = b_1\,\rho\,(1-e^2)/4$ and $\alpha := \gamma + 1/2$,

- Maxwellian pseudo-molecules ($\lambda = \gamma = 0$) decay exponentially fast towards the Dirac delta :

$$\mathrm{E}(f)(t) = \mathrm{E}(f_{in})\,e^{-\mathrm{C}_e\,t};$$

  Notice that the inequality in (3.25) is an identity for this case.

- Hard spheres ($\lambda = 1$, $\gamma = 0$) exhibit the seminal quadratic *Haff's cooling Law* [124]:

$$\mathrm{E}(f)(t) \leq \left(\mathrm{E}(f_{in})^{-1/2} + \mathrm{C}_e\, t/2\right)^{-2}. \tag{3.26}$$

- Anomalous gases ($\gamma \neq 0$) exhibit more general behaviors:

$$\mathrm{E}(f)(t) \leq \begin{cases} \left(\mathrm{E}(f_{in})^{\alpha} + \mathrm{C}_e \alpha\, t\right)^{-\frac{1}{\alpha}} & \text{if } \gamma > -1/2 \ (\alpha > 0, \ \text{ finite time extinction}); \\ \mathrm{E}(f_{in})\, e^{-\mathrm{C}_e\, t} & \text{if } \gamma = -1/2; \\ \left(\mathrm{E}(f_{in})^{\alpha} - \mathrm{C}_e \alpha\, t\right)^{-\frac{1}{\alpha}} & \text{if } \gamma < -1/2 \ (\alpha < 0). \end{cases}$$

All of these formal results have been proven to be rigorous and sharp, with explicit lower bounds, in [26, 27] for the Maxwellian and hard sphere cases [171], and in [Rey12] for the anomalous cases. Extension to the viscoelastic case can be found in [5], where the energy is shown to behave as

$$\mathrm{E}(f)(t) \sim_{t\to\infty} \mathrm{C}(1+t)^{-5/3}.$$

All these papers share a common approach of proof, using the fact that the space homogeneous granular gases equation admits a self-similar behavior. Hence, introducing some well chosen time-dependent scaling function ω and τ, the distribution f is written as

$$f(t,v) = \omega(t)^d\, g\left(\tau(t), \omega(t)\, v\right),$$

to take into account the concentration in the velocity variables[5]. The rescaled function g is then solution to the granular gases equation, with an *anti-drift* term in velocity:

$$\partial_t g + \nabla_v \cdot (v\, g) = \mathcal{Q}_{\mathcal{I}}(g, g).$$

Using some regularity estimates of the gain term of $\mathcal{Q}_{\mathcal{I}}$ "à la" Lions/Bouchut-Desvillettes [34] and some new Povzner-like estimates [3], [171] then obtains a lower bound for the energy of g, yielding the generalized Haff's law by coming back to f.

Remark 3.1.6. In the viscoelastic case, note that the rescaling in velocity induces a time dependency on the restitution coefficient, complicating the proof of the Haff's cooling law [4]. It is also the case in the anomalous setting [Rey12], where the rescaling function depends nonlinearly on the solution f.

The question of the uniqueness, stability and exponential return to an universal equilibrium profile (related to the very important question of *hypocoercivity* discussed in Chapter 4, see [213]) of the self-similar solutions has then been fully addressed in the series of work [172, 173], for a constant restitution coefficient, with and without a thermal bath.

3.1.3 Compressible hydrodynamic limits

Let us consider in this subsection the hyperbolic scaling ($\alpha = 0$, $\beta = 1$) of the granular gases equation:

$$\frac{\partial f_\varepsilon}{\partial t} + v \cdot \nabla_x f_\varepsilon = \frac{1}{\varepsilon} \mathcal{Q}_{\mathcal{I}}(f_\varepsilon, f_\varepsilon). \tag{3.27}$$

[5] One can see the velocity scaling function ω as the inverse of the variance of the distribution f. This scaling is then a continuous "zoom" on the blowup, and can be used to develop numerical methods for solving the full granular gases equation, see [FR13, RT16].

Determining the precise hyperbolic limit $\varepsilon \to 0$ of equation (3.27) is a fundamental, yet very difficult question.

Indeed, for the elastic case $e = 1$, one simply has to use the fact that the equilibria of the collision operator are at the thermodynamical equilibrium (gaussian distributions) and the conservation of mass, momentum and kinetic energy to obtain the classical compressible Euler-Fourier system (1.3). Because of the trivial Dirac equilibria, this question is more intricate for the true inelastic case.

Pressureless Euler dynamics. Adopting the same approach as in the elastic case, one can formally plug the "equilibrium" Dirac deltas in the pressure to obtain the following pressureless Euler system:

$$\begin{cases} \dfrac{\partial \rho}{\partial t} + \operatorname{div}(\rho\, \boldsymbol{u}) = 0, \\ \dfrac{\partial (\rho \boldsymbol{u})}{\partial t} + \operatorname{div}(\rho\, \boldsymbol{u} \otimes \boldsymbol{u}) = \mathbf{0}. \end{cases} \tag{3.28}$$

This system can describe various interesting physical situations, such as galactic clusters, but is notoriously difficult to study mathematically. Its solution are in general ill-posed, as classical solutions cannot exists for large times and weak solutions are not unique.

In the unidimensional case, it is however possible to recover a well posed theory by imposing a semi-Lipschitz condition on u. This theory was introduced in [35], and later extended in [36] and [133]. We cite below the main result of [133]

Theorem 3.1.3 (From [133]). *For any $\rho^0 \geq 0$ in $\mathrm{M}^1(\mathbb{R})$ and any $u^0 \in \mathrm{L}^2(\rho^0)$, there exists $\rho \in \mathrm{L}^\infty(\mathbb{R}_+, \mathrm{M}^1(\mathbb{R}))$ and $u \in \mathrm{L}^\infty(\mathbb{R}_+, \mathrm{L}^2(\rho))$ solution to (3.28) in the sense of distribution and satisfying the semi-Lipschitz Oleinik-type bound*

$$u(t,x) - u(t,y) \leq \frac{x-y}{t}, \quad \text{for a.e. } x > y. \tag{3.29}$$

Moreover the solution is unique if u^0 is semi-Lipschitz or if the kinetic energy is continuous at $t = 0$

$$\int_{\mathbb{R}} \rho(t, \mathrm{d}x)\, |u(t,x)|^2 \longrightarrow \int_{\mathbb{R}} \rho^0(\mathrm{d}x)\, |u^0(x)|^2, \qquad \text{as } t \to 0.$$

The proof of Th. 3.1.3 is quite delicate, relying on duality solutions. For this reason, we only explain the rational behind the bound (3.29), which can be seen very simply from the discrete *sticky particles* dynamics. We refer in particular to [42] for the limit of this sticky particles dynamics as $\mathrm{N} \to \infty$.

Consider N particles on the real line. We describe the i^{th} particle at time $t > 0$ by its position $x_i(t)$ and its velocity $v_i(t)$. Since we are dealing with a one dimensional dynamics, we can always assume the particles to be initially ordered

$$x_1^{in} < x_2^{in} < \ldots < x_{\mathrm{N}}^{in}.$$

The dynamics is characterized by the following properties

1. The particle i moves with velocity $v_i(t)$: $\frac{d}{dt} x_i(t) = v_i(t)$.
2. The velocity of the i^{th} particle is constant, as long as it does not collide with another particle: $v_i(t)$ is constant as long as $x_i(t) \neq x_j(t)$ for all $i \neq j$.

3. The velocity jumps when a collision occurs: if at time t_0 there exists $j \in \{1, \dots, N\}$ such that $x_j(t_0) = x_i(t_0)$ and $x_j(t) \neq x_i(t)$ for any $t < t_0$, then all the particles with the same position take as new velocity the average of all the velocities

$$v_i(t_0+) = \frac{1}{|j|x_j(t_0) = x_i(t_0)|} \sum_{j|x_j(t_0)=x_i(t_0)} v_j(t_0-).$$

Note in particular that particles having the same position at a given time will then move together at the same velocity. Hence, only a finite number of collisions can occur, as the particles aggregates.

This property also leads to the Oleinik regularity. Consider any two particles i and j with $x_i(t) > x_j(t)$. Because they occupy different positions, they have never collided and hence $x_i(s) > x_j(s)$ for any $s \leq t$. If neither had undergone any collision then $x_i(0) = x_i(t) - v_i(t)\,t > x_j(0) = x_j(t) - v_j(t)\,t$ or

$$\frac{(v_i - v_j)_+}{(x_i - x_j)_+} < \frac{1}{t}, \tag{3.30}$$

where $x_+ := \max(x, 0)$. It is straightforward to check that (3.30) still holds if particles i and j had some collisions between time 0 and t.

As one can see this bound is a purely dispersive estimate based on free transport and the exact equivalent of the traditional Oleinik regularization for Scalar Conservation Laws, see [182]. It obviously leads to the semi-Lipschitz bound (3.29) as $N \to \infty$.

We extended this result to the one dimensional (in space and velocity) granular gases equation (3.27) in [JR17]. The basic idea of the proof of this work is to compare the granular gases dynamics to the pressureless gas system (3.28). The main difficulty is to show that f_ε becomes monokinetic at the limit (see also the very recent paper [94]). This is intimately connected to the Oleinik property (3.29), just as this property is critical to pass to the limit from the discrete sticky particles dynamics.

Unfortunately it is not possible to obtain (3.29) directly. Contrary to the sticky particles dynamics, this bound cannot hold for any finite ε (or for any distribution that is not monokinetic). This is the reason why it is very delicate to obtain the pressureless gas system from kinetic equations (no matter how natural it may seem). Indeed we are only aware of one other such example in [144].

One of the main contributions of [JR17] is a complete reworking of the Oleinik estimate, still based on dispersive properties of the free transport operator $v\,\partial_x$ but compatible with kinetic distributions that are not monokinetic, through the introduction of a new, global nonlinear energy. The main result in this paper is the following:

Theorem 3.1.4 (Theorem 1.3 from [JR17]). *Consider a sequence of weak solutions*

$$(f_\varepsilon)_\varepsilon \in L^\infty([0,\ T],\ L^p(\mathbb{R}_x \mathbb{R}_v))$$

for some $p > 2$ and with total mass 1 to the granular gases Eq. (3.27) such that all initial v-moments are uniformly bounded in ε, some moment in x is uniformly bounded, and f_ε^0 is, uniformly in ε, in some L^p for $p > 1$. Then any weak- limit f of f_ε is monokinetic, $f = \rho(t,x)\,\delta(v - u(t,x))$ for a.e. t, where ρ, u are a solution in the sense of distributions to the pressureless system (3.28) while u has the Oleinik property (3.29).*

Quasi-elastic limit. The physical community usually considers another approach, that is assuming that the granular gas is in a quasi-elastic $1-e^2 \sim \varepsilon \to 0$ setting. This was first proposed in [137], using an approach very similar to the seminal Grad's 13 moments closure for rarefied gas dynamics. The difficulty of a hydrodynamic description of granular materials has been addressed in well reasoned terms in [114], and as already discussed in the introduction, the hydrodynamic equations obtained with the kinetic theory of granular gases have been shown to be insightful well beyond their supposed limit of validity, i.e., away from the quasi-elastic limit assumption with external sources of energy. In fact, assuming that solutions of the kinetic problem do not deviate from being Gaussians, one can then obtain in the hard sphere case the following quasi-elastic compressible Euler system

$$\begin{cases} \dfrac{\partial \rho}{\partial t} + \operatorname{div}(\rho\, \boldsymbol{u}) = 0, \\ \dfrac{\partial (\rho \boldsymbol{u})}{\partial t} + \operatorname{div}\left(\rho\, (\boldsymbol{u} \otimes \boldsymbol{u}) + \rho\, \mathrm{T}\, \mathrm{I}\right) = \mathbf{0}, \\ \dfrac{\partial \mathrm{W}}{\partial t} + \operatorname{div}(\boldsymbol{u}(\mathrm{E} + \rho\, \mathrm{T})) = -\mathrm{K}\, \rho\, \mathrm{T}^{3/2}. \end{cases} \tag{3.31}$$

This is a compressible Euler-type system, which dissipates the kinetic energy thanks to its nonzero right hand side. The particular expression of this RHS allows, after integration in space, to recover the correct Haff's cooling Law.

The assumption that the solutions are not far from Gaussians obviously degenerates in a free cooling granular gas at some point leading to the so-called clustering instability studied by means of (3.31), see for instance [56] and the references therein. In fact, this assumption can be shown to be valid in the quasi-elastic limit, see [173] for a rigorous justification of this property. It has been used successfully as a scaling factor in [FR13] for the rescaling velocity method. Physicists argue that this assumption is also generically true in practical experiments with external sources of energy such as the shock waves in granular flows under gravity [189], clustering [127], the Faraday instability for vibrating thin granular layers [95, 170, 55], and many other applications, see [143] and the references therein.

Passing from the granular gases equation (3.18) to (3.31) has not been established properly. It can still be done formally under the weak inelasticity hypothesis $1-e^2 \sim \varepsilon$, see [208]. This particular scaling insures that the granular gases operator converges towards the elastic Boltzmann operator, as was shown rigorously in [172] in the space homogeneous setting. Moreover, it allows to characterize the equilibrium distribution of the limit operator, which is Gaussian.

A first step towards a rigorous compressible hydrodynamic limit is available in [Rey13], where the study of the spectrum of the heated granular gases operator $\mathcal{Q}_{\mathcal{I}} + \tau \Delta_v$, linearized with respect to the equilibrium described in [173], is done. For small inelasticity $1-e^2 \sim 0$, this work provides a spectral decomposition, and more importantly the existence and computation of eigenvalue branches. This work generalizes the seminal paper [88] on the spectrum of the linearized Boltzmann operator in L^2 to the L^1 and inelastic setting.

Other types of fluid limits (such as viscous limits) of the granular gases equation have been described in the review paper [84] and in the recent survey [109] for many different physical regimes, but none has been rigorously established. To illustrate the kind of equations obtained through these procedures, we write the generalized Navier-Stokes compressible equations for granular media in

conservative form, see [55], as

$$\begin{cases} \dfrac{\partial \rho}{\partial t} + \nabla \cdot (\rho \boldsymbol{u}) = 0, \\ \dfrac{\partial (\rho \boldsymbol{u})}{\partial t} + \nabla \cdot [\rho\, (\boldsymbol{u} \otimes \boldsymbol{u})] = \nabla \cdot \mathbf{P} + \rho\, \mathbf{F}, \\ \dfrac{\partial \mathrm{E}}{\partial t} + \nabla \cdot [\boldsymbol{u} \mathrm{W}] = -\nabla \cdot q + \mathbf{P} : \mathbf{E} + \boldsymbol{u} \cdot (\nabla \cdot \mathbf{P}) - \gamma + \rho \boldsymbol{u} \cdot \mathbf{F}. \end{cases} \tag{3.32}$$

The symbol F stands for external forces applied to the system. The constitutive relations for the momentum and heat fluxes write, as usual,

$$\mathrm{P}_{ij} = \left[-p + \left(\lambda - \frac{2}{3}\mu \right) \sum_i \mathrm{E}_{ii} \right] \delta_{ij} + 2\mu \mathrm{E}_{ij}$$

for the stress tensor, with $\mathrm{E}_{ij} = \frac{1}{2}\left(\frac{\partial \mathrm{U}_i}{\partial x_j} + \frac{\partial \mathrm{U}_j}{\partial x_i} \right)$. The thermal conductivity relates linearly the heat flux q to the temperature gradient, $q = -\chi \nabla \mathrm{T}$.

A first attempt to derive rigorously these equations of compressible Navier-Stokes type was done in the paper [51] using singular perturbations of the collision operator $\mathcal{Q}_{\mathcal{I}}$ and a central manifold approach inspired from [96]. The fact is that transport coefficients for compressible Navier-Stokes like equations can be derived by moment closures under different assumptions and these equations are able to recover realistic phenomena in granular gases, see [109].

3.2 Spectral methods for the granular gases operator

Due to the complexity of the inelastic Boltzmann collision operator $\mathcal{Q}_{\mathcal{I}}(f, f)$, numerical simulation of granular gases is challenging and mostly done at the particle level. Over the past decade, the Fourier spectral method for this model has received a lot of popularity for its high accuracy and relatively low computational cost.

The first attempt was made in [179] for the one-dimensional model. Later in [101, 108], [FR13], both two and three dimensional cases were considered. Although the implementation details may differ, the essential ideas in these works are the same, that is, utilizing the translational invariance of the collision operator and convolution property of the Fourier basis to write the collision operator as a weighted convolution in the Fourier space. In this way, the $\mathcal{O}(\mathrm{N}^{3d})$ cost per evaluation of the collision operator in the Galerkin framework (since $\mathcal{Q}_{\mathcal{I}}(f, f)$ is quadratic) is readily reduced to $\mathcal{O}(\mathrm{N}^{2d})$, where N is the number of basis used in each velocity dimension. Even though this reduction is dramatic compared to other spectral basis, numerical implementation of the "direct" Fourier spectral method is still computationally demanding; what makes it worse is that the method also requires $\mathcal{O}(\mathrm{N}^{2d})$ memory to store the precomputed weights, which quickly becomes a bottleneck as N increases. Recently, a fast Fourier spectral method was introduced in [128], wherein the key idea is to shift some offline precomputed items to online computation so that the weighted convolution in the original method can be rendered into a few pure convolutions to be evaluated efficiently by the fast Fourier transform (FFT). As a result, both the computational complexity and the memory requirement in the direct Fourier method are reduced.

In this section, we briefly review the original direct Fourier spectral method proposed in [101] and then its fast version introduced in [128]. To this end, we shall work on the σ-representation (3.3).

3.2.1 The direct Fourier spectral method

We first perform a change of variable $v_* \to g = v - v_*$ in (3.6) to obtain

$$\int_{\mathbb{R}^d} \mathcal{Q}_{\mathcal{I}}(f,f)(v)\psi(v)\,\mathrm{d}v = \int_{\mathbb{R}^d}\int_{\mathbb{R}^d}\int_{\mathbb{S}^{d-1}} \mathrm{B}(|g|,\sigma\cdot\hat{g})f(v)f(v-g)\big(\psi(v')-\psi(v)\big)\,\mathrm{d}\sigma\,\mathrm{d}g\,\mathrm{d}v,$$

where

$$v' = v - \frac{1+e}{4}(g-|g|\sigma).$$

We then assume that f has a compact support: $\mathrm{Supp}_v(f) \approx \mathcal{B}_0(\mathrm{S})$. Hence it suffices to truncate the infinite integral in g to a larger ballwith radius $\mathrm{R} = 2\mathrm{S}$:

$$\int_{\mathbb{R}^d} \mathcal{Q}_{\mathcal{I}}(f,f)(v)\psi(v)\,\mathrm{d}v = \int_{\mathbb{R}^d}\int_{\mathcal{B}_0(\mathrm{R})}\int_{\mathbb{S}^{d-1}} \mathrm{B}(|g|,\sigma\cdot\hat{g})f(v)f(v-g)\big(\psi(v')-\psi(v)\big)\,\mathrm{d}\sigma\,\mathrm{d}g\,\mathrm{d}v. \quad (3.33)$$

Next we restrict v to a cubic computational domain $\mathcal{D}_{\mathrm{L}} = [-\mathrm{L},\mathrm{L}]^d$, and approximate f by a truncated Fourier series f_{N}. The constant L should be chosen at least as $\mathrm{L} \geq (3+\sqrt{2})\mathrm{S}/2$ to avoid aliasing, see [101] for more details. Now substituting f_{N} into (3.33) and choosing $\psi(v) = e^{-i\frac{\pi}{\mathrm{L}}k\cdot v}$, we can obtain the k-th mode of the collision operator as

$$\hat{\mathrm{Q}}_k = \sum_{\substack{l,m=-\mathrm{N}\\ l+m=k}}^{\mathrm{N}} \mathrm{G}(l,m)\hat{f}_l\hat{f}_m, \quad (3.34)$$

where the weight $\mathrm{G}(l,m)$ is given by

$$\mathrm{G}(l,m) = \int_{\mathrm{B}_{\mathrm{R}}} e^{-i\frac{\pi}{\mathrm{L}}m\cdot g}\left[\int_{\mathbb{S}^{d-1}} \mathrm{B}(|g|,\sigma\cdot\hat{g})\Big(e^{i\frac{\pi}{\mathrm{L}}\frac{1+e}{4}(l+m)\cdot(g-|g|\sigma)}-1\Big)\,\mathrm{d}\sigma\right]\mathrm{d}g.$$

In the original spectral method [101], the weight $\mathrm{G}(l,m)$ is precomputed and stored since it is independent of the solution f which leads to a memory requirement of $\mathcal{O}(\mathrm{N}^{2d})$. During the online computation, the weighted sum (3.34) is directly evaluated whose complexity is $\mathcal{O}(\mathrm{N}^{2d})$.

3.2.2 The fast Fourier spectral method

The Carleman representation is trickier to obtain in the inelastic case compared to the elastic one described in Chapter 2. Nevertheless, in order to reduce the complexity of the direct spectral method as well as to alleviate its memory requirement, the idea introduced in [128] is also to render the weighted convolution (3.34) into a pure convolution so that it can be computed efficiently by the FFT.

In the granular case, the way to achieve this is through the low-rank approximation of $\mathrm{G}(l,m)$

$$\mathrm{G}(l,m) \approx \sum_{p=1}^{\mathrm{N}_p} \alpha_p(l+m)\beta_p(m), \quad (3.35)$$

where α_p and β_p are some functions to be determined and the number of terms N_p in the expansion is small. Then (3.34) becomes

$$\hat{\mathrm{Q}}_k \approx \sum_{p=1}^{\mathrm{N}_p}\alpha_p(k)\sum_{\substack{l,m=-\mathrm{N}\\ l+m=k}}^{\mathrm{N}} \hat{f}_l\big(\beta_p(m)\hat{f}_m\big), \quad (3.36)$$

where the inner summation is a pure convolution of two functions $\hat{f}_l$ and $\beta_p(m)\hat{f}_m$. Hence the total complexity to evaluate $\hat{\mathrm{Q}}_k$ (for all k) is brought down to $\mathcal{O}(\mathrm{N}_p\mathrm{N}^d \log \mathrm{N})$, i.e., a few number of FFTs.

Specifically, we first split $\mathrm{G}(l,m)$ into a gain term and a loss term:

$$\mathrm{G}(l,m) = \mathrm{G}_{\mathrm{gain}}(l,m) - \mathrm{G}_{\mathrm{loss}}(m),$$

where

$$\mathrm{G}_{\mathrm{gain}}(l,m) := \int_{\mathrm{B_R}} e^{-i\frac{\pi}{\mathrm{L}}m\cdot g}\left[\int_{\mathbb{S}^{d-1}} \mathrm{B}(|g|,\sigma\cdot\hat{g}) e^{i\frac{\pi}{\mathrm{L}}\frac{1+e}{4}(l+m)\cdot(g-|g|\sigma)}\,\mathrm{d}\sigma\right]\mathrm{d}g,$$

and

$$\mathrm{G}_{\mathrm{loss}}(m) := \int_{\mathrm{B_R}} e^{-i\frac{\pi}{\mathrm{L}}m\cdot g}\left[\int_{\mathbb{S}^{d-1}} \mathrm{B}(|g|,\sigma\cdot\hat{g})\,\mathrm{d}\sigma\right]\mathrm{d}g.$$

Note that the loss term is readily a function of m, hence no approximation/decomposition is actually needed. This suggests to evaluate the loss term of the collision operator by a precomputation of $\mathrm{G}_{\mathrm{loss}}(m)$ and then compute

$$\hat{\mathrm{Q}}_k^- = \sum_{\substack{l,m=-\mathrm{N}\\ l+m=k}}^{\mathrm{N}} \hat{f}_l\left(\mathrm{G}(m)\hat{f}_m\right)$$

by FFT. For the gain term, to get a decomposition of form (3.35), we introduce a quadrature rule to discretize g, then $\mathrm{G}_{\mathrm{gain}}(l,m)$ can be approximated as

$$\mathrm{G}_{\mathrm{gain}}(l,m) \approx \sum_{\rho,\hat{g}} w_\rho w_{\hat{g}}\,\rho^{d-1} e^{-i\frac{\pi}{\mathrm{L}}\rho\, m\cdot\hat{g}}\mathrm{F}(l+m,\rho,\hat{g}), \tag{3.37}$$

where $\rho := |g| \in [0,\mathrm{R}]$ is the radial part of g and $\hat{g} \in \mathbb{S}^{d-1}$ is the angular part, and w_ρ and $w_{\hat{g}}$ are the corresponding quadrature weights. The function F is given by

$$\mathrm{F}(l+m,\rho,\hat{g}) := \int_{\mathbb{S}^{d-1}} \mathrm{B}(\rho,\sigma\cdot\hat{g}) e^{i\frac{\pi}{\mathrm{L}}\rho\frac{1+e}{4}(l+m)\cdot(\hat{g}-\sigma)}\,\mathrm{d}\sigma. \tag{3.38}$$

With this approximation, the gain term of the collision operator can be evaluated as

$$\hat{\mathrm{Q}}_k^+ \approx \sum_{\rho,\hat{g}} w_\rho w_{\hat{g}}\,\rho^{d-1}\,\mathrm{F}(k,\rho,\hat{g}) \sum_{\substack{l,m=-\mathrm{N}\\ l+m=k}}^{\mathrm{N}} \hat{f}_l\left[e^{-i\frac{\pi}{\mathrm{L}}\rho\, m\cdot\hat{g}}\hat{f}_m\right],$$

which is in the same form as explained in (3.36).

As for the quadratures, the radial direction ρ can be approximated by the Gauss-Legendre quadrature. Since the integrand in (3.37) is oscillatory on the scale of $\mathcal{O}(\mathrm{N})$, the number of quadrature points needed for ρ should be $\mathcal{O}(\mathrm{N})$. The angular direction in 2D can be discretized using simple rectangular rule which is expected to yield spectral accuracy due to the periodicity. In the 3D case, we choose to use the spherical design [215] which is the near optimal quadrature on the sphere.

To summarize, the total complexity to evaluate $\hat{\mathrm{Q}}_k$ is $\mathcal{O}(\mathrm{MN}^{d+1}\log \mathrm{N})$, where M is the number of points used on $\mathbb{S}^{d-1}$ and $\mathrm{M} \ll \mathrm{N}^{d-1}$. Furthermore, the only quantity that needs to be precomputed and stored is (3.38), which in the worst scenario only requires $\mathcal{O}(\mathrm{MN}^{d+1})$ memory.

N	CPU	GPU
8	7.68ms	5.89ms
16	61.2ms	5.97ms
32	546ms	12.1ms
64	5.38s	109ms

Table 3.1: Average running time per evaluation of the collision operator in 3D. Comparison between the CPU and GPU-parallelized implementation for various Ns.

3.3 Numerical experiments and results

The accuracy and efficiency of the fast spectral method hav been validated in [128]. In this section, we present some numerical experiments that were performed in [CHMR21] to demonstrate the potential of the method in predicting some mathematical theories.

We consider the following spatially homogeneous equation with a thermal bath:

$$\partial_t f = \mathcal{Q}_{\mathcal{I}}(f,f) + \tau \Delta_v f, \tag{3.39}$$

where τ is the parameter describing the strength of the thermal bath. Notice that it is not necessarily related to the inelasticity parameter e, contrarily to *e.g.* [173]. The thermal bath $\Delta_v f$ will also be discretized using the Fourier spectral method and Runge-Kutta method is used for time marching.

For the collision operator, we consider the simplified variable hard sphere kernel

$$\mathrm{B}(|g|, \sigma \cdot \hat{g}, \mathrm{E}) = \mathrm{C}_\lambda |g|^\lambda, \quad 0 \le \lambda \le 1, \tag{3.40}$$

where $\mathrm{C}_\lambda > 0$ is some constant (namely (3.7) with $b = \mathrm{C}_\lambda$ and $\gamma = 0$.

For Maxwell molecules, given the initial condition $f_0(v)$ whose macroscopic quantities are ρ_0, u_0 and T_0, the density and velocity are conserved so $\rho(t) = \rho_0$, $u(t) = u_0$ and the temperature will evolve as

$$\mathrm{T}(t) = \left(\mathrm{T}_0 - \frac{8\tau}{1-e^2}\right)\exp\left(-\frac{\rho_0(1-e^2)}{4}t\right) + \frac{8\tau}{1-e^2}, \tag{3.41}$$

We could see

$$\lim_{t\to\infty} \mathrm{T}(t) = \frac{8\tau}{1-e^2}.$$

As in [128], this analytical formula of temperature works as the reference solution to ensure the correctness of the numerical solution.

From the implementation perspective, we dramatically improve the efficiency of the fast spectral method by using GPU via Nivida's CUDA. As shown in Table 3.1, GPU version is up to 15 times faster than CPU version depending on different Ns.

Test 1. Investigation of tail behavior of the equilibrium in 2D We compare the different tail behaviors of the equilibrium solutions for the Maxwell molecules collision kernel (2.27) and for the hard spheres collision kernel

$$\mathrm{B}(|g|, \sigma \cdot \hat{g}) = |g|/(2\pi)$$

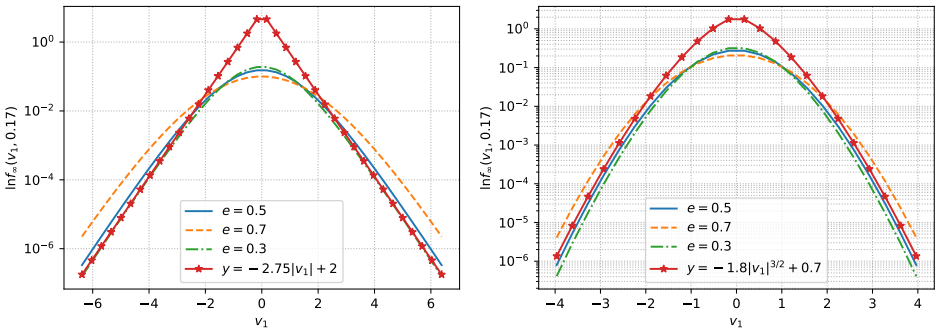

Figure 3.3: **Test 1.** The equilibrium profile of $e = 0.3, 0.5, 0.7$ with heat bath $\tau = 0.1$, initial data is the flat function (3.45). Left: Semi-log plot of $f_\infty(v_1, 0.17) = f(t = 55, v_1, 0.17)$ for Maxwell molecules. Right: Semi-log plot of $f_\infty(v_1, 0.17) = f(t = 55, v_1, 0.17)$ for hard spheres. The red lines are the reference profiles. Numerical parameters: $\mathrm{N}_v^2 = 128 \times 128$, $\mathrm{N}_\rho = 32$, $\mathrm{M}_{\hat{g}} = 16$, $\mathrm{R} = 20$, $\mathrm{L} = 5(3 + \sqrt{2})$ and $\Delta t = 0.01$.

in 2D. To see the tail we need higher resolution in velocity space so the velocity mesh is increased to $\mathrm{N}_v^2 = 128 \times 128$. We plot the profile in v_x (v_1) by choosing a fixed v_y (v_2) for different es (0.3, 0.5 and 0.7). From Fig. 3.3, we see that the numerical scheme generates overpopulated equilibrium tails: the Maxwell molecules case behaves like

$$f^\infty(v) \sim e^{-\alpha|v|},$$

and the hard spheres ones behaves like

$$f^\infty(v) \sim e^{-\alpha|v|^{3/2}}.$$

These results corresponds accurately to what was predicted theoretically in [89, 28] (summarized in Theorem 3.1.1).

Test 2. 3D hard sphere. This test is more related to physics, by simulating the so-called "Haff's cooling Law" (3.26). The initial data used is a Maxwellian with nonzero bulk velocity

$$f_0(v) = \frac{\rho_0}{(2\pi \mathrm{T}_0)^{3/2}} e^{-(v-u_0)^2}, \tag{3.42}$$

where $\rho_0 = 1$, $\mathrm{T}_0 = 2$ and $u_0 = (0.5, -0.5, 0)^\mathrm{T}$. We consider the hard spheres collision kernel in 3D, namely

$$\mathrm{B} = \frac{1}{4\pi}|g|.$$

In the first two tests, we consider a realistic set-up where the restitution coefficient e depends on the distance of the relative velocity, i.e., e is a function of $\rho = |g|$ instead of a constant,

$$e(\rho) = \frac{e_0 - 1}{2} \tanh(\rho - 4) + \frac{e_0 + 1}{2},$$

where $0 < e_0 < 1$. This allows to mimic the physically relevant visco-elastic hard spheres case (see also (3.5)). We numerically evaluate the temperature and the results for $e_0 = 0.2$ are shown in

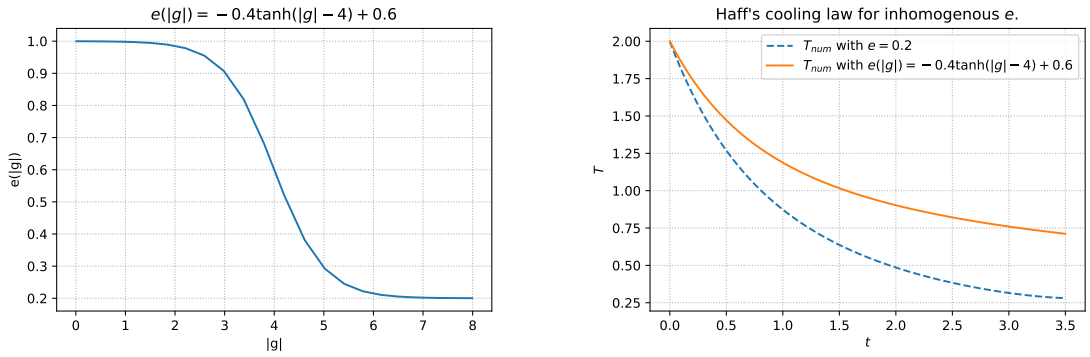

Figure 3.4: **Test 2.** Haff's cooling law with Maxwellian initial data (3.42). Left: plot of inhomogeneous e. Right: comparison of temperature between constant $e = 0.2$ (dash line) and $e(|g| = \rho) = -0.4\tanh(\rho - 4) + 0.6$. Numerical parameters: $\mathrm{N}_v^3 = 32 \times 32 \times 32$, $\mathrm{N}_\rho = 30$, $\mathrm{M}_{\hat{g}} = 32$, $\mathrm{R} = 8$, $\mathrm{L} = 5(3 + \sqrt{2})$ and $\Delta t = 0.01$.

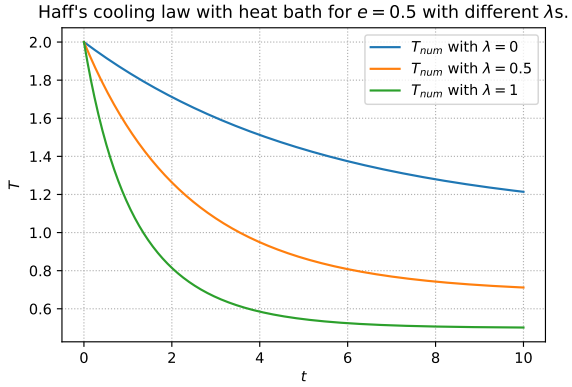

Figure 3.5: **Test 2.** Haff's cooling law with heat bath for different variable hard spheres exponent λs and Maxwellian initial data (3.42). The heat bath ($\tau = 0.1$). Numerical parameters: $\mathrm{N}_v^3 = 32 \times 32 \times 32$, $\mathrm{N}_\rho = 30$, $\mathrm{M}_{\hat{g}} = 32$, $\mathrm{R} = 8$, $\mathrm{L} = 5(3 + \sqrt{2})$ and $\Delta t = 0.01$.

Fig. 3.4. Compared with the cases where e is constant, we observe a slight slower decay of the temperature.

Another parameter that may affect the decay rate of temperature is the variable hard spheres exponent λ from (3.7). In Fig. 3.5 we show that, in the presence of thermal bath, for $e = 0.5$ but with $\lambda = 1$ (hard spheres), $\lambda = 0.5$ and $\lambda = 0$ (Maxwellian molecules), the decay rate of temperature will decrease after certain time (notice the slopes after $t = 5$).

Finally, with the thermal bath $\tau = 0.1$, we numerically evaluate the temperature up to time $t_{\text{final}} = 20$ for various values of restitution coefficients. The time evolution of T is shown in Fig. 3.6 where one can observe the transition of decays from $e = 0.5$ to $e = 0.95$ (near elastic case).

Test 3. Numerical dissipation of the Boltzmann's entropy We have seen that adding a drift term $\nabla_v(vf)$ or a thermal bath $\Delta_v f$ in velocity yields numerical entropy dissipation. These results were investigated thoroughly in my paper [GdSMM+15], that will be briefly presented in this Section.

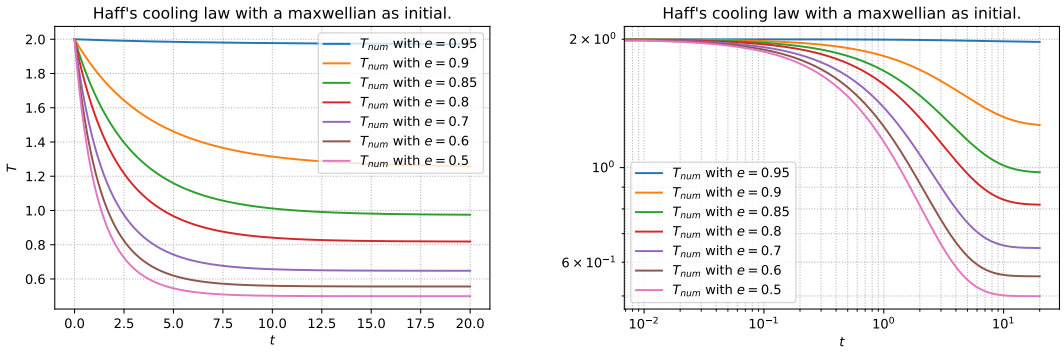

Figure 3.6: **Test 2.** Heated Haff's cooling law with Maxwellian initial data (3.42). Left: regular plot. Right: log-log plot. Numerical parameters: $N_v^3 = 32\times32\times32$, $N_\rho = 30$, $M_{\hat{g}} = 32$, $R = 8$, $L = 5(3+\sqrt{2})$ and $\Delta t = 0.01$.

Introduce the *Kullback-Leibler distance* (also called relative entropy) between the time dependent velocity distribution f and its long time limit f^∞:

$$\mathcal{H}(f|f^\infty) = \int f(t,v)\log\left[\frac{f(t,v)}{f^\infty(v)}.\right]\mathrm{d}v. \tag{3.43}$$

A convexity argument shows again that this quantity is nonnegative and is expected by construction to vanish at long times. Our central conjecture is that it does so monotonously in time, *i.e.* $d\mathcal{H}/dt < 0$.

We have implemented in [GdSMM+15] three complementary and independent simulation techniques to assess and illustrate our central statement that $d\mathcal{H}/dt < 0$: a spectral approach, the Direct Simulation Monte Carlo (DSMC) technique and Molecular Dynamics (MD) simulations.

- The spectral method is the one described in Section 3.2.
- The DSMC method is widely used in the present context, in aeronautics, and in microfluidics [21]: N particles follow a Kac's walk in velocity space and in the limit of large N, the corresponding first marginal f evolves according to the Boltzmann equation [175]. The method is Monte Carlo in spirit, and thus of stochastic nature.
- In the MD simulations the exact equations of motion are integrated, starting from a given initial configuration of N grains in a finite simulation box of volume, V, with periodic boundary conditions. This method does not rely on the validity of a kinetic description and by comparing to the outcome of DSMC, provides a stringent test of the theory and predictions under scrutiny. In particular, the spatial dependence is fully accounted for within MD –unlike in the DSMC approach used where spatial homogeneity is enforced from the outset– and does not rely on the molecular chaos assumption. If $N \to \infty$ and in the low-density limit (or more precisely, in the Grad's limit) the first marginal is expected to fulfill the Boltzmann equation.

In the simulations, the evolution of the one-particle distribution function has been measured for the two models, the Gaussian and stochastic thermostats, using different values of the inelasticity and starting with different initial velocity distributions. With that, the functional $\mathcal{H}$ can be computed through Eq. (3.43), where the knowledge of the late time distribution f^∞ is required. Hence, $\mathcal{H}$ cannot be obtained "on the flight", but is computed after f^∞ has been measured in the simulations. We have taken the grain's mass, m, as the unit of mass and the initial temperature, T(0), as the

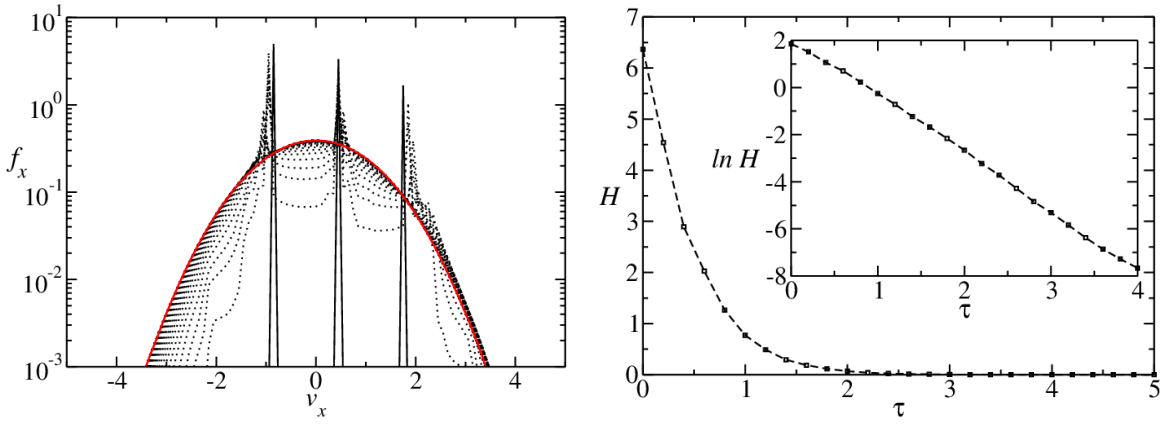

Figure 3.7: **Test 3.** Left) First marginal of the DSMC results with the initial data (3.44) (black solid line) and $e = 0.9$, $\mathrm{N} = 1000$. The results have been averaged over 10^5 realizations. The distribution is plotted for different values of the number of collisions per particle τ. The bell-shaped red solid line corresponds to the distribution at the end of the simulation ($\tau \simeq 14$). Right) Corresponding evolution of $\mathcal{H}(t)$. Inset: linear-log scale.

unit of temperature. In the MD simulations the unit of length is the diameter of the particle, σ. We always considered a two-dimensional system of $\mathrm{N} = 1000$ disks. The spectral method is used in 2 dimensions of the velocity space, with 64 modes in each space directions. It is known that such a number of modes gives a very good accuracy, thanks to the spectral convergence of the method. The Gaussian thermostat case has been studied by DSMC and MD, while the stochastic thermostat has been addressed via DSMC and spectral methods.

Fig. 3.7 displays DSMC results for a system with dissipation parameter $e = 0.90$ heated by the Gaussian thermostat with B chosen to have unit stationary temperature. The results have been averaged over 10^5 realizations and the initial distribution has been taken asymmetric with three peaks:

$$f_{in}(v) = \frac{3}{6}\delta(v-u_1) + \frac{2}{6}\delta(v-u_2) + \frac{1}{6}\delta(v-u_3), \quad \forall v \in \mathbb{R}^2, \tag{3.44}$$
$$u_2 = \frac{1}{3}\left[\frac{\mathrm{T}(0)}{m}\right]^{1/2}\begin{pmatrix}1\\1\end{pmatrix},\ u_1 = -3u_2,\ u_3 = 5\mathrm{u}_2.$$

In the left side of the figure, the first marginal of f has been plotted for different values of the number of collisions per particle, τ. Clearly, the behavior of $\mathcal{H}(t)$ on the right hand side is compatible with an asymptotic vanishing for $t \to \infty$, which simply indicates that f tends towards f^∞. More interestingly, $\mathcal{H}$ is nonincreasing from the shortest to the largest times one can reach in the simulations.

In Fig. 3.8, a comparison between MD and DSMC results is shown for a system with $e = 0.80$. The initial distribution is the same asymmetric distribution as in the previous case. The results have been averaged over 5×10^3 realizations in the two types of simulations. The density in the MD simulations is $n = 0.005\sigma^{-2}$, which corresponds to a rather dilute system. The excellent agreement between MD and DSMC is important, not only because it again points to the monotonicity of $\mathcal{H}(t)$ but also because the MD algorithm provides a reference benchmark ("true dynamics"), which does

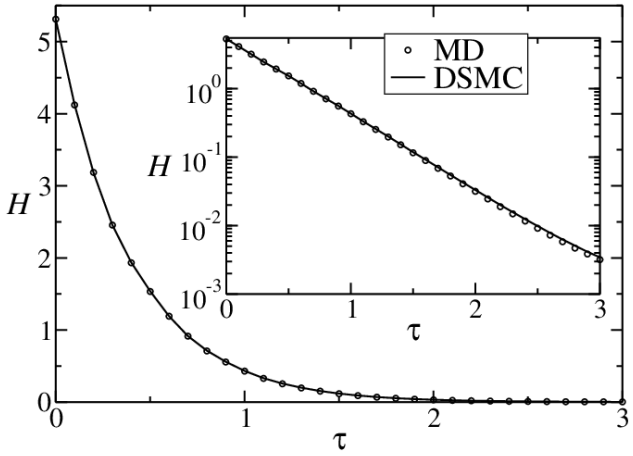

Figure 3.8: **Test 3.** Evolution of $\mathcal{H}(t)$ as a function of the number of collisions per particle for MD and DSMC simulations, with the initial distribution (3.44) and $e = 0.8$, N $= 1000$. The results have been averaged over 5×10^3 realizations. Inset: linear-log scale.

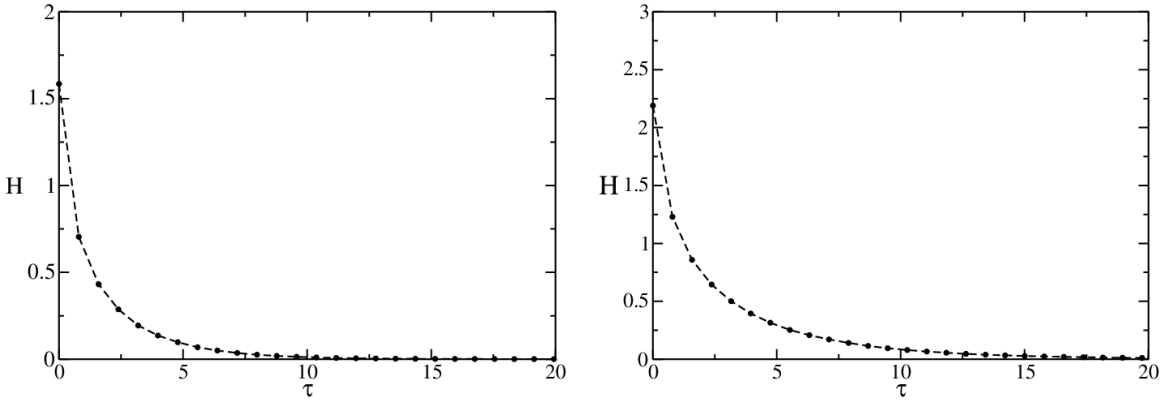

Figure 3.9: **Test 3.** Left) DSMC results of the time evolution of $\mathcal{H}(\tau)$ for the stochastic thermostat with $e = 0.9$, starting with the flat distribution (3.45). Right) Results for $e = 0.95$.

not rely on the hypothesis leading to the Boltzmann equation, and in particular does not *a priori* assume the system to be homogeneous. Let us mention that we have observed the same qualitative features for a large gamut of initial conditions (symmetric around the velocity origin or asymmetric) and different values of the inelasticity in the whole range, $0 < e < 1$.

In Fig. 3.9, DSMC results are shown for a system heated by the stochastic thermostat. We have considered two values of the inelasticity, $e = 0.9$ and $e = 0.95$, with an amplitude of the noise, ξ, such that the stationary temperature is $8.80\mathrm{T}(0)$ for $e = 0.9$ and $17.13\mathrm{T}(0)$ for $e = 0.95$. In the two cases, we have started with the same initial flat distribution:

$$f(\mathrm{v},0) = \begin{cases} \dfrac{1}{4w^2}, & \text{if } v_x \in [-w,w] \text{ and } v_y \in [-w,w] \\ 0, & \text{otherwise} \end{cases} \tag{3.45}$$

with $w = \left[\frac{6\mathrm{T}(0)}{m}\right]^{1/2}$. The results have been averaged over 10^5 trajectories. Clearly, as in the previous case, the functional $\mathcal{H}$ decays monotonically for all times. Again, as in the Gaussian thermostat case,

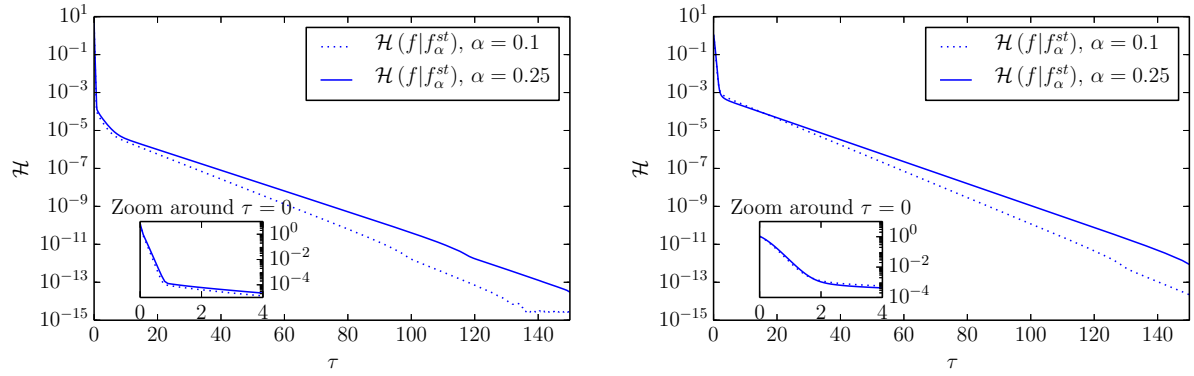

Figure 3.10: **Test 3.** Left) Time evolution of the entropy for the nonlinear Boltzmann equation with stochastic thermostat, solved with the spectral scheme (M = 64), for $e = 0.25$ (solid line) and $e = 0.1$ (dotted line), starting with the assymetric, three sharp peaks. Right) Same, for the flat initial distribution.

the same qualitative behavior is obtained for other initial conditions and values of the inelasticity.

Finally, we present in Fig. 3.10 the evolution of $\mathcal{H}$ for small normal restitution coefficients, namely $e = 0.1$ (almost sticky particles) and $e = 0.25$, in the stochastic thermostat case. The spectral scheme is used for these simulations. We show our results for both the assymetric distribution (3.44) composed of three peaks (left) and for the flat distribution (3.45) (right). As in the other simulations, we observe in all these cases a monotone decay of the entropy functional $\mathcal{H}$. Thanks to the accuracy of the spectral scheme, and owing to its deterministic nature, we can observe this decay up to the machine precision. Although it may be due to numerical artifacts (this behavior can be also observed in the elastic case $e = 1$), this decay seems to follow two exponential regimes, a very fast one in short time followed by a slower one in larger time. Nevertheless, these decays are always exponential.

All the simulation results point in the same direction: the functional $\mathcal{H}$ defined by Eq. (3.43) can be a good Lyapunov functional for the free-cooling case (Gaussian thermostat) and for the stochastic thermostat.

3.4 Perspectives

As we have seen, the granular gases equation is now pretty well understood in the space homogeneous setting, but not that much in the general space dependent case, specially in multiD. As such, the following questions would be very interesting to be addressed.

Pressureless Euler limit in the multidimensional case. We have seen that the fluid limit of the granular gases equation in one dimension of space and velocity towards the pressureless Euler system as been established in [JR17]. One of the main tools of the proof is the introduction of the following new nonlinear functional: for any η, $\mu > 0$, $k \geq 1$ and f solution to (1.1) with $d = 1$,

$$\mathcal{L}_{\eta,\mu,k}(f)(t) := \int \frac{(v - v_*)_+^{k+2}}{(x - y + \eta)^k} \chi_\mu(x - y) f(t,x,v) f(t,y,v_*) \, \mathrm{d}v \, \mathrm{d}v_* \, \mathrm{d}x \, \mathrm{d}y, \tag{3.46}$$

where the function χ_μ is a smooth, non-centered approximation of the Heaviside function. We showed that the uniform boundedness of $\mathcal{L}_{\eta,\mu,k}(f^\varepsilon)$ implies the monokineticity of f^ε. This functional

is a kinetic extension of the sticky particle strategy from [42], and is reminiscent of the so-called Bony-Cercignani functional, used in [32, 59, 22]. Unfortunately, the techniques used for bounding (3.46) are really unidimensional.

Generalizing this hydrodynamic limit result to the *higher dimensional* setting is then an open problem. One could try first to extend it to the two dimensional Vicsek flocking model introduced in [72]:

$$\partial_t f + v \cdot \nabla_x f + \nabla_v \cdot \left(\Pi_{v^\perp} \frac{\mathcal{I}_f(t,x)}{|\mathcal{I}_f(t,x)|} \right) = \Delta_v f,$$
$$\mathrm{I}_f(x,t) = \iint_{\mathbb{R}^2 \times \mathbb{S}^1} \mathrm{K}(|y-x|) f(t,y,v_*) \,\mathrm{d}y \,\mathrm{d}v_*,$$

where the velocity is defined on the one-dimensional sphere $\mathbb{S}^1$. The operator Π_e denotes the orthogonal projection on a vector e and K is an interaction potential. This mean-field equation has a dissipative structure similar to the one of the granular gases equation (1.27), and its solutions converge formally toward Dirac deltas in large times. One could try to extend the functional (3.46) to the scaled version of this equation, by first using a simple parametrization of the unit sphere. It would allow to obtain a fluid description of this model and prove a mathematically rigorous hydrodynamic limit toward this new model.

This strategy being successful, one could then tackle the true granular gases model in dimension 2 and 3, by extending an idea introduced in [197]. Indeed, this recent paper presents the first multidimensional generalization of the Cercignani-Bony functional. This could be used to generalize (3.46) to any dimensions.

Numerical simulations of planetary rings formation. It is largely believed in the physics community that the good way to describe planetary rings formations is to use granular gases. Nevertheless, to the best of my knowledge, such a system as never been simulated properly using a collisional kinetic approach (see [145, 63]). This is in particular due to the fact that the granular gases equation exhibits at the same time concentration in velocity, which means that the grids have to be very refined, and the high dimensionality of its collision operator which makes simulations very costly. The first problem has been resolved in my series of works [FR13, RT16], but the other one was open until the introduction of the fast algorithm that I have presented in this Chapter. I believe that combining these two tools would be the key to allow to perform simulations of planetary rings formation.

CHAPTER 4 | Asymptotic Behaviors of Numerical Approximations of Kinetic Equations

One of the reasons of the bewilderment which is sometimes felt at an unheralded appearance of the term entropy is the superabundance of objects which bear this name.

Harold Grad
The many faces of entropy [122]

Contents

4.1 Hydrodynamic limits of kinetic equations 68
4.2 Asymptotic Preserving numerical methods 75
4.3 Discrete Hypocoercivity 96
4.4 Hybridization through domain indicators 101
4.5 Perspectives 107

This chapter is based on the works [FR15, MRS17, MRS19, BHR20, BR22], *written in collaboration with Rafael Bailo, Marianne Bessemoulin-Chatard, Francis Filbet, Maxime Herda, Ward Melis, and Giovanni Samaey. Some parts are largely borrowed from these papers.*

One of the reasons the Boltzmann equation gained so much importance in the twentieth century is that it is one the main tools to rigorously derive the equations of fluid dynamics such as the Euler or Navier-Stokes systems (both compressible and incompressible, see *e.g.* [60]). These models are obtained as asymptotic regime(s) of the space inhomogenous kinetic equations, leading in a reduction of complexity from mesoscopic, kinetic models to macroscopic, fluid ones. Such asymptotic regimes can be reached by taking the large time limit $t \to \infty$ of the general kinetic equation (1.1). Equivalently, dimensional scaling techniques[1] can also help studying this problem, by taking the small parameter limit $\varepsilon \to 0$ for different types of scaling parameters α and β. We shall present in this Chapter some techniques that have been introduced to deal with these limits qualitatively and quantitatively, both theoretically and numerically.

[1] Such as taking $\widetilde{t} := \varepsilon t$ and $\widetilde{x} := \varepsilon x$, namely to consider the system at large scales in time and space.

4.1 Hydrodynamic limits of kinetic equations

Physically-relevant problems usually involves regimes of validity. These regimes are characterized by the relative size of some dimensionless numbers (such as the Mach or Reynolds ones in fluid dynamics). The main such quantity in kinetic theory is the so-called *Knudsen number* ε, and it somehow characterizes the average number of collisions that one particle undergoes in a typical amount of time.

We call *hydrodynamic limit of the Boltzmann equation* any limit $\varepsilon \to 0$ of the solution f^ε to the scaled equation (1.1) in the hyperbolic scaling $\alpha = 0,\ \beta = 1$ (namely any highly collisional limit of the kinetic equation considered). Note that formally, multiplying (1.1) by ε and taking the $\varepsilon \to 0$ limit means (if everything remains bounded) that the limiting distribution f^0 will be a zero of the collision operator $\mathcal{Q}$, a Maxwellian distribution. All the difficulty of studying such limits will be to characterize properly the description of this equilibrium, and more precisely the fluctuations around it.

4.1.1 Chapman-Enskog expansion

We shall present one of the techniques introduced to study hydrodynamic limits, in the case of the Boltzmann collision operator. Part of the content of this Section is going to be formal. The interested reader on this topic can consult the book [193] and the reference therein.

Let us consider a solution f^ε to the scaled Boltzmann equation (1.1). According to the conservative properties of the collision operator $\mathcal{Q}_\mathcal{B}$, one has

$$\begin{cases} \partial_t \rho^\varepsilon + \operatorname{div}_x(\rho^\varepsilon \boldsymbol{u}^\varepsilon) = 0, \\ \partial_t(\rho^\varepsilon \boldsymbol{u}^\varepsilon) + \operatorname{div}_x\left(\displaystyle\int_{\mathbb{R}^d} v \otimes v\, f^\varepsilon(v)\,\mathrm{d}v\right) = \mathbf{0}_{\mathbb{R}^d}, \\ \partial_t \mathrm{E}^\varepsilon + \operatorname{div}_x\left(\displaystyle\int_{\mathbb{R}^d} \frac{1}{2}|v|^2 v\, f^\varepsilon(v)\,\mathrm{d}v\right) = 0, \end{cases} \tag{4.1}$$

where we defined

$$(\rho^\varepsilon, \boldsymbol{u}^\varepsilon, \mathrm{E}^\varepsilon) = \int_{\mathbb{R}^d} f^\varepsilon(v)\left(1, v_1, \dots, v_d, \frac{|v|^2}{2}\right)\mathrm{d}v; \quad \mathrm{T}^\varepsilon = \frac{1}{d\,\rho^\varepsilon}\int_{\mathbb{R}^d} f^\varepsilon(v)\,|v - \boldsymbol{u}^\varepsilon|^2\,\mathrm{d}v.$$

Now, assuming that the distribution f^ε is close to equilibrium thanks to the H-theorem, we can do formally the *Chapman-Enskog* expansion

$$f^\varepsilon = \mathcal{M}_{\rho^\varepsilon, \boldsymbol{u}^\varepsilon, \mathrm{T}^\varepsilon}\left[1 + \varepsilon\, g^{(1)} + \varepsilon^2\, g^{(2)} + \dots\right], \tag{4.2}$$

where the fluctuations $g^{(i)}$ for $i \geq 0$ designate a function that depends smoothly on the moment vector $(\rho^\varepsilon, \boldsymbol{u}^\varepsilon, \mathrm{T}^\varepsilon)^\intercal$ and any finite number of its derivatives with respect to the x-variable at the same point (t, x), and on the v-variable.

Integrating (4.2) with respect to the first powers of v and using the conservative properties of the collision operator $\mathcal{Q}_\mathcal{B}$, the fluctuations have to verify that

$$\int_{\mathbb{R}^3} g^{(i)}(v)\left(1, v_1, \dots, v_d, \frac{|v|^2}{2}\right)\mathrm{d}v = \mathbf{0}^\intercal_{\mathbb{R}^{d+2}}.$$

Conservation of momentum. Denoting by $c(v) = v - u^\varepsilon$ the local velocity of a particle, one has

$$v \otimes v = c \otimes c + 2\, u^\varepsilon \otimes c + u^\varepsilon \otimes u^\varepsilon.$$

Since the first moment of f^ε is exactly ρu^ε, the second equation in (4.1) yields

$$\partial_t(\rho^\varepsilon u^\varepsilon) + \nabla_x \cdot (\mathbb{P}(f^\varepsilon) + \rho^\varepsilon u^\varepsilon \otimes u^\varepsilon) = 0, \tag{4.3}$$

where the *pressure* tensor $\mathbb{P}(g)$ is given by

$$\mathbb{P}(g) := \int_{\mathbb{R}^d} c(v) \otimes c(v) g(t,x,v)\, \mathrm{d}v.$$

Conservation of energy. Since $\int_{\mathbb{R}^d} c(v) f^\varepsilon(v)\, \mathrm{d}v = 0$, it comes that

$$\int_{\mathbb{R}^d} |v|^2 v\, f^\varepsilon(v)\, \mathrm{d}v = 2\, q(f^\varepsilon) + u^\varepsilon \left(\mathrm{tr}\,(\mathbb{P}(f^\varepsilon)) + \rho |u^\varepsilon|^2\right) + 2 u^\varepsilon \cdot \mathbb{P}(f^\varepsilon),$$

where the *heat flux* vector $q(g)$ has been defined by

$$q(g) := \frac{1}{2} \int_{\mathbb{R}^d} |c(v)|^2 c(v)\, g(v)\, \mathrm{d}v.$$

Using the fact that $\mathrm{tr}\,(\mathbb{P}(f^\varepsilon)) = d\rho^\varepsilon \mathrm{T}^\varepsilon = 2\mathrm{E}^\varepsilon - \rho^\varepsilon |u^\varepsilon|^2$, one gets the conservation law for the energy:

$$\partial_t \mathrm{E}^\varepsilon + \mathrm{div}_x \left(q(f^\varepsilon) + \mathrm{E}^\varepsilon u^\varepsilon + u^\varepsilon \cdot \mathbb{P}(f^\varepsilon)\right) = 0. \tag{4.4}$$

Hence, one can rewrite (4.1) as

$$\begin{cases} \partial_t \rho^\varepsilon + \mathrm{div}_x(\rho^\varepsilon u^\varepsilon) = 0, \\ \partial_t(\rho^\varepsilon u^\varepsilon) + \mathrm{div}_x \left(\rho^\varepsilon u^\varepsilon \otimes u^\varepsilon + \rho^\varepsilon \mathrm{T}^\varepsilon \left(\mathrm{I} + \bar{\mathrm{A}}^\varepsilon\right)\right) = 0_{\mathbb{R}^d}, \\ \partial_t \mathrm{E}^\varepsilon + \mathrm{div}_x \left(\frac{1}{2}\rho^\varepsilon |u^\varepsilon|^2 u^\varepsilon + \rho^\varepsilon \mathrm{T}^\varepsilon \left(\frac{d+2}{2}\mathrm{I} + \bar{\mathrm{A}}^\varepsilon\right) u^\varepsilon + \rho^\varepsilon (\mathrm{T}^\varepsilon)^{d/2} \bar{\mathrm{B}}^\varepsilon\right) = 0, \end{cases} \tag{4.5}$$

where the traceless matrix $\bar{\mathrm{A}}^\varepsilon \in \mathrm{M}_d$ and the vector $\bar{\mathrm{B}}^\varepsilon \in \mathbb{R}^d$ are given uniquely in terms of the fluctuations $\left(g^{(i)}\right)_i$:

$$\begin{cases} \bar{\mathrm{A}}^\varepsilon := \dfrac{1}{\rho^\varepsilon} \displaystyle\int_{\mathbb{R}^d} \mathbf{A}(\mathbf{V}) \left[f^\varepsilon(v) - \mathcal{M}_{\rho^\varepsilon, u^\varepsilon, \mathrm{T}^\varepsilon}\right] \mathrm{d}v, \quad \mathbf{A}(\mathbf{V}) = \mathbf{V} \otimes \mathbf{V} - \dfrac{|\mathbf{V}|^2}{d}\mathrm{I}, \\ \bar{\mathrm{B}}^\varepsilon := \dfrac{1}{\rho^\varepsilon} \displaystyle\int_{\mathbb{R}^d} \mathbf{B}(\mathbf{V}) \left[f^\varepsilon(v) - \mathcal{M}_{\rho^\varepsilon, u^\varepsilon, \mathrm{T}^\varepsilon}\right] \mathrm{d}v, \quad \mathbf{B}(\mathbf{V}) = \dfrac{1}{2}\left[|\mathbf{V}|^2 - (d+2)\right]\mathbf{V}, \end{cases} \tag{4.6}$$

and where we used the shorthand

$$\mathbf{V}(v) = \frac{v - u}{\sqrt{\mathrm{T}}}.$$

Therefore, depending on the order in ε of the truncation of the series (4.2), one will obtain different hydrodynamic descriptions of the fluid. Characterizations of the perturbations $g^{(i)}$ will then be needed. In particular, one will need to be able to evaluate expressions of the form

$$\mathcal{Q}_{\mathcal{B}}\left(\mathcal{M}_{\rho^\varepsilon, u^\varepsilon, \mathrm{T}^\varepsilon}\left(1 + \varepsilon\, g^{(i)}\right), \mathcal{M}_{\rho^\varepsilon, u^\varepsilon, \mathrm{T}^\varepsilon}\left(1 + \varepsilon\, g^{(i)}\right)\right).$$

A precise understanding of the linear part of this expression will then be of paramount importance.

4.1.2 On the linearized Boltzmann operator

Relative entropy and L^1 norm. We shall adopt a perturbative approach for studying the linearized Boltzmann operator. In particular, for a given Maxwellian distribution $\mathcal{M}$, we shall consider the Hilbert space $\mathrm{L}^2(\mathcal{M})$, endowed with its natural inner product

$$(h,g)_{\mathrm{L}^2(\mathcal{M})} = \int_{\mathbb{R}^d} h(v)\, g(v)\, \mathcal{M}(v)\, \mathrm{d}v\,, \quad \forall g,h \in \mathrm{L}^2(\mathcal{M})\,.$$

This scalar product is adapted to the study of perturbations of the thermodynamical equilibria. Indeed, it is strongly related to the relative entropy (2.28) of the system with respect to the equilibrium of $\mathcal{Q}$. Using some convexity arguments, one has the following

Theorem 4.1.1 (Csiszár-Kullback-Pinsker inequality [112]). *Let $f, g \in \mathrm{L}^1\left(\mathbb{R}^d\right)$ such that $f, g \geq 0$ and $\|f\|_{\mathrm{L}^1} = \|g\|_{\mathrm{L}^1} = 1$. Then, it holds that*

$$\|f-g\|_{\mathrm{L}^1} \leq 2\,\mathcal{H}[f\,|\,g]\,,$$

where the constant 2 is optimal.

This quantity is then particularly interesting to control the trends to equilibrium of f^ε. It is also linked to the $\mathrm{L}^2(\mathcal{M})$ norm. More precisely, if f^ε is close to $\mathcal{M}$, say that there is $\varepsilon \ll 1$ such that $f^\varepsilon = \mathcal{M}(1+\varepsilon g)$, by Taylor expansion one has

$$\mathcal{H}[f^\varepsilon|\mathcal{M}](t) = \frac{\varepsilon^2}{2}\int_{\mathbb{R}^d} \|g(t,x,\cdot)\|_{\mathrm{L}^2(\mathcal{M})}\,\mathrm{d}x + o\left(\varepsilon^2\right).$$

This yields up to terms of order 3 in ε that

$$\begin{aligned}\frac{d}{dt}\mathcal{H}[f\,|\mathcal{M}](t) &= \frac{\varepsilon^2}{2}\frac{d}{dt}\int_{\mathbb{R}^d} \|g(t,x,\cdot)\|_{\mathrm{L}^2(\mathcal{M})}\,\mathrm{d}x\,,\\ &= \int_{\mathbb{R}^d} \left(\varepsilon^2\,\partial_t g, g\right)_{\mathrm{L}^2(\mathcal{M})}\,\mathrm{d}x\,. \end{aligned} \tag{4.7}$$

Understanding the time evolution of the fluctuation is then essential to study the large time behavior/small ε limit of the Boltzmann equation.

The linearized Boltzmann operator. Let $\mathcal{M}$ be a Maxwellian distribution. We define the linearized Boltzmann operator for $g \in \mathrm{L}^2(\mathcal{M})$ by

$$\mathcal{L}_{\mathcal{M}} g := \frac{1}{\mathcal{M}}\left(\mathcal{Q}_{\mathcal{B}}(\mathcal{M}, \mathcal{M}\,g) + \mathcal{Q}_{\mathcal{B}}(\mathcal{M}\,g, \mathcal{M})\right). \tag{4.8}$$

In particular, one has for any $v \in \mathbb{R}^d$

$$\mathcal{L}_{\mathcal{M}} g(v) = \iint_{\mathbb{R}^d\times\mathbb{S}^{d-1}} \left[g'_* + g' - g_* - g\right]\mathcal{M}_*\, \mathrm{B}(v-v_*,\sigma)\,\mathrm{d}v_*\,\mathrm{d}\sigma\,, \tag{4.9}$$

where we used the fundamental property of the Maxwellian that

$$\mathcal{M}(v)\,\mathcal{M}(v_*) = \mathcal{M}(v')\,\mathcal{M}(v'_*).$$

Now, if $\mathcal{M}$ is a global equilibrium (namely it depends only on v), and if $f^\varepsilon = \mathcal{M}(1+\varepsilon g)$ is a solution to the scaled Boltzmann equation (1.1), since $\mathcal{Q}_\mathcal{B}(\mathcal{M},\mathcal{M}) = 0$ one has that

$$\partial_t g + v\cdot\nabla_x g = \mathcal{L}_\mathcal{M} g + \varepsilon \mathcal{Q}_\mathcal{B}(\mathcal{M}g, \mathcal{M}g)\,.$$

Neglecting the quadratic term (of order ε) gives the so-called *linearized Boltzmann equation*, whose solutions approximate the equilibrium fluctuations.

Using the identity (4.9), it is straightforward that the null space of the linearized operator $\mathcal{L}_\mathcal{M}$ is made of the collisional invariants:

$$\ker \mathcal{L}_\mathcal{M} = \mathrm{Span}\left\{1, v_1, \dots, v_d, |v|^2\right\}.$$

Using Grad's angular cutoff assumption, one can also decompose the linearized Boltzmann operator as a sum of a (local) multiplication operator and a (nonlocal) integral operator:

$$\mathcal{L}_\mathcal{M} g(v) = \mathcal{K} g(v) - \nu(v)\, g(v), \quad \forall v \in \mathbb{R}^d. \tag{4.10}$$

where the *collision frequency* ν is a radially symmetric function with polynomial grows at infinity, given by

$$\nu(v) = \iint_{\mathbb{R}^d\times\mathbb{S}^{d-1}} \mathcal{M}_*\, \mathrm{B}(v-v_*,\sigma)\,\mathrm{d}v_*\,\mathrm{d}\sigma\,, \quad \forall v\in\mathbb{R}^d, \tag{4.11}$$

and the operator $\mathcal{K}$ is compact on $\mathrm{L}^2(\mathcal{M})$ [121]. As a consequence, one has the following classical result [60]:

Theorem 4.1.2. *The operator $\mathcal{L}_\mathcal{M}$ is an unbounded, maximal, nonpositive, self-adjoint Fredholm operator on $\mathrm{L}^2(\mathcal{M})$. Its domains contains all the continuous functions of v with polynomial growth at infinity.*

The nonpositiveness and self-adjointness of $\mathcal{L}_\mathcal{M}$ means that if $g \in \mathrm{Dom}(\mathcal{L}_\mathcal{M})$, one has

$$(\mathcal{L}_\mathcal{M} g, g)_{\mathrm{L}^2(\mathcal{M})} \le 0.$$

This corresponds to a linearized version of the nonpositiveness of the entropy in the H-Theorem. More precisely, if g is solution to the linearized Boltzmann equation

$$\partial_t g + v\cdot\nabla_x g = \mathcal{L}_\mathcal{M}(g),$$

and $f^\varepsilon = \mathcal{M}(1+\varepsilon f)$, one has according to (4.7) that

$$\frac{d}{dt}\mathrm{H}[f^\varepsilon|\mathcal{M}](t) = \int_{\mathbb{R}^d} (\mathcal{L}_\mathcal{M} g, g)_{\mathrm{L}^2(\mathcal{M})}(t)\,\mathrm{d}x \le 0\,, \quad \forall t \ge 0\,.$$

The relative entropy and the $\mathrm{L}^2(\mathcal{M})$ norm of the fluctuation are then a dissipated energy of the linearized Boltzmann equation.

Spectrum of the scaled, linearized Boltzmann equation. Analyzing the spectrum of the linearized Boltzmann equation is then important to understand correctly the asymptotic behaviors of the Boltmann equation. In general, the linearized Boltzmann operator has a spectrum that consists of (i) a non-empty essential (purely continuous) part that is entirely determined by the continuous spectrum of $-\nu(|v|)\mathcal{I}$, and (ii) a set of discrete eigenvalues that is influenced by the operator $\mathcal{K}$, see, for instance [13]. In contrast, the spectrum of the linear kinetic relaxation operators and linearized BGK operator only consists of discrete eigenvalues. However, for Maxwellian particles with angular cut-off and, in particular, for pseudo-Maxwellian particles, it is known from [121] that the spectrum of $\mathcal{L}_{\mathcal{M}}$ contains only discrete eigenvalues spread inside the interval $[-\nu(0), 0]$.

Assuming that the perturbation g^ε is not small with respect to ε, the linearized Boltzmann equation reads

$$\partial_t g^\varepsilon + v \cdot \nabla_x g^\varepsilon = -\frac{1}{\varepsilon} \left(\nu(|v|)\mathcal{I} - \mathcal{K} \right) g^\varepsilon.$$

Let us apply the Fourier transform in the physical space: since the collision operator depends only on the velocity magnitude $|v|$, the only difference in the equation will be that the free transport term $v \cdot \nabla_x$ will become a multiplication operator (by $i\gamma \cdot v$, where γ is the spatial Fourier variable). One can then write the Fourier-transformed linear Boltzmann equation as:

$$\partial_t h^\varepsilon = \frac{1}{\varepsilon} \mathcal{K} h^\varepsilon - \left(\nu(|v|)/\varepsilon + i\,\varepsilon\gamma \cdot v \right) h^\varepsilon, \tag{4.12}$$

where h^ε is the Fourier transform in space of g^ε. Hence, the evolution of h^ε is given by a compact perturbation of a (complex-valued) multiplication operator. It was proven in a series of papers (see also [Rey13]) that the spectrum of this Fourier-transformed collision operator has the following behavior as a function of $|\gamma|$ and ε:

Theorem 4.1.3 ([181], Section 2, and [88], Theorem 3.1). *The spectrum of the RHS of equation (4.12) consists of an essential part Σ_e located to the left of a vertical line of negative real part and a discrete spectrum Σ_d composed of:*

- fast modes: *eigenvalues located at a distance at least $1/\varepsilon$ to the left of the imaginary axis;*
- *an essential spectrum located in an half-plane Σ_e even farther away on the left off the imaginary axis;*
- slow modes: *if $|\varepsilon| \ll 1$, there are* exactly *$d+2$ eigenvalues branches given by:*

$$\lambda^{(j)}(|\gamma|) := i\,\lambda_1^{(j)}\,\varepsilon|\gamma| - \lambda_2^{(j)}\,\varepsilon^2|\gamma|^2 + \mathcal{O}\left(\varepsilon^3|\gamma|^3\right), \quad j \in \{0, \dots, d+2\},$$

for explicit constants $\lambda_1^{(j)} \in \mathbb{R}$ and $\lambda_2^{(j)} > 0$.

A sketch of this result can be found in Fig. 4.1.

Proof. We shall give a very short sketch of the lengthy proof of this result, for $\varepsilon = 1$ (the general result is obtained by a scaling argument). Let us denote by $\mathcal{L}_\gamma$ the Fourier-transformed, linearized Boltzmann operator:

$$\mathcal{L}_\gamma h = \mathcal{K} h - \left(\nu(|v|) + i\,\gamma \cdot v \right) h.$$

This linear operator is the sum of the compact operator $\mathcal{K}$ in L^2 and of a multiplication operator M_γ. According to Weyl's Theorem, its spectrum in L^2 is then composed of the spectrum of M_γ and of discrete eigenvalues. Since M_γ is a multiplication operator, its spectrum is the numerical range of

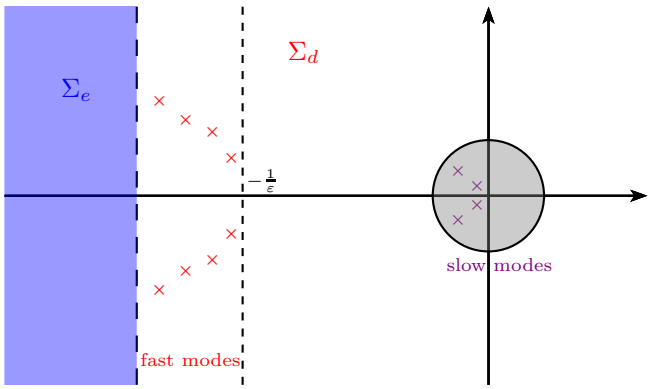

Figure 4.1: Spectrum of the Fourier transformed linearized Boltzmann operator, for small radial frequencies.

the function $v \mapsto -\nu(|v|) - i\,\gamma \cdot v$. Since M_γ is uniformly bounded by below by a negative constant [60], its spectrum is then located on the half-plane Σ_e. Moreover, since $v \mapsto -\nu(|v|) - i\,\gamma \cdot v$ is not unto, this spectrum is only composed of essential, continuous spectrum. The discrete part is located on the rightmost part of this set.

Concerning this discrete part, if λ_γ is an eigenvalue, with associated (nonzero) eigenfunction $h_\gamma \in \mathrm{L}^2$, one has

$$\mathcal{K} h_\gamma - (\nu(|v|) + i\,\gamma \cdot v + \lambda)\, h_\gamma = 0$$

Taking the inner product of this expression with h_γ yields:

$$\lambda = -\left[\nu(v) - \frac{\langle \mathcal{K} h_\gamma, h_\gamma \rangle_{\mathrm{L}^2}}{\|h_\gamma\|^2_{\mathrm{L}^2}} \right] - i\gamma \frac{\langle v, |h_\gamma|^2 \rangle_{\mathrm{L}^2}}{\|h_\gamma\|^2_{\mathrm{L}^2}}.$$

The careful study of the dependency of this relation on $|\gamma|$ yields the result.

All these properties will now be used to determine precisely a hierarchy of fluid description, depending on the order of truncation in the Chapman-Enskog expansion (4.2).

4.1.3 Hierarchy of fluid descriptions

Zeroth order: compressible Euler system. Truncating (4.2) at the zeroth order, namely replacing f^ε by a Maxwellian distribution, one has $\bar{\mathbf{A}}^\varepsilon = \mathbf{0}_{\mathrm{M}_d}$ and $\bar{\mathbf{B}}^\varepsilon = \mathbf{0}_{\mathbb{R}_d}$ Hence, the moments $(\rho, \boldsymbol{u}, \mathrm{T})$ are solution to the compressible Euler system (1.3):

$$\begin{cases} \partial_t \rho^\varepsilon + \mathrm{div}_x(\rho^\varepsilon \boldsymbol{u}^\varepsilon) = 0, \\ \partial_t(\rho^\varepsilon \boldsymbol{u}^\varepsilon) + \mathrm{div}_x\,(\rho^\varepsilon \boldsymbol{u}^\varepsilon \otimes \boldsymbol{u}^\varepsilon + \rho^\varepsilon \mathrm{T}^\varepsilon) = \mathbf{0}_{\mathbb{R}^d}, \\ \partial_t \mathrm{E}^\varepsilon + \mathrm{div}_x \left(\frac{1}{2} \rho^\varepsilon |\boldsymbol{u}^\varepsilon|^2 \boldsymbol{u}^\varepsilon + \frac{d+2}{2} \rho^\varepsilon \mathrm{T}^\varepsilon \boldsymbol{u}^\varepsilon \right) = 0. \end{cases}$$

We notice in particular that the Maxwellian distribution in (4.2) is independent on ε.

First order: compressible Navier-Stokes system. Going to the next order in ε, we plug the expansion (4.2) in the Boltzmann equation (1.1):

$$\frac{\partial}{\partial t}\left(\mathcal{M}_{\rho^\varepsilon,\boldsymbol{u}^\varepsilon,\mathrm{T}^\varepsilon}\left(1+\varepsilon\, g^{(1)}\right)\right)+v\cdot\nabla_x\left(\mathcal{M}_{\rho^\varepsilon,\boldsymbol{u}^\varepsilon,\mathrm{T}^\varepsilon}\left(1+\varepsilon\, g^{(1)}\right)\right)= \\ \frac{1}{\varepsilon}\mathcal{Q}_{\mathcal{B}}\left(\mathcal{M}_{\rho^\varepsilon,\boldsymbol{u}^\varepsilon,\mathrm{T}^\varepsilon}\left(1+\varepsilon\, g^{(1)}\right),\mathcal{M}_{\rho^\varepsilon,\boldsymbol{u}^\varepsilon,\mathrm{T}^\varepsilon}\left(1+\varepsilon\, g^{(1)}\right)\right).$$

Gathering the powers of ε, and using the fact that the Maxwellian distribution is an equilibrium of the collision operator, the fluctuation $g^{(1)}$ is a solution to

$$\partial_t\mathcal{M}_{\rho,\boldsymbol{u},\mathrm{T}}+v\cdot\nabla_x\mathcal{M}_{\rho,\boldsymbol{u},\mathrm{T}}=\mathcal{M}_{\rho,\boldsymbol{u},\mathrm{T}}\,\mathcal{L}_{\mathcal{M}_{\rho,\boldsymbol{u},\mathrm{T}}}\,g^{(1)}+\mathcal{O}(\varepsilon), \tag{4.13}$$

where $(\rho,\boldsymbol{u},\mathrm{T})$ are the unknowns to be determined and $\mathcal{L}_{\mathcal{M}}$ is the linearized collision operator around the Maxwellian distribution $\mathcal{M}_{\rho,\boldsymbol{u},\mathrm{T}}$ given by (4.8). The evolution of such a local Maxwellian distribution with respect to the free transport flow is computed as follow

$$\partial_t\mathcal{M}_{\rho,\boldsymbol{u},\mathrm{T}}+v\cdot\nabla_x\mathcal{M}_{\rho,\boldsymbol{u},\mathrm{T}}= \\ \mathcal{M}_{\rho,\boldsymbol{u},\mathrm{T}}\left[\partial_t\rho+v\cdot\nabla_x\rho+\frac{1}{\sqrt{\mathrm{T}}}(\mathbf{V}\cdot\partial_t\boldsymbol{u}+\mathbf{V}\otimes v:\nabla_x\boldsymbol{u})+\frac{1}{2\mathrm{T}}\left(|\mathbf{V}|^2-d\right)(\partial_t\mathrm{T}+v\cdot\nabla_x\mathrm{T})\right].$$

Then, using the conservation laws (4.5), we replace the time derivatives by spatial ones, and drop the terms of order ε in (4.13). After some tedious but elementary computations, one finds that

$$\mathcal{L}_{\mathcal{M}_{\rho,\boldsymbol{u},\mathrm{T}}}g^{(1)}=\left[\mathbf{A}(\mathbf{V}):\mathbf{D}(\boldsymbol{u})+2\mathbf{B}(\mathbf{V})\cdot\nabla_x\sqrt{\mathrm{T}}\right], \tag{4.14}$$

where $\mathbf{A}$, $\mathbf{B}$ and $\mathbf{V}$ are defined in (4.6) and the traceless *deformation tensor* $\mathbf{D}$ of $\boldsymbol{u}$ is given by

$$\mathbf{D}(\boldsymbol{u})=\nabla_x\boldsymbol{u}+(\nabla_x\boldsymbol{u})^{\intercal}-\frac{2}{d}(\mathrm{div}_x\,\boldsymbol{u})\,\mathbf{I}.$$

Since the collisional invariants span the null space of the linearized operator $\mathcal{L}_{\mathcal{M}_{\rho,\boldsymbol{u},\mathrm{T}}}$, one has that

$$\mathbf{A}(\mathbf{V}),\mathbf{B}(\mathbf{V})\perp\ker\mathcal{L}_{\mathcal{M}_{\rho,\boldsymbol{u},\mathrm{T}}}.$$

The linearized operator $\mathcal{L}_{\mathcal{M}_{\rho,\boldsymbol{u},\mathrm{T}}}$ being Fredholm, it is invertible on the orthogonal of its kernel. Using (4.14), it yields

$$g^{(1)}=\mathcal{L}^{-1}_{\mathcal{M}_{\rho,\boldsymbol{u},\mathrm{T}}}(\mathbf{A}(\mathbf{V}):\mathbf{D}(\boldsymbol{u}))+2\,\mathcal{L}^{-1}_{\mathcal{M}_{\rho,\boldsymbol{u},\mathrm{T}}}\left(\mathbf{B}(\mathbf{V})\cdot\nabla_x\sqrt{\mathrm{T}}\right). \tag{4.15}$$

We can then plug this expression into the definition (4.6) to obtain [160] that

$$\begin{cases}\bar{\mathbf{A}}^\varepsilon_{\mathrm{NS}}:=\dfrac{\varepsilon}{\rho}\displaystyle\int_{\mathbb{R}^d}\mathbf{A}(\mathbf{V})\,g^{(1)}(v)\,\mathrm{d}v=-\varepsilon\frac{\mu}{\rho\,\mathrm{T}}\mathbf{D}(\boldsymbol{u}),\\ \bar{\mathbf{B}}^\varepsilon_{\mathrm{NS}}:=\dfrac{\varepsilon}{\rho}\displaystyle\int_{\mathbb{R}^d}\mathbf{B}(\mathbf{V})\,g^{(1)}(v)\,\mathrm{d}v=-\varepsilon\frac{\kappa}{\rho\,\mathrm{T}^{d/2}}\nabla_x\mathrm{T}.\end{cases} \tag{4.16}$$

The scalar quantities μ and κ in (4.16), respectively the *viscosity* and the *thermal conductivity*, are given by

$$\mu:=-\mathrm{T}\int_{\mathbb{R}^d}\mathbf{A}(\mathbf{V}):\mathcal{L}^{-1}_{\mathcal{M}_{\rho,\boldsymbol{u},\mathrm{T}}}(\mathbf{A}(\mathbf{V}))(v)\,\mathrm{d}v,\quad \kappa:=-\mathrm{T}\int_{\mathbb{R}^d}\mathbf{B}(\mathbf{V})\cdot\mathcal{L}^{-1}_{\mathcal{M}_{\rho,\boldsymbol{u},\mathrm{T}}}(\mathbf{B}(\mathbf{V}))(v)\,\mathrm{d}v.$$

They depend on the collision kernel of the model. For example, for the Boltzmann operator in the hard sphere case $\gamma = 1$ and $d = 3$, there exists (see e.g. [118]) some positive constants μ_0, κ_0 such that $\mu = \mu_0\sqrt{\mathrm{T}}$ and $\kappa = \kappa_0\sqrt{\mathrm{T}}$. In that case, the evolution of the macroscopic quantities at first order with respect to ε is given by the compressible Navier-Stokes equations

$$\begin{cases} \partial_t \rho + \mathrm{div}_x(\rho\, \boldsymbol{u}) = 0, \\ \partial_t(\rho\, \boldsymbol{u}) + \mathrm{div}_x\left(\rho\, \boldsymbol{u} \otimes \boldsymbol{u} + \rho\, \mathrm{T}\, \mathbf{I}\right) = \varepsilon\, \mathrm{div}_x\left(\mu\, \mathbf{D}(\boldsymbol{u})\right), \\ \partial_t \mathrm{E} + \mathrm{div}_x\left(\boldsymbol{u}\,(\mathrm{E} + \rho\, \mathrm{T})\right) = \varepsilon\, \mathrm{div}_x\left(\mu\, \mathbf{D}(\boldsymbol{u}) \cdot \boldsymbol{u} + \kappa \nabla_x \mathrm{T}\right). \end{cases} \tag{4.17}$$

Second order: Burnett equations. Pushing the expansion (4.2) at second order in ε, we can use the same type of argument that for the compressible Navier-Stokes system to obtain another correction of the compressible Euler equations: the Burnett system. Although this system is ill-posed [118], the computation of its coefficients is still possible. In the simplified, BGK, 3D case, one has according to [201]:

$$\begin{aligned} \bar{\mathbf{A}}^{\varepsilon}_{Burnett} &:= \frac{1}{\rho}\int_{\mathbb{R}^3} \mathbf{A}(\mathbf{V})\left[\varepsilon\, g^{(1)}(v) + \varepsilon^2 g^{(2)}(v)\right] \mathrm{d}v \\ &= -\varepsilon \frac{\mu}{\rho\, \mathrm{T}} \mathbf{D}(\boldsymbol{u}) - 2\varepsilon^2 \frac{\mu^2}{\rho^2 \mathrm{T}^2}\Big\{ -\frac{\mathrm{T}}{\rho}\mathrm{Hess}_x(\rho) + \frac{\mathrm{T}}{\rho^2}\nabla_x\rho \otimes \nabla_x\rho - \frac{1}{\rho}\nabla_x \mathrm{T} \otimes \nabla_x \rho \\ &\qquad + (\nabla_x \boldsymbol{u})(\nabla_x \boldsymbol{u})^{\intercal} - \frac{1}{3}\mathbf{D}(\boldsymbol{u})\,\mathrm{div}_x(\boldsymbol{u}) + \frac{1}{\mathrm{T}}\nabla_x \mathrm{T} \otimes \nabla_x \mathrm{T}\Big\}; \end{aligned} \tag{4.18}$$

$$\begin{aligned} \bar{\mathbf{B}}^{\varepsilon}_{Burnett} &:= \frac{1}{\rho}\int_{\mathbb{R}^3} \mathbf{B}(\mathbf{V})\left[\varepsilon\, g^{(1)}(v) + \varepsilon^2 g^{(2)}(v)\right] \mathrm{d}v \\ &= -\varepsilon \frac{\kappa}{\rho\, \mathrm{T}^{3/2}} \nabla_x \mathrm{T} - \varepsilon^2 \frac{\mu^2}{\rho^2 \mathrm{T}^{5/2}}\Big\{ + \frac{25}{6}(\mathrm{div}_x\, \boldsymbol{u})\nabla_x \mathrm{T} \\ &\qquad - \frac{5}{3}\left[\mathrm{T}\,\mathrm{div}_x(\nabla_x \boldsymbol{u}) + (\mathrm{div}_x\, \boldsymbol{u})\nabla_x \mathrm{T} + 6(\nabla_x \boldsymbol{u})\nabla_x \mathrm{T}\right] \\ &\qquad + \frac{2}{\rho}\mathbf{D}(\boldsymbol{u})\nabla_x(\rho\, \mathrm{T}) + 2\,\mathrm{T}\,\mathrm{div}_x(\mathbf{D}(\boldsymbol{u})) + 16\mathbf{D}(\boldsymbol{u})\nabla_x \mathrm{T}\Big\}. \end{aligned} \tag{4.19}$$

4.2 Asymptotic Preserving numerical methods

We have seen that kinetic equations have a large variety of mathematically interesting and physically relevant asymptotic behavior. Developing numerical methods that are able to accurately reproduce such behaviors is then crucial when dealing with applications, whether theoretical or with an engineering goal. Nevertheless, because of the high dimensionality of the phase space (up to 7 dimensions), this can become a real challenge to develop implicit methods able to deal with the different time scales of the problems.

Historically, two different approaches are generally used to tackle kinetic equations numerically: deterministic methods, such as finite volume, semi-Lagrangian and spectral schemes [81], and probabilistic methods, such as Direct Simulation Monte Carlo (DSMC) schemes [21]. Both methodologies have strengths and weaknesses. Deterministic methods can normally reach high orders of accuracy. Nevertheless, stochastic methods are often faster, especially for solving steady problems, but, typically, exhibit lower convergence rates and difficulties in describing non-stationary and slow motion flows. In this Section, we will present deterministic strategies for solving kinetic equations while

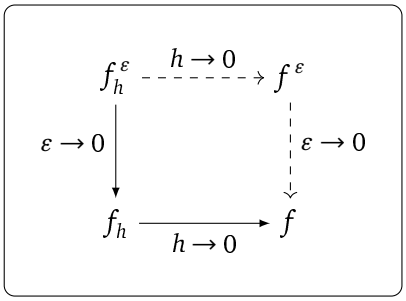

Figure 4.2: The AP diagram (h denotes the size of the discretization)

keeping the correct large time or small parameters behaviors. Such methods are called *Asymptotic Preserving* (AP).

From a numerical analysis point of view, the need to deal with large times or small parameters is related to stiffness in the equation. Such stiffness is usually characterized by the (small) mean free path ε, and becomes infinite when ε tends to zero. In that limit, a limiting macroscopic equation emerges in terms of a few moments of the particle distribution (density, momentum, energy); the full particle distribution then relaxes infinitely quickly to a Maxwellian distribution defined by these low-order moments. There is currently a large research effort in the design of algorithms that are uniformly stable in ε and approach a scheme for the limiting equation when ε tends to 0. The general principle of AP schemes can be roughly summarized as the commutative diagram presented in Fig. 4.2.

In the framework of kinetic equations, AP schemes first appeared two decades ago, on the one hand for kinetic semiconductors models in two papers, [147] for the linear BGK equation and [196] for the linear Boltzmann equation, and on the other hand for relaxation models (*e.g.* two velocities Goldstein-Taylor) in the article [141]. See the review papers [139, 81] for a large overview of the topic.

Here, we briefly review some achievements using different strategies. In [138, 142], separating the distribution function f into its odd and even parts in the velocity variable results in a coupled system of transport equations where the stiffness appears only in the source term, allowing to use a time-splitting technique with implicit treatment of the source term; see also related work in [148, 149]. Implicit-explicit (IMEX) schemes are an extensively studied technique to tackle this kind of problems, see [10, 99] and references therein. See also the recent results in this setting to deal with nonlinear collision kernels in [80], and an extension to hyperbolic systems in a diffusive limit is given in [33]. A different approach, based on well-balanced methods, was introduced by Gosse and Toscani [119, 120], see also [48]. When the collision operator allows for an explicit computation, an explicit scheme can be obtained subject to a classical diffusion CFL condition by splitting the particle distribution into its mean value and the first-order fluctuations in a Chapman-Enskog expansion form [113]. Also closure by moments, e.g. [65], can lead to reduced systems for which time-splitting provides new classes of schemes [54]. Alternatively, a micro-macro decomposition based on a Chapman-Enskog expansion has been proposed [159], leading to a system of transport equations that allows to design a semi-implicit scheme without time splitting. A non-local procedure based on the quadrature of kernels obtained through pseudo-differential calculus was proposed in [18].

I will present in the following sections some approaches that I have developed on this topic over the last few years.

4.2.1 Projective integration

A robust and fully explicit method that was developed recently and allows for time integration of (two-scale) stiff systems with arbitrary order of accuracy in time is called *projective integration* (PInt). I have devoted quite some time on this topic over the last few years, and this Section will summarize after an introduction on the topic some of my contributions on this topic.

PInt was proposed in [110] for stiff systems of ordinary differential equations with a clear gap in their eigenvalue spectrum. In such stiff problems, the fast modes, corresponding to the Jacobian eigenvalues with large negative real parts, decay quickly, whereas the slow modes correspond to eigenvalues of smaller magnitude and are the solution components of practical interest. PInt allows a stable yet explicit integration of such problems by first taking a few small (inner) steps using a step size δt with a simple, explicit method, until the transients corresponding to the fast modes have died out, and subsequently projecting (extrapolating) the solution forward in time over a large (outer) time step of size $\Delta t \gg \delta t$. In [154], PInt was analyzed for kinetic equations with a diffusive scaling. An arbitrary order version, based on Runge-Kutta methods, has been proposed recently in [152], where it was also analyzed for kinetic equations with an advection-diffusion limit. In [153], the scheme was used to construct a explicit, flexible, arbitrary order method for general nonlinear hyperbolic conservation laws, based on relaxation from a kinetic equation. Alternative approaches to obtain a higher-order PInt scheme have been proposed in [158, 191]. These methods fit within recent research efforts on numerical methods for multiscale simulation [86, 146].

We do not call PInt methods AP as such, because we cannot explicitly evaluate the scheme for $\varepsilon = 0$ to obtain a classical numerical scheme for the limiting equation. Nevertheless, PInt and telescopic PInt methods share important features with AP methods. In particular, their computational cost does (in many cases) not depend on the stiffness of the problem. To be specific, it was shown in [169], for linear kinetic equations, that the number of inner time steps at each level of the telescopic hierarchy is independent of the small-scale parameter ε, as is the step size of the outermost integrator. The only parameter in the method that may depend on ε is the *number* of levels in the telescopic hierarchy. For systems in which the spectrum of the collision operator falls apart into a set of clearly separated clusters (each corresponding to a specific time scale), the number of levels equals the number of spectral clusters. In this situation, the computational cost is completely independent on ε. When the collision operator represents a continuum of time scales, the number of PInt levels increases logarithmically with ε.

PInt is a method that is tailored to problems with exactly two distinct time scales. As such, in the context of kinetic equations, it matches nicely with the spectral properties of a linear BGK equation, as was shown in [154]. PInt combines a few small time steps with a naive (*inner*) timestepping method (here, a direct forward Euler discretization) with a much larger (*projective, outer*) time step. The idea is sketched in Fig. 4.3.

Inner integrators. At the innermost level, we introduce a uniform time mesh with time step δt and discrete time instants $t^k = k\delta t$. At this level, we choose the (explicit) forward Euler method

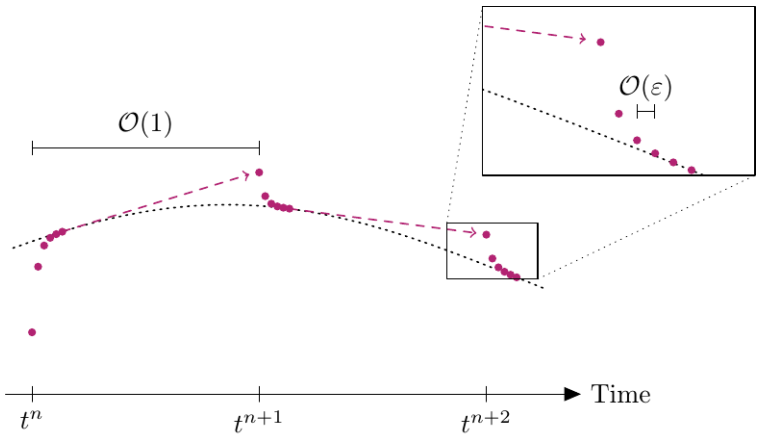

Figure 4.3: **Sketch of projective integration**. At each time step , an explicit method is applied over a number of small time steps so as to stably integrate the fast modes. As soon as these modes are sufficiently damped, the solution is extrapolated using a much larger time step (dashed lines).

with time step δt, for which we will, later on, use the shorthand notation:

$$f^{k+1} = \mathrm{S}_{\delta t}(f^k) = f^k + \delta t \mathrm{D}_t(f^k), \qquad k = 0, 1, \ldots, \tag{4.20}$$

where D_t is the right hand side of the kinetic equation considered, namely a possible semidiscretized operator acting on f^k. It will depend on the numerical methods chosen for approximating space and velocity.

The purpose of the inner integrator is to capture the fastest components in the numerical solution to the kinetic equation (1.1), and to sufficiently damp these out. We only require the innermost integrator to be stable for these components. The size of the inner time step δt and the required number of inner steps K will depend on the spectral properties of the semidiscretization of the equation considered. It will then strongly depend on the model. A lengthy discussion on this topic was made in [MRS19] (and summarized in Section 4.1.2), but for relaxation kinetic models, δt will be comparable with ε and K will be less than 3, as was showed in [154] for a simplified model.

Outer integrators. In equation (1.1), the small parameter ε leads to a classical time step restriction of the form $\delta t = \mathrm{O}(\varepsilon^{\alpha+\beta})$ for the inner integrator. However, as ε goes to 0, we obtain a limit of the form (4.1), for which a standard finite volume/forward Euler method only needs to satisfy a CFL stability restriction of the form $\Delta t \leq \mathrm{C}\Delta x$, with C a constant that depends on the specific choice of the scheme.

In [154], it was proposed to use a PInt method to accelerate such a brute-force integration; the idea, originating from [110], is the following. Starting from a computed numerical solution f^n at time $t^n = n\Delta t$, one first takes $\mathrm{K}+1$ *inner* steps of size δt using (4.20), denoted as $f^{n,k+1}$, in which the superscripts (n,k) denote the numerical solution at time $t^{n,k} = n\Delta t + k\delta t$. The aim is to obtain a discrete derivative to be used in the *outer* step to compute $f^{n+1} = f^{n+1,0}$ via extrapolation in time:

$$f^{n+1} = f^{n,\mathrm{K}+1} + \mathrm{M}\delta t \frac{f^{n,\mathrm{K}+1} - f^{n,\mathrm{K}}}{\delta t},$$

where $\mathrm{M} = \Delta t/\delta t - (\mathrm{K}+1)$. The size of the (macroscopic) extrapolation step Δt will result from the spectral analysis of the collision operator considered.

Higher-order projective Runge-Kutta (PRK) methods have been constructed [152, 153] by replacing each time derivative evaluation k_s in a classical Runge-Kutta method by $\mathrm{K}+1$ steps of an inner integrator as follows:

$$
\begin{aligned}
s=1: &\quad \begin{cases} f^{n,k+1} &= f^{n,k} + \delta t \mathrm{D}_t(f^{n,k}), \qquad 0 \le k \le \mathrm{K} \\ \mathrm{k}_1 &= \dfrac{f^{n,\mathrm{K}+1} - f^{n,\mathrm{K}}}{\delta t} \end{cases} \\
2 \le s \le \mathrm{S}: &\quad \begin{cases} f_s^{n+c_s,0} &= f^{n,\mathrm{K}+1} + (c_s \Delta t - (\mathrm{K}+1)\delta t) \displaystyle\sum_{l=1}^{s-1} \frac{a_{s,l}}{c_s} \mathrm{k}_l, \\ f_s^{n+c_s,k+1} &= f_s^{n+c_s,k} + \delta t \mathrm{D}_t(f_s^{n+c_s,k}), \qquad 0 \le k \le \mathrm{K} \\ \mathrm{k}_s &= \dfrac{f_s^{n+c_s,\mathrm{K}+1} - f_s^{n+c_s,\mathrm{K}}}{\delta t} \end{cases} \\
& f^{n+1} = f^{n,\mathrm{K}+1} + (\Delta t - (\mathrm{K}+1)\delta t) \sum_{s=1}^{\mathrm{S}} b_s \mathrm{k}_s.
\end{aligned}
$$

To ensure consistency, the Runge-Kutta matrix $\mathrm{a} = (a_{s,i})_{s,i=1}^{\mathrm{S}}$, weights $\mathrm{b} = (b_s)_{s=1}^{\mathrm{S}}$, and nodes $\mathrm{c} = (c_s)_{s=1}^{\mathrm{S}}$ satisfy the conditions $0 \le b_s \le 1$ and $0 \le c_s \le 1$, as well as:

$$
\sum_{s=1}^{\mathrm{S}} b_s = 1, \qquad \sum_{i=1}^{\mathrm{S}-1} a_{s,i} = c_s, \quad 1 \le s \le \mathrm{S}.
$$

4.2.2 Telescopic projective integration

In general, the stiff kinetic equation contains more than two distinct time scales. In this section, we therefore describe an extension of PInt, called *telescopic projective integration* (TPInt) and introduced in [111], that can handle multiple time scales. This method has been studied in the context of linear BGK equations with multiple relaxation times in [169].

TPInt employs a number of projective integrator levels, which, starting from a base (*innermost*) integrator, are wrapped around the previous level integrator [111]. In this way, a hierarchy of projective integrators is formed in which each level (except the innermost and outermost ones) fulfills both an inner and outer integrator role. This generalizes the idea of PInt, which contains only one projective level wrapped around an inner integrator. On that account, in the TPInt framework, the PInt method is called a level-1 TPInt method. The idea of a level-3 TPInt method with $\mathrm{K}=2$ on each projective level is sketched in Fig. 4.4. The different level integrators in a TPInt method can in principle be selected independently from each other, but in general one selects a first order explicit scheme (the forward Euler scheme) for all but the outermost integrator level, whose order is chosen to meet the accuracy requirements dictated by the problem.

Innermost integrator We intend to integrate the kinetic equation considered using a uniform time mesh with time step h_0 and discrete time instants $t^k = kh_0$. The innermost integrator of the TPInt method is chosen to be the forward Euler (FE) method,

$$
f^{k+1} = f^k + h_0 \mathrm{D}_t(f^k).
$$

In the sequel, we use the following shorthand notation:

$$
f^{k+1} = \mathrm{S}_0(f^k) \qquad (k = 0, 1, \ldots),
$$

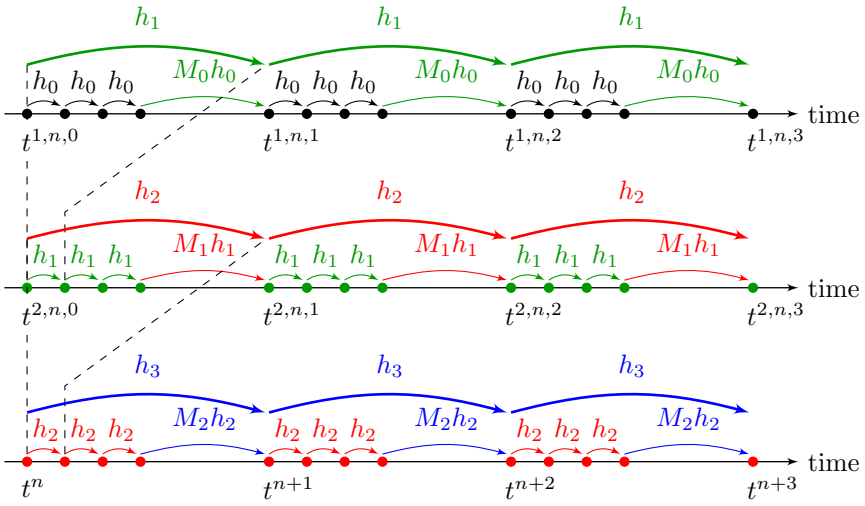

Figure 4.4: A level-3 TPInt method drawn for three outermost time steps h_3 (bottom row) with $\mathrm{K} = 2$ on all projective levels. The dots correspond to different time points at which the numerical solution is calculated. The time step and projective step size of each level $\ell = 0, \ldots, 2$ are denoted by h_ℓ and M_ℓ, respectively.

in which S_0 denotes the time stepper with corresponding time step h_0. Also in the TPInt method, the purpose of the innermost integrator is only to capture the fastest components in the numerical solution of the considered equation, and to sufficiently damp these out. As a consequence, it is ill-advised to use higher-order methods for the innermost integrator, see [169] for a more detailed discussion.

Projective (outer) levels The TPInt method employs in general L nested levels of projective integration that are constructed around the innermost integrator. In [111], the method has been introduced in a recursive way. Here, following [169], we describe the method in an alternative way, to make the presentation more similar to that of classical PInt.

To keep track of the time instant at which the numerical solution is computed throughout the TPInt method and at the same time desiring a compact notation, in what follows, we employ superscript triplets of the form (ℓ, n, k_ℓ) where ℓ denotes the integrator level ranging from 0 (innermost) to $\mathrm{L}-1$, n represents the index of the current outermost integrator time $t^n = nh_\mathrm{L}$, and k_ℓ corresponds to the iteration index of the integrator on level ℓ. The numerical time on each level $\ell = 0, \ldots, \mathrm{L}-1$ is then defined as (see also Fig. 4.4):

$$t^{\ell,n,k_\ell} = nh_\mathrm{L} + \sum_{\ell'=\ell}^{\mathrm{L}-1} k_{\ell'} h_{\ell'}. \tag{4.21}$$

Notice that, for a certain level ℓ, this time requires the iteration indices $k_{\ell'}$ of all its outer integrators. Therefore, it incorporates a memory that keeps up with the current time instants at which the outer integrators of a given level ℓ integrator have arrived at and is necessary to take into account to correctly reflect the numerical time of the solution on each level ℓ.

Starting from a computed numerical solution f^n at time $t^n = nh_\mathrm{L}$, one first takes $\mathrm{K}_0 + 1$ steps of

size h_0 with the innermost integrator:

$$f^{0,n,k_0+1} = \mathrm{S}_0(f^{0,n,k_0}) \qquad (0 \leq k_0 \leq \mathrm{K}_0), \tag{4.22}$$

in which f^{0,n,k_0} corresponds to the numerical solution at time t^{0,n,k_0} calculated by the innermost integrator. Since all outer integrator iteration indices $k_{\ell'}$, $\ell' = 1,\ldots,\mathrm{L}-1$ are initially zero in (4.21), we have $t^{0,n,k_0} = nh_\mathrm{L} + k_0 h_0$. The repeated action (4.22) of the innermost integrator is depicted by small black arrows in the upper row of Fig. 4.4, for which we chose $\mathrm{K}_0 = 2$.

In the TPInt framework, the scheme is set up from the lowest level up to the highest level. The aim is to obtain a discrete derivative to be used on each level to eventually compute $f^{n+1} = f^{0,n+1,0}$ via extrapolation in time. Using the innermost integrator iterations (4.22), we perform the extrapolation by a projective integrator on level 1, written as:

$$f^{1,n,1} = f^{0,n,\mathrm{K}_0+1} + (\mathrm{M}_0 h_0)\frac{f^{0,n,\mathrm{K}_0+1} - f^{0,n,\mathrm{K}_0}}{h_0}, \tag{4.23}$$

which corresponds to the projective forward Euler (PFE) method. In (4.23), $f^{1,n,1}$ represents the numerical solution at time $t^{1,n,1}$ calculated by one iteration of the first level projective integrator. Since $k_1 = 1$ and all its outer integrator iteration indices $k_{\ell'}$, $\ell' = 2,\ldots,\mathrm{L}-1$ are still zero in (4.21), we have $t^{1,n,1} = nh_\mathrm{L} + h_1$. One step of the first level integrator is visualized by a large green arrow in the upper row of Fig. 4.4. By repeating this idea, we construct a hierarchy of projective integrators on levels $\ell = 1,\ldots,\mathrm{L}-1$, given by:

$$f^{\ell,n,k_\ell+1} = f^{\ell-1,n,\mathrm{K}_{\ell-1}+1} + (\mathrm{M}_{\ell-1} h_{\ell-1})\frac{f^{\ell-1,n,\mathrm{K}_{\ell-1}+1} - f^{\ell-1,n,\mathrm{K}_{\ell-1}}}{h_{\ell-1}}, \tag{4.24}$$

in which, on each level ℓ, we iterate over $k_\ell = 0,\ldots,\mathrm{K}_\ell$. In (4.24), f^{ℓ,n,k_ℓ} denotes the numerical solution at time t^{ℓ,n,k_ℓ} calculated by the projective integrator on level ℓ. According to (4.21), this time depends on the values $k_{\ell'}$, $\ell' = \ell+1,\ldots,\mathrm{L}-1$ of all of its outer integrators. In Fig. 4.4, these projective integrator steps are shown by long arrows for each level $\ell = 1,\ldots,3$. Ultimately, the outermost integrator on level L computes f^{n+1} as:

$$f^{n+1} = f^{\mathrm{L}-1,n,\mathrm{K}_{\mathrm{L}-1}+1} + (\mathrm{M}_{\mathrm{L}-1} h_{\mathrm{L}-1})\frac{f^{\mathrm{L}-1,n,\mathrm{K}_{\mathrm{L}-1}+1} - f^{\mathrm{L}-1,n,\mathrm{K}_{\mathrm{L}-1}}}{h_{\mathrm{L}-1}}. \tag{4.25}$$

Since the outermost integrator (4.25) also constitutes a PFE scheme, the telescopic method resulting from the hierarchy of projective levels (4.24)-(4.25) is called telescopic projective forward Euler (TPFE).

It is straightforward to implement higher-order extensions of the outermost integrator, as is done in [152]. We mention the projective Runge-Kutta methods of order 2 and 4, leading to TPRK2 and TPRK4 method in the telescopic case. In general, the outermost integrator in a TPRK method replaces each time derivative evaluation k_s in a classical Runge-Kutta method by $\mathrm{K}_{\mathrm{L}-1}+1$ steps of its inner integrator on level $\mathrm{L}-1$.

4.2.3 Parameters for projective and telescopic projective integration

It still remains to select appropriate parameter values for the PInt and TPInt methods. These are determined by ensuring that all eigenvalues of the kinetic problem under study fall within the stability

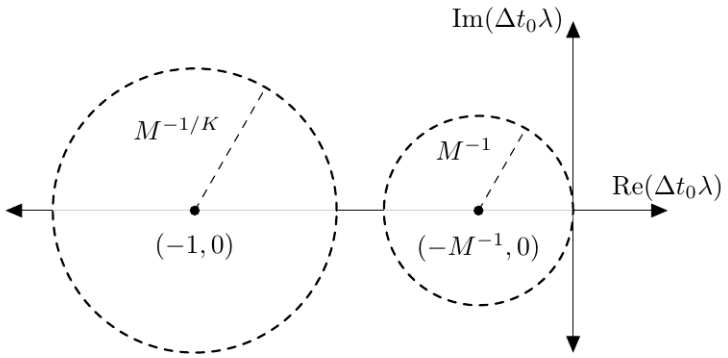

Figure 4.5: Asymptotic stability region for the projective forward Euler integrator, with $\mathrm{M} = \Delta t / \delta t - (\mathrm{K} + 1)$.

region of the full projective method. In Section 4.1.2 and [MRS19], we showed that the spectra of the linearized kinetic equations either appear in two stationary eigenvalue disks (linearized BGK equation with $\nu = 1$) or are continuously spread along (a part of) the negative real axis (linearized BGK equation with $\nu = \rho$ and linearized Boltzmann equation). Let us summarize below the main results on these topics, from [153, 169].

Stationary, well-separated spectrum. For the linearized BGK equation with $\nu = 1$, it was shown in [153] that the spectrum consists of two stationary, well-separated eigenvalue clusters (a fast and slow, dominant cluster). To accommodate these two clusters, the method parameters of PInt can be selected such that its stability region splits up into two parts.

1. First, the inner integrator time step δt is chosen corresponding to the fastest time scale of the problem, which is of the order of ε. This centers one stability region of the projective method around the fast eigenvalues.
2. Next, the number of inner integrator time steps K is chosen such that all fast eigenvalues lie inside this stability region. In [153], it was proven that we require $\mathrm{K} \geq 2$.
3. Last, the outer integrator time step Δt is selected such that all dominant eigenvalues fall into the second stability region of the projective method.

Since both K and Δt are independent of the small-scale parameter ε, the resulting projective method has a cost that is also independent of ε, which becomes increasingly advantageous for $\varepsilon \to 0$. Fig. 4.5 summarizes this parameters choice.

Continuously spread spectrum. When considering the linearized BGK equation with $\nu = \rho$, part of the spectrum varies continuously over the negative real axis. This also holds true for the linearized Boltzmann equation [Rey13], or mixtures of species [44], see Fig. 4.1. In this case, we require that the stability region of the numerical method does not split up but instead comprises the entire negative real axis up to the fastest eigenvalue of the problem (a numerical method with this property is termed $[0, 1]$-*stable*). Here, for simplicity, we assume that the fastest eigenvalue at $t = 0$ corresponds to the fastest possible eigenvalue for all other times $t > 0$. Since [0,1]-stable PInt methods lose practically all of their potential speed-up, [0,1]-stable TPInt methods can be designed with much higher speed-ups. We describe the strategy that was used in [169], to which we refer for

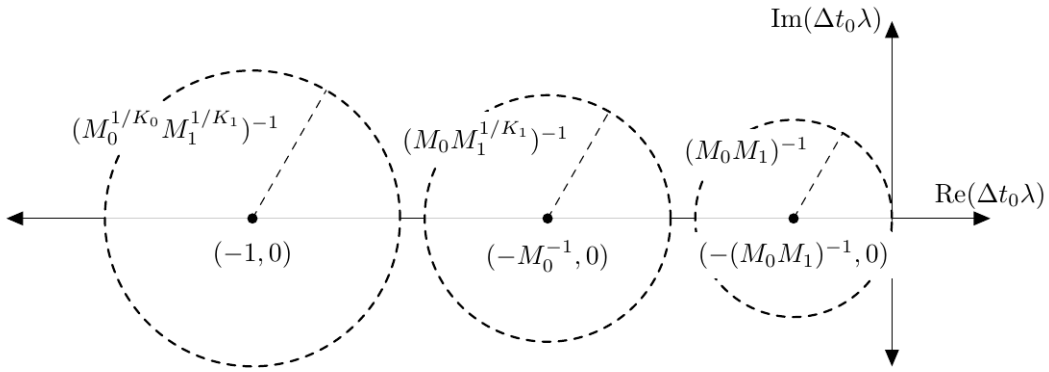

Figure 4.6: Asymptotic stability region for the telescopic projective forward Euler integrator.

more details.

1. Similarly to PInt, the innermost integrator time step h_0 of the TPInt method is chosen corresponding to the fastest time scale, which is of the order of $\varepsilon/\max_x \rho(x,0)$.
2. Next, we fix the outermost time step we would like to use, taking into account a CFL-like stability constraint, as follows: $h_{\mathrm{L}} = \mathrm{C}\Delta x$.
3. Before choosing the number of projective levels, we decide on the number of inner integrator time steps K, which we consider to be fixed on each projective level. For each chosen value of K there is a corresponding maximal value of M such that the stability region does not split up, see [111].
4. The required number of projective levels L to obtain a [0,1]-stable telescopic method is computed as:
$$\mathrm{L} \approx \frac{\log(h_{\mathrm{L}}) + \log(1/h_0)}{\log(\mathrm{M}+\mathrm{K}+1)}. \tag{4.26}$$
5. For the given values of h_0, h_{L}, K and L adapt the value of M on the different projective levels such that the following equation:
$$h_{\mathrm{L}} = \prod_{\ell=0}^{\mathrm{L}-1}(\mathrm{M}_\ell + \mathrm{K} + 1)h_0 \tag{4.27}$$
is valid.

For a [0,1]-stable telescopic method, the values of h_{L}, M_ℓ and K are independent of ε. However, as indicated by equation (4.26), the number of projective levels increases as $\mathrm{O}(\log(1/\varepsilon))$. As a consequence, the cost of a [0,1]-stable TPIntmethod is not completely ε-independent. However, the dependence is rather modest. Fig. 4.6 summarizes this parameters' choice.

4.2.4 Applications to single species gases

PInt and TPint where successfully used in the series of works [MRS17, MRS19] to simulate numerically solutions to the nonlinear BGK and Boltzmann equations. The collision frequency is the coefficient ν from (4.11) appearing in the former operator.

BGK in 1D/1D. We consider a Sod-like test case for $x \in [0,1]$ for the BGK equation (1.1) with the collision operator $\mathcal{Q}_{\mathrm{BGK}}$ (1.25) in 1D/1D. It consists of an initial centered Riemann problem with the

following left and right state values:

$$\begin{pmatrix}\rho_{\mathrm{L}}\\ \boldsymbol{u}_{\mathrm{L}}\\ \mathrm{T}_{\mathrm{L}}\end{pmatrix}=\begin{pmatrix}1\\ 0\\ 1\end{pmatrix},\qquad \begin{pmatrix}\rho_{\mathrm{R}}\\ \boldsymbol{u}_{\mathrm{R}}\\ \mathrm{T}_{\mathrm{R}}\end{pmatrix}=\begin{pmatrix}0.125\\ 0\\ 0.25\end{pmatrix}. \tag{4.28}$$

The initial distribution $f^{\varepsilon}(0,x,v)$ is then chosen as the Maxwellian distribution corresponding to the above initial macroscopic variables. We impose outflow boundary conditions and perform simulations for $t\in[0,0.15]$. As velocity space, we take the interval $[-8,8]$, which we discretize on a uniform grid using $\mathrm{J}=80$ velocity nodes. Below we regard three gas flow regimes, $\varepsilon=10^{-1}$ (kinetic regime), $\varepsilon=10^{-2}$ (transitional regime) and $\varepsilon=10^{-5}$ (fluid regime), and for each regime, we compare solutions for two cases of collision frequency ν in the BGK equation (1.25), $\nu=1$ and $\nu=\rho$.

Direct integration ($\varepsilon=10^{-1}$ *and* $\varepsilon=10^{-2}$). In the kinetic ($\varepsilon=10^{-1}$) and transitional ($\varepsilon=10^{-2}$) regimes, we compute the numerical solution for $\nu=1$ and $\nu=\rho$ using the fourth order Runge-Kutta (RK4) time discretization with time step $\delta t=0.1\Delta x$. The results are shown in Fig. 4.7 for $\nu=1$ (left) and $\nu=\rho$ (right), where we display the density ρ, macroscopic velocity $\boldsymbol{u}$ and temperature T at $t=0.15$. In addition, we plot the heat flux $\boldsymbol{q}$. The different regimes are shown by blue (kinetic) and purple (transitional) dots. The red line in each plot denotes the limiting ($\varepsilon\to 0$) solution of each macroscopic variable, which all converge to the solution of the Euler system (1.3) with ideal gas law $\mathrm{P}=\rho\mathrm{T}$ and heat flux $q=0$.

PInt ($\varepsilon=10^{-5}$ *and* $\nu=1$). In the fluid regime ($\varepsilon=10^{-5}$), direct integration schemes such as RK4 become too expensive due to a severe time step restriction, which is required to ensure stability of the method. Exploiting that the spectrum of the linearized BGK equation with $\nu=1$ resembles that of the linear kinetic models used in [153], we construct a PInt method to accelerate time integration in the fluid regime. As inner integrator, we select the forward Euler time discretization with $\delta t=\varepsilon$. As outer integrator, we choose the fourth-order projective Runge-Kutta (PRK4) method, using $\mathrm{K}=2$ inner steps and an outer step of size $\Delta t=0.4\Delta x$. Fig. 4.7 (left) shows the macroscopic observables in the fluid regime for $\nu=1$ at $t=0.15$ (green dots). From this, we observe that the BGK solution is increasingly dissipative for increasing values of ε since the rate with which f^{ε} converges to its equilibrium becomes slower. In contrast, for sufficiently small ε, relaxation to thermodynamic equilibrium occurs practically instantaneous and the Euler equations (1.3) yield a valid description. Since this is a hyperbolic system, it allows for the development of sharp discontinuous and shock waves which are clearly seen in the numerical solution.

Telescopic projective integration ($\varepsilon=10^{-5}$ *and* $\nu=\rho$). Next, we repeat the above experiment taking $\nu=\rho$ in the BGK equation. We now design a TPInt method, since, for this choice of ν, the spectrum of the linearized BGK equation is spread along the negative real axis and is time-dependent. Therefore, the previous two-scale nature becomes a multi-scale problem. We construct a $[0,1]$-stable TPRK4 method consisting of 2 projective levels with FE as innermost integrator with time step $h_0=\varepsilon$, constant $\mathrm{K}=6$ on each level and an outermost time step $h_2=0.4\Delta x$. The extrapolation step sizes M on each level are calculated as $\mathrm{M}=\{14.24,11.83\}$. The results are shown by green dots in figure 4.7 (right). We conclude that the effect of choosing $\nu=\rho$ primarily manifests itself in the transitional regime ($\varepsilon=10^{-2}$), for which the relaxation rate is not too slow nor too fast. Moreover, it is seen that this choice of collision frequency does not alter the hydrodynamic limit of the BGK equation, which is captured correctly by the telescopic scheme.

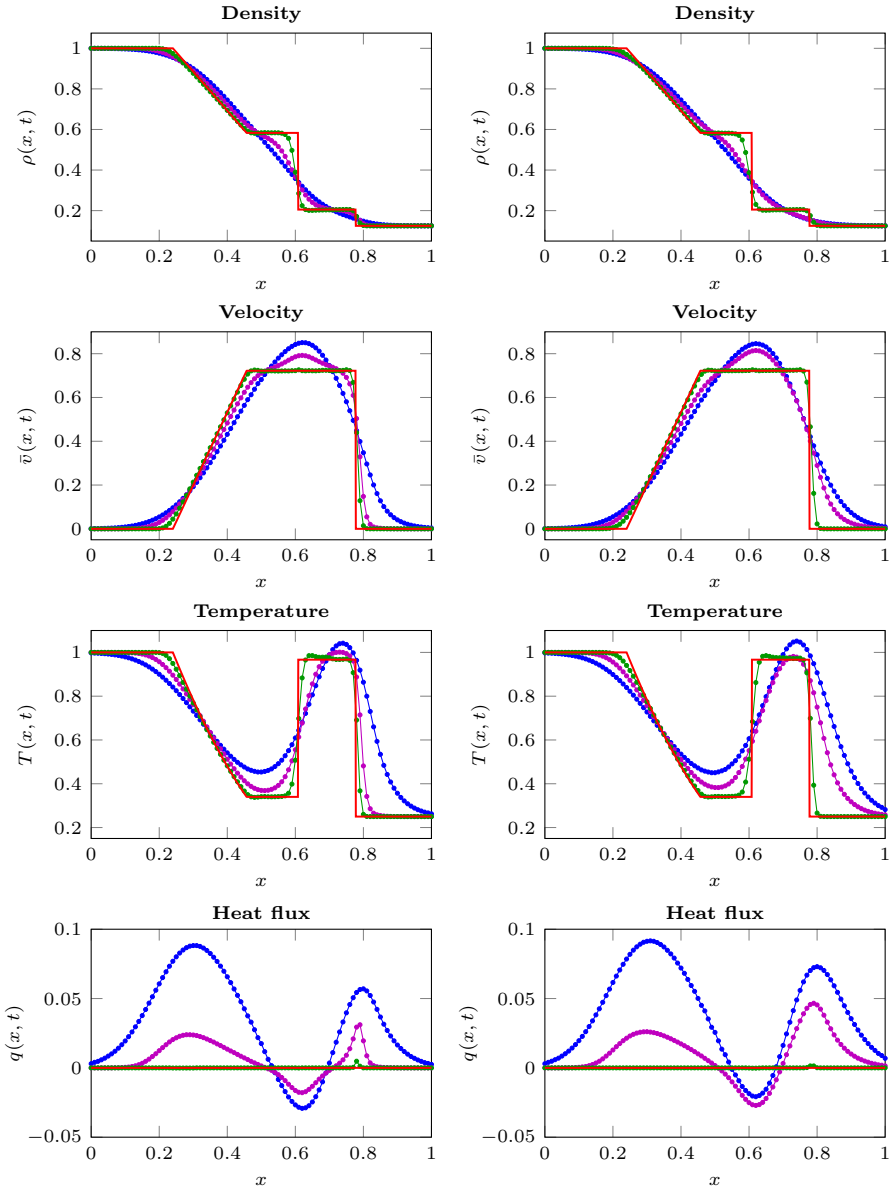

Figure 4.7: **BGK in 1D/1D.** We take $\nu = 1$ (left) and $\nu = \rho$ (right) at $t = 0.15$ for the Sod tube (4.28). RK4 is used for $\varepsilon = 10^{-1}$ (blue dots) and $\varepsilon = 10^{-2}$ (purple dots) with $\delta t = 0.1\Delta x$. The PRK4 (left) and level-2 TPRK4 (right) methods are used for $\varepsilon = 10^{-5}$ (green dots). Red line: limit solution ($\varepsilon \to 0$).

In this numerical test, the speed-up factor between the naive RK4 implementation and the PInt method is 130.3.It is 8.2 between RK4 and TPInt.

BGK and Boltzmann in 1D/2D. We perform the Sod test (4.28) of the previous section in 1D/2D, for the BGK and Boltzmann operators. As velocity space, we take the domain $[-8, 8]^2$, which we discretize on a uniform grid using $J_x = J_y = 32$ velocity nodes along each dimension. In all simulations, space is discretized using the WENO2 spatial discretization with $\Delta x = 0.01$. We compare again solutions in the transitional $\varepsilon = 10^{-2}$ and fluid $\varepsilon = 10^{-5}$ regimes, for BGK with $\nu = 1$, BGK with $\nu = \rho$ and Boltzmann with pseudo-Maxwellian particles. To approximate the Boltzmann collision

operator, we apply the fast spectral method described in Chapter 2 using $N_\theta = 4$ discrete angles.

Direct integration ($\varepsilon = 10^{-2}$). In the transitional regime, we perform all simulations using the RK4 method with time step $\delta t = 0.1\Delta x$, for which we display the results in Fig. 4.8 (left) for BGK with $\nu = 1$ (blue dots), BGK with $\nu = \rho$ (green dots) and the Boltzmann equation (red dots). From this, we observe that the BGK solution with $\nu = \rho$ is closer to the Boltzmann solution than the BGK solution with $\nu = 1$. This is as expected, since the BGK equation with $\nu = \rho$ correctly captures the loss term of the Boltzmann collision operator, see 1.3.1. Moreover, the discrepancy between Boltzmann and BGK with $\nu = \rho$ increases for higher order moments of f^ε; while the density appears to coincide, the heat flux reveals a clear difference between the models.

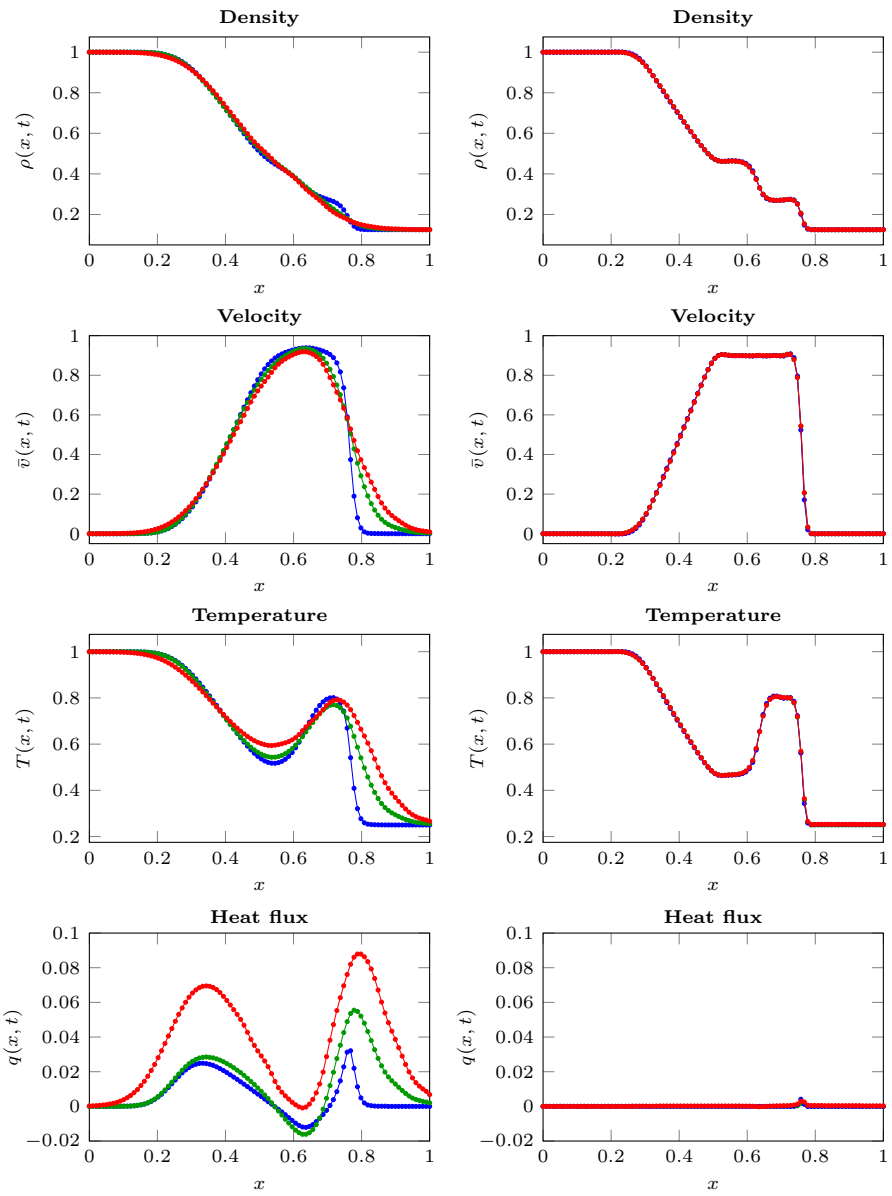

Figure 4.8: **BGK and Boltzmann in 1D/2D.** We take $\varepsilon = 10^{-2}$ (left) and $\varepsilon = 10^{-5}$ (right) at $t = 0.15$ for the Sod tube (4.28). Blue dots: BGK with $\nu = 1$; green dots: BGK with $\nu = \rho$; red dots: Boltzmann. For $\varepsilon = 10^{-2}$, RK4 with $\delta t = 0.1\Delta x$. For $\varepsilon = 10^{-5}$, PRK4 (blue dots) and level-2 TPRK4 (green and red dots) methods.

Projective methods ($\varepsilon = 10^{-5}$). In the fluid regime, the RK4 method becomes too expensive. To that end, for BGK with $\nu = 1$, we design a PRK4 method with FE as inner integrator using $\delta t = \varepsilon$, $\mathrm{K} = 2$ inner steps and $\Delta t = 0.4\Delta x$. Due to the multi-scale nature of both the BGK relaxation operator with $\nu = \rho$ and the Boltzmann collision operator, we construct a $[0, 1]$-stable level-2 TPRK4 method for both models using the FE scheme as innermost integrator with $h_0 = \varepsilon$. We set $\mathrm{K} = 4$ constant on each level, compute the extrapolation step sizes as $\mathrm{M} = \{14.24, 11.83\}$, and choose the outermost time step as $h_2 = 0.4\Delta x$. The results can be seen in Fig. 4.8 (right). For all models, the PInt and TPInt methods display the expected hydrodynamic limit.

In these numerical tests, the speed-up factor between a naive RK4 implementation and the PInt method for the PRK4 method for the BGK model with constant relaxation is 133.3. The speedup for the TPRK4 method for the BGK model with nonconstant relaxation rate and the Boltzmann equation is 13.

A Kelvin-Helmoltz like instability problem. Here, we consider the BGK equation in 2D/2D with constant collision frequency $\nu = 1$, for the so-called Kelvin-Helmoltz instability. This phenomenon occurs when two fluids of different densities and in thermodynamic equilibrium move at different speeds. Such system will exhibit turbulent, unstable vortices at the interface between the two fluids, because of the velocity shear [214]. In order for these instabilities to develop, the Reynolds number of the fluids considered must be large. Using the von Karman relation [199], which states that the Reynolds number is inversely proportional to the Knudsen number ε, we choose the very small Knudsen number $\varepsilon = 5 \cdot 10^{-5}$ along with the following initial condition inspired from [167]:

$$\begin{pmatrix} \rho_1 \\ \boldsymbol{u}_1^x \\ \boldsymbol{u}_1^y \\ \mathrm{T}_1 \end{pmatrix} = \begin{pmatrix} 1 \\ 0.5 \\ 0.01\sin(4\pi x) \\ 1 \end{pmatrix} \quad (y \geq 0), \qquad \begin{pmatrix} \rho_2 \\ \boldsymbol{u}_2^x \\ \boldsymbol{u}_2^y \\ \mathrm{T}_2 \end{pmatrix} = \begin{pmatrix} 2 \\ -0.5 \\ 0.01\sin(4\pi x) \\ 1 \end{pmatrix} \quad (y < 0). \tag{4.29}$$

The initial distribution $f^\varepsilon(0, x, v)$ is chosen as the Maxwellian corresponding to these moments. We impose periodic and outflow boundary conditions along the x- and y-directions, respectively, and we perform simulations for $t \in [0, 1.6]$. As velocity space, we take the domain $[-8, 8]^2$, which we discretize on a uniform grid using $\mathrm{J}_x = \mathrm{J}_y = 30$ velocity nodes along each dimension. We discretize space using the WENO2 method on $[-0.5, 0.5] \times [-0.5, 0.5]$ with $\mathrm{I}_x = \mathrm{I}_y = 100$.

Since we consider again the BGK equation with constant collision frequency $\nu = 1$, the spectrum of the linearized BGK operator consists of two eigenvalue clusters. Therefore, we construct a PInt method to speed up simulation in time, the PRK4 method with FE as inner integrator. The inner time step is fixed as $\delta t = \varepsilon$ and we use $\mathrm{K} = 3$ inner steps in each outer integrator iteration. The outer time step is chosen as $\Delta t = 0.45\Delta x$. The simulated density and pressure at time $t = 0.4$, 0.9 and 1.6 are displayed in Fig. 4.9.

In this numerical test, the speed-up factor between a naive RK4 implementation and the PInt method is 22.5.

Boltzmann in 2D/2D. As a last experiment, we concentrate on the Boltzmann equation with pseudo-Maxwellian particles in 2D/2D. As initial configuration for the gas, we consider the double

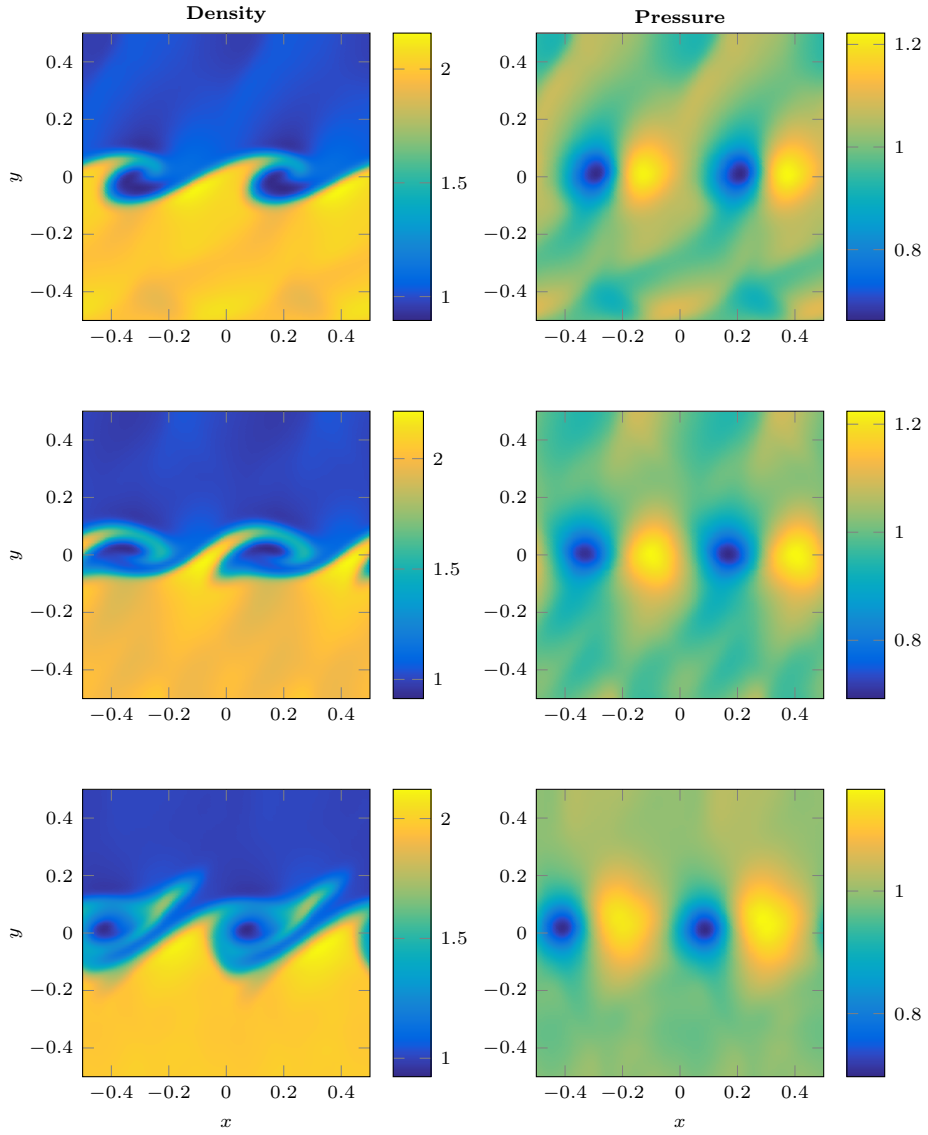

Figure 4.9: **BGK in 2D/2D.** Density (left) and pressure (right) of the Kelvin-Helmoltzm-like instability at times $t = 0.6$ (first row), 0.9 (second row) and 1.6 (third row).

Sod shock test, that is, for $(x, y) \in [-0.5, 0.5]^2$, we set:

$$\begin{pmatrix} \rho_1 \\ \boldsymbol{u}_1 \\ \mathrm{T}_1 \end{pmatrix} = \begin{pmatrix} 0.1 \\ \mathbf{0} \\ 1 \end{pmatrix} \quad (xy \leq 0), \qquad \begin{pmatrix} \rho_2 \\ \boldsymbol{u}_2 \\ \mathrm{T}_2 \end{pmatrix} = \begin{pmatrix} 1 \\ \mathbf{0} \\ 1 \end{pmatrix} \quad \text{(otherwise)}. \tag{4.30}$$

The initial distribution $f^\varepsilon(0, x, v)$ is then chosen as the Maxwellian distribution corresponding to the above macroscopic variables. We impose outflow boundary conditions along both dimensions and perform simulations for $t \in [0, 0.16]$. As velocity space, we take the domain $[-8, 8]^2$, which we discretize on a uniform grid with $\mathrm{J}_x = \mathrm{J}_y = 32$ velocity nodes along each dimension. Furthermore, we discretize the spatial domain using the WENO2 spatial discretization with $\mathrm{I}_x = \mathrm{I}_y = 64$ grid points along each dimension, and we fix $\varepsilon = 5 \cdot 10^{-5}$. The Boltzmann collision operator is approximated again using the fast spectral method with $\mathrm{N}_\theta = 4$ discrete angles.

For the time simulation of the Boltzmann equation, we apply a level-2 TPRK4 method with FE as innermost integrator using $h_0 = \varepsilon$ as innermost time step. We set $\mathrm{K} = 3$ constant on each level and compute the extrapolation step sizes as $\mathrm{M} = \{6.66, 4.80\}$. The outermost time step is chosen as $\Delta t = 0.3\Delta x$. In Fig. 4.10, we plot various macroscopic observables of interest at $t = 0.16$: density, macroscopic velocity along x, kinetic energy and temperature. Then, pressure and the Mach number are obtained, respectively, as $\mathbb{P} = \rho \mathrm{T}$ and $\mathrm{Ma} = |\boldsymbol{u}|/\sqrt{\mathrm{T}}$.

In this test, the speed-up factor between a naive RK4 implementation and the TPInt method is 5.9.

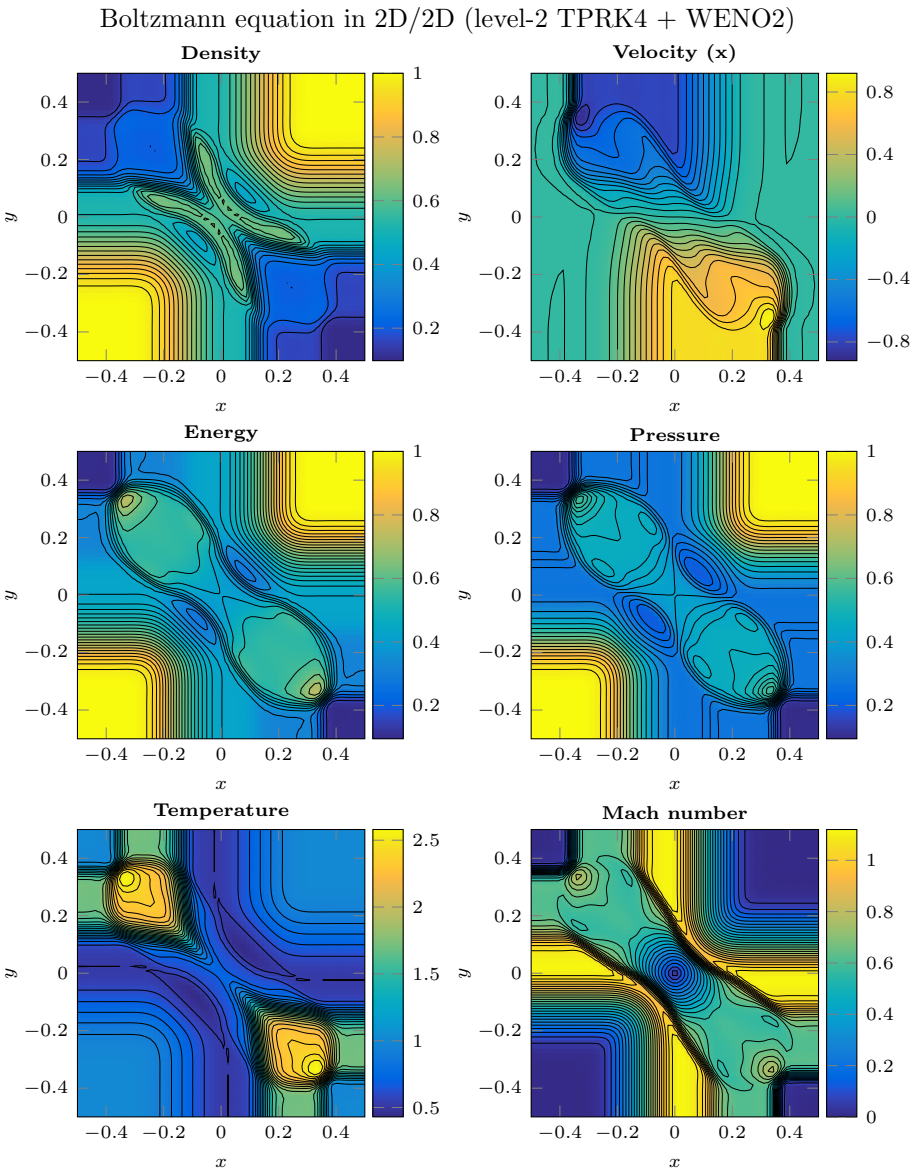

Figure 4.10: **Boltzmann in 2D/2D.** We choose the Maxwellian pseudo-molecule kernel at $t = 0.16$ for a double Sod shock test (4.30). Velocity space is discretized using $\mathrm{J}_x = \mathrm{J}_y = 32$. We applied a level-2 TPRK4 method with FE as innermost integrator and $h_0 = \varepsilon = 5 \cdot 10^{-5}$ together with WENO2 with $\mathrm{I}_x = \mathrm{I}_y = 64$.

4.2.5 Applications to gas mixtures

In this section, we apply our PInt and TPInt schemes to various physical scenarios of multiple species gases, in order to showcase the robustness and versatility of the methods. We shall then solve numerically the kinetic equation (1.1) with the BGK approximation of the multiple species collision operator (1.29) from [123]. All the figures are taken from [BR22].

Mixture Sod Tube & Extreme Mass Ratios (1D/1D) We shall employ here a setting inspired from the classical Sod Tube. Firstly, we entertain an analogue of the Riemann problem which involves two initially separate gases, whose solution can be constructed in the same fashion as that of the classical problem; see the appendix for the derivation. Secondly, rather than solving a multifluid Euler system, we solve the corresponding problem for the multispecies BGK model, and compare its moments to the aforementioned analytic solution, exploiting the limiting behaviour of the kinetic equation..

Mixture Sod Tube. We will consider two gases in a one-dimensional domain $\Omega = (0,1)$. The mass ratio m_2/m_1 and Knudsen number will vary through the examples. The initial configuration will emulate a Riemann problem with left state $(\rho_{\mathrm{L}}, \boldsymbol{u}_{\mathrm{L}}, \mathrm{T}_{\mathrm{L}}) = (1,0,1)$ and right state $(\rho_{\mathrm{R}}, \boldsymbol{u}_{\mathrm{R}}, \mathcal{P}_{\mathrm{R}}) = (2^{-3}, 0, 2^{-5})$, where the left state is entirely comprised of the first gas, and the right state of the second. To that end, we prescribe their initial distributions as Maxwellians with moments

$$\begin{cases} \rho_1 = (1-\delta)\rho_{\mathrm{L}}, & \rho_2 = \delta\rho_{\mathrm{L}}, & \boldsymbol{u}_1 = \boldsymbol{u}_2 = v_{\mathrm{L}}, & \mathrm{T}_1 = \mathrm{T}_2 = \mathrm{T}_{\mathrm{L}}, & \text{if } x \le 0.5; \\ \rho_1 = \delta\rho_{\mathrm{R}}, & \rho_2 = (1-\delta)\rho_{\mathrm{R}}, & \boldsymbol{u}_1 = \boldsymbol{u}_2 = v_{\mathrm{R}}, & \mathrm{T}_1 = \mathrm{T}_2 = \mathrm{T}_{\mathrm{R}}, & \text{if } x > 0.5. \end{cases} \tag{4.31}$$

Ideally, we would set $\delta = 0$, but this leads to an ill-defined temperature, so we let $\delta = 10^{-5}$. This pattern will also be used in later experiments whenever a density is zero. We henceforth refer to this problem as the *mixture Sod Tube problem*.

To begin, we verify the behavior of this problem in the hydrodynamic limit. We will compute numerically the solution with datum (4.31) with mass ratio $m_2/m_1 = 1$, for three different values of the Knudsen number: $\varepsilon = 10^{-1}$, 10^{-2}, and 10^{-6}. The larger values of epsilon do not pose significant stiffness, so a direct integration method can be used; for $\varepsilon = 10^{-6}$, we resort to a telescopic two-level method.

The solution is computed over the time interval $t \in (0, 0.15)$. The domain Ω is discretized with $\Delta x = 2^{-10}$, and the velocity space is set as $(-20, 20)$, with $\Delta v = 2^{-4}$. For the direct method employed on the larger values of ε, we let $\Delta t = 1.53 \times 10^{-5}$. In the telescopic method, we choose $h_0 = 5 \times 10^{-7}$, $h_1 = 2 \times 10^{-6}$, and $h_2 = 6.1 \times 10^{-5}$, and step numbers $\mathrm{K}_0 = 1$ and $\mathrm{K}_1 = 6$. We impose no-flux boundary conditions.

Fig. 4.11 shows the numerical solutions superimposed on the analytical limiting solution. As the Knudsen number decreases, the moments of the solution approach the correct hydrodynamic limit.

A CPU Benchmark. We now revisit the problem (4.31) to conduct a CPU benchmark. We will solve the problem for $\varepsilon = 10^{-5}$, $\varepsilon = 10^{-6}$, and $\varepsilon = 10^{-7}$ with the telescopic method as well as the direct method, and compare the measured and theoretical computational times. The domain Ω is discretized with $\Delta x = 2^{-8}$, and the velocity space is set as $(-20, 20)$, with $\Delta v = 2^{-4}$. For the direct method, we let $\Delta t = \varepsilon/2$. In the telescopic method, we choose $h_0 = \varepsilon/2$, $h_1 = 2\varepsilon$, and $h_2 = \Delta x/16$, and step numbers $\mathrm{K}_0 = 1$ and $\mathrm{K}_1 = 6$. We impose no-flux boundary conditions.

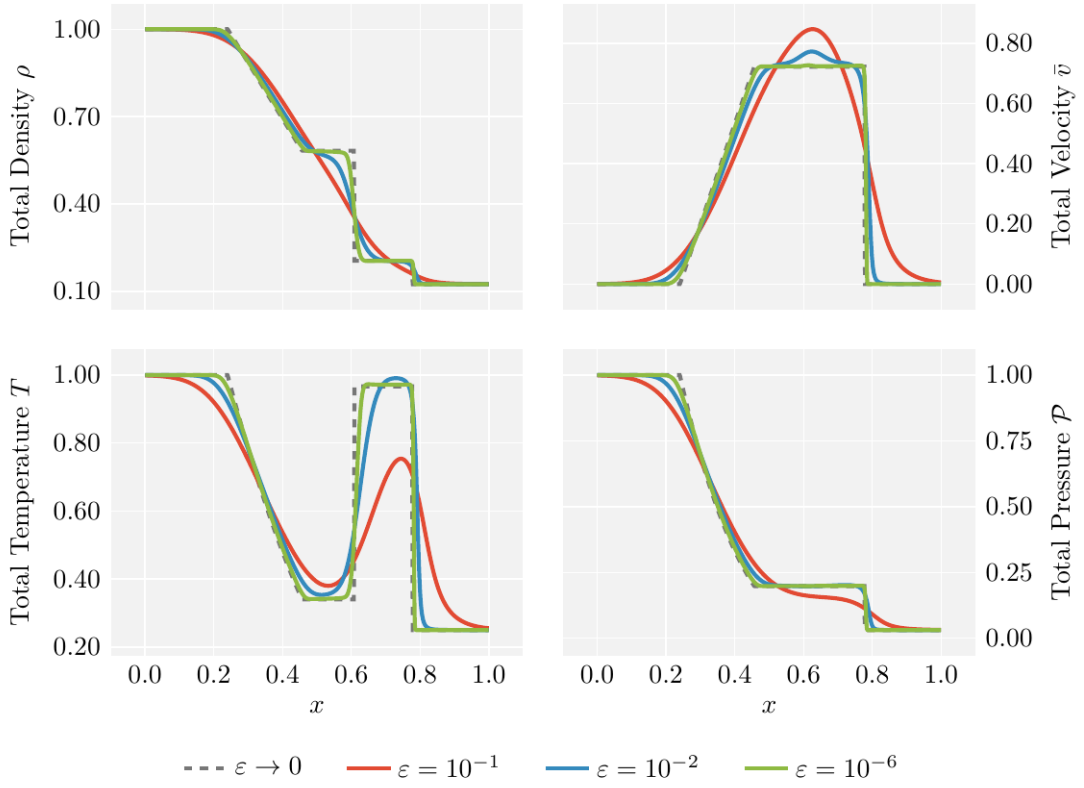

Figure 4.11: **Mixture Sod Tube.** Numerical solutions with decreasing Knudsen number and unit mass ratio. The solutions approach the correct $\varepsilon \to 0$ limit.

Table 4.1 shows the CPU time of each simulation, the real improvement factor (the ratio of CPU times of the direct method to the telescopic method), and the theoretical improvement factor. The theoretical factor is overly optimistic, as it assumes that the projection steps have negligible computational cost; nevertheless, the telescopic method is faster for $\varepsilon = 10^{-5}$ and vastly superior for smaller values of the Knudsen number.

Extreme Mass Ratios. It is of great interest to attempt the numerical solution of problems with extremely large mass ratios. Indeed, a simple mixture of Ar and He exhibits a mass ratio of 10, which can be a problem for some numerical methods, as noted in [217]. Their method can deal with mass ratios up to 35; however, ratios twice as large can easily be found in other scenarios, such as mixtures of H_2 and Xe.

We will demonstrate the behavior of our scheme in the context of a hydrodynamic limit under an

ε	CPU Time (s)		Improvement factor	
	Direct	Telescopic	Real	Theoretical
10^{-5}	54	47	1.15	3.49
10^{-6}	508	47	1.08×10^{1}	3.49×10^{1}
10^{-7}	5660	48	1.18×10^{2}	3.49×10^{2}

Table 4.1: **Mixture Sod tube.** CPU Time (rounded to nearest second) and improvement factor for the benchmark of the mixture Sod tube.

Physical		Phase space discretization		Time discretization		
m_1	1	Δx	2.5×10^{-2}	K_0	1	
m_2	5	Δy	2.5×10^{-2}	K_1	6	
ε	10^{-5}	Δv	2.5×10^{-1}	h_0	5×10^{-6}	$(= \varepsilon/2)$
				h_1	2×10^{-5}	$(= 2\varepsilon)$
				h_2	1.25×10^{-3}	$(= \Delta x/20)$

Table 4.2: Parameters for the shock-bubble interaction test.

extreme mass ratio. Conveniently, the asymptotic behavior of the mixture Sod Tube problem remains unchanged if we assume that the gases have different molecular masses; therefore, it remains a suitable validation case.

We solve the problem for mass ratios $m_2/m_1 = 5$, 30, and 100, in the hydrodynamic regime and compare the solutions. We let $\varepsilon = 10^{-6}$. The spatial discretization is done as before. The velocity space is set as $(-60, 60)$, with $\Delta v = 2^{-4}$; such large domain is unnecessary for the smaller mass ratios, but will be required for $m_2/m_1 = 100$. We again choose $h_0 = 5 \times 10^{-7}$, $h_1 = 2 \times 10^{-6}$, and $h_2 = 6.1 \times 10^{-5}$, though this time we set $\mathrm{K}_0 = 1$ and $\mathrm{K}_1 = 14$; again, the large step number is only required for the larger mass ratios. In order to justify our velocity discretization, we will also solve the $m_2/m_1 = 100$ case with varying velocity spaces $(-\mathrm{L}_v, \mathrm{L}_v)$, for $\mathrm{L}_v = 40$, 60, and 80, keeping the rest of the parameters fixed.

In all cases we deal with the large velocity supports directly. The recent work [47] has used a rescaling velocity approach reminiscent of [FR13] to overcome the same issue, but their strategy remains limited to mass ratios up to 20.

Fig. 4.12 shows the numerical solutions, again superimposed on the limiting solution. The effects of the extreme mass ratios can be seen at point of contact discontinuity (the boundary between the two gases), magnified in the figure. The left column shows the solutions with various mass ratios; the overall hydrodynamic limit is captured well. However, the interfacial effects are more pronounced as the mass ratio increases, and will require a smaller Knudsen number before they become imperceptible. The right column shows the effect of the choice of velocity domain in the solution: $\mathrm{L}_v = 40$ leads to widespread error, whereas $\mathrm{L}_v = 60$ recovers the correct behavior, and is in fact indistinguishable from $\mathrm{L}_v = 80$.

Shock-Bubble Interaction (2D/2D). We investigate the interaction between a traveling shock and a smooth stationary bubble. This is a multispecies adaptation of a one-species test case proposed in [206]; the original test has been used to validate numerical schemes, including PInt [MRS19].

We will consider a mixture of two gases with mass ratio $m_2/m_1 = 5$ in a rectangular domain $\Omega = (-1.5, 3) \times (-1.5, 1.5)$. The Knudsen number is chosen in the hydrodynamic regime, $\varepsilon = 10^{-5}$. The initial configuration of the first (lighter) gas is a normal shock wave of Mach number 2 propagating in the positive x-direction. Its initial distribution is chosen as the Maxwellian corresponding to the following Riemann datum:

$$\begin{cases} \rho_1 = 2, & \boldsymbol{u}_{1,x} = 1.414, & \boldsymbol{u}_{1,y} = 0, & \mathrm{T}_1 = 2.5, & \text{if } x \le -1; \\ \rho_1 = 1, & \boldsymbol{u}_{1,x} = 0, & \boldsymbol{u}_{1,y} = 0, & \mathrm{T}_1 = 1, & \text{if } x > -1. \end{cases} \tag{4.32}$$

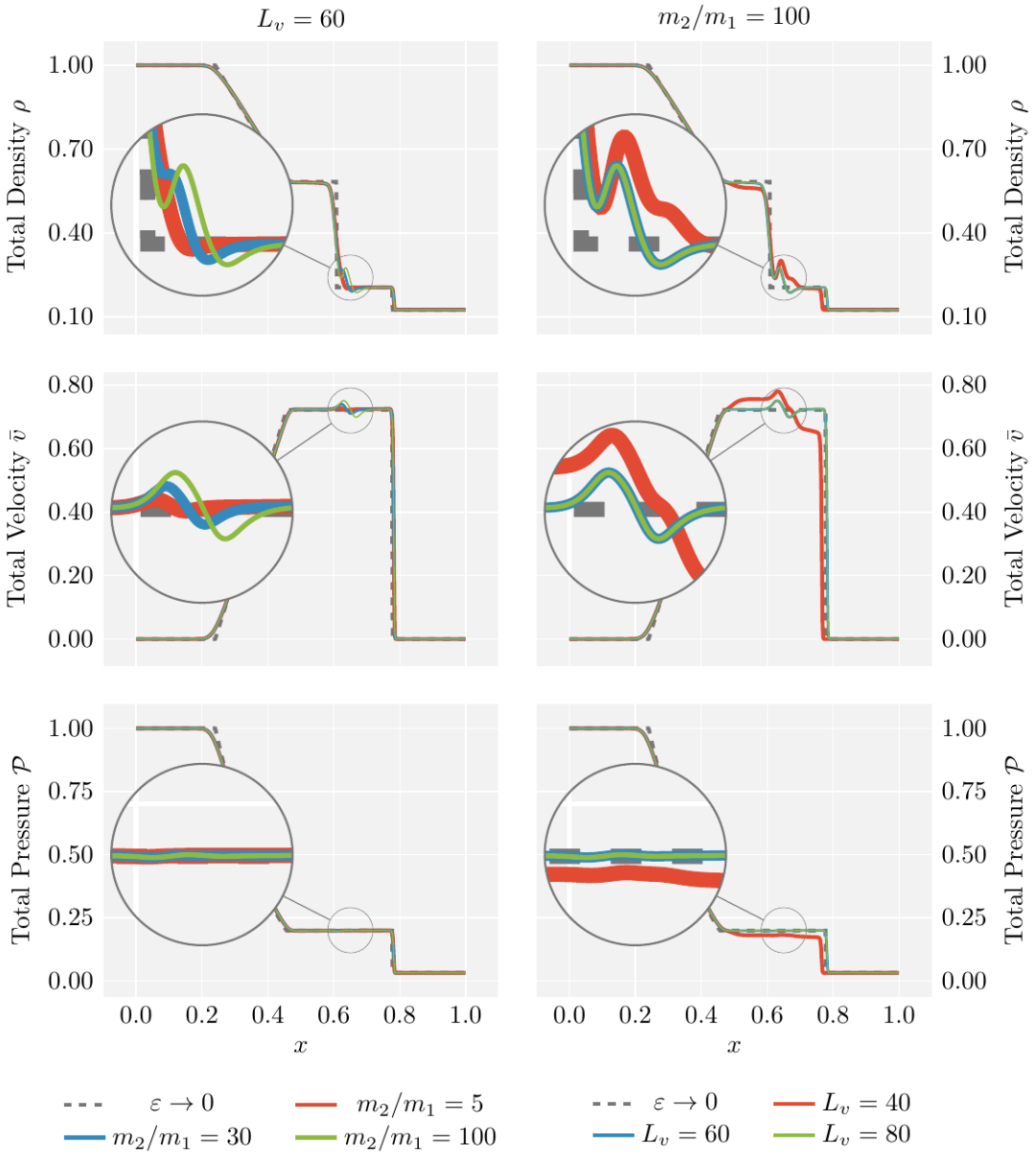

Figure 4.12: **Extreme mass ratios. Left**: higher mass ratios yield slower hydrodynamic convergence. **Right**: high mass ratios require larger velocity domains $(-\mathrm{L}_v, \mathrm{L}_v)$ in order to capture the correct behaviour.

The second (heavier) gas is initially stationary: a Maxwellian with density

$$\rho_2(0,x) = \exp(-16|x-x_0|^2). \tag{4.33}$$

The temperatures of both gases around the bubble are chosen equal to each other and in such a way that there is unit total pressure.

Numerically, the domain Ω is discretized with $\Delta x = \Delta y = 2.5 \times 10^{-2}$ (180×120 cells). The velocity space is set as $(-12, 12)^2$, with $\Delta v = 2.5 \times 10^{-1}$ (96^2 cells). In total, the phase space is discretized with 199,065,600 cells. We impose outflow boundary conditions.

The solution is computed over the time $t \in (0, 1.5)$. We employ the telescopic two-level method,

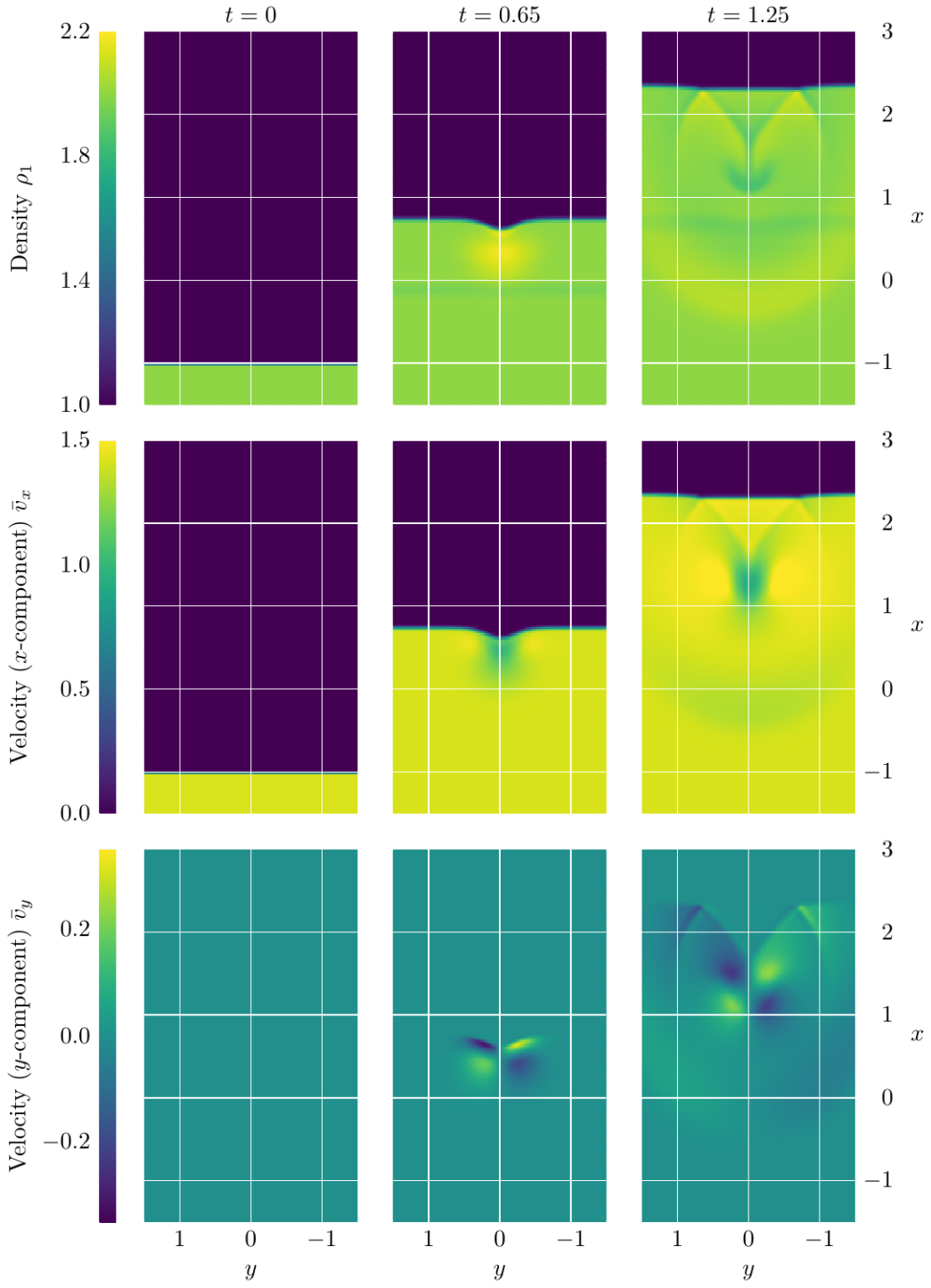

Figure 4.13: **Shock-bubble interaction.** evolution of the first (lighter) species. **Left**: datum. **Middle**: shock interacts with bubble. **Right**: pressure waves arise as a result of the shock-bubble interaction. Simulation parameters can be found in Table 4.2.

with step sizes $h_0 = 5 \times 10^{-6}$, $h_1 = 2 \times 10^{-5}$, and $h_2 = 1.25 \times 10^{-3}$, and step numbers $\mathrm{K}_0 = 1$ and $\mathrm{K}_1 = 6$. The inner steps follow the pattern $4h_0 = 2\varepsilon = h_1$. The outermost step is restricted by the stability of the transport scheme, rather than the PInt. The use of TPInt decreases the computational cost by a factor of $\mathrm{S} \simeq 18$. This factor, considering the fine and high-dimensional mesh employed

Physical		Phase space discretization			Time discretization		
m_1	1	Δx	2.5×10^{-4}		K_0	1	
m_2	5	Δy	2.5×10^{-4}	$(= \Delta x)$	K_1	6	
ε	10^{-6}	Δv	2.5×10^{-1}		h_0	5×10^{-7}	$(= \varepsilon/2)$
					h_1	2×10^{-6}	$(= 2\varepsilon)$
					h_2	6.25×10^{-5}	$(= \Delta x/4)$

Table 4.3: Parameters for the Richtmyer-Meshkov instability test.

here, is extremely beneficial, reducing the simulation time from a matter of days to a matter of hours!

Fig. 4.13 shows the evolution of the first (lighter) gas at several times. The shock travels to meet the bubble; when they meet, the central ($y \simeq 0$) portion of the shock is slowed down. As the shock traverses the bubble, two pressure waves are formed: one traveling upstream, appears as a reflection from the initial shock-bubble interaction; the second, traveling downstream, arises as the shock surrounds the obstacle and both "arms" meet behind the bubble.

Richtmyer-Meshkov Instability (2D/2D). We conclude with the so-called Richtmyer-Meshkov instability. This is a phenomenon which takes place when the perturbed interface between a thin and a dense gas is momentarily accelerated by a passing shock. The misalignment of the pressure gradient (due to the shock) and the density gradient induces vorticity, which leads to the formation of a mushroom-like interface. A more detailed physical background, as well as experimental images, can be found in [11].

We shall consider two gases with mass ratio $m_2/m_1 = 5$ in a rectangular domain $\Omega = (-0.5, 0.5) \times (0, 0.5)$. The Knudsen number is here chosen as $\varepsilon = 10^{-6}$ in order to correctly resolve the instability. The gases are initially separate: the first (lighter) gas occupies the $x \leq b(y)$ region, with a perturbed boundary given by $x = -10^{-2} \sin(20\pi y)$, whereas the second (heavier) gas lies in the rest of the domain. The initial configuration of the first gas is a normal shock wave of Mach number 1.21 propagating in the positive x-direction. Its initial distribution is chosen according to the following Riemann datum:

$$\begin{cases} \rho_1 = 1.268, & \boldsymbol{u}_{1,x} = 0.256, & \boldsymbol{u}_{1,y} = 0, & p_1 = 0.809, & \text{if } x \leq s_0; \\ \rho_1 = 1, & \boldsymbol{u}_{1,x} = 0, & \boldsymbol{u}_{1,y} = 0, & p_1 = 0.5, & \text{if } x > s_0; \end{cases} \tag{4.34}$$

s_0, the initial position of the shock, is a negative constant. The second gas is initially stationary, with density $\rho_2 = 5$, and pressure $p_2 = 0.5$ to ensure the boundary is initially not forced. The initial distribution of the gases are the Maxwellians corresponding to these moments. For convenience, in order to avoid the interface leaving the domain, all the horizontal velocities are decreased by 7×10^{-2}.

Numerically, the domain Ω is discretized with $\Delta x = \Delta y = 2.5 \times 10^{-4}$ (400×200 cells). The velocity space is set as $(-4, 4)^2$, with $\Delta v = 2.5 \times 10^{-1}$ (32^2 cells). In total, the phase space is discretized with 81,920,000 cells. We impose outflow boundary conditions.

The solution is computed over the time $t \in (-0.02, 1.0)$. We choose the negative initial time and let $s_0 = 2.42 \times 10^{-2}$ so that the shock crosses the $x = 0$ line exactly at $t = 0$. We employ the

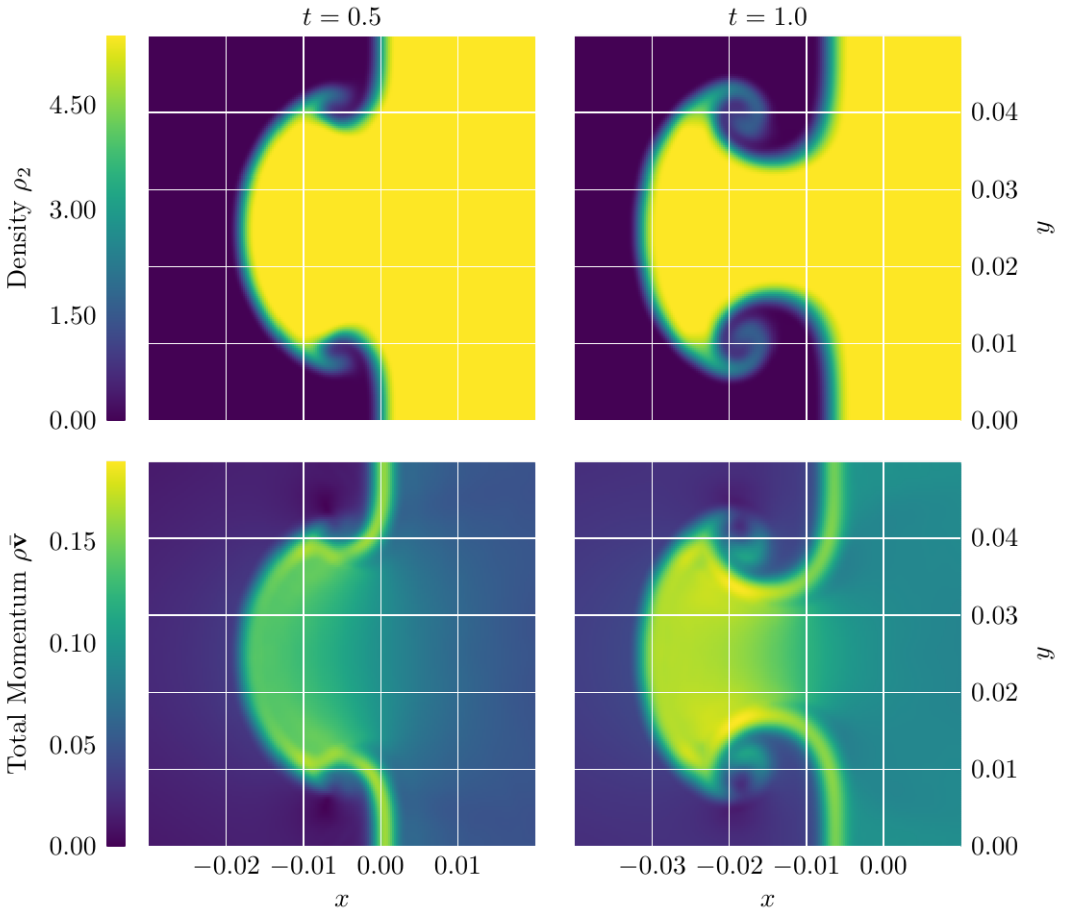

Figure 4.14: Richtmyer-Meshkov instability: density of the second species and modulus of the total momentum. **Left**: after the initial shock interaction, vortices arise. **Right**: the interface is deformed into a mushroom-like shape. Simulation parameters can be found in Table 4.3.

telescopic two-level method, with step sizes $h_0 = 5 \times 10^{-7}$, $h_1 = 2 \times 10^{-6}$, and $h_2 = 6.25 \times 10^{-5}$, and inner steps $\mathrm{K}_0 = 1$ and $\mathrm{K}_1 = 6$. Once more, the inner steps follow the pattern $4h_0 = 2\varepsilon = h_1$ and the outermost step is restricted by the hyperbolic CFL condition. The use of TPInt decreases the computational cost by a factor of $\mathrm{S} \simeq 9$.

Fig. 4.14 shows the density of the heavier gas and the modulus of the total momentum of the system at two different times. The gas interface is seen deforming as it develops a mushroom-like shape. Vortices are visible on either side of the perturbation, and much of the system's momentum is found at the interface.

4.3 Discrete Hypocoercivity

Investigating the theoretical behavior of numerical methods is also important to assess their validity. We will present in this Section a work that was done in [BHR20] to establish the exponential decay to equilibrium of the numerical solutions of toy kinetic equations, by mimicking the strategies developed for proofs in the continuous settings.

4.3.1 L^2—Hypocoercivity

Because of the overall gradient flow structure (in the $x-v$–phase space) of equation (1.1) with the linear Fokker-Planck operator, or the relaxation structure with the linearized Boltzmann operator [RT13], one can naturally believe that the solutions to this equation will exhibit a relaxation towards some global[2] Maxwellian equilibrium $\mathcal{M}$. This is a classical problem, which can be traced back to the seminal work of Hörmander [134] on the hypoellipticity of linear operators.

The first partial proof of this large time behavior can be found in [16]. It was then proved for a very large class of collision operators (with or without confinement in velocity) in [125], and in the series of papers [83, 39] (see also the references therein) that for a suitable norm, the rate of convergence towards the equilibrium is exponential: there exists some constants $\lambda > 0$ and $C \geq 1$ such that

$$\|f(t) - \mathcal{M}\|_{\mathcal{X}} \leq C \|f_0 - \mathcal{M}\|_{\mathcal{X}} e^{-\lambda t},$$

in a well chosen Hilbert space $\mathcal{X}$. We shall call this type of behavior *hypocoercivity* [213] (the case $C = 1$ corresponding to classical coercive behavior).

A very robust proof for establishing such a result can be found in the paper [83]. It uses a so-called "modified entropy functional" defined for a solution f^ε to (1.1) as:

$$H(f^\varepsilon(t)) = \frac{1}{2}\|f^\varepsilon(t)\|^2_{L^2(\mathcal{M}^{-1})} + \eta\,\varepsilon^2 \langle j^\varepsilon, \partial_x \phi^\varepsilon \rangle_{L^2_x}, \tag{4.35}$$

where ϕ^ε is solution to the Poisson equation $-\partial^2_{xx}\phi^\varepsilon = \rho^\varepsilon$. It is shown in [83] that for small enough η, this functional is equivalent to the norm on $L^2\left(\mathcal{M}^{-1}\right)$, and that if f^ε is of finite mass and velocity, $H(f^\varepsilon(t))$ decays exponentially fast toward the global Maxwellian equilibrium, at a rate which is essentially independent on ε on the *diffusive* scaling $\alpha = \beta = 1$. Note the strong link between this result and the solution to the full Boltzmann equation, through the analysis we have made in Section 4.1.2.

We extended in [BHR20] this result to the fully discrete setting for both the BGK and the Fokker-Planck equations. This is closely related to the recent result [85], which established a discrete hypocoercivity property in $H^1\left(\mathcal{M}^{-1}\right)$ for the Fokker-Planck equation. Let us present our results in the BGK case.

4.3.2 The full implicit scheme

In [BHR20], we introduced numerical schemes for Equation (1.1) in both the Fokker-Planck and the BGK cases. The schemes are of finite volume type [93], meaning that they are based on an approximation of the fluxes appearing in the integrated version of (1.1) on each cell K_{ij}. In the time variable we choose a backward Euler discretization so that we have almost for free some AP properties.

The mesh. We first restrict the velocity domain to a bounded symmetric segment $[-v_\star, v_\star]$, since it is not possible in practice to implement a numerical scheme on an unbounded domain. We consider a primal mesh of this interval composed of $2L$ control volumes arranged symmetrically around $v = 0$.

[2] due also to the mixing properties of the free transport operator on the torus.

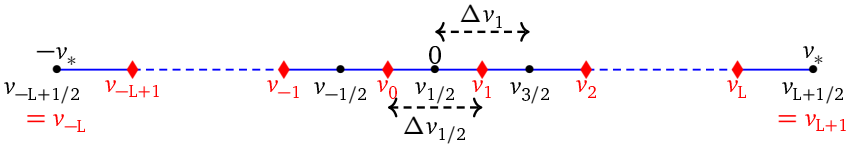

Figure 4.15: Discretization of the velocity domain.

We thus get $2L+1$ distinct interface points denoted by $v_{j+\frac{1}{2}}$ (for consistency with usual finite volume notations) with $j = -L, \dots, L$. In this way

$$v_{-L+1/2} = -v_\star\,, \quad v_{1/2} = 0\,, \quad v_{j+1/2} = -v_{-j+1/2} \quad \forall j = 0, \dots, L.$$

The cells of the primal mesh are given by

$$\mathcal{V}_j \;:=\; (v_{j-\frac{1}{2}}, v_{j+\frac{1}{2}}), \quad j \in \mathcal{J} := \{-L+1, \dots, L\}.$$

Each cell $\mathcal{V}_j$ has length $\Delta v_j = v_{j+\frac{1}{2}} - v_{j-\frac{1}{2}}$ and midpoint v_j. At the level of cells, the symmetry of the velocities reads $v_j \;=\; -v_{-j+1}$ for all $j = 1, \dots, L$. We also define the dual mesh with cells

$$\mathcal{V}^*_{j+1/2} \;:=\; (v_j, v_{j+1}), \quad j \in \mathcal{J}^* := \{-L, \dots, L\},$$

with $v_{-L} := v_{-L+1/2} = -v_\star$ and $v_{L+1} := v_{L+1/2} = v_\star$. The length of the dual cell $\mathcal{V}^*_{j+1/2}$ is $\Delta v_{j+1/2} = v_{j+1} - v_j$. Notations introduced are illustrated in Fig. 4.15.

In space, we consider a discretization of the torus $\mathbb{T}$ into N subintervals

$$\mathcal{X}_i \;:=\; (x_{i-\frac{1}{2}}, x_{i+\frac{1}{2}}), \quad i \in \mathcal{I} := \mathbb{Z}/N\mathbb{Z}$$

of length Δx_i and centers x_i. In what follows, we assume that N is odd. Indeed, this assumption is natural to obtain, among others, a discrete Poincaré inequality on the torus with our choice of discrete gradients, as explained in [BHR20].

The control volumes in phase space are defined by

$$K_{ij} \;:=\; \mathcal{X}_i \times \mathcal{V}_j\,, \qquad \forall (i,j) \in \mathcal{I} \times \mathcal{J}.$$

The size of the phase-space discretization is defined by $\delta \;=\; \max(\Delta x, \Delta v)$ where Δx and Δv are the maximum of $(\Delta x_i)_{i\in\mathcal{I}}$ and $(\Delta v_j)_{j\in\mathcal{J}}$ respectively. Finally, we set $\Delta t > 0$ the time step, and we define $t^n = n\Delta t$ for all $n \geq 0$.

First of all, we discretize the initial datum f_{in} by

$$f^0_{ij} = \frac{1}{\Delta x_i\, \Delta v_j} \iint_{K_{ij}} f(0,x,v)\, \mathrm{d}x\, \mathrm{d}v, \quad \forall (i,j) \in \mathcal{I} \times \mathcal{J}.$$

Discrete Maxwellians. The equilibria of the discrete BGK operator, the *discrete Maxwellians*, are defined in the following way: we assume that we are given cell values $\mathcal{M} = (\mathcal{M}_j)_{j\in\mathcal{J}} \in \mathbb{R}^{\mathcal{J}}$ satisfying the following assumptions

$$\begin{cases} \mathcal{M}_j > 0\,, \quad \mathcal{M}_j \;=\; \mathcal{M}_{-j+1}\,, \quad \forall j = 1, \dots, L; \\ \displaystyle\sum_{j\in\mathcal{J}} \mathcal{M}_j\, \Delta v_j \;=\; 1\,; \\ 0 < \underline{m}_2 \leq m_2^{\Delta v} \leq \overline{m}_2\,, \quad m_4^{\Delta v} \leq \overline{m}_4\,, \end{cases} \tag{4.36}$$

where for $k \in \mathbb{N}$

$$m_k^{\Delta v} := \sum_{j\in\mathcal{J}} |v_j|^k \mathcal{M}_j \Delta v_j$$

and $\underline{m}_2$, $\overline{m}_2$, $\overline{m}_4$ are some universal constants.

Fully discrete BGK equation. In the case of the BGK operator, the scheme is given as follows. For all $i \in \mathcal{I}$, $j \in \mathcal{J}$, $n \geq 0$,

$$\varepsilon \Delta x_i \Delta v_j (f_{ij}^{n+1} - f_{ij}^n) + \Delta t \left(\mathcal{F}_{i+\frac{1}{2},j}^{n+1} - \mathcal{F}_{i-\frac{1}{2},j}^{n+1} \right) = \frac{\Delta t}{\varepsilon} \Delta x_i \Delta v_j \left(\rho_i^{n+1} \mathcal{M}_j - f_{ij}^{n+1} \right), \tag{4.37}$$

where the numerical flux $\mathcal{F}_{i+\frac{1}{2},j}^{n+1}$ is defined by

$$\mathcal{F}_{i+\frac{1}{2},j}^{n+1} = v_j \frac{f_{i+1,j}^{n+1} + f_{ij}^{n+1}}{2} \Delta v_j, \quad \forall j \in \mathcal{J}, \quad \forall i \in \mathcal{I}, \tag{4.38}$$

and for all $i \in \mathcal{I}$ and $n \geq 0$, the discrete macroscopic density is given by the centered approximation

$$\rho_i^n := \sum_{j\in\mathcal{J}} \Delta v_j f_{ij}^n. \tag{4.39}$$

Existence and uniqueness of a solution to the fully implicit scheme (4.37) is established as a by-product of some discrete "entropy" estimate.

4.3.3 The discrete AP and hypocoercivity properties

Our discrete AP and hypocoercivity results can be summarized in the following Theorem.

Theorem 4.3.1 (Theorems 1 and 2 of [BHR20]). *Let us consider a discrete Maxwellian satisfying (4.36), and assume that the number of points* N *in the space discretization is odd. Then there are constants* $C \geq 1$ *and* $\beta > 0$ *such that for all* $\varepsilon \in (0,1)$*, all* $\Delta t \leq \Delta t_{\max}$ *and all initial data* $(f_{ij}^0)_{i\in\mathcal{I},j\in\mathcal{J}}$*, the solution* $\left(f_{ij}^n\right)_{i\in\mathcal{I},j\in\mathcal{J},n\in\mathbb{N}}$ *of (4.37) satisfies the following properties.*

- ***Unconditional stability in the diffusion limit.*** *there is* $\rho^n = (\rho_i^n)_{i\in\mathcal{I}}$ *for all* $n \geq 0$ *such that when* $\varepsilon \to 0$ *one has*

  $$f_\varepsilon^n \longrightarrow \rho^n \mathcal{M} \quad in \quad \mathbb{R}^{\mathcal{I}\times\mathcal{J}}, \quad for\ all \quad n \geq 1$$

  and the limit satisfies a finite difference scheme for the heat equation with initial data $\rho_i^0 = \sum_{j\in\mathcal{J}} \Delta v_j f_{ij}^0$.
- ***Discrete hypocoercivity.*** *One has for any n*

  $$\left\| f^n - \mu_f \mathcal{M} \right\|_{2,\gamma} \leq C \left\| f^0 - \mu_f \mathcal{M} \right\|_{2,\gamma} e^{-\frac{\beta}{2} t^n}. \tag{4.40}$$

Moreover, the constants C *and* β *do not depend on the size of the discretization* δ*, and* $\Delta t_{\max} > 0$ *can be chosen arbitrarily.*

The $\|\cdot\|_{2,\gamma}$ denotes a discretized $L^2\left(\mathcal{M}^{-1}\right)$ norm. Note that we also proved an analogous result for a Chang-Cooper-like discretization [62] of the Fokker-Planck operator.

Strategy of proof. In [BHR20], we adapted the strategy of proof of [83]. For this we introduced a *discrete modified entropy functional* which reads

$$\mathbb{H}(f^n) := \frac{1}{2}\|f^n\|_{2,\gamma}^2 + \eta\varepsilon^2 \sum_{i\in\mathcal{I}} \Delta x_i \mathrm{J}_i^n (\mathrm{D}_x\phi)_i^n + \frac{\eta\varepsilon^2}{2} \sum_{i\in\mathcal{I}} \Delta x_i \frac{\left((\mathrm{D}_x\phi)_i^n - (\mathrm{D}_x\phi)_i^{n-1}\right)^2}{\Delta t}, \tag{4.41}$$

where $\eta > 0$ will be determined later and $(\phi_i^n)_{i\in\mathcal{I}}$ is the solution of the following discrete Poisson equation

$$-\frac{(\mathrm{D}_x\phi)_{i+1}^n - (\mathrm{D}_x\phi)_{i-1}^n}{2} = \Delta x_i \rho_i^n, \quad \forall i \in \mathcal{I}, \tag{4.42}$$

$$\sum_{i\in\mathcal{I}} \Delta x_i \phi_i^n = 0. \tag{4.43}$$

This discrete version of the modified entropy functional has an additional third term compared to (4.35). It is of order $\mathcal{O}(\Delta t)$ and thus consistent with 0, so that taking limits in the discretization parameters, we recover (at least formally at this stage) the continuous modified entropy (4.35). It does not perturb the adaptation of the strategy of [83]. In particular, one has the following discrete energy estimate that allows to assess the well-posedness of the fully implicit numerical method and the validity of the AP property:

Lemma 4.3.2 (Discrete "energy" estimate). *Let us consider a discrete Maxwellian satisfying* (4.36) *and let* $(f_{ij}^n)_{i\in\mathcal{I},j\in\mathcal{J},n\in\mathbb{N}}$ *solve the scheme* (4.37)*). Then for every* $n \geq 0$*,*

$$\frac{\|f^{n+1}\|_{2,\gamma}^2 - \|f^n\|_{2,\gamma}^2}{2\Delta t} + \frac{1}{\varepsilon^2}\|f^{n+1} - \rho^{n+1}\mathcal{M}\|_{2,\gamma}^2 \leq 0. \tag{4.44}$$

In particular one has

$$\max\left(\sup_{n\geq 0}\|f^n\|_{2,\gamma}^2,\ \frac{2}{\varepsilon^2}\sum_{n=1}^{\infty}\Delta t\,\|f^n - \rho^n\mathcal{M}\|_{2,\gamma}^2\right) \leq \|f^0\|_{2,\gamma}^2. \tag{4.45}$$

We also have discrete estimates on the solution to the discrete Poisson equation $(\phi_i)_{i\in\mathcal{I}}$:

Lemma 4.3.3 (Discrete elliptic estimates). *Under the assumptions of Theorem 4.3.1, one has*

$$\|\mathrm{D}_x\phi^n\|_2 \leq \mathrm{C_P}\,\|\rho^n\|_2, \quad \forall n \geq 0, \tag{4.46}$$

$$\left\|\frac{(\mathrm{D}_x\phi)_i^{n+1} - (\mathrm{D}_x\phi)_i^n}{\Delta t}\right\|_2 \leq \|\mathrm{J}_i^{n+1}\|_2, \quad \forall n \geq 0, \tag{4.47}$$

where $\mathrm{C_P}$ *is the discrete Poincaré constant.*

Finally, these two results allow to obtain the decay of the modified entropy functional, which is the core of the proof of the discrete hypocoercivity result:

Proposition 4.3.4. *Under the assumptions of Theorem 4.3.1, there is* $\eta_2 > 0$ *such that for all* $\varepsilon \leq 1$*,* $\Delta t \leq \Delta t_{max}$ *and* $\eta \leq \eta_2$*,*

$$\frac{\mathbb{H}(f^{n+1}) - \mathbb{H}(f^n)}{\Delta t} + \mathrm{K}(\eta)\left(\|f^{n+1} - \rho^{n+1}\mathcal{M}\|_{2,\gamma}^2 + \|\rho^{n+1}\|_2^2\right) \leq 0, \qquad \forall n \geq 1,$$

with $\mathrm{K}(\eta) = \frac{1}{2}\min\left(1 - \eta\overline{m}_2, \eta\underline{m}_2\right)$.

A very robust implementation, as well as many numerical simulations are also available in the main paper. They confirm the interests of our strategy of mimicking continuous properties to design numerical methods.

4.4 Hybridization through domain indicators

The last technique we will present is this Chapter is a different paradigm of AP schemes, that was presented in [FR15]. It consists in using the theoretical Chapman-Enskog expansion to design a so-called *hybrid kinetic/fluid scheme* with an automatic domain-decomposition criterion allowing to identify accurately spatial zones were the fluid equations are more relevant than the kinetic ones, and conversely. For the sake of computational efficiency, we will present a space decomposition which minimizes the size of the kinetic layer, allowing to take advantage of the low computational cost of numerical methods for fluid systems. As far as possible, this method will also be *non-intrusive* for the solvers. More precisely, except for the implementation of the domain decomposition indicators, it will be independent on the kinetic and fluid solvers, which will not necessitate deep modifications. The macroscopic description will always by of the compressible type, and the regime of interest will be the hydrodynamic $\alpha = 0$, $\beta = 1$ one.

4.4.1 Domain indicators

There are several different works about hybrid methods for the BGK and Boltzmann equations (1.1) in the literature, the largest part relying on the same domain decomposition technique introduced in [40]. This paper uses a macroscopic criterion to pass from the hydrodynamic description (easy to compute numerically, but inaccurate near shocks or boundary layers) to the kinetic one (computationally expansive but accurate in most of the situations). This criterion is based on the local Knudsen number of the problem: when this quantity is below a (problem-dependent) threshold, the kinetic description is used. The first practical use of this method is due to [150], by using a discrete velocity model of the Boltzmann equation for the kinetic part, and a kinetic scheme for the hydrodynamic part. It has been more recently used in [79, 70], with a Monte-Carlo solver for solving the kinetic equation and a finite volume method for the macroscopic ones.

The hydrodynamic breakdown indicator introduced in [203] is also very close to the previous criterion, as it is based on the viscous and heat fluxes of the Navier-Stokes equation, through a Grad's 13-moments expansion. It has been used for deterministic solver in [71, 204, 205]. Some hybrid deterministic/kinetic approaches were then used in [2, 78, 66] to solve the more complex Vlasov-Poisson-BGK system.

Nevertheless, these criteria, being based only on a macroscopic criterion, prevent the domain decomposition technique to accurately deal with cases where the spatial variations are small, but the regime is far from the thermodynamical equilibria. We then need criteria in both regimes: one to know when the hydrodynamic description breaks down, and another one to know when the kinetic description is actually in hydrodynamic regime. We shall use the Chapmann-Enskog expansion presented in Section 4.1.1.

From Fluid to Kinetic: the Moment Realizability Criterion. Let f^ε be a solution to the scaled kinetic equation (1.1) in the hydrodynamic scaling. The matrix $\mathbf{A}^\varepsilon$ and the vector $\mathbf{B}^\varepsilon$ defined in (4.6) will allow us to define our hydrodynamic break down criterion, using an idea from [160].

Let us define the (reduced) moment realizability matrix by setting

$$\mathcal{V} := \mathbf{I} + \mathbf{A}^\varepsilon - \frac{2}{3\,\mathrm{C}^\varepsilon}\mathbf{B}^\varepsilon \otimes \mathbf{B}^\varepsilon \tag{4.48}$$

where $\bar{\mathrm{C}}^\varepsilon$ is the dimensionless fourth order moment of f^ε:

$$\bar{\mathrm{C}}^\varepsilon := \frac{2}{3\rho}\int_{\mathbb{R}^3}\left[\frac{|\mathrm{V}|^2}{2} - \frac{3}{2}\right]^2 f^\varepsilon(v)\,\mathrm{d}v.$$

One can show (see [FR15]) that the fluctuations in the Chapman-Enskog expansion (4.2) of f^ε are small if, and only if, $\mathcal{V}$ is a positive definite matrix. It allows to define a criterion to determine the appropriate model – fluid or kinetic – to be used, based on the signe of the eigenvalues of $\mathcal{V}$.

For example, let us consider the zeroth order model with respect to ε, the compressible Euler system. We have that $\mathbf{A}_{Euler} = \mathbf{0}_{\mathrm{M}_3}$, $\mathbf{B}_{Euler} = \mathbf{0}_{\mathrm{R}^3}$, and $\bar{\mathrm{C}}^\varepsilon = 1$ and then

$$\mathcal{V}_{Euler} := \mathcal{V}_1 = \mathbf{I}.$$

On the other hand, consider the first order model, that is the compressible Navier-Stokes system. By cutting the Chapman-Enskog expansion (4.2) at the first order with respect to ε (*i.e.* Navier-Stokes order), we can compute explicitly the matrix $\mathcal{V}_\varepsilon$. We have in this case using the expressions (4.16) and by symmetry arguments that $\bar{\mathrm{C}}^\varepsilon = 1$, and

$$\mathcal{V}_{\mathrm{NS}} := \mathcal{V}_\varepsilon = \mathbf{I} - \varepsilon\frac{\mu}{\rho\mathrm{T}}\mathbf{D}(\boldsymbol{u}) - \varepsilon^2\frac{2}{3}\frac{\kappa^2}{\rho^2\mathrm{T}^3}\nabla_x\mathrm{T}\otimes\nabla_x\mathrm{T}, \tag{4.49}$$

where $(\rho, \boldsymbol{u}, \mathrm{T})$ are solution to the Navier-Stokes equations (4.17).

Hence, we claim that the compressible Euler system is correct when the matrix $\mathcal{V}_{\mathrm{NS}}$ behaves like the matrix $\mathcal{V}_{Euler} = \mathbf{I}$, that is, it is positive definite and if *its eigenvalues are close to* 1 *or not*: The Euler description of the fluid will be considered incorrect if

$$|\lambda_{\mathrm{NS}} - 1| > \eta_0, \qquad \forall\lambda_{\mathrm{NS}} \in \mathrm{Sp}(\mathcal{V}_{\mathrm{NS}}), \tag{4.50}$$

where η_0 is a small parameter (here we take $\eta_0 = 10^{-2}$).

More generally, we denote by f_k^ε the k^{th} order truncation of the Chapman-Enskog expansion (4.2):

$$f_k^\varepsilon := \mathcal{M}_{\rho,\boldsymbol{u},\mathrm{T}}\left[1 + \varepsilon\, g^{(1)} + \varepsilon^2 g^{(2)} + \ldots + \varepsilon^k\, g^{(k)}\right]. \tag{4.51}$$

For a given truncation (4.51) of order k, we will say that the fluid model associated is *incorrect* at point (t, x) if we have

$$|\lambda_{\varepsilon^k} - \lambda_{\varepsilon^{k+1}}| > \eta_0, \quad \forall\,\lambda_{\varepsilon^k} \in \mathrm{Sp}(\mathcal{V}_{\varepsilon^k}),\ \lambda_{\varepsilon^{k+1}} \in \mathrm{Sp}(\mathcal{V}_{\varepsilon^{k+1}}). \tag{4.52}$$

This strategy has been more recently refined for more complex kinetic equations in [103], and by my PhD student Tino Laidin for the Vlasov-BGK model in the diffusive scaling in [155], with a rigorous numerical analysis of the hybrid method.

From Kinetic to Fluid. Knowing the full kinetic description of a gas, there exists a large number of methods to decide how far this gas is from the thermal equilibrium, namely the fluid regime. We decide to use a simple comparison between the kinetic density f^ε, solution to the collisional equation (1.1) and the truncated Chapman-Enskog distribution f_k^ε given by (4.51), whose moments match the one of f^ε, and whose order k corresponds to the order of the macroscopic model considered.

Our criterion is then the following: The kinetic description at point (t,x) corresponds to an *hydrodynamic closure of order* k if

$$\left\| f^\varepsilon(t,x,\cdot) - f_k^\varepsilon(t,x,\cdot) \right\|_{\mathrm{L}^1_v} \leq \delta_0, \tag{4.53}$$

where δ_0 is a small parameter (we take $\delta_0 = 10^{-4}$) and if the eigenvalues of the moment realizability matrix $\mathcal{V}_{\varepsilon^k}$ computed using the moments of f^ε does not verify the criterion (4.52).

If $k=1$ (Compressible Euler setting), this criterion corresponds to the natural one

$$\| f^\varepsilon(t,x,\cdot) - \mathcal{M}^\varepsilon_{\rho,\boldsymbol{u},\mathrm{T}}(t,x,\cdot) \|_{\mathrm{L}^1} \leq \delta_0,$$

namely to check if the system is locally at the thermodynamic equilibrium or not.

In particular, if we perform the Chapman-Enskog expansion (4.2) of f^ε, the criterion (4.53) corresponds to the fact that the remainder term in this expansion is small in L^1 norm, because it is then given by

$$\left\| \sum_{n>k} \varepsilon^i \, g^{(i)}(t,x,\cdot) \right\|_{\mathrm{L}^1_v} \leq \delta_0.$$

4.4.2 Numerical simulations

We take in all the simulations $d_x = 1$. In particular, the moment realizability matrices $\mathcal{V}_{\varepsilon^k}$ are diagonal. In the *e.g.* Navier-Stokes case, it is given by

$$\mathcal{V}_{\mathrm{NS}} = \begin{pmatrix} 1 - \varepsilon \dfrac{\mu}{\rho \mathrm{T}} \partial_x u^x - \varepsilon^2 \dfrac{\kappa^2}{\rho^2 \mathrm{T}^3} (\partial_x \mathrm{T})^2 & 0 & 0 \\ 0 & 1 + \varepsilon \dfrac{\mu}{\rho \mathrm{T}} \partial_x u^x & 0 \\ 0 & 0 & 1 + \varepsilon \dfrac{\mu}{\rho \mathrm{T}} \partial_x u^x \end{pmatrix},$$

where $\boldsymbol{u} = (u^x, u^y, u^z)$. We can then read its eigenvalues on its diagonal. The criterion for $k=0$ for a fluid cell to be kinetic at the next iteration is then

$$\left| \varepsilon \frac{\mu}{\rho \mathrm{T}} \partial_x u^x + \varepsilon^2 \frac{\kappa^2}{\rho^2 \mathrm{T}^3} (\partial_x \mathrm{T})^2 \right| \leq \eta_0 \quad \text{or} \quad \left| \varepsilon \frac{\mu}{\rho \mathrm{T}} \partial_x u^x \right| \leq \eta_0. \tag{4.54}$$

Using the expression of the Burnett coefficients (4.18)-(4.19), we can easily write the same type or criterion for the Navier-Stokes closure $k=1$.

Let us present some numerical simulations of the non homogeneous 1D×3D BGK equation (1.25), for the one dimensional Sod tube problem. We will compare them with the numerical solution obtained by solving the full kinetic equation on a fine mesh. We have computed an approximation for different Knudsen numbers from rarefied regime up to the fluid limit and report the results for

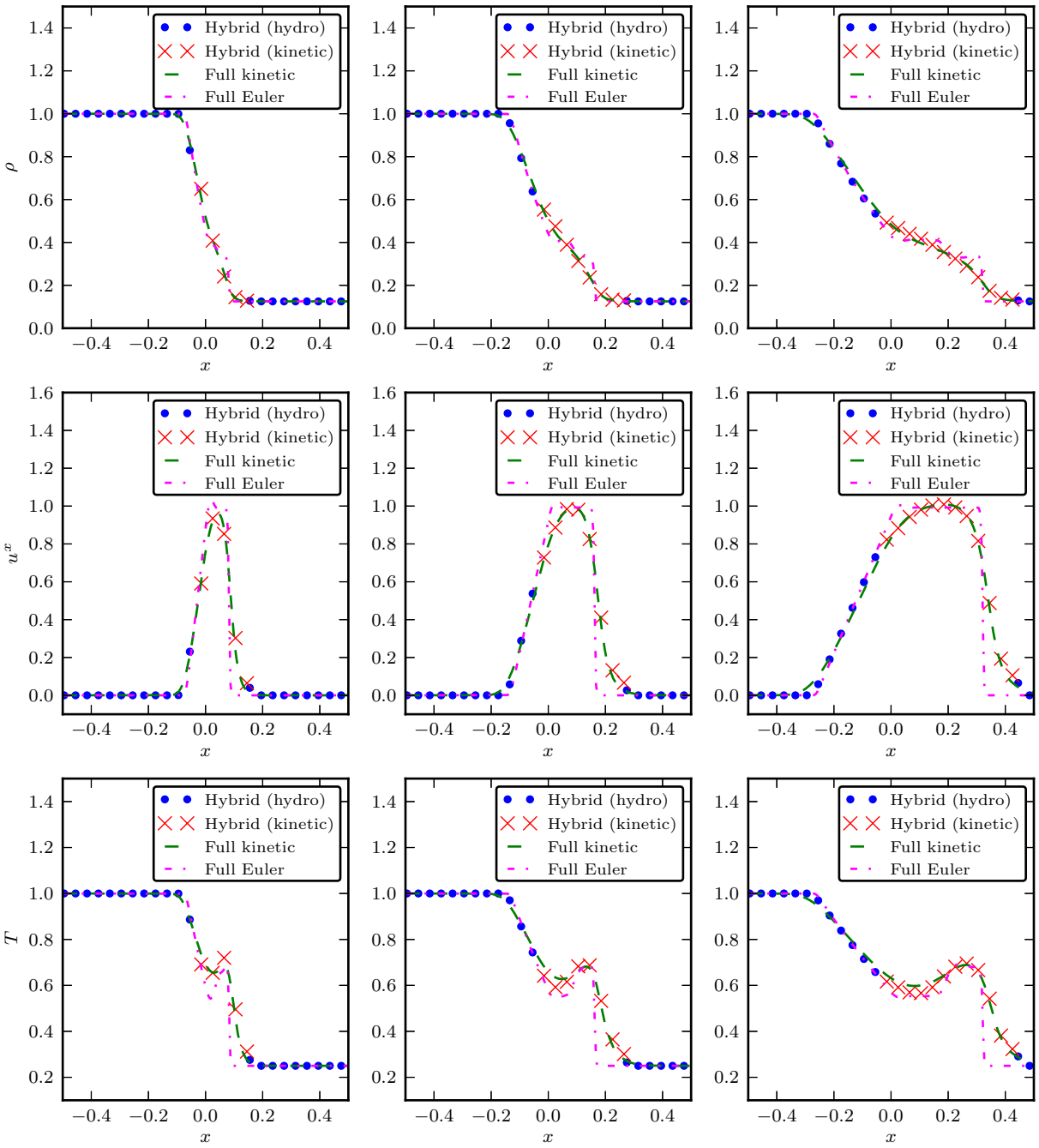

Figure 4.16: **Hybrid Sod tube with $\varepsilon = 10^{-2}$:** *Order 0 (Euler)*; Density, mean velocity and temperature at times $t = 0.05$, 0.10 and 0.20.

$\varepsilon = 10^{-2}$ and 10^{-3}. The time integrator is the RK4 method and the space integrator is a WENO2 method.

On the one hand, in Fig. 4.16 and 4.18, we plot the results obtained in the rarefied regime with $\varepsilon = 10^{-2}$, for the zeroth order model, namely the Euler dynamics. The kinetic reference solution is computed with $200 \times 128 \times 32 \times 21$ cells in phase space, the fluid reference solution with 200 points whereas the hybrid scheme is used with 100 points in x and the size of the velocity grid is $32 \times 32 \times 32$ points. We observe that the fluid solution is far from the kinetic one, which was expected

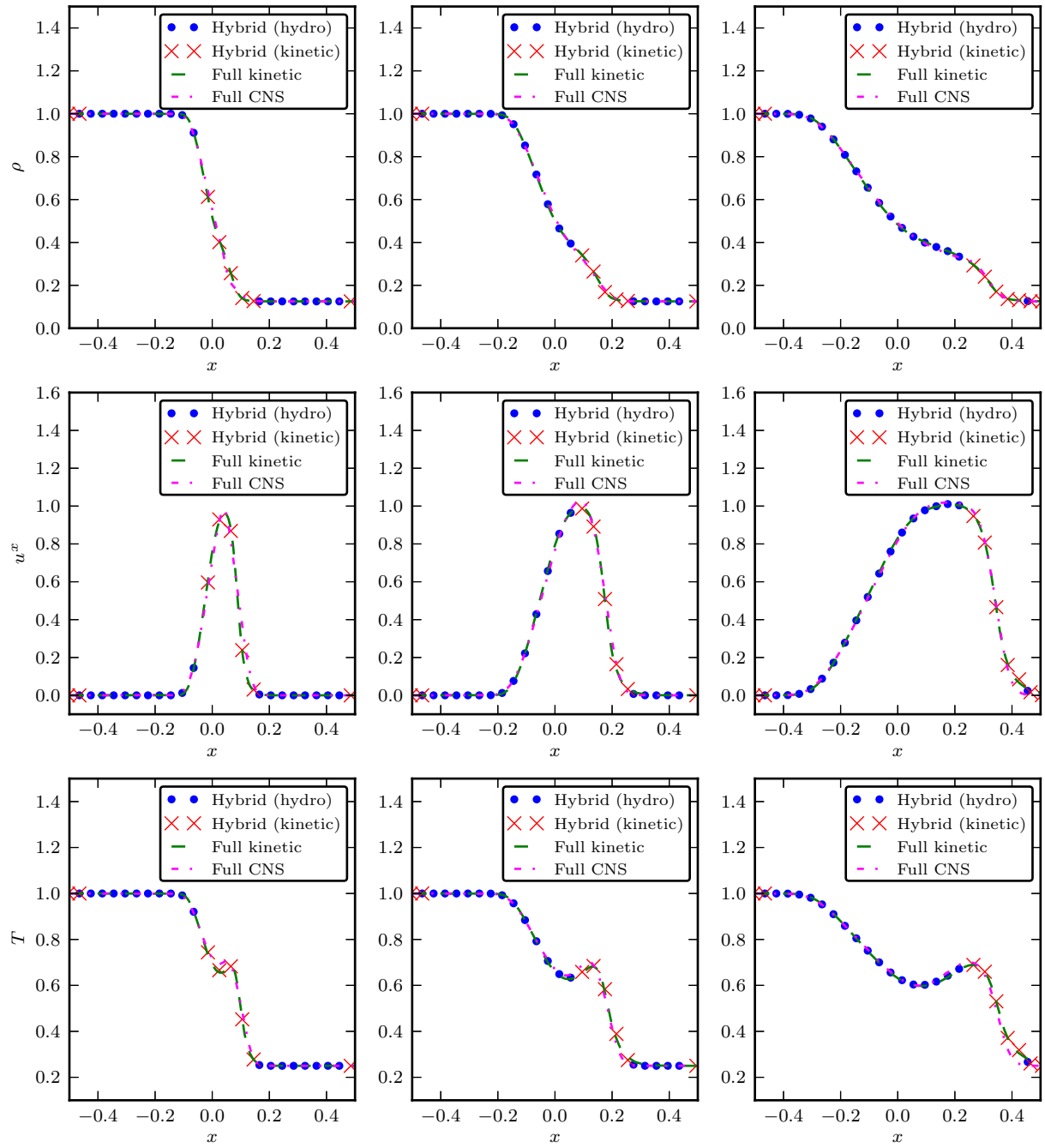

Figure 4.17: **Hybrid Sod tube with $\varepsilon = 10^{-2}$:** *Order 1 (CNS)*; Density, mean velocity and temperature at times $t = 0.05$, 0.10 and 0.20.

since the Knudsen number is large. Nevertheless, the hybrid scheme behaves very nicely in this case, detecting correctly the non-equilibrium zone and the solution is close to the kinetic one. This error is mainly due to the application of the Euler equations for which the heat flux is zero (hence some errors in this particular quantity, see Fig. 4.18). Then, in Fig. 4.17 and 4.19, we perform the same simulations for the first order, Compressible Navier-Stokes (CNS) model. Although the fluid solution is still far from the kinetic one, we observe that the result of the kinetic solver is in almost perfect agreement with the reference solution, even in large time. This can also be observed in the values

of the heat flux, which are close to the reference ones.

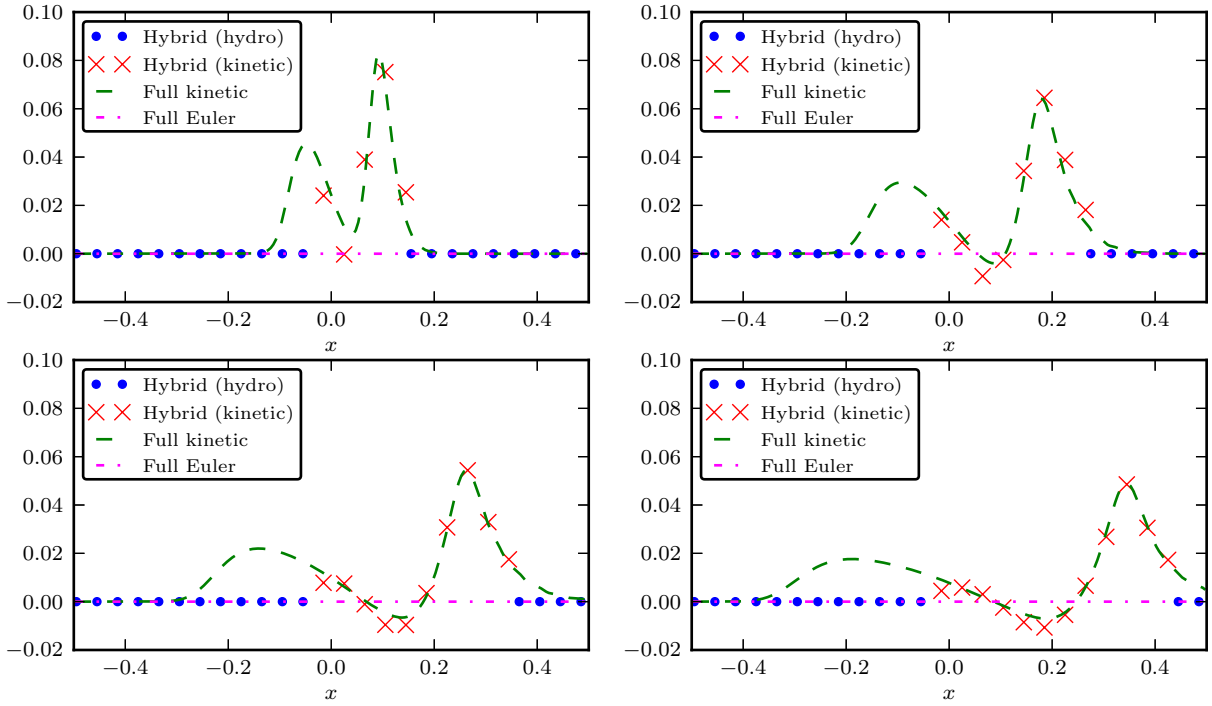

Figure 4.18: **Hybrid Sod tube with $\varepsilon = 10^{-2}$:** *Order 0 (Euler)*; heat flux at times $t = 0.05$, 0.10, 0.15 and 0.20.

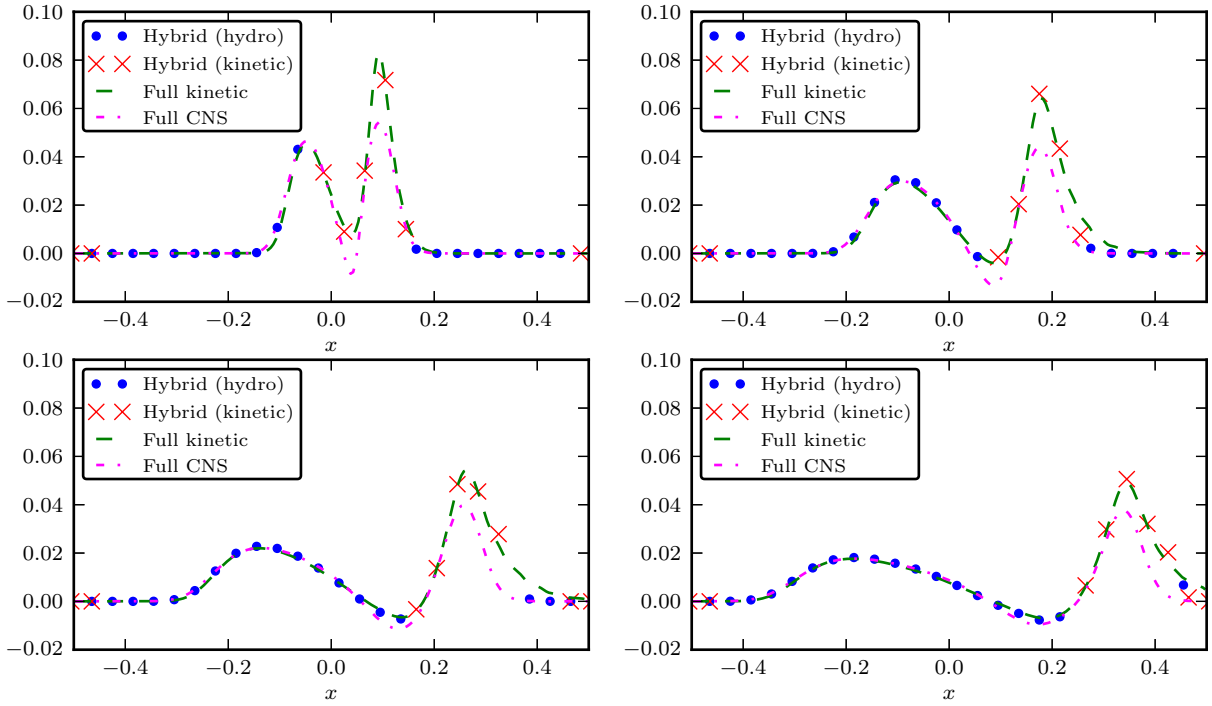

Figure 4.19: **Hybrid Sod tube with $\varepsilon = 10^{-2}$:** *Order 1 (CNS)*; heat flux at times $t = 0.05$, 0.10, 0.015 and 0.20.

Test	Sod 10^{-2}	Sod 10^{-3}	Blast 10^{-2}	Blast $5 \cdot 10^{-3}$	Blast 10^{-3}
Euler	0.03	0.03	0.02	0.02	0.02
CNS	0.08	0.09	0.1	0.1	0.11
BGK	113	120	160	161	158
Hybrid (Euler)	61.2	20.1	57	11	0.12
Hybrid (CNS)	25.6	4.9	23	18	3.3

Table 4.4: Comparison of the computational times (sec), $t = 0.10$, $\mathrm{N}_x = 100$, $\mathrm{N}_v = 32^3$.

Concerning the computational times for the same configuration ($\mathrm{N}_x = 100$ and $\mathrm{N}_v = 32^3$), the hybrid schemes, both zeroth and first order, are more efficient than the kinetic models. Indeed, we ran in the paper [FR15] an extensive amount on simulations, with many different models, test cases and values of the Knudsen number. We reproduce the speed up test in Table 4.4.

4.5 Perspectives

Projective integration of the kinetic Keller-Segel model. We have seen that PInt and TPInt are good strategies to develop (almost) AP numerical integrator for a very large class of kinetic equation, in both the hydrodynamic and diffusive scaling, and with very lightly intrusive ways. One particular model still resisting the development of general purpose AP strategy is the Run-and-tumble chemotactic model (1.31). In the diffusive scaling, it was shown in particular that its diffusive limit is the seminal Patlak-Keller-Segel equation. Nevertheless, some open questions remain on the blowup behavior of this limit for a certain range of the initial parameters. Having a robust AP scheme would help answer these questions.

There is only a handful numerical methods AP in the diffusive limit for this model [58, 64], but they are limited to very restricted cases because of the use of an odd-even decomposition of the initial data, with local grid refinement for taking the blowup into account. Nevertheless, a high order "spectral" method in velocity for this model has been recently introduced in [49], using orthogonal polynomials. We plan to use this solver in velocity and the PInt approach introduced in [MRS19, BR22] in time to write arbitrarily high order methods for the run-and-tumble model.

In order to prove the convergence, a study of the spectral structure of this chemotaxis model is envisaged: this is expected to be a difficult problem, because of the possibility of blowup in finite time for this model, which complicates the spectral analysis. Nevertheless, some of the techniques developed in [Rey13] would come in handy.

Projective integration of the granular gases equation. As was pointed out in [Rey13], the granular gases equation with a thermal bath shares a lot of spectral properties with the Boltzmann equation. In particular, the spectrum of such equation separates into a series of clusters, and the use of a TPInt integrator could provide an AP scheme for this model. This would be a true novelty, because no such time integrator exists for granular gases.

Discrete hypocoercivity with confinement. A natural followup of the results of [BHR20] on discrete hypocoercivity will be the adjunction of a mean-field-like confinement term in the kinetic equation, for the study of the numerical drift-diffusion limit

$$\partial_t \rho + \nabla_x \cdot \mathrm{J} = 0, \text{where } \mathrm{J} = -\nabla_x \rho + \rho \nabla_x \mathrm{V},$$
$$-\Delta_x \mathrm{V} = \rho.$$

and for obtaining a discrete hypocoercivity result on the whole space. This could also be done by generalizing the results of [83]. This direction of work is part of the PhD thesis of Tino Laidin. Generalizing this results to the linearized Vlasov-Poisson-BGK equation could then be envisaged, using the ideas introduced in [1].

This modified entropy technique has already been extended to study the large time behavior of many other phenomena modeled by collisional kinetic equations. Let us mention for example the Fokker-Planck-like equation used to model the extrusion of synthetic fiber on a conveyer belt described in [82]; the modeling with equation (1.31) of bacteria such as E. Coli moving via biased velocity jumps in [50]; or the system of BGK-like nonlinear equations describing the behavior of two chemical reactants produced by the decay of another specie introduced in [180]. We believe that these are also candidates models for extending our discrete entropy approach to build numerical methods exhibiting the correct numerical trend to equilibrium.

Hybrid schemes for mixtures. The development of a systematic technique to derive hierarchy of hybrid numerical methods in [FR15] opens a large number of followups. It has already been extended to the multidimensional in space case with high order Discontinuous Galerkin method in [103] for the ES-BGK model. It has also been analysed in the simplified linear BGK case in [155].

Extension to mixtures seems pretty straightforward, because the correct Chapman-Enskog expansion has been established recently in [31]. This would allow for the development of regime indicators as in [FR15] for more realistic models of gas mixtures. Extension to complex geometries in space would also be very interesting in that context, in order to model realistic situations such as the atmospheric reentry of a space shuttle. A very heavy computational engineering effort would also be required for the development of an efficient code for this problem.

Bibliography

[1] Addala, L., Dolbeault, J., Li, X., and Lazhar Tayeb, M. L2-Hypocoercivity and large time asymptotics of the linearized Vlasov-Poisson-Fokker-Planck system. *J. Stat. Phys. 184*, 1 (2021), 4.

[2] Alaia, A., and Puppo, G. A hybrid method for hydrodynamic-kinetic flow, Part II: Coupling of hydrodynamic and kinetic models. *J. Comput. Phys. 231*, 16 (2012), 5217–5242.

[3] Alonso, R., Cañizo, J. A., Gamba, I., and Mouhot, C. A new approach to the creation and propagation of exponential moments in the boltzmann equation. *Commun. Partial Differ. Eq. 38*, 1 (2013), 155–169.

[4] Alonso, R., and Lods, B. Uniqueness and regularity of steady states of the Boltzmann equation for viscoelastic hard-spheres driven by a thermal bath. *Commun. Math. Sci. 11*, 4 (2013), 851–906.

[5] Alonso, R., and Lods, B. Boltzmann model for viscoelastic particles: Asymptotic behavior, pointwise lower bounds and regularity. *Commun. Math. Phys. 331*, 2 (2014), 545–591.

[6] Alonso, R. J., Gamba, I. M., and Tharkabhushanam, S. H. Convergence and error estimates for the Lagrangian-based conservative spectral method for Boltzmann equations. *SIAM J. Numer. Anal. 56*, 6 (2018), 3534–3579.

[7] Alonso, R. J., and Lods, B. Free cooling and high-energy tails of granular gases with variable restitution coefficient. *SIAM J. Math. Anal. 42*, 6 (2010), 2499–2538.

[8] Andries, P., Le Tallec, P., Perlat, J.-p., and Perthame, B. The Gaussian-BGK model of Boltzmann equation with small Prandtl number. *Eur. J. Mech. B Fluids 19*, 6 (Nov. 2000), 813–830.

[9] Araki, S., and Tremaine, S. The Dynamics of Dense Particle Disks. *Icarus 65*, 1 (Jan. 1986), 83–109.

[10] Ascher, U. M., Ruuth, S. J., and Wetton, B. T. Implicit-explicit methods for time-dependent partial differential equations. *SIAM J. Numer. Anal. 32*, 3 (1995), 797–823.

[11] Aure, R., and Jacobs, J. W. Particle image velocimetry study of the shock-induced single mode Richtmyer–Meshkov instability. *Shock Waves 18*, 3 (Aug. 2008), 161–167.

[12] Avogadro, A. Essai d'une manière de déterminer les masses relatives des molécules élémentaires des corps, et les proportions selon lesquelles elles entrent dans ces combinaisons. *Journal de physique, de chimie, d'histoire naturelle et des arts 73* (1810), 58–76.

[13] Baranger, C., and Mouhot, C. Explicit spectral gap estimates for the linearized boltzmann and landau operators with hard potentials. *Rev. Mat. Ibér. 21*, 3 (2005), 819–841.

[14] Barron, J. The Mathematicians Who Ended the Kidnapping of an N.Y.U. Computer. *New York Times* (2015).

[15] Benedetto, D., and Pulvirenti, M. On the one-dimensional Boltzmann equation for granular flows. *M2AN Math. Model. Numer. Anal. 35*, 5 (Apr. 2002), 899–905.

[16] Bensoussan, A., Lions, J. L., and Papanicolaou, G. C. Boundary layers and homogenization of transport processes. *Publications of the RIMS 15*, 1 (1979), 53–157.

[17] Bernoulli, D. *Hydrodynamica, sive de viribus et motibus fluidorum commentarii : opus academicum ab auctore, dum Petropoli ageret, congestum*. J. H. Deckeri, 1738.

[18] Besse, C., and Goudon, T. Derivation of a non-local model for diffusion asymptoticsapplication to radiative transfer problems. *Commun. Comput. Phys 8*, 5 (2010), 1139.

[19] Bessemoulin-Chatard, M., and Filbet, F. A finite volume scheme for nonlinear degenerate parabolic equations. *SIAM J. Sci. Comput. 34*, 5 (2012), B559–B583.

[20] Bhatnagar, P., Gross, E., and Krook, M. A Model for Collision Processes in Gases. I. Small Amplitude Processes in Charged and Neutral One-component Systems. *Phys. Rev. 94*, 3 (1954), 511–525.

[21] Bird, G. *Molecular Gas Dynamics and the Direct Simulation of Gas Flows*, 2nd ed. Oxford University Press, 1994.

[22] Biryuk, A., Craig, W., and Panferov, V. Strong solutions of the Boltzmann equation in one spatial dimension. *C. R. Math. Acad. Sci. Paris 342*, 11 (2006), 843–848.

[23] Bisi, M., Cañizo, J. A., and Lods, B. Uniqueness in the weakly inelastic regime of the equilibrium state to the Boltzmann equation driven by a particle bath. *SIAM J. Math. Anal. 43*, 6 (2011), 2640–2674.

[24] Bobylev, A., and Rjasanow, S. Difference scheme for the Boltzmann equation based on the fast Fourier transform. *Eur. J. Mech. B Fluids 16*, 2 (1997), 293–306.

[25] Bobylev, A. V. Exact solutions of the Boltzmann equation. *Dokl. Akad. Nauk SSSR 225*, 6 (1975), 1296–1299.

[26] Bobylev, A. V., Carrillo, J. A., and Gamba, I. On some properties of kinetic and hydrodynamic equations for inelastic interactions. *J. Stat. Phys. 98*, 3 (2000), 743–773.

[27] Bobylev, A. V., Cercignani, C., and Toscani, G. Proof of an asymptotic property of self-similar solutions of the Boltzmann equation for granular materials. *J. Stat. Phys. 111*, 1-2 (2003), 403–417.

[28] Bobylev, A. V., Gamba, I., and Panferov, V. Moment inequalities and high-energy tails for Boltzmann equations with inelastic interactions. *J. Stat. Phys. 116*, 5 (2004), 1651–1682.

[29] Bobylev, A. V., and Rjasanow, S. Fast deterministic method of solving the Boltzmann equation for hard spheres. *Eur. J. Mech. B Fluids 18*, 5 (1999), 869–887.

[30] Boltzmann, L. Weitere studien über das wärmegleichgewicht unter gasmolekl̈en. *Wiener Berichte 66* (1872), 275–370.

[31] Bondesan, A., Boudin, L., Briant, M., and Grec, B. Stability of the spectral gap for the Boltzmann multi-species operator linearized around non-equilibrium Maxwell distributions. *Commun. Pure Appl. Anal. 19*, 5 (2020), 2549–2573.

[32] Bony, J.-M. Solutions globales bornées pour les modèles discrets de l'équation de Boltzmann, en dimension 1 d'espace. In *Journées "Équations aux derivées partielles" (Saint Jean de Monts, 1987)*. École Polytechnique, Palaiseau, 1987. Exp. No. XVI, 10 pp.

[33] Boscarino, S., Pareschi, L., and Russo, G. Implicit-explicit Runge–Kutta schemes for hyperbolic systems and kinetic equations in the diffusion limit. *SIAM J. Sci. Comput. 35*, 1 (2013), A22–A51.

[34] Bouchut, F., Golse, F., and Pulvirenti, M. *Kinetic equations and asymptotic theory*, vol. 4 of *Series in Applied Mathematics (Paris)*. Gauthier-Villars, Éditions Scientifiques et Médicales Elsevier, Paris, 2000. Edited and with a foreword by Benoît Perthame and Laurent Desvillettes.

[35] Bouchut, F., and James, F. Duality solutions for pressureless gases, monotone scalar conservation laws, and uniqueness. *Comm. Partial Diff. Eq. 24*, 11-12 (1999), 2173–2189.

[36] Boudin, L. A Solution with Bounded Expansion Rate to the Model of Viscous Pressureless Gases. *SIAM J. Math. Anal. 32*, 1 (2000), 172–193.

[37] Bougie, J., Kreft, J., Swift, J. B., and Swinney, H. Onset of patterns in an oscillated granular layer: continuum and molecular dynamics simulations. *Phys. Rev. E 71* (2005), 021301.

[38] Bougie, J., Moon, S. J., Swift, J., and Swinney, H. Shocks in vertically oscillated granular layers. *Phys. Rev. E 66* (2002), 051301.

[39] Bouin, E., Dolbeault, J., Mischler, S., Mouhot, C., and Schmeiser, C. Hypocoercivity without confinement. *Pure Appl. Anal. 2*, 2 (2020), 203–232.

[40] Boyd, I. D., Chen, G., and Candler, G. V. Predicting failure of the continuum fluid equations in transitional hypersonic flows. *Phys. Fluids 7*, 1 (1995), 210.

[41] Boyd, R., Richerson, P. J., and Henrich, J. The cultural niche: Why social learning is essential for human adaptation. *Proc. Natl. Acad. Sci. U.S.A. 108*, Supplement 2 (2011), 10918–10925.

[42] Brenier, Y., and Grenier, E. Sticky particles and scalar conservation laws. *SIAM J. Numer. Anal. 35*, 6 (1998), 2317–2328 (electronic).

[43] Briant, M. Stability of global equilibrium for the multi-species Boltzmann equation. *Discrete Contin. Dyn. Syst. A 36*, 12 (2016), 6669–6688.

[44] Briant, M., and Daus, E. S. The Boltzmann equation for a multi-species mixture close to global equilibrium. *Arch. Ration. Mech. Anal. 222*, 3 (2016), 1367–1443.

[45] Briant, M., and Einav, A. On the Cauchy problem for the homogeneous Boltzmann-Nordheim equation for bosons: local existence, uniqueness and creation of moments. *J. Stat. Phys. 163*, 5 (June 2016), 1108–1156.

[46] Brilliantov, N. V., and Pöschel, T. *Kinetic Theory of Granular Gases*. Oxford University Press, USA, 2004.

[47] Brull, S., and Prigent, C. Local Discrete Velocity Grids for Multi-Species Rarefied Flow Simulations. *Commun. Comput. Phys. 28*, 4 (June 2020), 1274–1304.

[48] Buet, C., and Cordier, S. An asymptotic preserving scheme for hydrodynamics radiative transfer models. *Numer. Math. 108*, 2 (2007), 199–221.

[49] Calvez, V., Gosse, L., and Twarogowska, M. Travelling chemotactic aggregates at mesoscopic scale and bistability. *SIAM J. Appl. Math. 77*, 6 (2017), 2224–2249.

[50] Calvez, V., Raoul, G., and Schmeiser, C. Confinement by biased velocity jumps: aggregation of Escherichia Coli. *Kinet. Relat. Models 8*, 4 (2015).

[51] Carlen, E., Chow, S.-N., and Grigo, A. Dynamics and hydrodynamic limits of the inelastic Boltzmann equation. *Nonlinearity 23*, 8 (2010), 1807–1849.

[52] Carlen, E. A., Carrillo, J. A., and Carvalho, M. C. Strong convergence towards homogeneous cooling states for dissipative Maxwell models. *Ann. I. H. Poincare 26* (2009), 1675–1700.

[53] Carnot, S. Réflexions sur la puissance motrice du feu et sur les machines propres à développer cette puissance. *Bachelier, Libraire* (1824), 1–38.

[54] Carrillo, J.-A., Goudon, T., and Lafitte, P. Simulation of fluid and particles flows: Asymptotic preserving schemes for bubbling and flowing regimes. *J. Comput. Phys. 227*, 16 (2008), 7929–7951.

[55] Carrillo, J. A., Poëschel, T., and Salueña, C. Granular hydrodynamics and pattern formation in vertically oscillated granular disk layers. *J. Fluid Mech. 597* (2008), 119–144.

[56] Carrillo, J. A., and Salueña, C. Modelling of Shock Waves and Clustering in Hydrodynamic Simulations of Granular Gases. In *Modelling and Numerics of Kinetic Dissipative Systems*. Nova Science, New York, 2006, pp. 175–189.

[57] Carrillo, J. A., and Toscani, G. Asymptotic L^1-decay of solutions of the porous medium equation to self-similarity. *Indiana Univ. Math. J. 49*, 1 (2000), 113–142.

[58] Carrillo, J. A., and Yan, B. An asymptotic preserving scheme for the diffusive limit of kinetic systems for chemotaxis. *Multiscale Model. Simul. 11*, 1 (2013), 336–361.

[59] Cercignani, C. A remarkable estimate for the solutions of the Boltzmann equation. *Appl. Math. Lett. 5*, 5 (1992), 59–62.

[60] Cercignani, C., Illner, R., and Pulvirenti, M. *The Mathematical Theory of Dilute Gases*, vol. 106 of *Applied Mathematical Sciences*. Springer-Verlag, New York, 1994.

[61] Chainais-Hillairet, C., and Peng, Y. Finite volume approximation for degenerate drift-diffusion system in several space dimensions. *Math. Models Methods in Appl. Sci. 14* (2004), 461–481.

[62] Chang, J. S., and Cooper, G. A practical difference scheme for Fokker-Planck equations. *J. Comput. Phys. 6*, 1 (1970), 1–16.

[63] Charles, F., Massimini, A., and Salvarani, F. Mathematical and numerical study of a kinetic model describing the evolution of planetary rings. HAL preprint hal-03788536, Sept. 2022.

[64] Chertock, A., Kurganov, A., Lukáčová-Medviďová, M., and Özcan, . N. An asymptotic preserving scheme for kinetic chemotaxis models in two space dimensions. *Kinet. Relat. Models 12*, 1 (2019), 195.

[65] Coulombel, J.-F., Golse, F., and Goudon, T. Diffusion approximation and entropy-based moment closure for kinetic equations. *Asymptotic Anal. 45*, 1, 2 (2005), 1–39.

[66] Crestetto, A., Crouseilles, N., Dimarco, G., and Lemou, M. A new deviational Asymptotic Preserving Monte Carlo method for the homogeneous Boltzmann equation. *Communications in Mathematical Sciences 18*, 8 (2020), 2305–2339.

[67] Cucker, F., and Smale, S. On the Mathematical Foundations of Learning. *Bull. Amer. Math. Soc., 39*, 1 (2002), 1–49.

[68] Cucker, F., and Smale, S. Emergent behavior in flocks. *IEEE Trans. Autom. Control 52*, 5 (May 2007), 852–862.

[69] Daerr, A. *Dynamique des Avalanches*. PhD thesis, Université Denis Diderot Paris ğ7, 2000.

[70] Degond, P., and Dimarco, G. Fluid simulations with localized Boltzmann upscaling by direct simulation Monte-Carlo. *J. Comput. Phys. 231*, 6 (2012), 2414–2437.

[71] Degond, P., Dimarco, G., and Mieussens, L. A multiscale kinetic-fluid solver with dynamic localization of kinetic effects. *J. Comput. Phys. 229*, 13 (2010), 4907–4933.

[72] Degond, P., Frouvelle, A., Liu, J.-G., Motsch, S., and Navoret, L. Macroscopic models of collective motion and self-organization. *Seminaire Laurent Schwartz–EDP et applications, Exp. No. I,(2012-2013)* (2013), 1–27.

[73] Delarue, F., Lagoutìère, F., and Vauchelet, N. Convergence analysis of upwind type schemes for the aggregation equation with pointy potential. *Ann. H. Lebesgue 3* (2020), 217–260.

[74] Dimarco, G., and Loubère, R. Towards an ultra efficient kinetic scheme. Part I: Basics on the BGK equation. *J. Comput. Phys. 255* (2013), 680–698.

[75] Dimarco, G., and Loubère, R. Towards an ultra efficient kinetic scheme. Part II: The high order case. *J. Comput. Phys. 255* (2013), 699–719.

[76] Dimarco, G., Loubère, R., and Narski, J. Towards an ultra efficient kinetic scheme. Part III: High-performance-computing. *J. Comput. Phys. 284* (2015), 22–39.

[77] Dimarco, G., Loubère, R., and Rispoli, V. A multiscale fast semi-Lagrangian method for rarefied gas dynamics. *J. Comput. Phys. 291* (2015), 99–119.

[78] Dimarco, G., Mieussens, L., and Rispoli, V. An asymptotic preserving automatic domain decomposition method for the Vlasov–Poisson–BGK system with applications to plasmas. *J. Comput. Phys. 274* (2014), 122–139.

[79] Dimarco, G., and Pareschi, L. Hybrid Multiscale Methods II. Kinetic Equations. *Multiscale Model. Simul. 6*, 4 (Jan. 2008), 1169–1197.

[80] Dimarco, G., and Pareschi, L. Asymptotic preserving implicit-explicit Runge–Kutta methods for nonlinear kinetic equations. *SIAM J. Numer. Anal. 51*, 2 (2013), 1064–1087.

[81] Dimarco, G., and Pareschi, L. Numerical methods for kinetic equations. *Acta Numerica 23* (2014), 369–520.

[82] Dolbeault, J., Klar, A., Mouhot, C., and Schmeiser, C. Exponential rate of convergence to equilibrium for a model describing fiber lay-down processes. *Appl. Math. Res. eXpress 2013*, 2 (2012), 165–175.

[83] Dolbeault, J., Mouhot, C., and Schmeiser, C. Hypocoercivity for linear kinetic equations conserving mass. *Trans. Amer. Math. Soc. 367*, 6 (2015), 3807–3828.

[84] Dufty, J. W. Nonequilibrium Statistical Mechanics and Hydrodynamics for a Granular Fluid. In *2nd Warsaw School on Statistical Physics* (2008), E. Cichocki, M. Napiorkowski, and J. Piasekcki, Eds., no. June 2007, Warsaw University Press, p. 64.

[85] Dujardin, G., Hérau, F., and Lafitte, P. Coercivity, hypocoercivity, exponential time decay and simulations for discrete Fokker–Planck equations. *Numer. Math. 144*, 3 (2020), 615–697.

[86] E, W., Engquist, B., Li, X., Ren, W., and Vanden-Eijnden, E. Heterogeneous multiscale methods: a review. *Commun. Comput. Phys 2*, 3 (2007), 367–450.

[87] E, W., Rykov, Y. G., and Sinai, Y. G. Generalized variational principles, global weak solutions and behavior with random initial data for systems of conservation laws arising in adhesion particle dynamics. *Commun. Math. Phys. 177*, 2 (1996), 349–380.

[88] Ellis, R. S., and Pinsky, M. A. The First and Second Fluid Approximations to the Linearized Boltzmann Equation. *J. Math. Pures Appl. 54*, 9 (1975), 125–156.

[89] Ernst, M., and Brito, R. Scaling solutions of inelastic Boltzmann equations with over-populated high energy tails. *J. Stat. Phys. 109*, 3-4 (2002), 407–432. Special issue dedicated to J. Robert Dorfman on the occasion of his sixty-fifth birthday.

[90] Escobedo, M., and Mischler, S. On a quantum Boltzmann equation for a gas of photons. *J. Math. Pures Appl. 80* (2001), 471–515.

[91] Escobedo, M., and Velázquez, J. J. L. Finite time blow-up for the boson Nordheim equation. *Invent. Math. 200*, 3 (2015), 761–847.

[92] Esteban, M., and Perthame, B. On the modified Enskog equation for elastic and inelastic collisions. Models with spin. *Ann. Inst. H. Poincaré Anal. Non Linéaire 8*, 3-4 (1991), 289–308.

[93] Eymard, R., Gallouët, T., and Herbin, R. Finite volume methods. In *Handbook of numerical analysis, Vol. VII*, Handb. Numer. Anal., VII. North-Holland, Amsterdam, 2000, pp. 713–1020.

[94] Fabisiak, M., and Peszek, J. Inevitable monokineticity of strongly singular alignment. *arXiv preprint arXiv:2211.01448* (2022).

[95] Faraday, M. On a peculiar class of acoustical figure and on certain forms assumed by groups of particles upon vibrating elastic surfaces. *Philos. Trans. Roy. Soc. London 121* (1831), 299.

[96] Fenichel, N. Geometric singular perturbation theory for ordinary differential equations. *J. Differ. Eq. 31*, 1 (1979), 53–98.

[97] Filbet, F. A spectral collocation method for the Landau equation in plasma physics. arXiv preprint 2006.15885, 2020.

[98] Filbet, F., Hu, J. W., and Jin, S. A Numerical Scheme for the Quantum Boltzmann Equation Efficient in the Fluid Regime. *ESAIM Math. Model. Numer. Anal. 42* (2012), 443–463.

[99] Filbet, F., and Jin, S. A Class of Asymptotic-Preserving Schemes for Kinetic Equations and Related Problems with Stiff Sources. *J. Comput. Phys. 229*, 20 (2010), 7625–7648.

[100] Filbet, F., and Mouhot, C. Analysis of Spectral Methods for the Homogeneous Boltzmann Equation. *Trans. Amer. Math. Soc. 363* (2011), 1947–1980.

[101] Filbet, F., Pareschi, L., and Toscani, G. Accurate Numerical Methods for the Collisional Motion of (Heated) Granular Flows. *J. Comput. Phys. 202*, 1 (2005), 216–235.

[102] Filbet, F., and Russo, G. High order numerical methods for the space non-homogeneous Boltzmann equation. *J. Comput. Phys. 186*, 2 (Apr. 2003), 457–480.

[103] Filbet, F., and Xiong, T. A hybrid discontinuous Galerkin scheme for multi-scale kinetic equations. *J. Comput. Phys. 372* (2018), 841–863.

[104] Filbet, F., and Yang, C. Numerical simulations of kinetic models for chemotaxis. *SIAM J. Sci. Comput. 36*, 3 (2014), B348–B366.

[105] Fournier, N., and Méléard, S. A Microscopic Probabilistic Description of a Locally Regulated Population and Macroscopic Approximations. *Ann. Appl. Probab. 14*, 4 (2004), 1880–1919.

[106] Gallagher, I., Saint-Raymond, L., and Texier, B. *From Newton to Boltzmann: hard spheres and short-range potentials*. European Mathematical Society, 2014.

[107] Gamba, I., Haack, J., Hauck, C., and Hu, J. A fast spectral method for the Boltzmann collision operator with general collision kernels. *SIAM J. Sci. Comput. 39* (2017), B658–B674.

[108] Gamba, I. M., and Tharkabhushanam, S. H. Spectral-Lagrangian methods for collisional models of non-equilibrium statistical states. *J. Comput. Phys. 228*, 6 (Apr. 2009), 2012–2036.

[109] Garzó, V. *Granular Gaseous Flows: A Kinetic Theory Approach to Granular Gaseous Flows*. Springer, Berlin, 2019.

[110] Gear, C. W., and Kevrekidis, I. G. Projective methods for stiff differential equations: problems with gaps in their eigenvalue spectrum. *SIAM J. Sci. Comput. 24*, 4 (2003), 1091–1106.

[111] Gear, C. W., and Kevrekidis, I. G. Telescopic projective methods for parabolic differential equations. *J. Comput. Phys. 187*, 1 (2003), 95–109.

[112] Gilardoni, G. L. On Pinsker's and Vajda's type inequalities for Csiszár's f-divergences. *IEEE Trans. Inform. Theory 56*, 11 (2010), 5377–5386.

[113] Godillon-Lafitte, P., and Goudon, T. A coupled model for radiative transfer: Doppler effects, equilibrium, and nonequilibrium diffusion asymptotics. *Multiscale Model. Simul. 4*, 4 (2005), 1245–1279.

[114] Goldhirsch, I. Scales and kinetics of granular flows. *Chaos 9*, 3 (1999), 659–672.

[115] Goldhirsch, I. Rapid granular flows. *Ann. Rev. Fluid Mech. 35* (2003), 267.

[116] Goldhirsch, I., and Zanetti, G. Clustering instability in dissipative gases. *Phys. Rev. Lett. 70*, 11 (Mar. 1993), 1619–1622.

[117] Goldshtein, A., and Shapiro, M. Mechanics of collisional motion of granular materials. Part 1: General hydrodynamic equations. *J. Fluid. Mech. 282* (1995), 75.

[118] Golse, F. The Boltzmann equation and its hydrodynamic limits. In *Handbook of Differential Equations: Evolutionary Equations Vol. 2*, C. Dafermos and E. Feireisl, Eds. North-Holland, 2005, pp. 159–303.

[119] Gosse, L., and Toscani, G. Space localization and well-balanced schemes for discrete kinetic models in diffusive regimes. *SIAM J. Numer. Anal. 41*, 2 (2003), 641–658.

[120] Gosse, L., and Toscani, G. Asymptotic-preserving & well-balanced schemes for radiative transfer and the rosseland approximation. *Numer. Math. 98*, 2 (2004), 223–250.

[121] Grad, H. Principles of the kinetic theory of gases. In *Thermodynamik der Gase/Thermodynamics of Gases*. Springer, 1958, pp. 205–294.

[122] Grad, H. The many faces of entropy. *Comm. Pure Appl. Math. 14*, 3 (1961), 323–354.

[123] Haack, J. R., Hauck, C. D., and Murillo, M. S. A Conservative, Entropic Multispecies BGK Model. *J. Stat. Phys. 168*, 4 (Aug. 2017), 826–856.

[124] Haff, P. Grain flow as a fluid-mechanical phenomenon. *J. Fluid Mech. 134* (1983), 401–30.

[125] Hérau, F. Hypocoercivity and exponential time decay for the linear inhomogeneous relaxation boltzmann equation. *Asymptot. Anal. 46*, 3, 4 (2006), 349–359.

[126] Hilbert, D. Mathematical problems (transl. M.W. Newson). *Bull. Amer. Math. Soc 8* (1902), 437–479.

[127] Hill, S. A., and Mazenko, G. F. Granular clustering in a hydrodynamic simulation. *Phys. Rev. Lett. 67* (2003), 061302.

[128] Hu, J., and Ma, Z. A fast spectral method for the inelastic Boltzmann collision operator and application to heated granular gases. *J. Comput. Phys. 385* (2019), 119–134.

[129] Hu, J., Qi, K., and Yang, T. A New Stability and Convergence Proof of the Fourier–Galerkin Spectral Method for the Spatially Homogeneous Boltzmann Equation. *SIAM Journal on Numerical Analysis 59*, 2 (2021), 613–633.

[130] Hu, J., and Wang, L. An asymptotic-preserving scheme for the semiconductor Boltzmann equation toward the energy-transport limit. *J. Comput. Phys. 281* (2015), 806–824.

[131] Hu, J., and Ying, L. A fast spectral algorithm for the quantum Boltzmann collision operator. *Commun. Math. Sci. 10*, 3 (2012), 989–999.

[132] Hu, J., and Ying, L. A fast algorithm for the energy space boson Boltzmann collision operator. *Math. Comput. 84* (2015), 271–288.

[133] Huang, F., and Wang, Z. Well Posedness for Pressureless Flow. *Comm. Math. Phys. 222*, 1 (Aug. 2001), 117–146.

[134] Hörmander, L. Hypoelliptic second order differential equations. *Acta Math. 119* (1967), 147–171.

[135] Jabin, P.-E., and Hauray, M. Particles approximations of Vlasov equations with singular forces: Propagation of chaos. *Ann. Sci. École Norm. Sup.* (2015), 891–940.

[136] Jabin, P.-E., and Wang, Z. Quantitative estimates of propagation of chaos for stochastic systems with $W^{1,\infty}$ kernels. *Invent. Math 214*, 1 (2018), 523–591.

[137] Jenkins, J., and Richman, M. Grad's 13-moment system for a dense gas of inelastic spheres. *Arch. Ration. Mech. Anal. 87* (1985), 355–377. 10.1007/BF00250919.

[138] Jin, S. Efficient Asymptotic-Preserving (AP) Schemes for some Multiscale Kinetic Equations. *SIAM J. Sci. Comput. 21*, 2 (1999), 441–454.

[139] Jin, S. Asymptotic preserving (AP) schemes for multiscale kinetic and hyperbolic equations: a review. *Riv. Math. Univ. Parma (N.S.) 3*, 2 (2012), 177–216.

[140] Jin, S., and Pareschi, L. Discretization of the Multiscale Semiconductor Boltzmann Equation by Diffusive Relaxation Schemes. *J. Comput. Phys. 330* (2000), 312–330.

[141] Jin, S., Pareschi, L., and Toscani, G. Diffusive relaxation schemes for multiscale discrete-velocity kinetic equations. *SIAM J. Numer. Anal. 35*, 6 (1998), 2405–2439.

[142] Jin, S., Pareschi, L., and Toscani, G. Uniformly accurate diffusive relaxation schemes for multiscale transport equations. *SIAM J. Numer. Anal. 38*, 3 (2000), 913–936.

[143] Johnson, C. G., and Gray, J. M. N. T. Granular jets and hydraulic jumps on an inclined plane. *J. Fluid Mech. 675* (2011), 87116.

[144] Kang, M.-J., and Vasseur, A. Asymptotic Analysis of Vlasov-type Equation Under Strong Local Alignment Regime. preprint arXiv 1412.3119.

[145] Kawai, T., and Shida, K. An Inelastic Collision Model for the Evolution of Planetary Rings. *J. Phys. Soc. Japan 59*, 1 (Jan. 1990), 381–388.

[146] Kevrekidis, I., Gear, W., Hyman, J., Kevrekidis, P., Runborg, O., and Theodoropoulos, C. Equation-free, coarse-grained multiscale computation: Enabling microscopic simulators to perform system-level analysis. *Commun. Math. Sci. 1*, 4 (2003), 715–762.

[147] Klar, A. An asymptotic-induced scheme for nonstationary transport equations in the diffusive limit. *SIAM J. Numer. Anal. 35*, 3 (1998), 1073–1094.

[148] Klar, A. A Numerical Method for Kinetic Semiconductor Equations in the Drift-Diffusion Limit. *SIAM J. Sci. Comput. 20*, 5 (1999), 1696–1712.

[149] Klar, A. An asymptotic preserving numerical scheme for kinetic equations in the low mach number limit. *SIAM J. Numer. Anal. 36*, 5 (1999), 1507–1527.

[150] Kolobov, V., Arslanbekov, R., Aristov, V., a.a. Frolova, and Zabelok, S. Unified solver for rarefied and continuum flows with adaptive mesh and algorithm refinement. *J. Comput. Phys. 223*, 2 (May 2007), 589–608.

[151] Kurganov, A., and Tsynkov, S. On spectral accuracy of quadrature formulae based on piecewise polynomial interpolations. *IMA J. of Math. Anal. 25*, 4 (2005).

[152] Lafitte, P., Lejon, A., and Samaey, G. A high-order asymptotic-preserving scheme for kinetic equations using projective integration. *SIAM J. Numer. Anal. 54*, 1 (2016), 1–33.

[153] Lafitte, P., Melis, W., and Samaey, G. A high-order relaxation method with projective integration for solving nonlinear systems of hyperbolic conservation laws. *J. Comput. Phys. 340* (2017), 1–25.

[154] Lafitte, P., and Samaey, G. Asymptotic-preserving projective integration schemes for kinetic equations in the diffusion limit. *SIAM J. Sci. Comput. 34*, 2 (2012), A579–A602.

[155] Laidin, T. Hybrid Kinetic/Fluid numerical method for the Vlasov-BGK equation in the diffusive scaling. arXiv preprint 2202.03696, 2022.

[156] Landau, L., and Lifshitz, E. *Course of Theoretical Physics*. Butterworth-Heinemann, 1976.

[157] Landau, L., and Lifshitz, E. *Course of Theoretical Physics Vol 6. Fluid Mechanics*. Butterworth-Heinemann, 1987.

[158] Lee, S. L., and Gear, C. W. Second-order accurate projective integrators for multiscale problems. *J. Comput. Appl. Math. 201*, 1 (2007), 258–274.

[159] Lemou, M., and Mieussens, L. A new asymptotic preserving scheme based on micro-macro formulation for linear kinetic equations in the diffusion limit. *SIAM J. Sci. Comput. 31*, 10 (2008), 334–368.

[160] Levermore, C. D., Morokoff, W. J., and Nadiga, B. T. Moment realizability and the validity of the Navier-Stokes equations for rarefied gas dynamics. *Phys. Fluids 10*, 12 (1998), 3214–3226.

[161] Li, H., and Toscani, G. Long-Time Asymptotics of Kinetic Models of Granular Flows. *Arch. Ration. Mech. Anal. 172*, 3 (May 2004), 407–428.

[162] Li, W., and Lu, X. Global existence of solutions of the Boltzmann equation for Bose–Einstein particles with anisotropic initial data. *J. Funct. Anal. 276*, 1 (2019), 231–283.

[163] Lowenberg, P. The Collected Papers of Albert Einstein: Vol. 1, The Early Years, 1879-1902. *Science 239*, 4839 (1988), 510–513.

[164] Lu, X. The Boltzmann equation for Bose-Einstein particles: regularity and condensation. *J. Stat. Phys. 156*, 3 (2014), 493–545.

[165] Maxwell, J. C. On the Stability of the Motion of Saturn's Rings; an Essay which obtained the Adams' Prize for the Year 1856, in the University of Cambridge. *Mon. Not. R. Astron Soc. 19*, 8 (1859).

[166] Maxwell, J. C. On the dynamical theory of gases. *Philos. Trans. Roy. Soc. London 157* (1867), 49–88.

[167] McNally, C. P., Lyra, W., and Passy, J.-C. A Well-posed Kelvin-Helmholtz Instability Test and Comparison. *Astrophys. J. Suppl. Ser. 201*, 2 (2012), 18.

[168] McNamara, S., and Young, W. R. Inelastic collapse in two dimensions. *Phys. Rev. E 50* (1993), R28–R31.

[169] Melis, W., and Samaey, G. Telescopic projective integration for kinetic equations with multiple relaxation times. *J. Sci. Comput. 76*, 2 (2018), 697–726.

[170] Melo, F., Umbanhowar, P., and Swinney, H. L. Hexagons, kinks, and disorder in oscillated granular layers. *Phys. Rev. Lett. 75* (1995), 3838–3841.

[171] Mischler, S., and Mouhot, C. Cooling process for inelastic Boltzmann equations for hard spheres, Part II: Self-similar solutions and tail behavior. *J. Stat. Phys. 124*, 2 (2006), 703–746.

[172] Mischler, S., and Mouhot, C. Stability, convergence to self-similarity and elastic limit for the Boltzmann equation for inelastic hard spheres. *Commun. Math. Phys. 288*, 2 (2009), 431–502.

[173] Mischler, S., and Mouhot, C. Stability, convergence to the steady state and elastic limit for the Boltzmann equation for diffusively excited granular media. *Discrete Contin. Dyn. Syst. 24*, 1 (2009), 159–185.

[174] Mischler, S., Mouhot, C., and Ricard, M. Cooling process for inelastic Boltzmann equations for hard spheres, Part I: The Cauchy problem. *J. Stat. Phys. 124*, 2 (2006), 655–702.

[175] Mischler, S., Mouhot, C., and Wennberg, B. A new approach to quantitative propagation of chaos for drift, diffusion and jump processes. *Probab. Theory Relat. Fields 161*, 1-2 (2015), 1–59. Preprint Arxiv 1101.4727.

[176] Motsch, S., and Tadmor, E. Heterophilious dynamics enhances consensus. *SIAM Rev. 56*, 4 (2014), 577–621.

[177] Mouhot, C. Stabilité orbitale pour le système de Vlasov-Poisson gravitationnel. *Séminaire Bourbaki 64* (Novembre 2011), 45.

[178] Mouhot, C., and Villani, C. On Landau damping. *Acta Math. 207*, 1 (Dec. 2011), 29–201.

[179] Naldi, G., Pareschi, L., and Toscani, G. Spectral methods for one-dimensional kinetic models of granular flows and numerical quasi elastic limit. *ESAIM Math. Model. Numer. Anal. 37*, 1 (2003), 73–90.

[180] Neumann, L., and Schmeiser, C. A kinetic reaction model: Decay to equilibrium and macroscopic limit. *Kinet. Relat. Models 9*, 3 (2016), 571–585.

[181] Nicolaenko, B. Dispersion Laws for Plane Wave Propagation. In *The Boltzmann Equation Seminar - 1970 to 1971* (1971), F. Grunbaum, Ed., Courant Institute of Mathematical Sciences, pp. 125–172.

[182] Oleinik, O. On Cauchys problem for nonlinear equations in a class of discontinuous functions. *Doklady Akad. Nauk SSSR (N.S.) 95* (1954), 451–454.

[183] Othmer, H. G., Dunbar, S. R., and Alt, W. Models of dispersal in biological systems. *J. Math. Biol. 26*, 3 (1988), 263–298.

[184] Pallard, C. Moment Propagation for Weak Solutions to the Vlasov-Poisson System. *Commun. Partial Differ. Eq. 37*, 7 (July 2012), 1273–1285.

[185] Pareschi, L., and Markowich, P. Fast, conservative and entropic numerical methods for the Bosonic Boltzmann equation. *Numer. Math. 99* (2005), 509–532.

[186] Pareschi, L., and Perthame, B. A Fourier Spectral Method for Homogeneous Boltzmann Equations. *Transport Theory Statist. Phys. 25*, 3 (1996), 369–382.

[187] Pareschi, L., and Russo, G. Numerical Solution of the Boltzmann Equation I : Spectrally Accurate Approximation of the Collision Operator. *SIAM J. Numer. Anal. 37*, 4 (2000), 1217–1245.

[188] Pareschi, L., Toscani, G., and Villani, C. Spectral methods for the non cut-off Boltzmann equation and numerical grazing collision limit. *Numer. Math. 93*, 3 (Jan. 2003), 527–548.

[189] Rericha, E. C., Bizon, C., Shattuck, M. D., and Swinney, H. L. Shocks in supersonic sand. *Phys. Rev. Lett. 88* (Dec 2001), 014302.

[190] Richerson, P. J., and Boyd, R. *Not by genes alone*. University of Chicago Press, 2010.

[191] Rico-Martinez, R., Gear, C. W., and Kevrekidis, I. G. Coarse projective kMC integration: forward/reverse initial and boundary value problems. *J. Comput. Phys. 196*, 2 (2004), 474–489.

[192] Saffirio, C. Derivation of the Boltzmann equation: hard spheres, short-range potentials and beyond. In *From Particle Systems to Partial Differential Equations III*. Springer, 2016, pp. 301–321.

[193] Saint-Raymond, L. *Hydrodynamic Limits of the Boltzmann Equation*. Hydrodynamic Limits of the Boltzmann Equation. Springer, 2009.

[194] Saragosti, J., Calvez, V., Bournaveas, N., Buguin, A., Silberzan, P., and Perthame, B. Mathematical description of bacterial traveling pulses. *PLoS Comput. Biol. 6*, 8 (2010), e1000890.

[195] Scharfetter, D., and Gummel, H. Large signal analysis of a silicon Read diode. *IEEE Trans. Elec. Dev. 16* (1969), 64–77.

[196] Schmeiser, C., and Zwirchmayr, A. Convergence of moment methods for linear kinetic equations. *SIAM J. Numer. Anal. 36*, 1 (1999), 74–88.

[197] Serre, D. Divergence-free positive symmetric tensors and fluid dynamics. *Ann. Inst. H. Poincaré Anal. Non Linéaire 35*, 5 (2018), 1209–1234.

[198] Shen, J., Tang, T., and Wang, L.-L. *Spectral methods: algorithms, analysis and applications*, vol. 41. Springer Science & Business Media, 2011.

[199] Sone, Y. *Molecular Gas Dynamics: Theory, Techniques, and Applications*. Modeling And Simulation in Science, Engineering And Technology. Birkhäuser, 2007.

[200] Spohn, H. *Dynamics of charged particles and their radiation field*. Cambridge university press, 2004.

[201] Struchtrup, H. *Macroscopic transport equations for rarefied gas flows*, 1 ed. Interaction of Mechanics and Mathematics. Springer, 2005.

[202] Tindall, M. J., Maini, P. K., Porter, S. L., and Armitage, J. P. Overview of mathematical approaches used to model bacterial chemotaxis ii: bacterial populations. *Bull. Math. Biol. 70*, 6 (2008), 1570.

[203] Tiwari, S. Coupling of the Boltzmann and Euler equations with automatic domain decomposition. *J. Comput. Phys. 144*, 2 (Aug. 1998), 710–726.

[204] Tiwari, S., Klar, A., and Hardt, S. A particle-particle hybrid method for kinetic and continuum equations. *J. Comput. Phys. 228*, 18 (2009), 7109–7124.

[205] Tiwari, S., Klar, A., and Hardt, S. Simulations of micro channel gas flows with domain decomposition technique for kinetic and fluid dynamics equations. In *21st International Conference on Domain Decomposition Methods* (2012), pp. 197–206.

[206] Torrilhon, M. Two-dimensional bulk microflow simulations based on regularized Grad's 13-moment equations. *Mult. Mod. & Sim. 5*, 3 (2006), 695–728.

[207] Toscani, G. One-dimensional kinetic models of granular flows. *M2AN Math. Model. Numer. Anal. 34*, 6 (Apr. 2000), 1277–1291.

[208] Toscani, G. Kinetic and Hydrodynamic Models of Nearly Elastic Granular Flows. *Monatsh. Math. 142*, 1 (2004), 179–192.

[209] Tristani, I. Boltzmann equation for granular media with thermal force in a weakly inhomogeneous setting. *J. Funct. Anal. 270*, 5 (2016), 1922–1970.

[210] Uehling, E., and Uhlenbeck, G. Transport phenomena in Einstein-Bose and Fermi-Dirac gases. I. *Phys. Rev. 43* (1993), 552–561.

[211] Villani, C. *A Review of Mathematical Topics in Collisional Kinetic Theory*. Elsevier Science, 2002.

[212] Villani, C. Mathematics of Granular Materials. *J. Stat. Phys. 124*, 2 (2006), 781–822.

[213] Villani, C. Hypocoercivity. *Mem. Amer. Math. Soc. 202* (2009), 184.

[214] Von Helmoltz, H. Über Discontinuierliche Flüssigkeits-Bewegungen [On the Discontinuous Movements of Fluids]. *Monatsberichte der Königlichen Preussiche Akademie der Wissenschaften zu Berlin 23*, 215-228 (1868).

[215] Womersley, R. S. Efficient spherical designs with good geometric properties. In *Contemp. Comput. Math.* Springer, 2018, pp. 1243–1285.

[216] Wu, L., White, C., Scanlon, T. J., Reese, J. M., and Zhang, Y. Deterministic numerical solutions of the Boltzmann equation using the fast spectral method. *J. Comput. Phys. 250* (2013), 27–52.

[217] Wu, L., Zhang, J., Reese, J. M., and Zhang, Y. A fast spectral method for the Boltzmann equation for monoatomic gas mixtures. *J. Comput. Phys. 298* (Oct. 2015), 602–621.

[218] Wu, L., Zhang, Y., and Reese, J. M. Fast spectral solution of the generalized Enskog equation for dense gases. *J. Comput. Phys. 303* (2015), 66–79.

[219] Wu, Z. L^1 and BV-type stability of the inelastic Boltzmann equation near vacuum. *Continuum Mech. Thermodyn. 22*, 3 (Nov. 2009), 239–249.

[220] Wu, Z. On the inelastic Enskog equation near vacuum. *J. Math. Phys. 51*, 3 (2010), 033508.

Résumé

Cette habilitation couvre une grande partie des recherches effectuées depuis mon doctorat. Les principales questions que je me suis posées concernent le champ de la modélisation, de l'analyse et des simulations numériques de systèmes composés d'un grand nombre de particules ou agents en interaction, grâce à l'utilisation d'équations cinétiques collisionnelles comme l'équation de Boltzmann, l'équation des gaz granulaires, ou des modèles cinétiques de comportement collectifs. Ces modèles décrivent de nombreuses situations complexes et vitales pour le monde moderne, comme par exemple la pollution, les transports ou les maladies. Les comprendre mathématiquement, les analyser, et savoir les résoudre numériquement de manière précise et efficace est un problème important.

Avec mes collaborateurs scientifiques, nous avons donc travaillé sur trois grandes thématiques qui sont présentées dans ce texte. La première concerne le développement de nouvelles méthodes spectrales pour calculer efficacement et avec la plus grande précision possible les opérateurs dits de collision qui interviennent dans ces modèles, les analyser et les implémenter efficacement. La deuxième concerne la compréhension de l'équation des gaz granulaires, modèle encore très largement ouvert et incompris, et notamment ses limites hydrodynamiques de type compressibles. La troisième, enfin, concerne l'étude des comportements asymptotiques en temps longs et petits paramètres de ces équations, et le développement de méthodes numériques préservant ces comportements, les méthodes dites AP.

Abstract

This habilitation thesis covers a large part of the research I have carried out since the end of my PhD training. This work has been essentially aimed at modeling, analyzing and simulating systems composed of a large number of interacting particles or agents. These systems can be described through the framework of collisional kinetic equations, such as the seminal Boltzmann's equation, the granular gases equations, or kinetic systems of collective behavior. Such models describes complex and sometimes vital situations in a modern, evolving world, such as pollution, traffic and disease spreading, to name but a few. To understand them mathematically, to analyze them, and to be able to solve them accurately and efficiently with numerical methods is an important modern problem.

With my scientific collaborators, we have worked on three main topics that are presented in this text. The first one concerns the development of new spectral methods to calculate efficiently and with the highest possible accuracy the so-called collision operators which intervene in these models, to analyze them and to implement them efficiently. The second one concerns the understanding of the granular gas equation, a model which is still largely open and misunderstood, and in particular its hydrodynamic limits of the compressible type. The third, finally, concerns the study of asymptotic behaviors in long time and small parameters of these equations, and the development of numerical methods preserving these behaviors, the so-called AP methods.